Alternative Substrates for Sustainable and Earth-abundant Thin Film Photovoltaics

Ignacio Becerril Romero

Alternative Substrates for Sustainable and Earth-abundant Thin Film Photovoltaics

Memòria presentada per optar al grau de doctor per la

Universitat de Barcelona

Programa de doctorat en

Enginyeria i Ciències Aplicades

Autor: Ignacio Becerril Romero

Directors: Dr. Edgardo Saucedo Silva i Dr. Paul Pistor

Tutor: Prof. Dr. Alejandro Pérez-Rodríguez

UNIVERSITAT DE BARCELONA

Institut de Recerca en Energia de Catalunya
Catalonia Institute for Energy Research

Every human civilization has inevitably collapsed. Ours is not going to be different. However, this time we have the knowledge and capacity to decide how we want it to happen. Let’s make it softly, peacefully and living long and happy lives in harmony with nature.

Acknowledgments

I could not have done this thesis without the help, support, guidance and wisdom of many, many people. I will try to show my gratitude to all of them but, if I forget anybody, do not take it personally. My brain is really exhausted after the hard work of the last months.

I would like to start by thanking Edgardo for giving me the opportunity of doing my PhD studies in IREC under his supervision. Likewise, I would like to thank Paul, my second supervisor, for his knowledge and valuable inputs. I have learned a lot from you both and I hope I can keep learning from you in the future. Of course, I would also like to thank Alejandro, my thesis tutor, for his guidance and for always finding some time to help everybody despite the stress and the huge amount of work to which he is usually exposed.

Now, I will try to thank all the people with whom I have worked and/or that have contributed to this thesis either professionally, personally or both. For the sake of equality, I will stick to the following order:

1. IREC workers
    a. Time-based: the different stage of the thesis in which I met you or work with you.
    b. Alphabetically
2. Other places
3. Family and friends

IREC workers

Old times

Alex → Thank you for your unconditional friendship and support that, I am sure, will last for very long after you leave IREC and find your own way.

Diouldé → I could write at least 30 pages to express my sincere gratitude for everything you have done for me in the last years. Unfortunately, this thesis is already too long. You are an extraordinary person. Thank you for EVERYTHING.

Florian → Thank you for sharing with me so many nice moments inside and outside IREC and for being my sparring in the Kung Fu classes.

Haibing → You are an extremely gifted researcher and a super nice person. In addition, you are my ping pong and Kung Fu master. I appreciate all the time we have spent together. Thank you very much.

Laura → Thank you for being by my side (literally), for giving me so much support in my first two years in IREC and for not forgetting about me when you left.

Marcel → I have learned so much from you…: sputtering, guarradas, coffee, bikes… Thank you for that, for being such a nice and wise guy and for your invaluable support.

Markus → Thank you for teaching me so much, for your wisdom and for always being in a positive mood.

Max → Thank you for you calmed friendship, your nice company and your professionality.

Moisés → I am very thankful for letting me continue your research on transparent substrates and use it for this thesis. Thank you also for everything else.

Mónica → Thank you for your friendship and for all the support you gave me at the first stages of my thesis.

Rokas → Thank you for eating pizza with me on Fridays in the old times, for your support (especially with the 5th chapter of this thesis) and for your friendship.

Sergio → Thank you for all these years working together, for all the times you have helped me and for all the nice moments we have shared.

Simón → I am very thankful to you. You were the person taking care of me in my first days in IREC with your special style (I still remember my first day when you bombarded me with all your research mixed with "mona" and "clin clin") but with great research abilities. I owe you a lot about my research and way I do it which is clearly inspired in yours. In addition, you supported me from day one. Thank you very much.

Víctor → Thank you for your wisdom, your enthusiasm, your support, the Monday beers and for caring about me.

Yudania → Thank you for being always on my side supporting me, for teaching me all I know about chemical processing and for being the good person you are.

I would also like to thank other people from the old times in IREC with whom I shared part of my thesis: Cristina, Doris, Matías, Mirjana and Xavi.

More recent times

Jacob → Thank you for being my friend, for your scientific discussions, your company until 10 pm in the lab, for your support, for sharing so many things with me both inside and outside IREC, for always supporting me and for making me a part of your life.

Mohamed → Thank you for being always in a pleasant mood and for always thinking good of me.

Pedro → Thank you for your nice and relaxed character, for your support and for inviting me to join you so many times to smoke (even though I am not a smoker) and to other healthier activities.

Very recent times

Alex gallego → Thank you for your support and for being such a nice guy and a good colleague in the short time you have been in IREC.

Robert → Thank you for your hard work, your professionality and your calmed character.

Zak → Thank you for being there every single time I have asked you for help and for your knowledge and support.

I would also like to thank the newest guys, Kunal and Oriol, for being so nice to me during the little time they have been in IREC.

LATAM

Thanks to all the LATAM people in IREC for sharing with me their culture and friendliness.

Esteban → Thank you for your friendship and for being always so kind and positive.

Jacob → See previous section. But also thank you for making me part of the LATAM community.

Parce → Thank you for being such a good friend and for sharing so much with me during the time you were here.

Roberto → Thank you for all the help you gave us, your professionality and for being such a nice person.

Thanks also to César and el Perú for the moments we have shared.

MASCIR

I would like to thank all the people in MAScIR for becoming my family during my secondment there: Prof Sekkat, Safae, Siham, Sara, Sanaa, Nadjet, Nada, Yahya, Tarik, Hatim and Abderrahim and, of course, to Zakaria.

A very special thanks goes to my dear Imad. Thank you for being such a good friend and colleague and for taking care of me in Morocco.

Others

Thanks to Diego and Iván, from UJI, for the ceramic substrates as well as for their help and friendliness during the ECOART project.

In addition, I would like to thank Alfonso for making me pass from looking comfortably into the abyss of growth, energy and sustainability to making me fall into it.

Finally, there is a person that should also be thanked because, without her, this and many scientific works would not be possible: Alexandra Elbakyan. Thanks for making science freely available for everybody, as it should be.

Family and friends

This work would have not been possible at all without the support given to me by my family and friends.

Thanks to my friends from Zaragoza: Alb, Basti, Blesa, Eric, Nacho y Quílez; for always being there when I needed them regardless our ups and downs.

I would of course like to thank my parents: my father José Luis and my mother Elda. All that I am and all that I have achieved is thanks to you. I will always be grateful to you. Likewise, I would also like to thank my sister Sofía, my grandmothers, Aurora y Ángeles, my grandfathers (wherever they are), Pepe y Pascual, and the rest of my family for everything they have done for me and given to me.

And, last but not least, thanks to my beloved wife Anita. Thank you for being always by my side, for suffering my grumpy mood all the times that I have been stressed (i.e. 90% of the days), for dealing with my frequent migraines, for helping me in every way you can, for caring so much about me and for your unconditional and true love.

Table of contents

Preface and publications

The work presented in this thesis was carried out at the Catalonian Institute for Energy Research (IREC) in Sant Adrià de Besòs (Barcelona, Spain) from 2015 to 2019 in the framework of the ECOART project (RTC-2014-2426-7) from the Ministry of Economy and Competitiveness (MINECO) of the Government of Spain; and of the INFINITE-CELL project (H2020-MSCA-RISE-2017-777968) from the European Commission. The main subject of the thesis is the development of Earth-abundant $Cu_2ZnSn(S_x,Se_{1-x})_4$ (kesterite) solar cells on three strategic alternative substrates (polyimide, ceramic and transparent substrates) which have the potential to sustainably reduce the energy fabrication cost of photovoltaics through their compatibility with mass production processes and/or advanced applications. The thesis is structured in six chapters: the first chapter gives a general introduction and expounds the main motivations behind this work, the second chapter describes the experimental methodology employed, the three following chapters cover the main results obtained throughout the thesis and, finally, the last chapter summarizes and highlights the outcomes and conclusions of this work. A more detailed description of the different chapters that comprise the structure of the thesis is presented below:

· **The first chapter** is subdivided in well differentiated sections. It starts with an analysis of the role of photovoltaics in the current socioeconomic system taking into account the lights and shadows of this way of renewable energy with a focus on its energy return on energy investment (EROI). Then, the fundamentals of solar cells are briefly examined in order to provide an understanding of the key concepts behind their structure and operation. This is followed by a review of the state-of-the-art and sustainability of the current commercial photovoltaic technologies comparing 1st generation (Si-based) and 2nd generation (thin film) devices with a stress on the main issues that may limit their present and future EROI. Next, kesterite-based 2nd generation solar cells are introduced as a sustainable alternative to such commercial technologies. The evolution of the technology from its early stages until the present state-of-the-art is thoroughly reviewed together with its main limitations and technological challenges. Finally, as a result of the ideas presented throughout the different parts of the chapter, the importance of developing kesterite solar cells on alternative substrates to the conventional Mo-coated soda-lime glass is expounded giving rise, in turn, to the objectives the thesis.

· **The second chapter** covers the experimental methodology employed throughout this work. First, a brief overview of such methodology is presented. Then, the main characterisation, deposition and synthesis techniques used throughout the thesis as well as the pieces of equipment employed to carry them out are described and explained. Finally, the fabrication process followed for the fabrication of kesterite solar cells is thoroughly detailed.

The next three chapters cover the main results obtained with the three different types of alternative substrates investigated: polyimide (light-weight and flexible), ceramic and transparent. The third (polyimide) and fourth (ceramic) chapters are based on scientific papers published in high impact factor peer-reviewed journals,as will be detailed below, while the material presented in the fifth chapter has not been published yet. All of them start with a brief examination of the advantages and possibilities of each of the substrates for photovoltaics compared to conventional Mo-coated soda-lime glass. This is followed by a review of the best results obtained so far with each substrate focusing on kesterite and closely related Cu(In,Ga)Se_2-based devices. Then, the main limiting factors as well as the technological challenges of the substrates for the fabrication of kesterite solar cells are explored and suitable strategies to overcome them are proposed.

· **The third chapter** is based on the following publication (reproduced with permission, copyrighted by John Wiley and Sons):

I. Becerril-Romero, L. Acebo, F. Oliva, V. Izquierdo-Roca, S. López-Marino, M. Espíndola-Rodríguez, M. Neuschitzer, Y. Sánchez, M. Placidi, A. Pérez-Rodríguez, E. Saucedo, P. Pistor, *CZTSe solar cells developed on polymer substrates: Effects of low-temperature processing*, Prog. Photovolt. Res. Appl. (2017). doi:10.1002/pip.2945. Impact factor: 6.726

The chapter explores the fabrication of $Cu_2ZnSnSe_4$ solar cells on polyimide: a light-weight and flexible substrate. The main limitations of the substrate are identified to be its lack of alkaline elements and its low thermal robustness that limits process temperatures below 500°C. These issues are experimentally addressed throughout the chapter. First, different doping strategies are investigated for the incorporation of Na and K on devices fabricated on polyimide at 470°C. Pre-annealing synthesis is shown to be an effective doping strategy that causes important improvements in solar cell performance and carrier concentration when doping either with NaF or KF. Then, the effect of working at different kesterite synthesis temperatures (450-490°C) is studied both on polyimide and standard soda-lime glass. Working at low temperature is linked to the formation of a detrimental $SnSe_2$ secondary phase, especially on polyimide. This phase is found to decrease the open-circuit voltage of the devices and to be the main factor controlling their performance. Further experimentation leads to a 4.9% efficiency record device on polyimide by combining NaF and Ge doping at a 480°C.

· **The fourth chapter** is based on the following publication (reproduced with permission, copyrighted by Elsevier):

I. Becerril-Romero, S. Giraldo, S. López-Marino, M. Placidi, Y. Sánchez, D. Sylla, A. Pérez-Rodríguez, E. Saucedo, P. Pistor, Vitreous enamel as sodium source for efficient kesterite solar cells on commercial ceramic tiles, Sol. Energy Mater. Sol. Cells. 154 (2016) 11–17. doi:10.1016/j.solmat.2016.04.035. Impact factor: 4.732

The work presented in this chapter studies the feasibility of producing efficient $Cu_2ZnSnSe_4$ solar cells on ceramic substrates which have a direct application in building-integrated photovoltaics. An innovative approach is employed to overcome the limitations of ceramic substrates for solar cell fabrication: high roughness, lack of alkaline elements and presence of detrimental impurities. This way, vitreous enamels with controlled amounts of Na_2O in their composition (2-20% wt%) are used as surface smoothers, diffusion barriers for impurities and sodium sources. It is observed that trying to accommodate large amounts of Na_2O in the enamels results in high densities of three surface defects: undulations, pinholes and cracks. While undulations and pinholes do not affect cell performance critically, cracks are identified as very detrimental since they strongly deteriorate the conductivity of the back contact. Besides surface defects, enamelled ceramic substrates are observed to behave in a similar way to conventional soda-lime glass. In particular, an effective Na diffusion from the enamel is detected which leads to significant improvements on device performance. In addition, the annealing process is found to be critical. In a first attempt, a too long annealing time leads to the formation of $SnSe_2$ degrading the performance of the devices. However, this phase is completely eliminated by reducing the annealing time yielding a record device on ceramic with a 7.5% efficiency.

· **The fifth chapter** investigates the development of $Cu_2ZnSnSe_4$, Cu_2ZnSnS_4 and $Cu_2ZnSn(S,Se)_4$ solar cells on SnO_2:F-coated soda-lime glass transparent substrates. In particular, the effect of adding thin layers of a wide selection of transition metal oxides and/or of Mo:Na on top of such substrates is studied as an approach to improve the non-optimum p-kesterite/n-contact back interface of the devices. Firstly, the optical and electrical properties of the deposited transition metal oxides nanolayers are studied before and after being submitted to an annealing process to verify their compatibility with the fabrication of kesterite devices. Then solar cells are fabricated on the different oxide-containing substrate configurations. Shunting appears as the main limitation of kesterite devices fabricated on the bare transparent substrate while the addition of transition metal oxides introduces a severe current blockage. On the other hand, the use of a Mo:Na nanolayer and its subsequent transformation into $Mo(S_x,Se_{1-x})_2$ is found to alleviate shunting and to protect SnO_2:F from degradation during annealing leading to highly improved devices. Then, the combination of the different transition metal oxides with Mo:Na is investigated. Although it does not lead to significant improvements for most of the oxides, TiO_2 and V_2O_5 are observed to further increase the performance of $Cu_2ZnSnSe_4$ and $Cu_2ZnSn(S,Se)_4$ devices, respectively, while degrading the performance of Cu_2ZnSnS_4 ones. In addition, an improvement in charge collection towards the back interface is also observed for these substrate configurations although they exhibit a complex behaviour. Despite this complexity, record efficiencies of 6.2%, 6.1% and 7.9% are obtained for $Cu_2ZnSnSe_4$, Cu_2ZnSnS_4 and $Cu_2ZnSn(S,Se)_4$ devices, respectively. Finally, morphological, structural and in-depth compositional characterisation of the best devices is carried out for a better understanding of the results.

· **The sixth chapter** summarizes the main results and conclusions of the thesis.

Prefacio y publicaciones

El trabajo presentado en esta tesis fue llevado a cabo en el Institut de Recerca en Energia de Catalunya (IREC) situado en Sant Adrià del Besòs (Barcelona, España) entre los años 2015 y 2019 en el marco del proyecto ECOART (RTC-2014-2426-7) del Ministerio de Economía y Competitividad (MINECO) del Gobierno de España; y del proyecto INFINITE-CELL (H2020-MSCA-RISE-2017-777968) de la Comisión Europea. El tema principal de la tesis es el desarrollo de células solares de $Cu_2ZnSn(S_x,Se_{1-x})_4$ (Kesterita), las cuales están basadas en elementos abundantes en la corteza terrestre, sobres tres sustratos alternativos estratégicos con potencial para reducir de manera sostenible los costes energéticos de fabricación de la fotovoltaica a través de su compatibilidad con procesos de producción en masa y/o con aplicaciones avanzadas. La tesis se estructura en seis capítulos: el primer capítulo consiste en una introducción general en la que se exponen las principales motivaciones detrás de este trabajo, el segundo capítulo describe la metodología experimental utilizada, los tres capítulos siguientes recogen los principales resultados obtenidos durante la tesis y, finalmente, el último capítulo resume y puntualiza las conclusiones obtenidas en este trabajo. A continuación, se describen con más detalles los distintos capítulos que componen la estructura de la tesis:

· **El primer capítulo** se divide en secciones bien diferenciadas. Comienza con un análisis del papel de la fotovoltaica en el sistema socioeconómico actual en el que se discuten los puntos fuertes y débiles de esta forma de energía renovable centrándose en su tasa de retorno energético (EROI). Posteriormente, se examinan brevemente los fundamentos de las células solares con el fin de establecer un pequeño marco teórico que permita comprender los conceptos clave detrás de su estructura y funcionamiento. Seguidamente, se lleva a cabo una revisión del estado del arte y de la sostenibilidad de las tecnologías fotovoltaicas comerciales actuales en la que se comparan los dispositivos de 1ª generación (basados en Si) y los de 2ª generación (de capa delgada) haciendo hincapié en los principales limitantes de su EROI tanto en el presente como para el futuro. A continuación, se presentan las células solares de 2ª generación basadas en Kesterita como una alternativa a las tecnologías comerciales actuales. Se describe la evolución de la tecnología desde sus inicios hasta el estado del arte actual y se analizan las principales limitaciones y retos tecnológicos que presenta. Finalmente, como resultado de las ideas presentadas a los largo del capítulo, se expone la importancia de desarrollar células solares de Kesterita sobre sustratos alternativos al vidrio soda-lima recubierto de Mo lo que da lugar, a su vez, al establecimiento de los objetivos de la tesis.

· **El segundo capítulo** abarca la metodología experimental utilizada a lo largo de este trabajo. Primero, se realiza un pequeño resumen de dicha metodología. Seguidamente, se describen y explican las principales técnicas de caracterización, depósito y síntesis usadas a lo largo de la tesis así como los equipos utilizados para llevarlas a cabo. Finalmente, se detalla minuciosamente el proceso seguido para la fabricación de células solares de Kesterita.

Los siguientes tres capítulos recogen los resultados obtenidos con los tres tipos de sustratos alternativos estudiados: poliimida (ligero y flexible), cerámico y transparente. El tercer (poliimida) y cuarto (cerámica) capítulos están basados en artículos científicos publicados en revistas de revisión por pares de alto impacto, como se detalla más abajo, mientras que el material presentado en el quinto capítulo no ha sido publicado todavía. Los tres capítulos comienzan con una breve descripción de las ventajas y posibilidades de cada uno de los sustratos de cara a su aplicación en fotovoltaica con respecto al sustrato estándar vidrio soda-lima recubierto de Mo, seguida de una revisión de los mejores resultados obtenidos con ellos en dispositivos fotovoltaicos basados en Kesterita y en $Cu(In,Ga)Se_2$. Seguidamente, se analizan sus principales limitaciones y los retos tecnológicos que plantean para la fabricación de células solares de Kesterita y se proponen estrategias para superarlos.

· **El tercer capítulo** está basado en la siguiente publicación (reproducida con permiso, copyright de John Wiley and Sons):

I. Becerril-Romero, L. Acebo, F. Oliva, V. Izquierdo-Roca, S. López-Marino, M. Espíndola-Rodríguez, M. Neuschitzer, Y. Sánchez, M. Placidi, A. Pérez-Rodríguez, E. Saucedo, P. Pistor, *CZTSe solar cells developed on polymer substrates: Effects of low-temperature processing*, Prog. Photovolt. Res. Appl. (2017). doi:10.1002/pip.2945. Factor de impacto: 6.726

Este capítulo explora la fabricación de células solares de $Cu_2ZnSnSe_4$ sobre poliimida: un sustrato ligero y flexible. Su falta de elementos alcalinos y su baja robustez térmica, la cual limita las temperaturas de procesado por debajo de los 500ºC, se identifican como los principales limitantes del sustrato. Estos factores son abordados experimentalmente a lo largo del capítulo. Primero se investigan diferentes estrategias de dopado para la incorporación de Na y K en dispositivos fabricados sobre poliimida a 470ºC. Se observa que "síntesis pre-recocido" es una estrategia de dopado efectiva que causa importantes mejoras en el funcionamiento de las células solares y en su densidad de portadores cuando se dopa con NaF o KF. A continuación se estudia el efecto de trabajar a distintas temperaturas de fabricación (450ºC-490ºC) tanto sobre poliimida como sobre vidrio soda-lima. Se observa que trabajar a baja temperatura provoca la formación de una fase secundaria perjudicial de $SnSe_2$, especialmente en el caso de la poliimida. Esta fase disminuye el voltaje de circuito abierto de los dispositivos fotovoltaicos y se perfila como el principal factor que controla su funcionamiento. Experimentos adicionales llevan a la obtención de un dispositivo record de 4.9% de eficiencia en poliimida combinando el dopado con NaF y Ge a 480ºC.

· **El cuarto capítulo** está basado en la siguiente publicación (reproducida con permiso, copyright de Elsevier):

I. Becerril-Romero, S. Giraldo, S. López-Marino, M. Placidi, Y. Sánchez, D. Sylla, A. Pérez-Rodríguez, E. Saucedo, P. Pistor, Vitreous enamel as sodium source for efficient kesterite solar cells on commercial ceramic tiles, Sol. Energy Mater. Sol. Cells. 154 (2016) 11–17. doi:10.1016/j.solmat.2016.04.035. Factor de impacto: 4.732

El trabajo presentado en este capítulo estudia la factibilidad de producir células solares eficientes de $Cu_2ZnSnSe_4$ sobre sustratos cerámicos con aplicación directa en la fotovoltaica integrada en edificios. Se utiliza un enfoque innovador para superar las limitaciones de los sustratos cerámicos para la fabricación de células solares: su alta rugosidad, falta de elementos alcalinos y la presencia de impurezas perjudiciales. Así, se utilizan esmaltes vítreos con contenido controlado de Na_2O en su composición (2-20% en peso) para alisar la superficie de la cerámica, como barrera contra la difusión de impurezas y como fuente de sodio. Se observa que intentar acomodar grandes cantidades de Na_2O en el esmalte produce una alta densidad de tres defectos superficiales: ondulaciones, agujeros y grietas. Por un lado, las ondulaciones y agujeros no afectan el funcionamiento de las células solares de manera crítica. Sin embargo, las grietas deterioran fuertemente la conductividad del contacto trasero resultando altamente perjudiciales. Dejando a un lado los defectos de superficie, se observa que los sustratos cerámicos esmaltados se comportan de manera similar al vidrio soda-lima convencional. Concretamente, se detecta una difusión efectiva de Na que mejora significativamente el funcionamiento de los dispositivos fotovoltaicos. Por otra parte, se detecta que el proceso de recocido es crítico. En un primero intento, un recocido excesivamente largo resulta en la formación de la fase $SnSe_2$, la cual degrada el funcionamiento de los dispositivos. Sin embargo, esta fase se consigue eliminar completamente reduciendo el tiempo de recocido los que conduce a la obtención de un dispositivo record con una eficiencia de 7.5% sobre cerámica.

· **El quinto capítulo** investiga el desarrollo de células solares de $Cu_2ZnSnSe_4$, Cu_2ZnSnS_4 and $Cu_2ZnSn(S,Se)_4$ sobre sustratos transparentes de vidrio recubierto con SnO_2:F. En concreto, se estudia el efecto de añadir capas delgadas de óxido de metales de transición y/o de Mo:Na sobre dichos sustratos como estrategia para mejorar la interfaz trasera no óptima kesterita-p/contacto-n de los dispositivos. Primero se lleva a cabo un estudio de las propiedades ópticas y eléctricas de las nanocapas de óxidos de metales de transición, antes y después de ser sometidas a un proceso de recocido, para comprobar su compatibilidad con el proceso de fabricación de dispositivos de kesterita. A continuación se fabrican células solares sobre configuraciones de sustrato que incluyen los distintos óxidos. Las corrientes de deriva (shunts) se muestran como la principal limitación de los dispositivos de kesterita fabricados sobre los sustratos transparentes sin capas adiciones mientras que la adición de óxidos de metales de transición ocasiona una barrera para el flujo de corriente. Por otra parte, el uso de Mo:Na y su transformación en $Mo(S_x,Se_{1-x})_2$ disminuyen los shunts y protegen el SnO_2:F durante el proceso de recocido lo que conlleva una gran mejora de los dispositivos. Seguidamente, se investiga la combinación de los diferentes óxidos de metales de transición con Mo:Na. Aunque esto no produce mejoras significativas para la mayoría de los óxidos, se observa que el TiO_2 y el V_2O_5 incrementan los efectos beneficiosos de las capas de Mo:Na en los dispositivos de $Cu_2ZnSnSe_4$ y $Cu_2ZnSn(S,Se)_4$, respectivamente, mientras que degradan el funcionamiento de los de Cu_2ZnSnS_4. Además, se observa una mejora de la colección de cargas fotogeneradas en la región de la interfaz trasera de los dispositivos aunque muestra un comportamiento complejo. A pesar de dicha complejidad, se obtienen eficiencias record de 6.2%, 6.1% y 7.9% en dispositivos de $Cu_2ZnSnSe_4$ y Cu_2ZnSnS_4 y $Cu_2ZnSn(S,Se)_4$, respectivamente. Finalmente, se lleva a cabo una caracterización morfológica, estructural y de composición en profundidad para una mejor comprensión de los resultados.

· **El sexto capítulo** resume los resultados y conclusiones principales de la tesis.

List of acronyms and abbreviations

4pp	Four point probe
A	Diode quality/ideality factor
ARC	Anti-reflective coating
a-Si	Amorphous silicon
at%	Percentage in atomic concentration
AZO	Al-doped ZnO
BAPV	Building-attached photovoltaics
BIPV	Building-integrated photovoltaics
CAS	Complex adaptive system
CB	Conduction band
CBD	Chemical bath deposition
CIGS	$Cu(In,Ga)Se_2$
CIS	$CuInSe_2$
CPV	Concentrated photovoltaics
c-Si	Crystalline silicon
CSP	Concentrated solar thermal power
CSS	Closed-space sublimation
CTE	Coefficient of thermal expansion
C-V	Capacitance -Voltage
CVD	Chemical vapour deposition
CZTS	Cu_2ZnSnS_4
CZTSe	$Cu_2ZnSnSe_4$
CZTSSe	$Cu_2ZnSn(S_x,Se_{1-x})_4$
DC	Direct current
E_{bi}	Built-in electric field
E_c	Position of the conduction band minimum
EDX	Energy-disperssive X-ray spectroscopy
E_g	Energy gap/Bandgap
EHP	Electron-hole pair
EQE	External quantum efficiency
EROI	Energy return on energy investment
E_U	Urbach's energy
E_v	Position of the valence band maximum
eV	Electron-Volt
FESEM	Field emission scanning electron microscopy
FF	Fill factor
FTO	Fluorine-doped SnO_2
FWHM	Full width at half maximum
GDP	Gross domestic product
GR	Growth rate
HOMO	Highest occupied molecular orbital
HP	Hot plate
HVDC	High-voltage direct current

ICP	Inductively coupled plasma mass spectroscopy
IoT	Internet of things
ITO	$SnO_2:In_2O_3$
J	Current density
J_0	Reverse saturation current
J_{mp}	Current density at the maximum power point
J_{ph}	Photogenerated current density
J_{sc}	Short-circuit current density
k_B	Boltzmann's constant
LED	Light-emitting diode
LT-PAT	Low temperature post-annealing treatment
LWF	Light-weight flexible
MPP	Maximum power point
Mtoe	Million tonnes of oil equivalent
n	Concentration of electrons/electron doped
N_A	Concentration of acceptor defects
N_D	Concentration of donor defects
n_i	Intrinsic concentration
NIR	Near infrared
OPEC	Organization of the Petroleum Exporting Countries
OPV	Organic photovoltaics
p	Concentration of holes/hole doped
PAS	Pre-absorber synthesis
p_B	Base vacuum
PDT	Post-deposition treatment
PI	Polyimide
P_{in}	Power reaching a solar cell
P_{max}	Maximum power
p-Si	Polycrystalline silicon
P_{theo}	Maximum theoretical power
PV	Photovoltaics
PVD	Physical vapour deposition
q	Elemental charge
R2R	Roll-to-roll
R_a	Average roughness
RF	Radio frequency
R_{rms}	Root mean square roughness
R_s	Series resistance
R_{sh}	Shunt resistance
R_{sheet}	Sheet resistance
RTP	Rapid thermal annealing
SCR	Space charge region
SLG	Soda-lime glass
SQ	Shockley-Queisser
SRH	Shockley-Read-Hall
T	Temperature

TCO	Transparent conductive oxide
TF	Tubular furnace
TJ	Terajoule
TMO	Transition metal oxide
TOF-SIMS	Time-of-flight secondary ion mass spectroscopy
UV	Ultraviolet
V	Voltage/Volts
VB	Valence band
vis	Visible
V_{mp}	Voltage at the maximum power point
V_{oc}	Open-circuit voltage
W_p	Peak Watt
wt%	Percentage in weight
XRD	X-ray diffraction
XRF	X-ray fluorescence
η	Power conversion efficiency
λ_{ex}	Excitation wavelength
μc-Si	Micro-crystalline silicon
μ_e	Electron mobility
μ_p	Hole mobility
σ_e	Electron conductivity
σ_p	Hole conductivity

Table of figures

Chapter 1

List of tables

1. Introduction

1.1 Energy supply in a growth-addicted financial system: what is the role of photovoltaics in all this?

1.1.1 The threat of fossil-fuel dependence: the hidden link between economy, growth, complexity and energy

Although most people tend to ignore it, either because they do not know or want to think about it, human civilization and our current model of society might be at the edge of collapse. The main reason for this is that the global financial system on which our current civilization is founded has developed in such a way that it requires continuous and sustained growth in order to function correctly and provide “stability” [1–3]. The most clear aspect of its growth-dependency is the use of debt as the motor driving the economy: banks, companies and governments create different types of debt with interest rates that can only be repaid in the future when the global economy has grown [3,4]. But, what is growth, where does it come from and why is it threatening for our society?

It is necessary to start this brief analysis by understanding that our financial system and even our civilization behaves and can be accurately modelled as a complex adaptive system (CAS), i.e. a system comprised by individual parts that are able to adapt as a whole to generate a collective shift in its internal behaviour in order to prolong its existence [2,3,5,6]. Living organisms and ecosystems are typical examples of CASs. In this context, growth can be defined and understood as an increase in the complexity of the system. The complexity of a CAS is represented by its size, the distinctiveness of its constituent parts, the diversity of specialised roles that it incorporates, the information exchange between its parts and the self-organising mechanisms that convert these into a coherent, functioning whole [3,7]. In the case of human civilization, we commonly identify the increase of complexity as “progress”: rise of world population, globalised economy, advances in science and technology, high degree of interconnection through the development of transport and telecommunication infrastructures, etc.

The evolution of every complex system found in nature, including our global economy and civilization, is subjected to the laws of thermodynamics [2,3,5]. In particular, the second law of thermodynamics states that physical systems, such as CASs, tend to dissipate energy (in the form of heat) and increase their entropy until reaching equilibrium with their surroundings. Therefore, growth or increased complexity (which denotes ordered or low entropy states) goes against the natural thermodynamic flow toward randomness [6]. However, CASs are open systems that are able to overcome thermodynamic decay by using low entropy energy and transforming it into useful work before dissipating it in the form of heat to their surroundings and, this way, maintain and even increase their complexity [2,3,5,6]. In other words, CASs can only exist at the expense of a continuous energy input. What is more, this also implies that the level of complexity that can be attained by CASs depends on the availability of low entropy energy sources and on the ability of the system to exploit them.

Consequently, economy, growth, progress and energy consumption are inherently connected by the fundamental laws of thermodynamics that govern the evolution of CASs and cannot be treated separately. This may be difficult to conceive for some or sound too simplistic to others but whether we like it or not the laws of thermodynamics lie at the foundations of life itself and it would be pretentious to think that they cannot be applied to understand the way humans behave at a global scale. Actually, it is not difficult to find solid evidences that support this idea. Figure 1 gives proof of the deep connection between energy, growth and economy. It shows that the world energy consumption has been increasing year after year for the last 40 years along with the world economy (Figure 1, left) and that every growth of the world's gross domestic product (GDP) has been driven by an increasing and adaptive energy input (Figure 1, right) [8]. This means that our financial system behaves as a complex system and needs a continuous and increasing flow of energy in order to keep growing and avoid collapse. This would not pose an immediate problem to our society if we had access to a clean and inexhaustible energy source that could meet the world increasing demand for energy but, currently, 90% of this demand is supplied by fossil and nuclear fuels (Figure 2) which are far from cleanness and inexhaustibility [9].

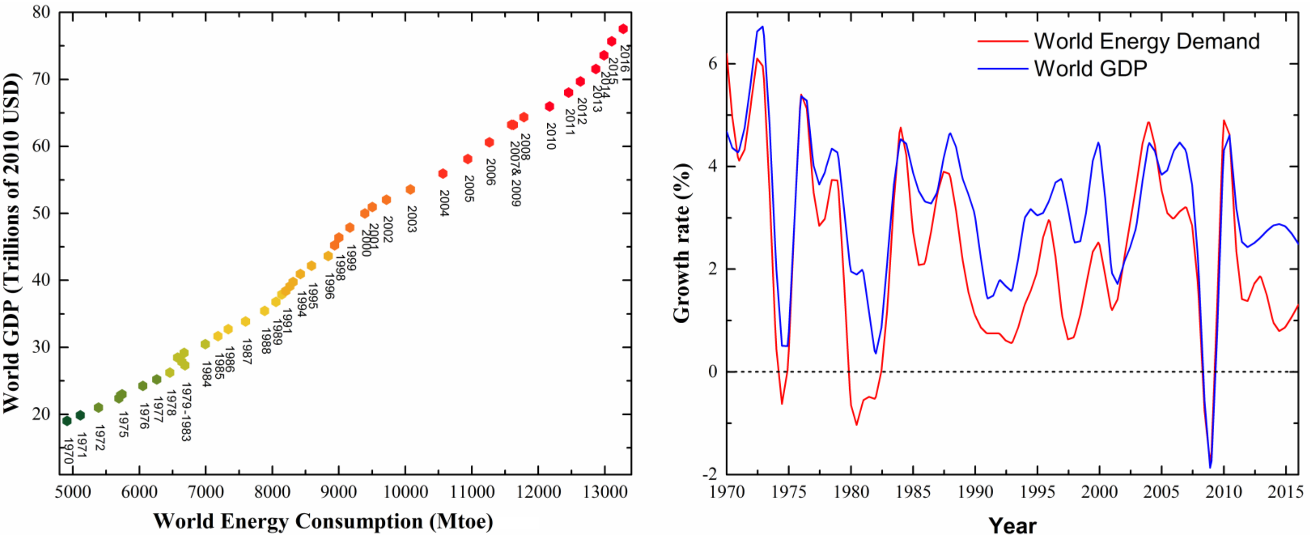

Figure 1. Left: World GDP vs World energy consumption. Right: Growth rate of the world GDP and world energy demand. Sources: World energy consumption extracted from BP's Statistical Review of World Energy - underpinning data, 1965-2016; real world GDP from United States Department of Agriculture

Fossil fuels are the result of ancient organic matter, mainly vegetation, buried under an enormous amount of sediment rocks in low-oxygen and extreme pressure and temperature conditions for hundreds of millions of years. This organic matter grew and stored energy through photosynthesis in the form of carbon-based chemical bonds [10]. As a consequence of the extreme conditions, the energy stored in the matter gets highly concentrated resulting in burnable fuels. Depending on the nature of the organic matter and the conditions of the process three different kinds of fossil fuel can arise: coal, oil and natural gas.

Even though it took the Earth hundreds of millions of years to create fossil fuels, human kind has managed to drain the planet's reserves at an astonishing speed in little more than 200 years, since the dawn of the Industrial Revolution. As can be seen in Table 1, the proven reserves of oil, gas and coal will last for just 54, 53 and 150 years respectively at the current consumption rate. However, this prediction is far too optimistic for several reasons. Firstly, if the world economy is to keep growing, the energy consumption will increase accordingly. The U.S. Energy Information Administration forecasts a 28% increase in energy demand by 2040 [11]. Consequently, the reserves will decrease much faster (last row of Table 1). Secondly, the size of the reserves and the consumption rate do not provide a realistic view of the situation. A very important factor that needs to be taken into account is the energy return on energy investment (EROI) of fossil fuels, i.e. the ratio of the amount of primary energy contained in the fuel to the amount of energy employed to extract that energy from it:

$$EROI = \frac{Energy\ output}{Energy\ input} \tag{1}$$

When a reservoir (coal mine or oil/gas field) is first discovered it is relatively easy to extract its resources and, thus, its EROI is very high. It can be regarded as taking the "low hanging fruit" from a tree [1]. However, as the easy-to-exploit resources deplete, exploitation becomes harder and more resources (viz. money and energy) need to be put into extracting the fuels thus decreasing their EROI. As an example, when the first oil fields in the USA were discovered in 1919 they had an EROI of 30:1 that decreased below 10:1 in 2010 [12]. In addition, the purity of the fuel also affects its EROI. For example, oil extracted from tar sands is estimated to have an EROI as low as 4:1 [13]. This means that not the whole reserves are viably exploitable. And, thirdly, as one of the fuels starts to deplete or becomes more expensive to exploit, it will be partially substituted by the others thus increasing the overall depletion rate [1].

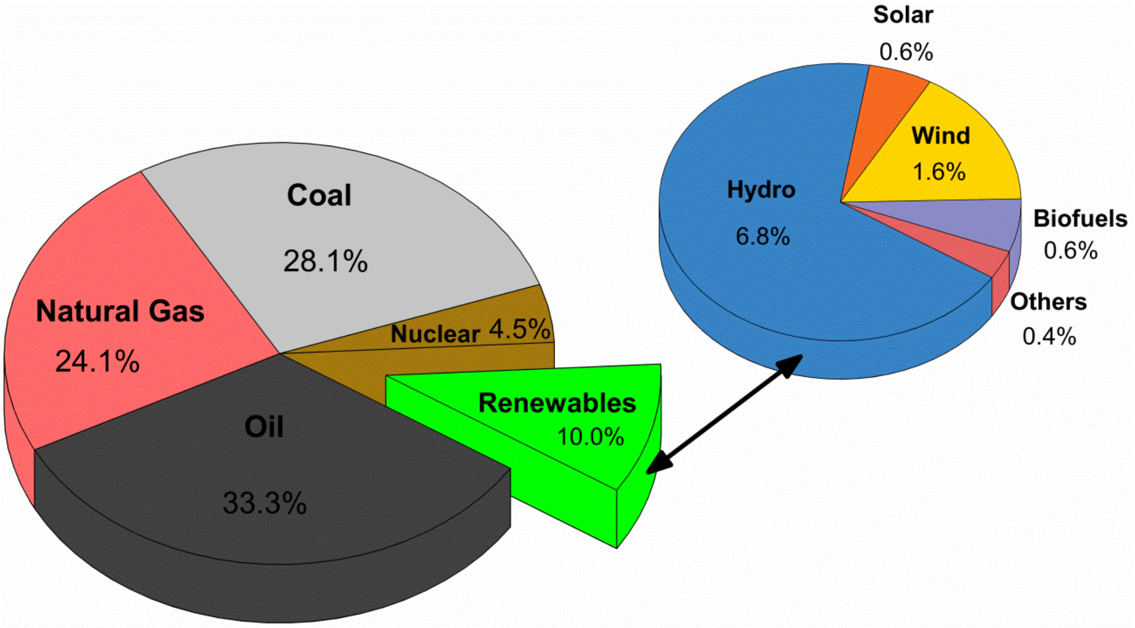

Figure 2. World energy consumption by fuel during 2016. Source: [9] and BP's Statistical Review of World Energy - underpinning data, 1965-2016.

One might argue that we should not worry about the availability of fossil fuels in the future because more reserves will be found and technological improvements will allow us to exploit the current reserves to a larger extent. However, fuel scarcity is not the only issue for a fossil fuel-based civilization. Even in the unlikely scenario of everlasting cheap fossil fuels, the environmental effects of burning oil, coal and gas would force us to put an end to the fossil fuel era before their depletion. It is widely known that burning fossil fuels releases enormous amounts of CO_2 to the atmosphere. Only during 2016 human-related emissions ascended to the unconceivable amount of 10 Gigatonnes of carbon [14]. Earth's CO_2 sinks (mainly forests and oceans) can only absorb around 50% of human emissions so the rest simply accumulates in the atmosphere [15]. Just in the last 40 years the atmospheric CO_2 has raised from around 340 ppm to more than 400 ppm [14]. CO_2 is a greenhouse gas and, consequently, its accumulation in the atmosphere causes the Earth's temperature to rise in a process commonly referred to as "global warming" which may have serious impacts on global climate with potential disastrous consequences for our civilization. Abrupt climate change can lead to the decline and collapse of many ecosystems leading to widespread extinctions and it can even endanger food supply by decreasing the productivity of the oceans and by causing crops to fail more regularly [16]. In addition to CO_2 and its climatic consequences, burning fossil fuels also releases numerous pollutants (especially particulates, sulphur oxides and nitrogen oxides) to the environment that affect ecosystems and pose serious risks for human health [17].

Table 1. Reserves and depletion year of fossil fuels. Source: BP's Statistical Review of World Energy - underpinning data, 1965-2016 and [11].*Assuming 2016's proven reserves and consumption. †Assuming a 28% linear increase of consumption for every fossil fuel from 2016 to 2040. ‡Assuming estimated 2040's remaining reserves and consumption.

	Oil	Coal	Natural Gas
Proven reserves (2016)	240710 Mt	1139331 Mt	186574 km^3
Consumption (2016)	4418 Mt	7615 Mt	3542 km^3
Depletion year*	2069	2165	2068
Remaining reserves in 2040†	109134 Mt	912567 Mt	81096 km^3
Consumption in 2040†	5655 Mt	9747 Mt	4534 km^3
Depletion year‡	2059	2134	2058

In summary, the astonishing degree of complexity achieved by our society has only been possible thanks to the enormous amount of energy provided by fossil fuels. We depend on a continuous and growing supply of cheap fossil fuels in order to avoid the collapse of civilization as we know it. However, such a system is completely unsustainable since fossil fuels are a limited resource approaching depletion and, in addition, their massive employment is threatening our society by globally altering Earth's climate and polluting the planet. Thus, we need to shift towards a more sustainable model if we want to delay or, more optimistically, avoid collapse.

1.1.2 Lights and shadows of photovoltaics: potential, EROI and limitations

In order to develop a more sustainable energy model, we need to start by decreasing our huge dependency on fossil fuels. Their substitution by renewable energies is often regarded as the solution or, at least, as the roadmap to follow for the decarbonisation of the current socioeconomic system. Renewables can generate energy from inexhaustible natural phenomena without emitting CO_2 or pollutants to the atmosphere. This is why they are usually referred to as green energies. There is a wide variety of phenomena that can be used for power generation. These can be Sun-triggered (e.g. sunlight, rain, wind or biomass growth) or can have other origins (e.g. geothermal heat or tides).

Among all renewable sources, sunlight has by far the highest theoretical potential to substitute fossil fuels with 89300 TJ of energy reaching the Earth's surface every second of which roughly 7500 TJ are estimated to be viably convertible into electricity [18]. To put this figure into perspective, at that power rate the current yearly world primary (not only electricity) energy demand (see Figure 1) could be met in around one day. In another work, it was estimated that covering a total area of just 785000 km^2 (~8.5% of the Sahara desert) distributed throughout different "sweet spots" in Earth (blue discs in Figure 3) with 8% energy conversion efficiency solar power generators would suffice to meet the world energy demand [19]. Hence, at first glance it seems that all the energy problems of our civilization can be easily solved by shifting towards a solar-based energy model and, moreover, that there is still huge room for our financial system to keep growing so there is nothing to worry about. Surely, these rough figures give a sense of the huge availability of solar energy. However, if one wants to assess the real capacity of solar energy in replacing fossil fuels there are other factors that should be taken into account.

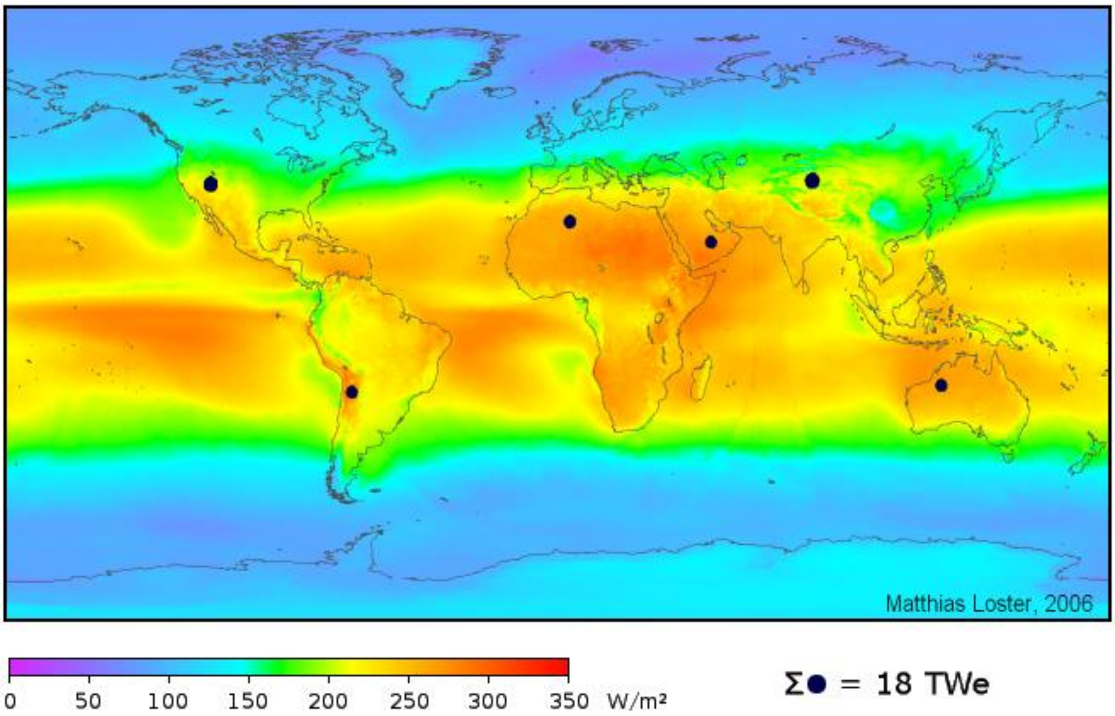

Figure 3. Average solar irradiance from 1991 to 1993. The blue discs represent the area needed to be covered with PV power generators to meet the world energy demand assuming an 8% energy conversion efficiency. For more details of the origin of the data check source. Source: [19]

Before addressing this issue, let us start by analysing the different ways of capturing the energy contained in sunlight. There are two types of solar energy harvesting technologies: solar photovoltaics (PV) and solar thermal. PV technologies are based on the use of semiconductor materials that convert sunlight into electricity while solar thermal devices transform sunlight into heat. In both cases light can be concentrated prior to its conversion by the use of mirrors or lenses combined with sun trackers. This way, concentrating photovoltaics (CPV) allow to obtain greater conversion efficiencies and concentrated solar thermal power (CSP) can be employed to drive steam-based generators and produce electricity [20]. However, concentrating technologies (both CPV and CSP) only work with direct sunlight, present difficult technological challenges and cannot currently compete with conventional photovoltaics due to their higher cost [21]. In addition, conventional solar PV presents several advantages versus concentrating technologies: 1) module manufacturing can be done in large production factories allowing for economies of scale; 2) it is a very modular technology which results in very flexible generation; and 3) in contrast to CPV and CSP conventional PV can generate power from diffuse sunlight increasing its range of favourable geographical locations [20]. Consequently, conventional PV is the dominant solar technology in the market representing 98% of all solar power plants in the world with an accumulated capacity of 303 GW in 2016 [22]. As such, PV is the only relevant solar technology in the present day.

Now we can return to the evaluation of the capacity of solar energy (mainly PV) to replace fossil fuels to power our current socioeconomic system. In this context, EROI is a very valuable tool since it gives a clear numeric picture of the energetic profitability of different energy sources (both renewable and non-renewable) and allows direct comparison between them. In the case of burnable fuels, the calculation of EROI from Eq.(1) is rather straightforward: it is the ratio between the primary energy contained in the fuel (energy output) over the energy needed to extract and process it (energy input). In the case of PV, the inputs necessary for computing the two terms involved in Eq.(1) are a bit more complicated but, in general, are as following:

- Energy output → energy produced by solar panels during their lifetime
- Energy input → energy necessary for extraction of raw materials, manufacturing of the final product, transportation, installation, operation, maintenance and end-of-life management.

Our modern society has been estimated to require energy sources with an EROI of at least 14:1 in order to maintain the present living standards such as health care, education, art, etc. [23]. Oil, gas and coal surpass this limit with current EROIs around 15:1, 50:1 and 70:1, respectively, and 30:1 for the combination of the three fossil fuels together [24]. So, what about PV? It should be noted that there is no consensus in how to estimate the EROI of PV since a lot of different datasets, assumptions and boundaries can be used to calculate the energy in and energy out terms depending on the PV technologies analysed, the geographical locations examined or the objective of the study generating a wide range of results (for more information about EROI calculation procedures for PV see references [25–27]). This fact becomes especially critical when trying to calculate a global value. However, some moderately optimistic studies point towards an average EROI value of around 10:1 for the current state of the technology [13,23,28–30]. This value states that PV is a viable means of power generation but, at the same time, it also renders clear that direct substitution of fossil fuels by PV is not currently viable.

This result might be shocking because the PV community often tends to focus on the huge availability of solar energy and to overlook (or even forget about) its inherent drawbacks. However, in order to understand the motivation behind this thesis, it is necessary to analyse and comprehend the limitations of this way of renewable energy generation. On the one hand, solar irradiance is not equally distributed throughout the globe and strongly depends on latitude and climate as shown in Figure 3. In addition, only direct sunlight is truly useful for power generation. Thus, the energy yield of PV is very location-specific with the most productive locations (like American Southwest or the Saharan Africa) distant to the places of consumption [1]. On the other hand, in contrast to fossil fuels, PV generation is intermittent (also called non-dispatchable) due to day-night cycles and difficult-to-predict weather (especially cloudiness) variability. This prevents the use of solar energy as baseload generation and poses serious challenges for its integration in the current electricity grid in which supply and demand need to be precisely balanced at every time [1,13,23,31,32]. In this framework, penetrations of non-dispatchable energy sources of just around 20% are considered to be acceptable [1,13,23,32]. All this variability translates into a low energy output that affects EROI very negatively. It would be possible to overcome intermittency by employing energy storage but at the current status of storage technologies this is not economically viable or, in order words, it increases the energy input necessary to generate power from PV further decreasing its EROI [33]. Another fact that is usually overlooked by the PV community is that, nowadays, solar energy is totally dependent on fossil fuels for two main reasons. Firstly, the production of PV power generators has a very high upfront energy cost (i.e. extraction of raw material and manufacturing) that currently can only be assumed by fossil-fuels [1,28,34]. Hence, paradoxically an increase in the share of solar energy in the global energy mix can only be realized at the expense of employing great amounts of fossil fuels and, thus, aggravate the fuel scarcity and environmental problems mentioned before. And secondly, without storage an increasing amount of non-dispatchable energy sources has to be compensated with an increasing number of natural gas fast-reacting backup generators [1,31,33]. These factors greatly contribute to limit the EROI of PV by increasing the energy input term in Eq.(1).

To sum up, despite the huge availability of sunlight, direct substitution of fossil fuels by PV is not currently viable due to its low EROI arising from its inherent variability and its high production cost. In addition, these two issues also make PV to be highly dependent on fossil fuels. So, unfortunately, at the current state of the technology, solar energy is not capable of maintaining our high living standards, of sustaining the greed for continuous growth of our financial system and, consequently, of avoiding the collapse of our socioeconomic system.

Then, does all this mean that solar energy is useless? Of course it does not. Two main conclusions can be extracted from this analysis:

1. It is of utmost importance to find strategies and technological solutions to boost the EROI of PV and make it as independent as possible from fossil fuels.
2. Contrarily to what most people tend to believe, solar energy is not likely to be able to solve humanity energy problems by itself and a deep change of paradigm has to be adopted. We need to start thinking in the long term as a whole, living in greater harmony with nature and reducing our energy needs in a sustainable financial and political framework not based on debt, profit and continuous economic growth. Inside

this framework, every form of renewable generation will be of utmost importance. However, due to its greater potential solar PV is called to be one the game-changing forms of energy generation.

Although the second conclusion above is extremely interesting and challenging, apart from the obvious intention of raising awareness and pushing the PV community to think beyond its comfort zone, it is out of the scope of this work.

1.1.3 Focus and motivation of this work

This thesis is motivated by the urgent necessity of exploring ways to increase the EROI of PV. As explained in the previous section, both the energy input and energy output terms in Eq.(1) are taking part in limiting the EROI of PV and this thesis aims to address both of them:

i. On the one hand, it investigates the reduction of the high energy upfront cost (energy input) of PV through the development of Earth-abundant and sustainable kesterite thin film solar cells onto substrates that enable high throughput production and integration as well as advanced applications and functionality.
ii. On the other hand, strategies are designed and implemented to try to maximise the power conversion efficiency (energy output) of the kesterite-based photovoltaic devices fabricated on such substrates by adapting the solar cell fabrication process to their characteristics.

Before getting down to business, though, it is necessary to review the main commercial PV technologies and their limitations in the context of energy production cost and EROI which, in turn, requires a previous understanding of the working principles, structure and main parameters of solar cells. These topics are thoroughly covered in sections 1.2 and 1.3.

1.2 Fundamentals of solar cells

1.2.1 What is a solar cell and how does it work?

Solar cells are devices that can convert light into electricity. This is possible thanks to the so-called photovoltaic effect that consists in the creation of a voltage and an electric current in a material upon exposure to light. It was first observed by Edmond Becquerel in 1839 [35]. Although the first solid state solar cell based on selenium was developed in 1877 by Adams and Day [36], it was not until 1954 that the first device with a significant power conversion efficiency was developed by Bell laboratories [37]. Bell's solar cell was based on silicon under the influence of the rapid development of the electronics industry and set the basis for the future development of PV. At first, intensive research on PV solar cells was triggered by their successful application in satellite-powering at the beginning of the space era [38]. However, once that the technology was well-established for space applications and after 1973 OPEC's oil embargo the focus changed towards terrestrial power generation [38]. Since then, there has been a huge development of PV owing to continuous research efforts that have made PV a competitive means of power generation. Si-based solar cells are the dominant technology today. However, the intensive research carried out in the last decades has allowed the development of many other successful and emerging technologies that will be analysed later on.

Regardless the technology, the same concept lies behind the operation of every photovoltaic device:

1. A material capable of generating electric carriers under illumination
2. An internal structure capable of selectively separating and transporting those carriers out of the material and into an external circuit to generate a useful electric current.

A p-n junction diode possesses those two properties. As for the first point, diodes are formed by semiconductor materials which, due to their band structure with a full valence band and an empty conduction band (at T = 0 K, at higher temperatures some electrons have enough thermal energy to jump to the conduction band), are capable of transforming radiative energy into electric carriers. More specifically, if a photon with an energy equal or higher than the energy gap (E_g) between the bands (bandgap) hits an electron in the valence band (VB), the latter can be promoted to the conduction band (CB) leaving a hole (equivalent to a positively charged particle) behind thus creating and electron-hole pair (EHP) (Figure 4). However, if the charges are not separated and extracted, the EHP will eventually recombine giving off the energy absorbed. This is why not just a semiconductor but a p-n junction is necessary for a solar cell.

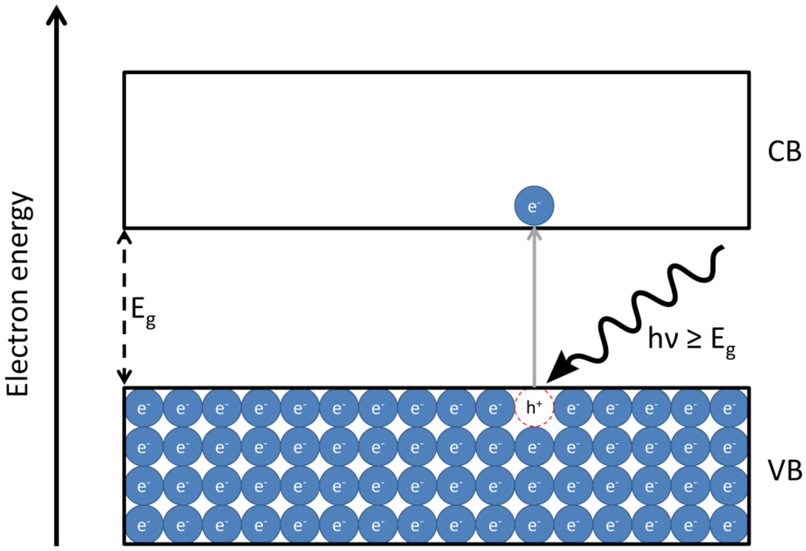

Figure 4. Band diagram of a semiconductor. VB and CB stand for valence and conduction band, respectively; Eg stands for the energy of the bandgap and hv is the energy of an incident photon,

A p-n junction is the junction between an n-type semiconductor and a p-type semiconductor. In an intrinsic semiconductor, the concentration of electrons (n) and holes (p) is always equal:

$$n = p = n_i \tag{2}$$

where n_i is called intrinsic concentration. In contrast to intrinsic semiconductors, n-type semiconductors possess donor impurities or defects with a concentration N_D that give away electrons to the conduction band where they become mobile charges. The number of free electrons donated by the donor atoms exceeds n_i and unbalances Eq.(2) so that

$$n >> p = n_i \tag{3}$$

This makes the conductivity of n-type semiconductors much greater than that of intrinsic semiconductors. The semiconductor is called n-type because the majority carriers have a negative charge. Similarly, in p-type semiconductors there are acceptor impurities or defects within the semiconductor with a concentration N_A that are filled with electrons from the valence band leaving holes behind so that

$$p >> n = n_i \tag{4}$$

The conductivity is also greatly improved compared to an intrinsic semiconductor. In this case, the semiconductor is called p-type because the majority carriers have a positive charge.

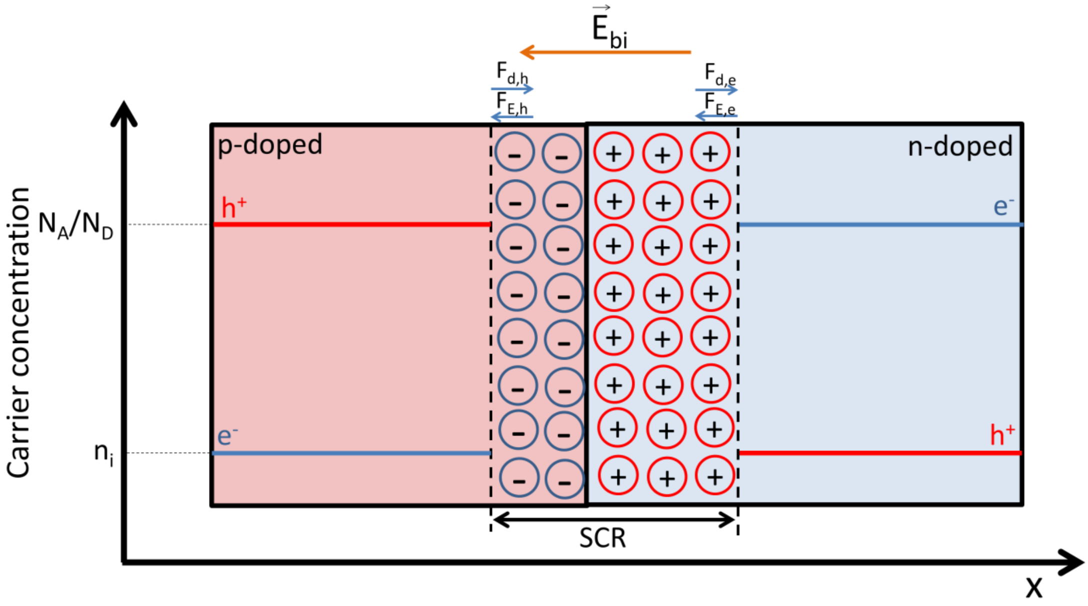

Figure 5. Diagram of a p-n junction. E_{bi} stands for the built-in electric field, $F_{d,x}$ and $F_{E,x}$ with x=h,e stands for the diffusion and electric force acting on holes (h) and on electrons (e).

A p-n junction can be fabricated by introducing donor impurities and acceptor impurities in opposite sides of a semiconductor (homojunction) or by putting in close contact an n-type semiconductor with a p-type semiconductor (heterojunction). When this is done, due to the different charge concentrations (i.e. charge chemical potential) at both sides of the junction, holes diffuse out from the p side towards the n side and free electrons diffuse out from the n side towards the p side leaving uncompensated ions behind (Figure 5). This causes the p-type side to become negatively charged and the n-type side to become positively charged generating an electric field (E_{bi}) across the junction directed from the n to the p side that, in turn, opposes the diffusion process. When the force exerted on the carriers by the electric field equals the diffusion force, equilibrium is reached. This process leaves a carrier-free zone around the junction called the depletion region or the space-charge region (SCR). If an EHP is generated by photon absorption and reaches the SCR, the hole and the electron will be drifted away from each other (the electron towards the n region and the hole towards the p region) by the built-in electric field generating an electric current.

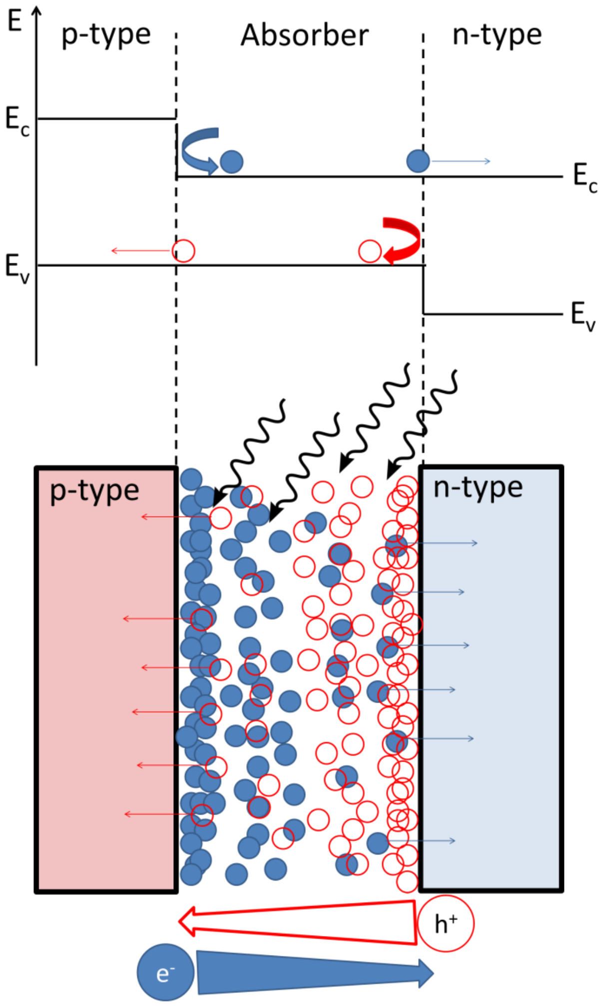

Figure 6. Schematic of selective membrane behaviour (top) and charge separation (bottom) of p-doped and n-doped semiconductors. E_c and E_v are the positions of the conduction band minimum and valence band maximum, respectively. Filled blue circles represent electrons (e^-) and hollow red circles holes (h^+). The tapered arrows represent the concentrations of the carriers. This figure should only be taken as an illustration and not as a real physical system.

However, a build-in electric field is not really mandatory to fabricate a solar cell but rather a material capable of generating carriers (absorber) and selective membranes for each kind of carrier [39]. With a proper band alignment like the one depicted at the top part of Figure 6, an n-type semiconductor can allow electrons to pass and block most of the holes and, vice versa, a p-type semiconductor can be very permeable to holes and almost impermeable to electrons. In addition, the conductivity of a semiconductor can be expressed as

$$\sigma_T = \sigma_e + \sigma_h = n\mu_e q + p\mu_h q \tag{5}$$

where σ_e and σ_h are the conductivities and μ_e and μ_h are the mobilities for electron and holes, respectively. Taking into account Eqs.(3) and (4), it is easy to see that $\sigma_e >> \sigma_h$ for n-type semiconductors and $\sigma_h >> \sigma_e$ for p-type semiconductors. Blocking one type of carrier while efficiently conducting the other provides n and p-type semiconductors with the properties required for a selective membrane. Forgetting about the built-in electric field, when EHPs are being generated continuously in the absorber of such a device they diffuse in every direction. Since they cannot pass efficiently through the membranes, holes and electrons will tend to accumulate near the n and the p semiconductors, respectively (bottom of Figure 6). This, in turn, will cause a gradient in the chemical potential of the carriers along the device that will eventually drive holes towards the p part and electrons towards the n part selectively separating the charges [39]. Thus, such a device can transform light into an electric current without the effect of a build-in electric field.

It should be noted that the electrons promoted to the conduction band are in an excited state so recombination is always present in solar cells during the processes described above. When a solar cell is at a steady state it means that generation and recombination processes keep continuously taking place but they have reached equilibrium.

Now that the fundamentals behind EHP generation and separation have been analysed, the question that follows is how to extract power from the devices. For this matter, it is useful to look at what happens in solar cells under illumination in two limiting operating conditions: open circuit and short-circuit.

In open circuit conditions (i.e. charges cannot escape the solar cell), at some point the concentration of charges inside and outside the membranes will be the same and no more diffusion can take place. In addition, as the number of charges increases so does recombination. In equilibrium, all the new charges generated will recombine. Since both membranes are “filled” with the highest possible number of charges, the electrochemical potential between them (which translates into a voltage) is at its maximum. This voltage is called the open circuit voltage (V_{oc}). Logically, since charges cannot leave the device, there is no current and no power can be extracted from the cell.

In short-circuit conditions (i.e. charges can freely escape the solar cell through an external ideal non-resistive wire), once equilibrium is reached all the charges generated that do not recombine inside the device, will reach the membranes and flow outside towards the opposite membrane generating a current. Since all the charges reaching the membranes are escaping the device, the current generated by the cell is at its maximum. This current is called the short-circuit current (J_{sc}). However, since the charges can flow freely towards the opposite membrane through the wire and recombine, the membranes are “empty” so there is no electrochemical potential between them, no voltage can build up and no power can be extracted from the cell.

Logically, in order to extract power from a cell, an intermediate situation is needed. If an external load is connected to the device, the charges generated can accumulate inside the membranes to a certain extent until the electrochemical potential (voltage) between them is high enough to leave the cell generating a current and producing work at the load.

Finally, it is necessary to take a quick look at the internal structure of a solar cell to understand how the light reaches the devices and how the charges are extracted from the cells. As depicted in Figure 7, the basic structure of a p-n solar cell consists of:

- An absorber (or base) → Most of the light is absorbed and the carriers are generated in this part. Its bandgap should be around 1-1.5 eV in order to efficiently absorb sunlight [40]. Depending on the technology it can be either an n-type or a p-type or even an intrinsic semiconductor.
- An emitter → It must be as transparent as possible to sunlight so this can reach the absorber. In p-n junction cells it must the opposite type of semiconductor than that of the absorber.
- A back and a front contact → The contacts collect the carriers and allow them to travel into an external circuit. Metals are usually employed due to their high conductivity. However, other materials like transparent conductive oxides are also commonly employed.

Each part is usually composed of a combination of different layers to optimise its properties for charge generation, separation and/or collection and to avoid any incompatibilities between them that can cause losses. This way, each technology has its own optimised layer structure.

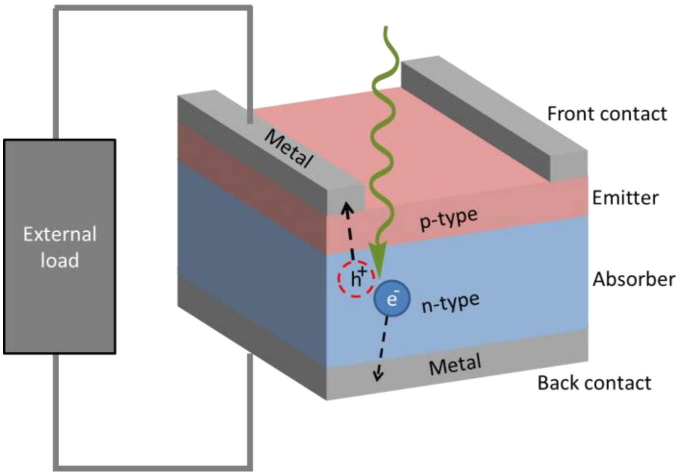

Figure 7. Basic structure of a p-n junction solar cell.

1.2.2 Main parameters of solar cells

From the previous section, it can be concluded that, grosso modo, solar cells are just light-sensitive p-n diodes. This is why they are commonly modelled with a one-dimensional diode equation. Thus, in the dark, the current density-voltage (J-V) dependency of a solar can be expressed as:

$$J(V) = J_0 \left[exp\left(\frac{q}{k_B T} V \right) - 1 \right] \quad \textbf{(6)}$$

where J_0 is the reverse saturation current of the diode (i.e. the current due to the diffusion of minority carriers from the n and p regions towards the SCR), q is the elemental charge, k_B is Boltzmann's constant and T is the temperature. Under illumination, it is necessary to add to the former equation an extra term to include the photocurrent generated by the cell (J_{ph}):

$$J(V) = J_0 \left[exp\left(\frac{q}{k_B T} V \right) - 1 \right] - J_{ph} \quad \textbf{(7)}$$

This equation is equivalent to a circuit with a current source and a diode connected in parallel.

Figure 8 represents the previous equations graphically. From it, it is possible to extract the main parameters that describe the operation of solar cells. The maximum possible voltage of a solar cell, V_{oc}, is obtained at J = 0 and the maximum current density, J_{sc}, at V = 0. Their product defines the maximum theoretical power (P_{theo}) of the cell (it should be noted that this power is not achievable even in perfect devices). However, in real operating conditions, the maximum power that can be extracted from a solar cell (P_{max}) is given by the point of the J-V curve that maximizes the product of J by V and is called the maximum power point (MPP). The MPP defines the current density and voltage at maximum power denoted by J_{mp} and V_{mp}, respectively. The ratio between P_{max} and P_{theo} is called the fill factor (FF):

$$FF = \frac{P_{max}}{P_{theo}} = \frac{J_{mp}V_{mp}}{J_{sc}V_{oc}} \tag{8}$$

This parameter measures the squareness of a J-V curve with respect to an ideal diode. Finally, the power conversion efficiency (η) of a solar cell, i.e. the ratio between the maximum power generated by the device (P_{max}) and the power reaching the cell (P_{in}), is usually expressed as:

$$\eta = \frac{P_{max}}{P_{in}} = \frac{J_{sc}V_{oc}FF}{P_{in}} \tag{9}$$

In standard measuring conditions, P_{in} corresponds to the power extracted from the integration of the solar spectrum AM1.5G (~1000 W/m^2 or 1 Sun).

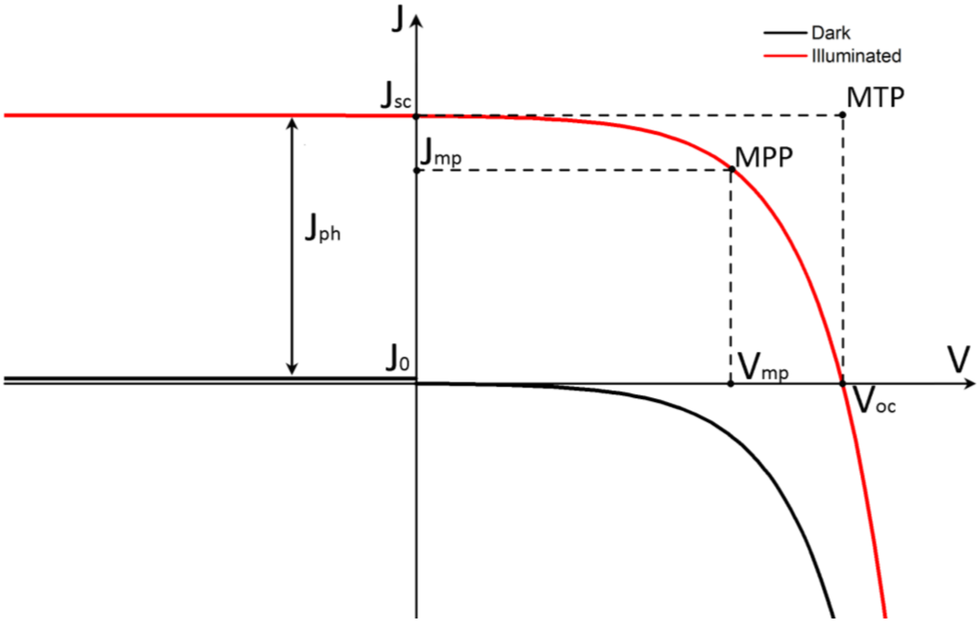

Figure 8. Characteristic J-V curves of a solar cell represented by equations (6) and (7) (with the sign of the Y axis inverted) and the main parameters used for its description. MTP stands for maximum theoretical power point.

Up to this point, it has been assumed that solar cells behave as ideal diodes. However, a real solar cell exhibits manifold losses. These can be encompassed in two terms: the series resistance (R_s) and the shunt resistance (R_{sh}). The former includes all the resistive losses along the device (i.e. due the electrical resistance of the different layers and the contact resistance between them at the interfaces) while the latter accounts for losses caused by alternative current paths (shunts). These terms can be included in Eq.(7) as follows:

$$J(V) = J_0\left[exp\left(\frac{qV - qJR_s}{k_BT}\right) - 1\right] + \frac{V - JR_s}{R_{sh}} - J_{ph} \tag{10}$$

This equation describes the circuit depicted in Figure 9. Eq.(10) works well for ideal p-n homojunction solar cells in which the main recombination process is radiative (i.e. an electron falls directly from the conduction to the valence band emitting a photon) and takes place in the neutral region. However, in the case of far from ideal p-n junctions, like heterojunctions, there are important losses due to recombination in the SCR. This recombination can have both radiative and non-radiative components. Inside non-radiative, the main recombination mechanisms are Shockley-Read-Hall (SRH) in which an electron falls from the conduction band to a mid-bandgap state and, then, to the valence band; and Auger in which an electron falls from the conduction to the valence band and the energy difference is given to another electron. These losses can be included in Eq.(10) by means of an extra term called the diode quality factor, A:

$$J(V) = J_0\left[exp\left(\frac{qV - qJR_s}{Ak_BT}\right) - 1\right] + \frac{V - JR_s}{R_{sh}} - J_{ph} \tag{11}$$

The factor A typically varies from 1 (ideal solar cell with mainly radiative recombination at the neutral regions) to 2 (main recombination at the SCR) [41,42].

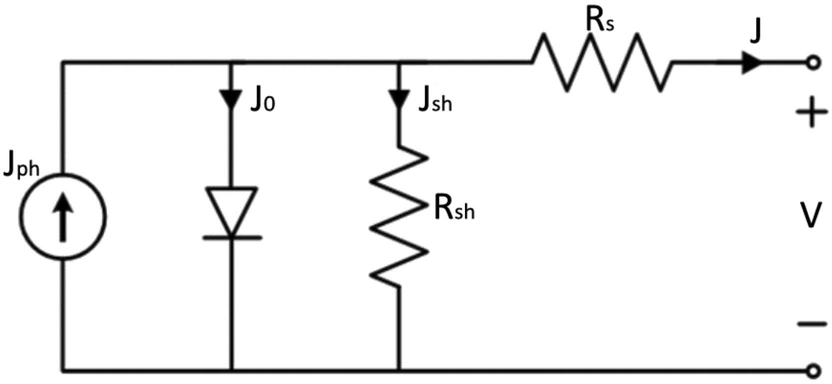

Figure 9. Equivalent circuit of a solar cell with resistive and shunt losses. J_{sh} stands for the shunt current density.

1.3 Photovoltaics: current commercial technologies and EROI

1.3.1 1st generation PV: crystalline Si solar cells

Nowadays, crystalline Si-based solar cells are the dominant PV technology with around a 95% of market share [43]. These are based in p-n homojunctions in which boron (p-type impurity) is diffused into a phosphorus-doped (n-type) Si wafer or vice versa (see (11)Figure 10) although heterojunction concepts have also been very successfully developed [44].

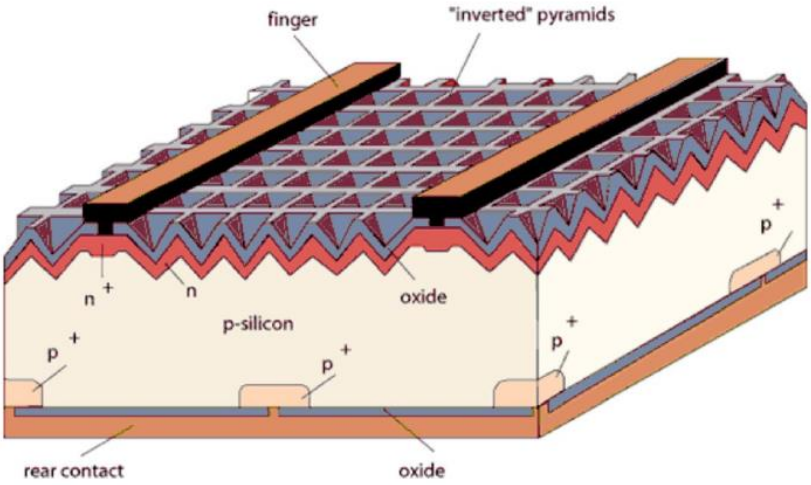

Figure 10. Structure of a monocrystalline Si PERL solar cell. Reproduced with permission from [45]. Copyrighted by John Wiley and Sons.

There are two main types of crystalline Si-based solar cells in the market: monocrystalline (c-Si) and polycrystalline (p-Si) (Figure 11). The former rely on very high purity monocrystalline Si wafers. The lack of defects and grain boundaries in the semiconductor material allows obtaining very high efficiencies. This, combined with an intensive electrical and optical engineering at the front and back sides of the devices has set the current record efficiency at 26.7% for an heterojunction c-Si solar cell [46]. Commercial c-Si solar panels show average efficiencies around 15-19% with the best ones exceeding 20% [47]. Their market share is around 45% [43]. However, their high efficiencies carry a counterpart: their production is very energy intensive, complicated and expensive since it requires a very precise control to obtain flawless monocrystalline ingots through the so-called Czochralski crystal pulling process [48]. In order to reduce production costs by avoiding pulling processes, p-Si technology was developed. Multicrystalline ingots are casted from molten Si controlling the cooling temperature so that the grains grow in a columnar structure [48]. Although the individual grains possess high crystalline quality, there is a higher density of crystallographic defects due to dangling bonds at the grain boundaries but also to dislocations and point defects [49]. However, extensive research on crystal growth and on the passivation of such defects, together with front and back side optical engineering has allowed the technology to get very close to c-Si with a record efficiency of 22.3% [50]. Commercial modules currently range 13-17% efficiency and represent a market share of around 50% [43].

Figure 11. Pictures of p-Si (left) and c-Si (right) solar cells. Source: http://www.tindosolar.com.au/learn-more/poly-vs-mono-crystalline/ (Accessed on 12/03/19)

Si is a very mature and well-performing technology. However the fabrication costs, even of p-Si, are very high. This is due to several reasons [48,51]:

1. Although Si is very abundant in nature, it mainly occurs in the form of SiO_2. In order to reduce it to metallurgic-grade (98% pure) Si, very high temperatures (~1800°C) are necessary. This process requires around 50 MJ to produce 1 kg of Si.
2. The covalent nature of silicon-silicon bonds, in combination with an indirect 1.14 eV bandgap, results in poor defect tolerance, which necessitates high-purity material so additional purifying and high temperature (~1300°C) chemical vapour deposition (CVD) processes are necessary.
3. The manufacturing of Si ingots requires melting the purified material again (~1400°C) as well as complex pulling/casting process. This is especially critical for c-Si.
4. Wafers need to be cut from ingots with thicknesses usually >100 µm due to the low light absorption and fragility or Si. During the sawing process, there is a considerable loss of material so that 3-9 g of raw (before sawing) Si are necessary per peak watt (W_p) at the module level.

Although the price of Si modules has strongly decreased in the last years, the high upfront energy cost of Si wafer production described above translates into solar panels with a very high embedded energy or, in other words, into a high value of the energy input term in Eq.(1), that yields low EROI values for the crystalline Si PV technologies as shown in Table 2 and Figure 15. These data show that the superior performance of c-Si does not compensate the high amount of energy necessary for its production. In addition, they show how critical energy production cost is since, by reducing the energy needs associated to bullet point 3 above it is possible to decrease a 30-35% the embedded energy of p-Si compared to c-Si and obtain a significantly higher EROI despite its lower efficiency. A more efficient wafer sawing process with less Si waste and wafer thickness reduction (bullet point 4) may slightly increase the EROI of the technology. However, the energy costs associated to bullet points 1 and 2 are inherent to the technology and, thus, extremely challenging to be reduced suggesting that the employment of less energy costly technologies might be a better approach to increase the EROI of PV.

1.3.2 2nd generation PV: thin film solar cells

The so-called 2nd generation PV started to be developed as a response to the high production costs of Si solar cells. This generation of PV is based on the usage of direct bandgap and highly light-absorbent materials that allow reducing the thickness of solar cells down to a few microns, in contrast to Si wafers. The fabrication of such devices consists on the deposition of thin layers with different functionalities (back contact, absorber, emitter, etc.) onto a low cost substrates. This is why they are widely known as thin film PV. The wide range of substrates, materials and deposition techniques that can be employed for its fabrication provide 2nd generation PV with an enormous versatility, a large potential for cost reduction and opens the door to many innovative applications. Currently, there are 3 main technologies competing with crystalline Si with a non-negligible market share: amorphous silicon (a-Si), CdTe and $Cu(In,Ga)Se_2$ (CIGS).

Amorphous Si

Amorphous Si was the first thin film PV technology to be commercialised. It has been successfully powering low power consumer electronics since the 1980s (Figure 12, left). It is a mixture of Si and H (5-20at% H) and is usually deposited at low temperature by plasma enhanced CVD (PECVD) [52,53]. Hydrogen plays a critical role improving the quality of the material by passivating the dangling bonds occurring naturally due to its amorphous structure. This hydrogenated material has a 1.7 eV bandgap and a very high absorption coefficient (~10^5 cm^{-1}) that allows reducing the absorber layer below 1 µm resulting in a solar cell with a total thickness of ~2 µm [53–55]. Devices are usually fabricated based on a p-i-n junction (Figure 12, right) either in superstrate or substrate configuration with the light entering from the p-side [55].

The main advantages of this technology are its simplicity, low temperature processing and the extremely reduced usage of Si. However, the presence of H in the semiconductor structure causes a light-induced degradation known as the Staebler-Wronski effect. The stability and efficiency of the devices can be improved by employing multiple p-i-n junctions with different bandgaps or by tandems a-Si/µc-Si (µc-Si stands for microcrystalline Si, a form of Si with crystalline nanograins embedded in an a-Si matrix) [54,56]. The record efficiencies (stabilised after degradation) for laboratory single junction solar cells are around 10% (12.6% for tandem) while commercial modules typically present efficiencies around 7% [56,57]. The market share of a-Si is currently below 1% due its limited efficiency compared to other thin film PV technologies and the price reduction experienced by crystalline Si panels in the last years.

Figure 12. Left: a-Si powered calculator. Right: structure of a single junction a-Si solar cell in superstrate configuration. Sources: pixabay.com (right) and [55] (left).

CdTe

CdTe is the oldest among thin film PV technologies with the first device with a significant efficiency (6%) being produced back in 1972 [58]. It is a II-IV binary chalcogenide semiconductor with a zinc blende structure (see Figure 16) and an inherent p-doping. In its polycrystalline form it has a bandgap of 1.45 eV, very close to the optimum bandgap for PV, and possesses a large absorption coefficient (>10^4 cm^{-1}) that allows to efficiently absorb incident light in just a few microns [40,59–61]. CdTe solar cells are based on a heterojunction with the n-type semiconductor CdS. Although both superstrate and substrate configurations work well for this technology, the latter yields a lower performance due to problems with forming an ohmic contact at the back [62]. In superstrate configuration, the basic deposition process consists on the deposition of a transparent conductive oxide (TCO) on a glass substrate followed by the deposition of a CdS buffer layer, a CdTe absorber layer and a back contact (see Figure 13). CdTe can be deposited employing a wide variety of techniques including physical vapour deposition (PVD) or electrodeposition with the best cells being usually fabricated by close space sublimation (CSS) at relatively low temperature (500-600°C) [63].

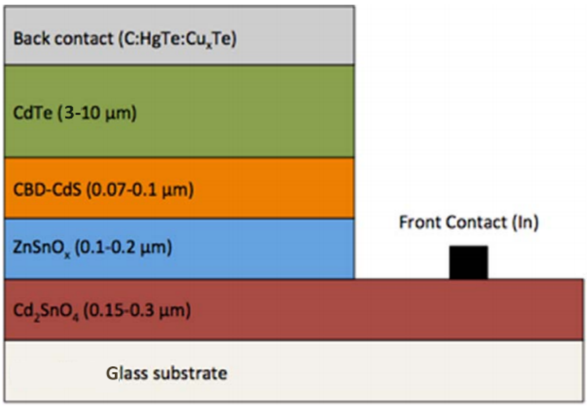

Figure 13. Structure of a CdTe solar cell. Reproduced with permission from [54]. Copyrighted by Elsevier.

Its favourable properties and the continuous development of the technology have converted CdTe in a mature PV technology with efficiencies similar to those of p-Si. The record laboratory cell was achieved by First Solar, the largest CdTe manufacturer, with a 22.1% efficiency [64]. Commercial modules range 15-18% and directly compete against Si [57,65]. CdTe has currently the highest market share among thin film technologies with around a 3% [43]. In addition, First Solar claims that CdTe has the lowest energy production cost and, thus, is the most environmentally friendly PV technology in the market [57,66]. However, its high performance and low embedded energy are clouded by concerns about the toxicity of Cd and the scarcity of Te that may limit their future production [67].

CIGS

$CuInSe_2$ (CIS) started to be regarded as a potential material for PV in 1976, when the first thin film solar cell was fabricated with a ~5% efficiency [68]. CIS is a ternary I-III-VI_2 chalcogenide semiconductor with a chalcopyrite crystal structure (see Figure 16), naturally occurring p-doping and a high absorption coefficient (>10^5 cm^{-1}) [69]. It has a direct bandgap of 1.04 eV but it was realized soon after the first stages of development of the technology that it was possible to substitute In atoms by Ga atoms to widen its bandgap and improve the overall properties of the material [53]. This way, by alloying $CuInSe_2$ and $CuGaSe_2$ in different proportions $Cu(In_xGa_{1-x})Se_2$, it is possible to tune the bandgap of the material from 1 to 1.7 eV [70]. Likewise, the substitution of Se by S allows further bandgap tuning [71]. As in the case of CdTe, CIGS devices are based on the heterojunction with CdS although Cd-free alternatives like $Zn(O,S,OH)_x$ have also been successfully employed [72]. The fabrication of devices is carried out in substrate configuration employing typically soda-lime glass (SLG) since Na plays a fundamental role in the synthesis of the material [73–76]. A Mo back contact is deposited onto soda-lime glass (SLG) followed by the deposition of the CIGS absorber and a CdS/TCO window layer (Figure

14). CIGS can be deposited in different ways employing both physical and chemical routes although physical routes usually result in better performances [72,77]. Inside physical procedures, sputtering of a metallic CuInGa precursor followed by a reactive annealing in S/Se atmosphere and co-evaporation of Cu, In, Ga and S/Se are the most successful deposition routes [72,78]. These techniques can proffer a precise control of In/Ga composition along the thickness of the absorber layer that enables bandgap grading engineering which has been found to be mandatory in order to achieve high efficiencies [79,80].

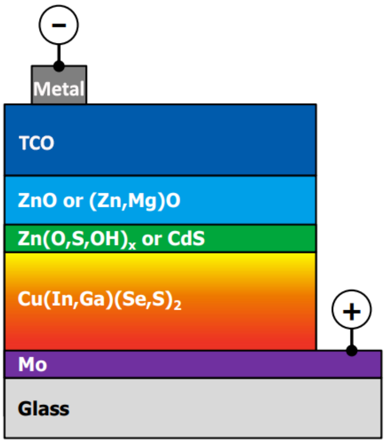

Figure 14. Structure of a CIGS solar cell. Reproduced with permission from [72]. Copyrighted by IOPscience.

Nowadays, it is the thin film commercial technology with the highest reported efficiency 23.35%, even higher than p-Si [81]. Commercial modules normally range 14-17% efficiency with the most advanced ones, by Solar Frontier, exceeding 18% [57,82]. Its market share is around 2% [43]. Despite its high efficiency, since it is a quaternary compound its fabrication process requires a very precise compositional control so it has a higher capital cost than CdTe [83]. In addition, as in the case of CdTe, there are concerns about its future due to In and Ga scarcity issues [67].

EROI and future prospects

Thin film PV technologies offer good performance devices while reducing the thickness of the active material by two orders of magnitude compared to 1st generation PV. In addition, the fabrication techniques are relatively simple, low cost and low energy consumption. But, does this represent a real advantage in terms of EROI?

It has been shown above that CdTe and CIGS solar panels perform very similarly to c-Si and p-Si ones. In addition, their lifetimes are also similar [28]. These two factors dominate the P_{output} term for EROI calculation in Eq.(1) so no great differences are expected amongst the different technologies. Therefore, the critical term for EROI, in this case, is the P_{input}. Table 2 shows average values of the embedded energy of solar panel for the different technologies. As explained in section 1.3.1, shifting from c-Si to p-Si entails a significant reduction in energy production requirements (30-35%). However, the low material usage as well as the low-cost and low energy-intensive techniques employed for thin film module fabrication represent one step forward in energy reduction with CIGS and CdTe requiring around 40% and 60%, respectively, less energy than p-Si for their production.

Table 2. Embedded energy of module fabrication of the main PV technologies. Data source: [28].

	Embedded energy
c-Si	6200 MJ/m^2
p-Si	3900 MJ/m^2
a-Si	1700 MJ/m^2
CdTe	1600 MJ/m^2
CIGS	2300 MJ/m^2

Figure 15 shows the EROI of each PV technology employing the values shown in Table 2 and under harmonized performance conditions. In effect, the lower embedded energy of thin film technologies at similar performance rates translates into higher EROI values. An impressive 30:1 EROI is obtained for CdTe, around 3 times higher than that of Si-based technologies and even above that of fossil fuels combined. In the case of CIGS, due to its higher energy production cost, its EROI is around 20:1, still very superior to Si. These values should only be taken as illustrative and not as absolute due the many factors influencing the calculation of EROI (see section 1.1.2). However, they show the great potential of 2nd generation technologies for increasing the EROI of PV to levels compatible with our current energy needs.

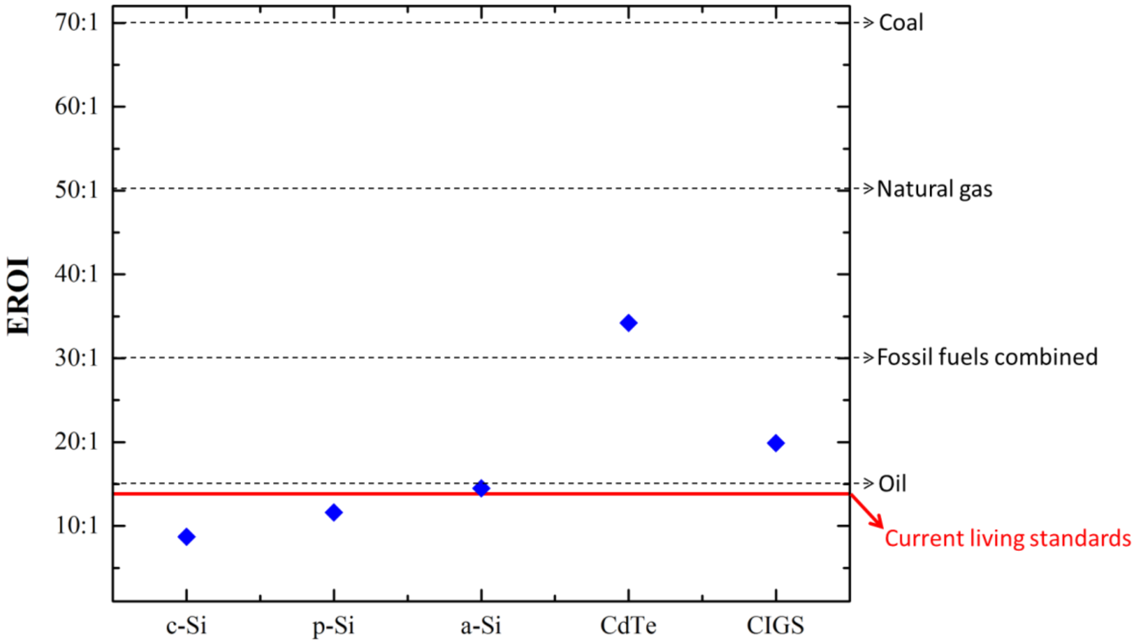

Figure 15. EROI of the main PV technologies. Data sources: [23,24,28].

On the other hand, it should be taken into account that the EROI of an energy source varies with time. Despite the high EROI of CdTe and CIGS one should not forget that they are made of scarce elements: Te, In and Ga. It is difficult to perform predictions on the precise impact the scarcity of these materials will have in PV module production since they are mainly obtained as by-products of Cu (Te), Zn (In) and Al (Ga) purification processes, but some authors point out towards price volatility, problems with short-term availability and, more importantly, towards a limitation of module production below the TW/year level which is necessary for a true exploitation of the cost reduction capabilities of thin films technologies through mass production [67,84–88]. However, as in the case of fossil fuels, it is clear that the more scarce these resources become, the higher the energy input required for their extraction. Thus, their EROI is likely to fluctuate and decrease in the near future. So, CdTe and CIGS should not be considered as the ultimate thin film PV technologies but rather as a kind of medium-term solution which has to be succeeded by other technologies based on more abundant materials.

Finally, the case of a-Si is very interesting. Despite its considerably lower performance compared to crystalline Si technologies, its EROI is higher. As with the previous c-Si versus a-Si comparison, but more markedly, these data show how critical fabrication energy is for the EROI of PV and that high efficiencies, although desirable, are not indispensable to increase this factor.

To sum up, thin films are the right direction to follow to effectively increase the EROI of PV widely surpassing 1st generation technologies. This is mainly due to the fact that the energy required for fabrication is a very critical parameter for the EROI of PV technologies, even more than power conversion efficiency (to a certain extent). However, current commercial high efficiency thin film technologies rely on scarce elements that will reduce their EROI in the near future. Therefore, the future of PV depends upon the development of thin film technologies based on Earth-abundant elements.

1.4 Earth-abundant thin films: kesterite solar cells

1.4.1 Fundamental properties

The necessity of developing thin film technologies based on Earth-abundant elements that boost the EROI of solar energy in a long-lasting and sustainable manner is patently clear from the analysis carried out in the previous sections. The excellent performance achieved with CdTe and CIGS devices suggests that inorganic chalcogenide compounds with zinc blende-derived crystal structure make good candidates for developing high efficiency thin film technologies. In this regard, there is a family of chalcogenide compounds that possesses ideal characteristics to take up the torch in thin film photovoltaics: kesterites. These are I_2-II-IV-VI_4 materials that owe their name to their crystal structure. Figure 16 shows how the kesterite crystal structure can be derived from zinc blende (CdTe) passing through chalcopyrite (CIGS).

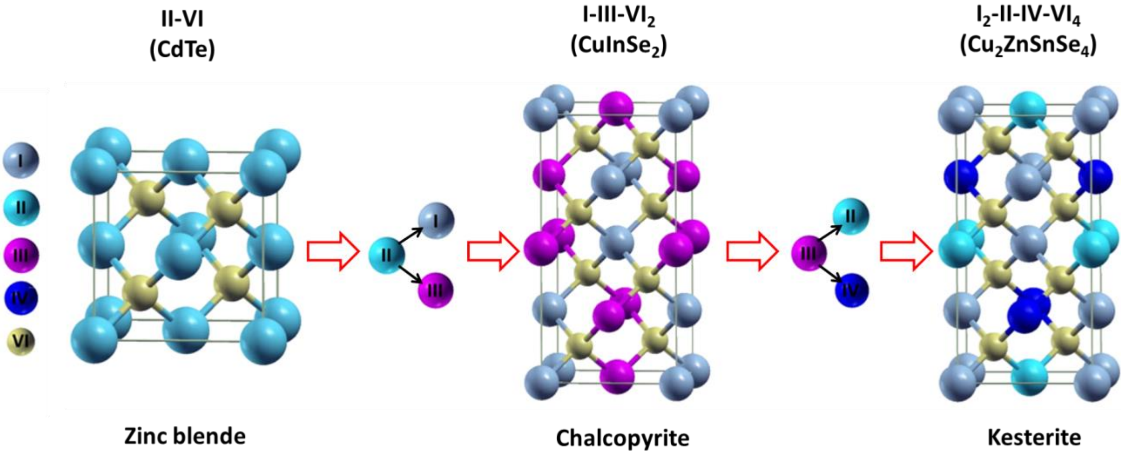

Figure 16. Derivation of kesterite crystal structure from zinc blende and chalcopyrite. Adapted with permission from [89]. Copyrighted by American Physical Society.

The great similarity between chalcopyrite and kesterite structures entails that different materials with both structures (and a close composition) will exhibit similar electrical properties. Inside the kesterite family, $Cu_2ZnSnSe_4$ (CZTSe), Cu_2ZnSnS_4 (CZTS) and their solid solution $Cu_2ZnSn(S_xSe_{1-x})_4$ (CZTSSe) are particularly interesting since they present ideal physical properties for thin film photovoltaics, very close to those of CIGS, while being formed solely by non-toxic and Earth-abundant elements. This way, CZTSSe compounds display a natural p-doping and optimum bandgap values (for single junction) that range from 1.0 eV for CZTSe to 1.5 eV for CZTS enabling the possibility of fine bandgap tuning in the solid solution compound by controlling the S-Se composition [40,90–92]. In addition, they possess a very high absorption coefficient (>10^4 cm^{-1}) that allows to absorb most of the incident light in just a few microns [92]. Thus, from the fundamental properties perspective, CZTSSe compounds are ideal candidates for the development of a thin film PV technology that can ensure a long lasting high EROI.

1.4.2 Evolution and state-of-the-art

Cu_2ZnSnS_4 thin films were first synthesised, studied and identified as a potential material for PV for the first time in 1988 under the influence of the success of $CuInSe_2$ solar cells [93]. The great similarity between both materials, led the PV community to try and apply the available knowledge on CIGS to the development of kesterite based-solar cells. This way, the first CZTS-based solar cell with a significant power conversion efficiency (0.66%) was fabricated by Katagiri et al. in 1997 by sulfurization of electron beam evaporated Cu/Sn/Zn precursors and using a similar cell configuration as CIGS: SLG/Mo/CZTS/CdS/ZnO/Al [94]. The possibility of successfully applying CIGS's already developed PVD-based techniques and knowledge allowed the group of Katagiri to rapidly optimise their process and increase 10-fold the efficiency of their devices in a decade reaching a 6.8% in 2008 by sulfurization of RF-sputtered Cu/SnS/ZnS precursors [95]. At that time, IBM was researching on solution deposition processes as a possible route to reduce the cost of high vacuum-based CIGS manufacturing. Mitzi et al. succeeded and obtained efficiencies >10% employing a hydrazine-based chemical route [96]. With the feasibility of producing efficient kesterite solar cells proven, they joined the quest for improving the technology and, in 2010, by applying their novel CIGS solution-based process to CZTSSe they achieved a remarkable 9.6% efficiency device [97]. Further optimisation of their hydrazine process led IBM in 2013 to the current certified record: 12.6% efficiency [98].

Nowadays, CZTSe, CZTS and CZTSSe have been widely studied and successfully synthesised by a wide variety of vacuum and non-vacuum routes. Despite the compound synthesised, all the fabrication routes yielding high performance kesterite absorbers involve a two-step process with the following stages:

1. Precursor synthesis and/or deposition
2. High temperature (>500°C) annealing to synthesise the kesterite phase and/or promote grain growth.

In contrast to CIGS, solution-based routes resulted traditionally in better performing devices but, nowadays, both vacuum and solution-based routes have attained comparable efficiency levels. Table 3 shows a selection of the best solar cells reported with different deposition techniques. In every case, the same cell configuration was employed following the basic substrate-like structure depicted in Figure 17. There have been some attempts of employing a superstrate configuration but the efficiencies achieved are well below the standard configuration [99]. In addition, the superstrate configuration limits the choice for cell structural support to only transparent materials. However, in substrate configuration, any material can be employed increasing the range of applicability of the technology as will be shown later on.

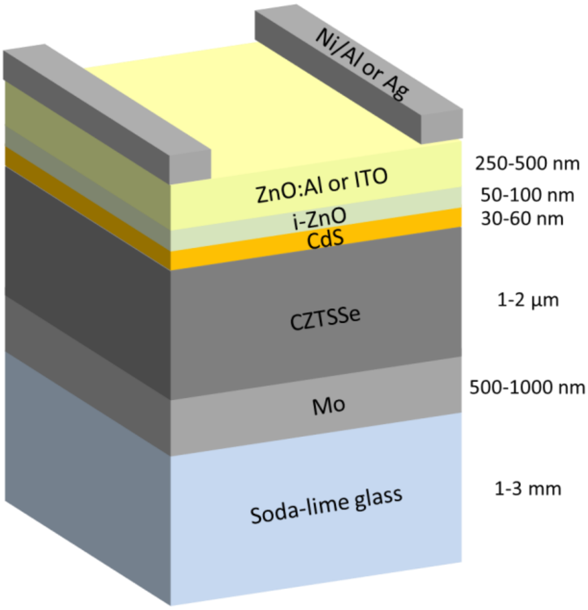

Figure 17. Standard cell configuration and typical layer thicknesses of kesterite solar cells.

Table 3. Selection of the best solar cells reported for different kesterite compounds and synthesis routes. The best devices of each compound are highlighted in bold. The '/' symbol in the 'Precursor Type' column indicates that the precursor is composed by different stacked layers. In the 'Annealing Technique' column HP stands for Hot Plate, RTP for Rapid Thermal Processing and TF for Tubular Furnace. The '-' symbol is used when no information is available. ****Homemade halogen lamp-based furnace.***

Material	Optoelectronic parameters					Precursor		Annealing			Ref
	E_g (eV)	V_{oc} (mV)	J_{sc} (mA/cm^2)	FF (%)	η (%)	Type	Deposition Technique	Technique	Atmosphere	T (°C)	
CZTSSe	**1.13**	**466**	**38.9**	**69.8**	**12.6**	**Hydrazine CuZnSnSSe**	**Spin coating**	**HP**	**-**	**>500**	[98]
	1.07	485	37.5	64.9	11.8	Zn/Sn/Cu	Sputtering	RTP	S+Se	520	[100]
	1.13	531	33.7	64.8	11.6	DMSO CuZnSnS	Spin coating	RTP	Se	550	[101]
	1.07	471	31.6	69.6	10.3	DMSO CuZnSnS	Doctor blade	RTP*	Se	540	[102]
CZTSe	1.0	423	40.6	67.3	11.6	CuZnSnSe	Co-evaporation	Hot plate	Se	590	[103]
	1.04	463	36.0	66.3	11.0	Cu/Sn/Zn	Sputtering	TF	Se	550	[104]
	1.03	**443**	**38.1**	**68.0**	**11.4**	**Zn/CuSn/Zn**	**Sputtering**	**TF**	**Se**	**530**	[105]
	1.06	400	35.2	66.2	9.3	Nanoparticles CuZnSnS	Doctor blade	-	Se	550	[106]
	1.05	440	31.3	60.0	8.2	Cu/Sn/Zn	Electrodeposition	TF	Se+Sn	550	[107]
CZTS	**1.5**	**731**	**21.7**	**69.3**	**11.0**	**CuZnSnS**	**Co-Sputtering**	**RTP**	**S+Sn**	**560**	[108]
	1.5	661	19.5	65.8	8.4	CuZnSnS	Co-evaporation	HP	S	570	[109]
	1.5	746	19.1	62.0	8.8	Sol-gel CuZnSnS	Spin coating	-	S+Sn	560	[110]
	1.5	567	22.0	58.1	7.3	Cu/Zn/Sn	Electrodeposition	TF	S	585	[111]

1.4.3 V_{oc} deficit: the main limitation of kesterites

In spite of the similarity between CIGS and CZTSSe absorbers, there is a very large performance gap between the record devices of each technology as shown in Table 4. The main parameter limiting the efficiency of kesterite solar cells is their high V_{oc} deficit. This parameter is defined as the difference between the maximum V_{oc} theoretical value according to the Shockley–Queisser (SQ) limit and the measured V_{oc} of the device [112]:

$$V_{oc\,deficit} = V_{oc\,SQ} - V_{oc} \tag{12}$$

Table 4. Comparison of the record CIGS and CZTSSe devices.

	E_g (eV)	V_{oc} (mV)	J_{sc} (mA/cm^2)	FF (%)	η (%)	V_{oc} deficit (mV)
CZTSSe [98]	1.13	466	38.9	69.8	12.6	664
CIGS [113]	1.13	746	38.5	79.7	22.9	384

There have been intense research efforts trying to understand the origin this problem and kesterites have been found to possess a manifold of intrinsic problems that can lie at the origin of the V_{oc} deficit. The main issues limiting the V_{oc} of kesterite solar cells are reviewed below.

Formation of secondary phases

Kesterites are complex quaternary compounds and their single phase formation thermodynamic region is very narrow compared to that of CIGS (Figure 18) [92,114–116]. This implies that the formation of unwanted secondary phases is very likely to occur together with the kesterite phase. In addition, high efficiency devices have been shown to require Cu-poor Zn-rich compositions [90,116–121]. Taking a look at the bottom-right part of Figure 18, it is easy to see how the size of the stable region decreases for Cu-poor conditions aggravating the situation. Working in this regime, the formation of Zn(S,Se) phases is, thus, extremely likely to happen [90,122].

What is more, the loss of Sn and Se during high temperature absorber synthesis has been identified as a critical issue for kesterites due to the high volatility of Sn(S,Se) compounds [122–124]. A common approach to minimize the loss of these materials is to increase their vapour pressure by working in an excess Se and Sn atmosphere. However, besides preventing material loss, these annealing conditions also promote the formation of $Sn(S,Se)_x$ secondary phases.

Other secondary phases like Se^0, $Cu_x(S,Se)$, $Cu_2Sn(S,Se)_3$ or SnO_2, although less likely to be formed in Cu-poor Zn-rich conditions, have also been reported, especially at the front and back sides of the absorber [125,126].

Secondary phases could be avoided by a very precise control of the kesterite formation mechanism, and, especially, of the partial pressures of the different compounds during annealing processes. However, this is very challenging technologically. A more practical approach proposed by several authors is to accept defeat and allow some secondary phase formation only to later eliminate them from the surface of as-annealed CZTSSe absorbers using selective chemical etchings [119,125,127–129].

Either way, the formation of these phases within the bulk of the absorber is very difficult to eliminate completely and can lead to compositional fluctuations at the kesterite/secondary phase interfaces that can induce the formation of defects that act as recombination centres and ultimately cause V_{oc} losses [127,128,130–132].

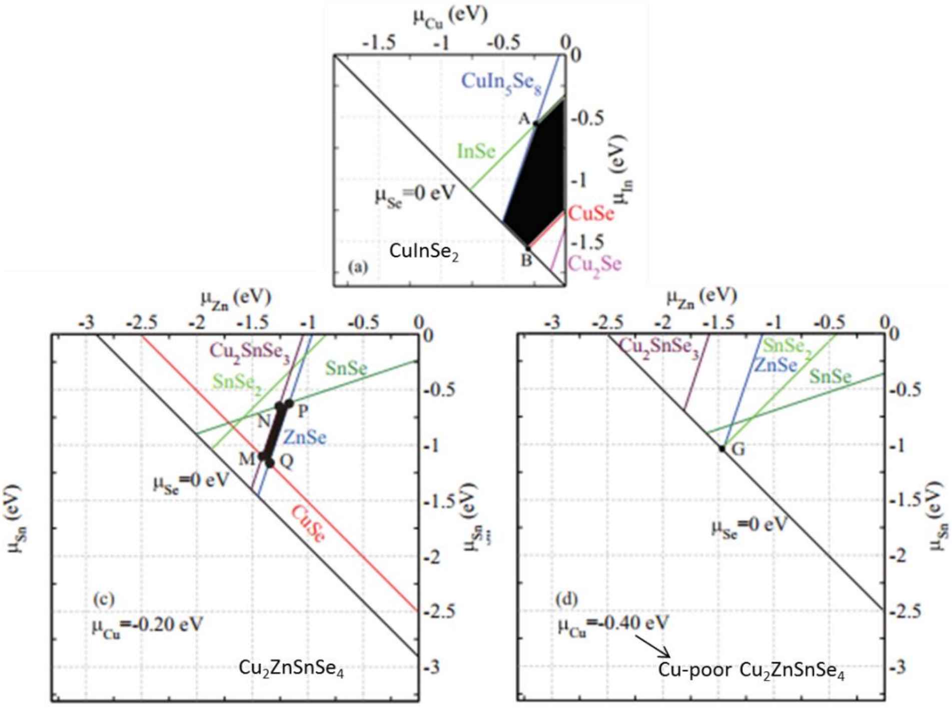

Figure 18. Chemical potential equilibrium diagrams for $CuInSe_2$ (top) and $Cu_2ZnSnSe_4$ (bottom). The black area represents the stable one phase region. Reproduced with permission from [92]. Copyrighted by John Wiley and Sons.

High density of defects

Although theoretical calculations have proven that the kesterite crystal structure is the most energetically favourable for CZTSSe compounds, the energy difference with the stannite crystal structure (see Figure 19, up-left) is very small [133]. This small difference, together with the isoelectronicity and similar ionic radii of Cu and Zn, induces a strong tendency to the formation of Cu_{Zn} and Zn_{Cu} anti-site defects [134]. In particular, the donor–acceptor defect complex [Cu_{Zn} + Zn_{Cu}] has an extremely low formation energy which results in a high concentration of these defects, widely known as the Cu/Sn disorder [92,134,135].

On the other hand, in Cu-poor Zn-rich compositions, V_{Cu} is the defect with lowest formation energy and is expected to be the main responsible for p-type conductivity of CZTSSe absorbers (Figure 19, up-right) [92]. This way, a high concentration of V_{Cu}, Cu_{Zn} and Zn_{Cu} is expected in CZTSSe absorbers. In addition, it has been proposed that deep defects like Sn_{Zn} and defect clusters such as [$2Cu_{Zn}$ + Sn_{Zn}] can also occur during kesterite formation even in Zn-rich conditions [136–138].

All these charged defects and defect clusters, depending on their spatial distribution, induce point defects (isolated defects), bandgap fluctuations (spatial correlation of the defects in the VB and the CB) and/or potential fluctuations (uneven spatial distribution of charged defects) that translate into a series of permitted states within the bandgap (see Figure 19, bottom)

[137,139–141]. This phenomenon is known as band tailing since it is characterised by sub-bandgap absorption that can be described as

$$\alpha \sim exp\left(-\frac{E_g - E}{E_U}\right) \tag{13}$$

where α represents absorption and E_U stands for the so called Urbach energy. The states within the bandgap can act as recombination centres and, thus, strongly reduce the V_{oc} in kesterite devices. In fact, a near-linear correlation between E_U and the V_{oc} deficit of different technologies was found a De Wolf et al. [142].

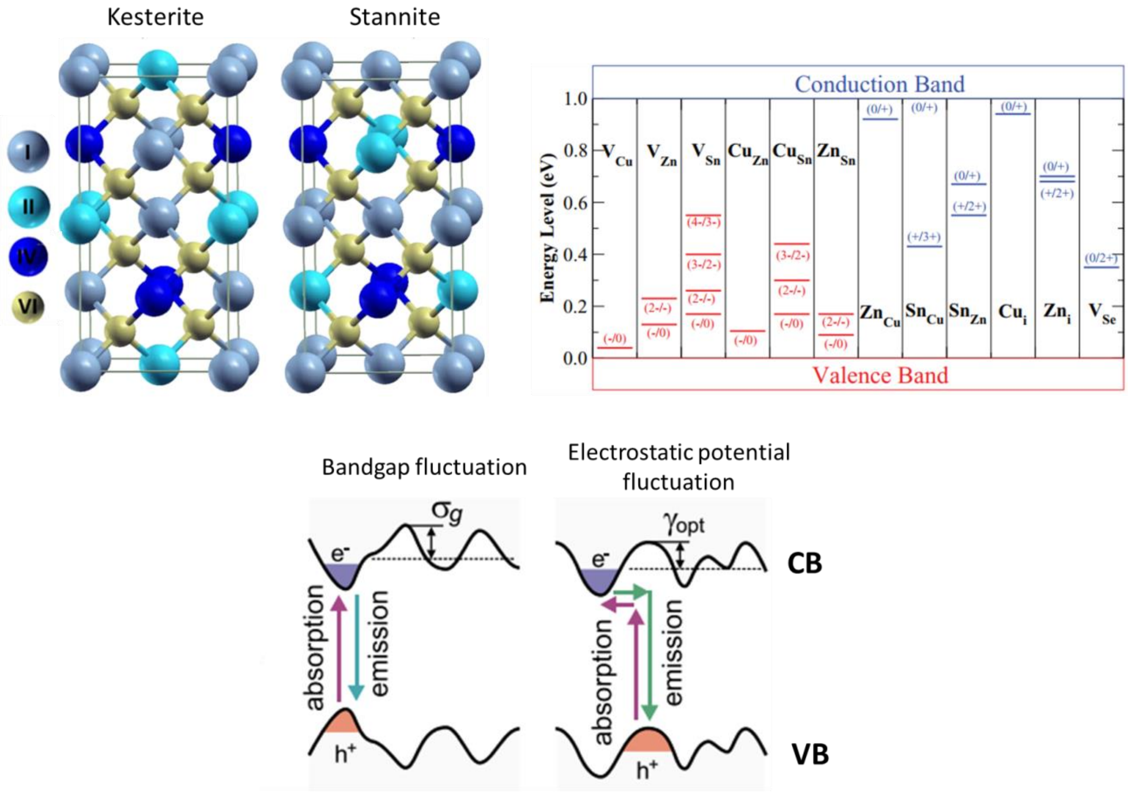

Figure 19. Up-Left: Comparison between the kesterite and stannite crystal structures. Adapted with permission from [89]. Copyrighted by American Physical Society. Up-Right: Ionization levels of intrinsic defects in the band gaps of $Cu_2ZnSnSe_4$. The red bars show the acceptor levels and the blue bars show the donor levels, with the initial and final charge states labelled in parentheses. Reproduced with permission from [92]. Copyrighted by John Wiley and Sons. Bottom: bandgap and electrostatic potential fluctuations due to the uneven spatial distribution of defects. Reproduced with permission from [139]. Copyrighted by AIP Publishing.

Other limiting factors

Some other factors that have been considered to limit the V_{oc} of kesterite solar cells to a lesser extent are:

- Front interface (CdS/CZTSSe) recombination due to non-optimum band alignment, especially for wide bandgaps [143–145]
- Back interface recombination due to a defective CZTSSe/Mo coupling and chemical instability [120,143,144,146,147]
- Short minority carrier lifetime [139,148]
- Grain-to-grain nonuniformities [149,150]

As a final remark, it should be born in mind that all the different factors affecting the V_{oc} deficit of kesterites discussed above are not isolated one from each other and that there are deep relationships between them (see Figure 20) [151,152].

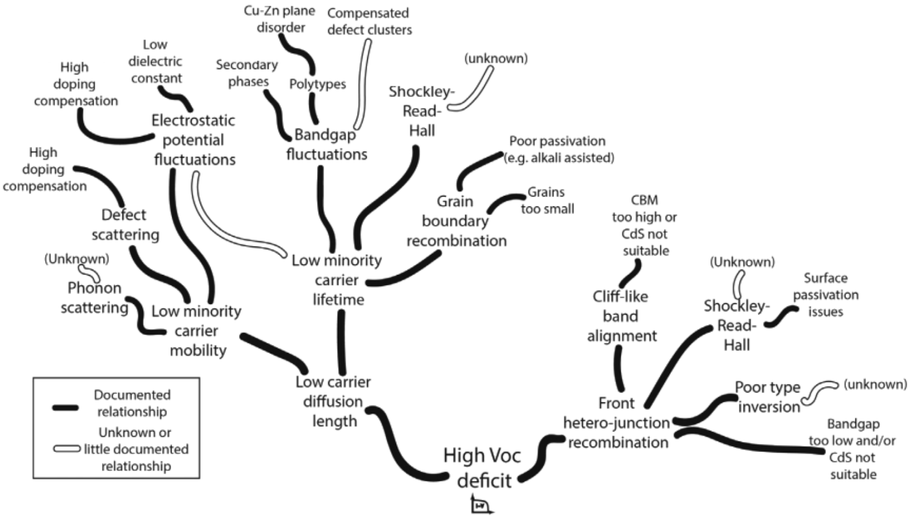

Figure 20. Relationship between different factors affecting the V_{oc} deficit of kesterites. Reproduced with permission from [151]. Copyrighted by Elsevier.

1.4.4 Alkali doping

Doping the absorbers with alkaline elements has been observed to be a critical issue for the development of CIGS and CZTSSe solar cells and an effective way of reducing the large V_{oc} deficit of the technologies. Alkalis, especially Na, have the ability of modifying the synthesis process and improving the morphological and electrical properties of the absorbers which results in enhanced device performance. The following sections review the evolution and main effects of alkaline doping in kesterite solar cells.

Sodium and doping strategies

The discovery of the beneficial effects of Na doping in CIGS absorbers was one of the major breakthroughs in the development of the technology [136,153,154]. They were first described by Hedström et al. in 1993 [155]. They fabricated CIGS devices in different substrates (soda-lime glass, borosilicate, sapphire, and alumina) and observed that the absorbers grown on soda-lime glass exhibited a superior crystal structure and performance and associated it to the presence of Na coming from SLG [156]. Since then, Na doping became a hot research topic and its presence was ultimately found to be a requirement to achieve high efficiencies [153,154].

Following the success of Na doping in CIGS, the beneficial effects of alkali doping in kesterites solar cells have also been a major topic of research in the last years. Na has been found to produce similar effects in kesterite devices than in CIGS and to be crucial to achieve high efficiencies [154,157,158]. The main effects attributed to Na in CZTSSe absorbers commonly reported in the literature are summarised in Table 5. Principally, Na acts three-fold:

i. As a fluxing agent and increasing crystal size
ii. As a grain boundary passivator

iii. As a carrier concentration booster

All these effects translate into devices with a highly improved performance due to enhanced V_{oc} and FF, mainly. It is widely accepted that Na ions have a large mobility in kesterites during high temperature annealings easily migrating through Cu vacancies due to the low energy formation of Na_{Cu} [159–161] and that Na tends to accumulate at the grain boundaries where, due to their synergy with oxygen, help passivating defects like $V_{S,Se}$ [162,163] or create a positive potential that facilitates charge separation [163]. However, the precise mechanisms behind the effects of Na in kesterite (and CIGS) solar cells described in Table 5 are still not clear and remain a matter of debate.

Table 5. Main effects of Na in CZTSSe absorbers reported in the literature.

General effect	Proposed Mechanisms	Remarks	Effect on devices	References
Crystal growth enhancement and <112> texturing	Formation on liquid Na-Se phases (not directly observed)	Depends on alkali incorporation strategy It has a threshold behaviour Too much Na can hinder crystal growth	Improved V_{oc} and FF (correlation morphology-performance not clear)	[162–170]
Grain boundary passivation and enhanced carrier transport	Na accumulates in grain boundaries and attracts oxygen. Oxygen passivates Se dangling bonds Creation of a positive potential at grain boundaries that attract electrons and repels holes	Passivation supresses non-radiative recombination Separation of charges leads to an enhanced carrier collection	Improved V_{oc} and FF	[162,163,171, 172]
Increase of carrier concentration	Na occupies Cu vacancies (Na_{Cu}) and avoids the formation of Zn_{Cu} donor defect Na_{Cu} is formed at high temperature but becomes less stable during cooling down. Na out-diffuses from Cu positions and leaves V_{Cu} Formation of acceptor Na_{Zn} Suppression of $V_{S,Se}$ Reduction of activation energy of shallow acceptor	Mechanism not well understood	Improved V_{oc}	[116,161,163, 167,168,173, 174]

The optimum amount of Na incorporation in order to obtain observable and beneficial effects has been found to be around 0.1-0.5 at% which is the amount of Na typically incorporated when using a SLG substrate and a high temperature (>500°C) annealing [175–177]. This way, the employment of SLG is a very effective and, probably, the most extended doping strategy. However, it presents two major drawbacks that prevent a proper control of Na incorporation:

1. SLG presents spatial and batch to batch inhomogeneities
2. Na ions diffuse through oxygen bonds at the Mo back contact grain boundaries [178–180]. Therefore, the total diffused amount of Na depends on the:
    a. Thickness of Mo back contact
    b. Number and oxidation state of grain boundaries
    c. Annealing temperature

The eagerness for a more precise control of Na incorporation together with the fabrication of solar cells on Na-free substrates have motivated the development of alternative doping strategies. The most commonly employed are:

- Na-containing Mo back contacts (Mo:Na) [158,181–183]
- Extrinsic deposition of a Na-containing layer (NaF, $Na_2(S,Se)$, etc.) [73,74,158,184,185]. Depending on where the layer is deposited, there are two different strategies:
    - Pre-absorber synthesis (PAS): the layer is deposited on the Mo back contact prior to the deposition of the precursor and synthesis of the absorber.
    - Post-annealing treatment (PDT): the layer is deposited on the synthesised absorber and a re-annealing process is carried out to diffuse the alkaline element into it.
- Incorporation of Na compounds into precursor solution [157,186,187]

The strategy employed has an important influence on the effects produced by Na. If Na is available during the synthesis process (SLG, Mo:Na, PAS, etc.), it can strongly affect the crystallization process and morphology of the absorbers while in PDT treatments, since are applied once the absorber has been crystallized, it will mainly affect its electrical properties.

Potassium and other alkalis

Owing to the success of Na-doping, the CIGS community soon started to research the potential of other alkaline elements. In particular, a lot of attention was put onto the closest relative of Na which is also present (although in a very small concentration) in SLG substrates: potassium. The first works showed that it was possible to incorporate K into the CIGS structure and that it also improved the V_{oc} of the devices [74]. However, the first major success of K doping was made by Chirilă et al. who demonstrated a 20.3% efficiency device on a polyimide substrate by combining NaF and KF PDT [188]. Since then, many groups included KF PDT treatments in their processes and most of them noticed significant increases in the V_{oc} and FF of their devices [189–192].

Some of the observed effects of K are very similar to the ones described for Na like crystal growth enhancement, grain boundary passivation and carrier concentration increase [74,193]. However, the most critical effect of KF PDT in CIGS was observed to be a Cu-depletion of the surface of the absorbers that promotes an enhanced growth of the CdS buffer layer due to Cd diffusion into the Cu-depleted regions [190,194]. The beneficial effects of potassium seem to be more profound when combined with Na due to an ion exchange mechanism between the two alkalis in which K tends to replace Na within the absorber and, thus, it is more effectively incorporated [161,185,195].

As for kesterites, K doping has also been thoroughly investigated trying to reproduce the positive results obtained for CIGS. KF PDT treatments do not seem to have the same beneficial effects than for CIGS and even decrease the performance of the devices due to a current blocking behaviour [196,197]. However, a Cu-depleted surface has in fact been observed when adding KOH to the precursor solution that, as in the case CIGS, enables a better growth of CdS and improves the J_{sc} of the devices [186]. On the other hand, some similarities with Na have also been spotted in CZTSSe absorbers. This way, it has been detected that the addition of a K source into the precursor solution results in an improved carrier concentration [186,198]. Similarly, K has also been observed to increase crystal size and enhance <112> orientation with a fewer dopant amount compared to Na due a lower melting point of K-Se species [165,199]. A passivation effect related to its tendency to remain at the grain boundaries has also been spotted [132,159,198]. Finally, differently to Na, the addition of K has been related to the avoidance of ZnS formation and the promotion of $SnSe_2$ formation [199,200]. The mechanisms behind these effects are expected to be similar to those described above for Na (Table 5) although the incorporation and mobility of K in Cu vacancies is expected to be lower due to the higher formation energy of K_{Cu} caused by its larger ionic size [159,161].

Other alkaline elements have also been studied with fruitful results. In the case of CIGS, heavy alkali PDT has enabled boosting the efficiency of devices beyond 22%. In particular, Jackson et al. achieved a world-record 22.6% efficiency device employing a RbF PDT treatment [78].

As for kesterites, heavy alkaline elements have been observed to enhance crystal growth but neither clear electrical nor performance enhancements have been reported [157,186]. However, the lightest alkali, Li, has demonstrated the capability of incorporating into kesterite absorbers very easily (due to the low formation energy of Li_{Cu}) and boost the V_{oc} and efficiency of the devices [101,157]. This way, an huge improvement from ~5% (no doping) up to 11.6% (6 at% of Li) was reported by Cabas-Vidani et al.. However, the amount of Li employed and the widening of the bandgap reported for the best devices (3-7 at%) indicate that Li is not acting as a dopant but as an alloyer.

1.4.5 Summary and final remarks

Kesterite is a very promising thin film PV technology based on Earth-abundant elements. The fact that the best efficiencies have been obtained by high-vacuum-free processes indicates that it has a large potential for increasing the EROI of PV through low cost mass production. Although the current efficiency levels combined with a low cost production could suffice for an adequate and long-lasting medium-high EROI, or at least superior to that of Si technologies, there is still a huge room for improvement. The main problem of the technology is the large V_{oc} deficit of the devices due to the formation of secondary phases and the high density of defects. However, continuous research efforts and process optimisation are likely to increase the open-circuit voltage of kesterites. The study of alkali doping is crucial for a successful improvement of the technology, especially for its development on alkali-free substrates which have the potential of exploiting its true potential regarding cost reduction and EROI increase.

1.5 Context and objectives of the thesis

1.5.1 The limitations of soda-lime glass and Mo

As described in the previous section, the standard substrate employed for kesterite solar cells is SLG covered with a Mo back contact. SLG is a very convenient substrate for thin film photovoltaics for several reasons

i. Its mechanical stability [201]
ii. Its thermal resistance (softening point ~550°C) [42]

iii. Its coefficient of thermal expansion (CTE) matching that of kesterite (SLG ~$9\cdot10^{-6}$ K^{-1} [201], CZTSSe ~$8.5\cdot10^{-6}$ K^{-1} [202])
iv. Its chemical inertness
v. Very low surface roughness (R_{rms}~0.5 nm) [42]
vi. Extensively and cheaply produced for glazing (0.8-1.7 $/kg or 6-13 $/$m^2$ for a 3 mm glass) [201]
vii. Beneficial Na-containing composition [42,201]

In fact, all the high efficiency devices reported in Table 3 were fabricated on glass substrates. However, the stiffness, fragility and high weight of glass set limits to PV module industrial fabrication processes (in particular to production throughput), require careful handling of modules and strongly limits the applicability of kesterite solar cells.

As stated before, the true potential of 2nd generation PV and, especially, of an Earth-abundant thin film technology like kesterites to increase the EROI of PV resides in a large cost reduction through high-throughput production, advanced applications and ubiquity which cannot be attained only with SLG substrates.

Regarding Mo, it has been proven to be the best choice of back contact for kesterite solar cells due to its excellent conductivity, thermal resistance and limited chemical degradation during the synthesis process [203]. In addition, its reaction with S/Se in a controlled manner produces a back $Mo(S,Se)_2$ buffer layer of which aids in forming an ohmic contact [147]. However, its lack of transparency also limits the possibilities of kesterite-based photovoltaics.

In this context, the development of kesterite solar cells on alternative substrates to the standard SLG/Mo should clearly be a must for the kesterite community in order to provide a bright future not only for kesterites but for PV in general. Yet, soda-lime glass is still the quintessential substrate used in research for kesterite solar cells.

1.5.2 Objectives of the thesis

The main objective of this thesis is to shed light on the feasibility of developing kesterite solar cells onto alternative substrates to the standard SLG/Mo that can fully exploit the capabilities of this Earth-abundant thin film PV technology. In particular, the substrates investigated possess the potential to increase the EROI of PV by reducing the overall fabrication costs through their compatibility with low cost mass production processes and/or with advanced PV applications. Thus, the substrates investigated are the following:

- **Polyimide (PI):** a light-weight and flexible substrate compatible with roll-to-roll mass production processes
- **Ceramics:** the fabrication of solar cells onto a building material like ceramics offers a direct application in building-integrated photovoltaics.
- **SLG/SnO_2:F:** a transparent substrate which enables the fabrication of bifacial and tandem solar cells as well as transparent devices with an application in building-integrated photovoltaics.

Nevertheless, these substrates present a series of drawbacks with respect to the standard SLG/Mo that hinder the development of kesterite solar cells. This thesis aims to identify and address the main issues of each substrate to enable the development of kesterite solar cells onto them. In particular, their lack of alkalis, the low thermal robustness of polyimide, the rough surface of ceramics and the hindered carrier collection of SLG/TCO will be investigated.

2. Methodology

2.1 Overview

In this chapter, the general aspects of the methodology employed throughout this work will be presented. However, the specific experimental features of the different investigations presented in this thesis will be detailed in their corresponding chapters.

In order to carry through the objectives exposed above and study the feasibility of developing high efficiency kesterite solar cells on different alternative substrates, the methodology employed is based on the following basics:

1. Substrate analysis and identification of the main issues for solar cell fabrication
2. Fabrication of solar cells on the substrates by a two-step process involving the chalcogenisation of sputtered metallic precursors
3. Characterisation of absorbers and devices

First, the main processing and characterization techniques employed throughout the thesis as well as the pieces of equipment utilised to carry them out will be briefly presented. Then, the standard procedure employed for the fabrication of kesterite solar cells will be explained in detail.

2.2 Techniques and pieces of equipment

2.2.1 Structural, compositional and morphological characterisation

Optical and confocal microscopy

Confocal microscopy is a type of optical microscopy in which a pinhole/screen is placed at the conjugated focal point of the objective lens system. This way, most of the out-of-focus signal is blocked and an image corresponding to only a thin section of the sample is acquired. By scanning the sample in the Z-axis and combining the 2D acquired images with the Z position information, it is possible to reconstruct the 3D surface morphology (topography) of the sample.

A Sensofar PLu neox confocal microscope (Figure 21) was employed for this purpose. This microscope features a white and a blue LED light sources and three objectives with 20x, 50x and 100x magnification. The system can be used both in optical and confocal modes. This system was employed to study the surface morphology of ceramic substrates both in optical (standard image) and confocal (3D topographies) modes. Additionally, it was also used to measure the thickness of the X-ray fluorescence calibration samples.

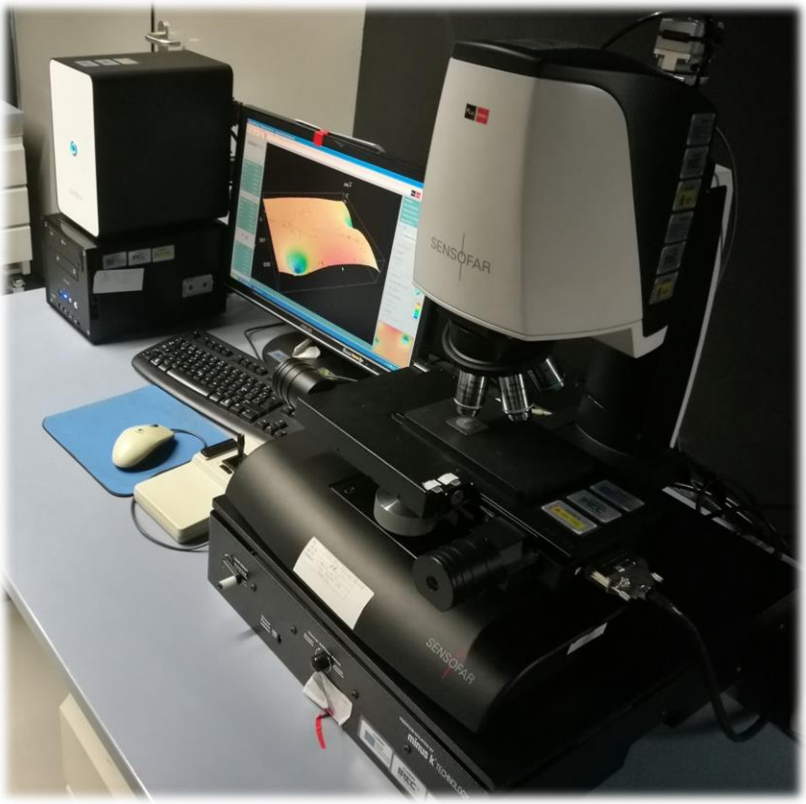

Figure 21. Sensofar PLu neox confocal microscope.

Field emission scanning electron microscopy and energy dispersive X-ray spectroscopy

An electron microscope is a type of microscope that uses electrons as the source of illumination. Owing to the shorter wavelength of electrons compared to visible photons, the resolving power of an electron microscope is far higher than that achievable with standard optical microscopes. In a field emission scanning electron microscope (FESEM), a small-diameter and highly coherent beam of electrons is generated by a field emission gun, focused on the surface of the sample and raster-scanned in a rectangular area. The beam interacts with the atoms in the specimen producing several signals that can be detected individually using different types of detectors. The FESEM microscope employed in this work, a ZEISS Series Auriga (Figure 22), is capable of detecting, mainly, three types of signal:

- **Back scattered electrons**: This signal corresponds to the electrons from the scanning beam which are elastically back-scattered by the atoms of the sample. Since the probability of back scattering increases with the atomic number of the element, this signal produces micrographs in which areas with different composition appear with a different contrast and thus provides spatial-compositional information.
- **Secondary electrons**: This signal is generated by low energy electrons ejected from the surface of the sample as a result of an inelastic scattering process. The number of emitted secondary electrons depends on the interaction volume of the beam with the sample which, in turn, depends on the angle between them. This way, edges and steep surfaces (in which the interaction volume is higher) appear brighter than flat surfaces

providing micrographs with a well-defined contrast that enable structural and topographical analyses.

- **Characteristic X-rays**: This signal arises from the interaction of the incident electron beam with the low-energy electrons located at the inner shells of the atoms of the sample. The incident beam can promote these electrons to an excited state. A high-energy electron from an outer shell can then occupy the low energy vacancy emitting the energy difference between both states as an X-ray photon. Since the energy difference between the different electronic shells is dependent on the atom itself, each element generates photons with characteristic energies. Thus, by analysing the radiation emitted by the sample, it is possible to get precise information about its elemental composition. This process is called energy dispersive X-ray spectroscopy (EDX).

The results presented in this thesis are based, mainly, on secondary electron imaging employing a standard Everhart-Thornley detector. This detector consists of a collector which is at around +350 V in order to attract the electrons emitted by the sample, a scintillator system and a photomultiplier to overcome the low emission rate and energy of secondary electrons and obtain a sufficiently strong signal useful for imaging [204]. This way, FESEM was employed to analyse the surface of kesterite absorbers (top view) and/or the layer structure of complete devices (cross section) through detailed micrographs acquired from secondary electrons. The micrographs were normally obtained using a 5 kV accelerating voltage and a 30 µm aperture for the electron beam as well as a working distance ranging from 4 to 7 mm.

Additionally, the FESEM microscope was employed to analyse the surface composition of some selected kesterite absorbers employing an EDX Oxford Instruments XMax detector integrated in the system. A 15 kV accelerating voltage was employed for this purpose.

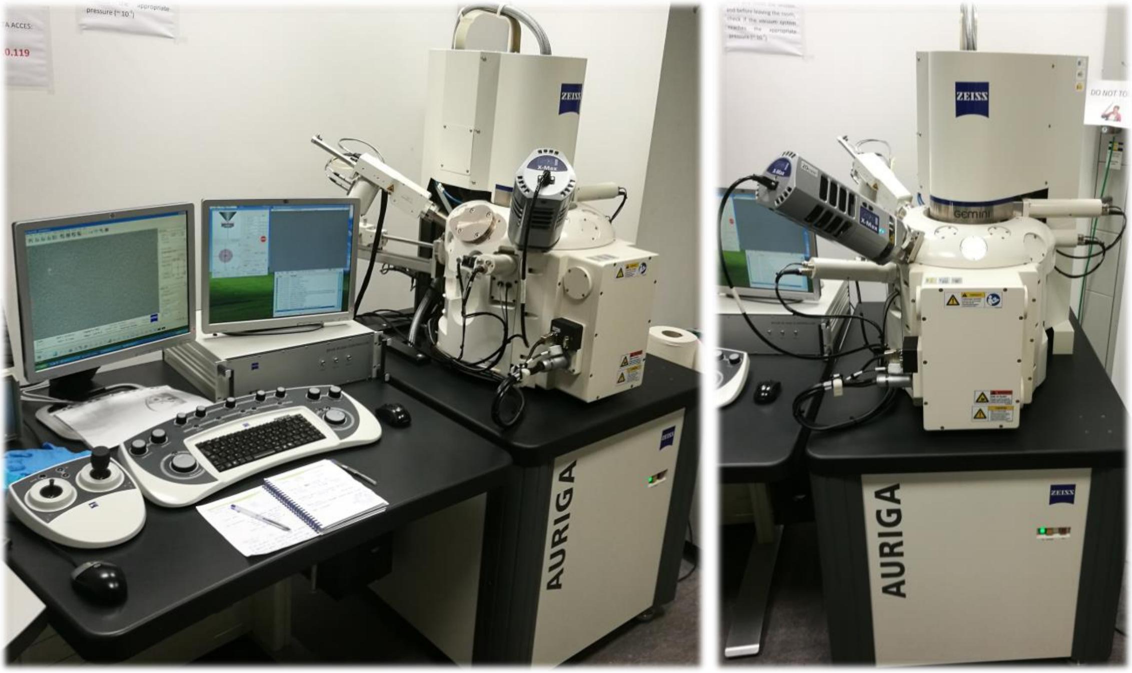

Figure 22. ZEISS Series Auriga field emission scanning electron microscope.

X-ray fluorescence

X-ray fluorescence (XRF) is a phenomenon in which atoms emit radiation upon X-ray illumination. Energetic X-rays can be absorbed by electrons located at the inner shells of an atom which are subsequently promoted to an excited state leaving a vacancy behind. An electron from a higher energy shell can then fall into the low-energy vacancy emitting the energy difference between both energy levels as a photon. The possible energies of the emitted photons depend on the electronic structure of the atom and, thus, are characteristic of each element. By analysing the spectrum emitted by a sample under X-ray illumination, it is possible to obtain information about its elemental composition.

However, different elements possess distinct mass absorption coefficients so the intensity of their fluorescence is different. In addition, this factor is also influenced by the density of the material which largely depends on the technique employed for its synthesis/deposition. Finally, for complex multilayers stacks like the ones employed in this work, the radiation emitted by the layers at the bottom is attenuated by the upper layers before escaping the sample. This attenuation will depend on the thickness and density of the different layers above. Therefore, it is not possible to extract quantitative information from XRF measurements in a direct way. The spectra obtained need to be fitted employing a model that takes all these issues into consideration.

A Fischerscope XVD XRF analyser (Figure 23) was employed to measure and control the thickness and composition of Mo back contact layers, precursor metallic stacks and kesterite absorbers, mainly. The software of this XRF system allows creating complex layer models (recipes) and fits the obtained spectra to them through an iterative process in order to provide information about the composition and thickness of the different layers. Three types of layer model have been mainly employed throughout this work:

1. **SLG/Mo:** for measuring the thickness of Mo back contacts
2. **SLG/Mo/CuZnSn:** for measuring the thickness and composition of precursor metallic stacks
3. **SLG/Mo/CuZnSnSSe:** for measuring the thickness and composition of kesterite absorbers

The same measuring parameters were employed in the three recipes: an accelerating voltage of the primary X-ray source of 50 kV, a Ni10 filter to reduce background signal, a spot size of 1 mm and an integration time per measuring point of 45 s. Usually, a 9 to 16-point measuring grid was distributed throughout the surface of the sample and the mean compositional and thickness values were calculated.

Due to the fairly complex layer systems measured and to the fact that the density of the materials deposited and synthesised in this thesis differs from standard bulk values, in order to obtain accurate values from the fittings of the measuring recipes, these had to be calibrated employing reference samples with known thicknesses and compositions. In addition, the calibration samples were fabricated at IREC's laboratory employing the standard procedure described in section 2.3 so that the samples had layer structures, thicknesses, densities and compositions close to those of the samples measured afterwards with each of the recipes. The thickness and composition of the reference samples was measured by high-precision techniques prior to the calibration of the XRF system. The following sets of samples were fabricated for this purpose:

1. **SLG/Mo:** Three samples with different thicknesses. The thickness of the samples was at IREC measured by FESEM.
2. **SLG/Mo/CuZnSn:** Seven samples with standard thickness and different compositions: one sample with a standard Cu-Sn-Zn composition and six samples in which one the metals was varied either +10 at% or -10 at%, approximately. The composition of the samples was determined by an external laboratory employing inductively coupled plasma mass spectrometry (ICP) while the thickness was measured at IREC by means of FESEM and confocal measurements.
3. **SLG/Mo/CuZnSnSSe:** Seven absorbers obtained from the chalcogenisation of identical precursors to the ones described above. The composition of the samples was externally determined by ICP and the thickness was measured at IREC by FESEM and confocal measurements.

Finally, it should be noted that the recipes employed for the XRF measurements shown above are based on the standard SLG/Mo substrate. The reason for this is that in IREC most of the research on kesterites is carried out employing this substrate. Instead of creating and calibrating different measuring recipes for each substrate configuration, a more practical approach is employed: a SLG/Mo reference sample is processed simultaneously with the samples processed on other substrates. This way, the XRF measurements can be carried out on the SLG/Mo sample and the values obtained for it are assumed to be similar to the other substrate configurations.

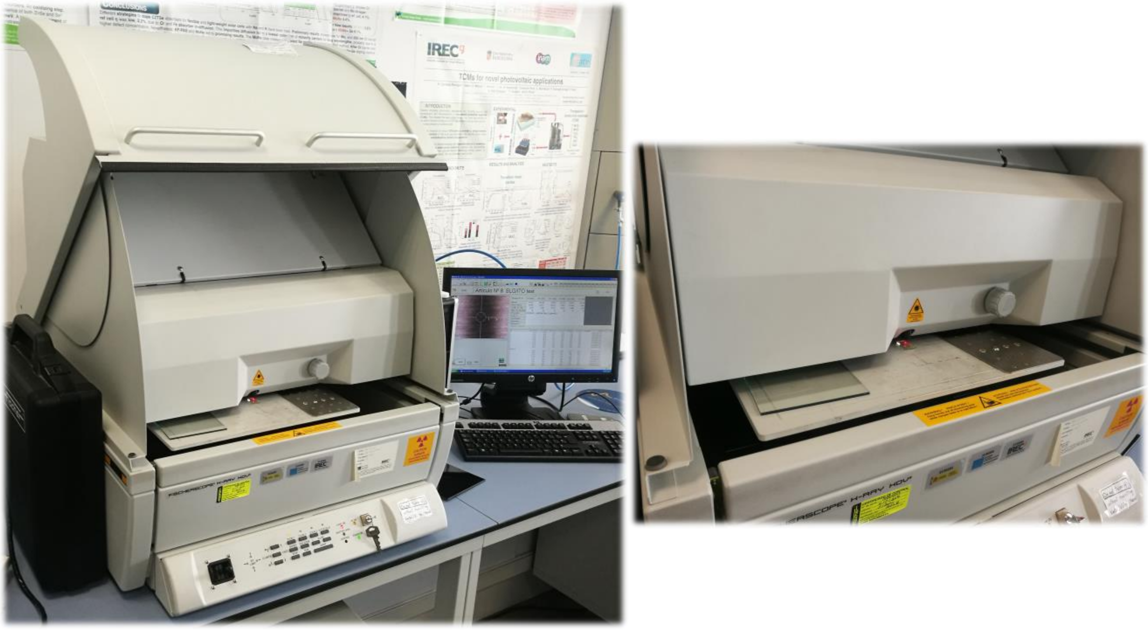

Figure 23. Fischerscope XVD X-ray fluorescence analyser.

X-ray diffraction

X-ray diffraction (XRD) is a powerful technique that allows the identification of crystalline phases in a target material and provides information about their orientation, crystallinity and texture. It is based on the interaction of monochromatic X-ray electromagnetic waves with a regular array of atoms. The incident radiation makes the electrons in the sample to re-emit secondary X-ray waves (elastic scattering). These secondary waves interact with each other through interference processes. In a crystalline structure, where atoms are ordered in different planes, these waves interfere constructively if the Bragg's law is fulfilled:

$$2dsin\theta = n\lambda \tag{14}$$

where d is the spacing between diffracting planes, θ is the incident angle, n is an integer number and λ is the wavelength of the incident radiation (see Figure 24). By scanning a sample in the θ coordinate, it is possible to detect the different diffracting planes present in the sample which are parallel to its surface. Then, comparing the position of the peaks in the obtained diffractogram with reference patterns, it is possible to identify the crystalline phases present in the sample as well as their crystallographic orientation. In addition, by analysing the height and shape of the peaks, it is possible to get an insight on the crystalline quality and texture of the material.

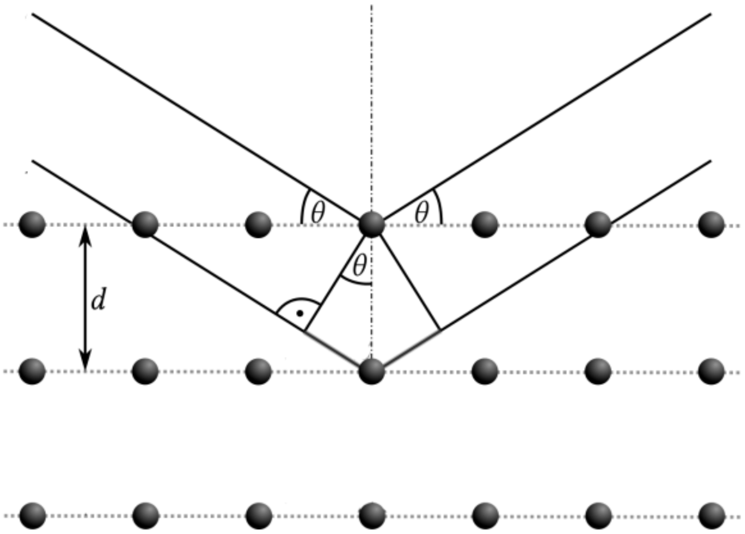

Figure 24. Constructive interference between elastically scattered secondary X-ray waves fulfilling Bragg's law.

A Bruker D8 Advance XRD system (Figure 25) was employed for phase identification an to analyse the crystal structure of Mo layers and kesterite absorbers. The measurements were carried out employing a Cu K_α radiation source (λ = 1.5418 Å) at 40 kV and 40 mA, in θ-2θ (Bragg-Brentano) configuration, at 2θ angles from 10° to 90° in 0.017° steps, with an integration time of 2 s per step and with sample rotation. The diffractograms where anaylised and compared with reference patterns using X'pert High Score Plus software.

Figure 25. Bruker D8 Advance X-ray diffraction system.

Raman spectroscopy

Raman spectroscopy is an advanced characterisation technique based on the analysis of inelastic scattering processes of light with the vibrations (phonons) of the atoms or molecules in a material. A Raman spectrum is obtained by illuminating the material and measuring the inelastically scattered radiation arising from it as a function of its frequency (usually called Raman shift). For crystalline materials, a Raman spectrum consists of individual Lorentzian-shaped peaks, each of them related to an individual phonon. The parameters of the individual peaks can be directly related to the vibrational properties of a material which, in turn, depend on its composition and internal structure. This way, the symmetries of its crystalline structure determine the type of vibrations, the number of atoms in the unit cell influences the number of possible phonons and the frequency of the phonons is defined by the type of atoms (i.e. chemical composition). Thus, Raman spectroscopy can be used to determine the presence of different phases in a material, their composition, crystalline structure and crystalline quality.

Raman measurements were carried out to investigate different properties of selected kesterite absorbers synthesised throughout this work. In particular, their crystalline quality, S-Se composition and/or the presence of secondary phases were evaluated. A Raman setup developed at IREC (Figure 26) was employed for this purpose. It consists of a Raman probe coupled by optical fibres to two spectrometers: a Horiba Jobin Yvon FHR640 (optimised for the ultraviolet-visible spectral region) and a Horiba Jobin Yvon iHR320 (optimised for the near infrared-infrared region) which are coupled, in turn, to cooled CCD detectors. Several lasers with wavelengths ranging from 325 to 1024 nm are available as excitation sources depending on the properties and materials studied. The selection of the laser is particularly important for investigating the presence of secondary phases. By coupling the excitation wavelength with the bandgap of a specific secondary phase (usually called resonant Raman conditions), a highly increased sensitivity is achieved enabling the detection of very small concentrations almost undetectable otherwise.

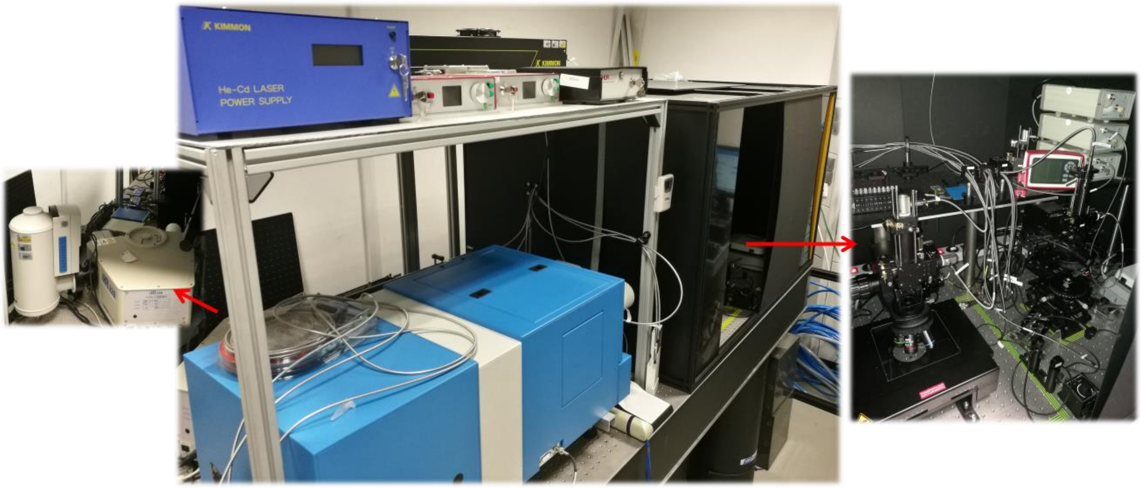

Figure 26. Raman spectroscopy setup developed at IREC.

2.2.2 Optical and electrical characterisation

Ultraviolet-visible-near infrared spectroscopy

In ultraviolet-visible-near infrared (UV-vis-NIR) spectroscopy, a monochromated beam of light is used to study the optical properties of a material through the analysis of the wavelength dependence of its transmittance, reflectance and/or absorbance.

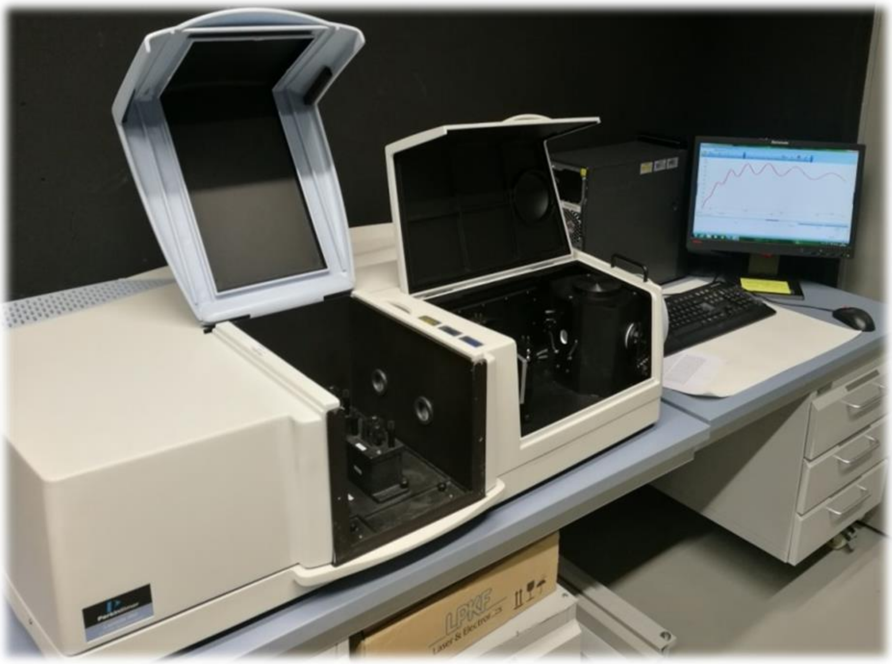

Figure 27. UV-vis-NIR spectrophotometer.

A Perkin Elmer Lambda 950 spectrophotometer (Figure 27) was employed to analyse the transparency of the different transparent substrate/back contact configurations of employed. It is equipped with deuterium (for UV-vis) and halogen (for vis-NIR) light sources, a monochromator, an integrating sphere and high-sensitivity photomultiplier and Peltier-controlled PbS detectors.

Four point probe

A four point probe (4pp) is an electrical measurement setup consisting of four terminals: a pair of outer current-carrying electrodes and a pair of inner voltage-sensing electrodes. By applying a current through the outer electrodes and due to the high impedance of the voltmeter, almost no current will flow through the sensing wires avoiding contact and wire resistances and enabling the measurement of very small resistances.

This technique was employed to measure the sheet resistance (R_{sheet}) of conductive layers such as Mo and TCOs. An Everbeing setup with 4 equidistant measuring tips connected to a Keithley 2420 power source (Figure 28) was employed for this purpose.

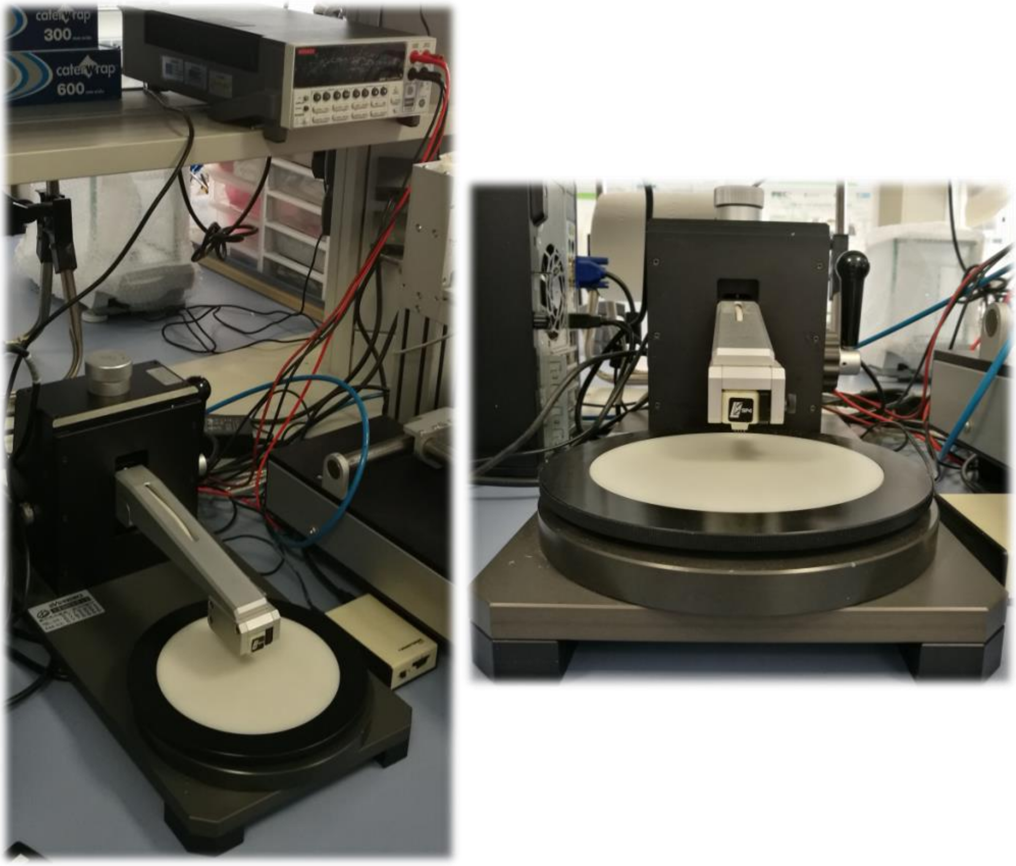

Figure 28. Everbeing four point probe.

Capacitance-voltage

Capacitance-voltage (C-V) measurements provide information about the carrier concentration and the width of the SCR of a solar cell based on the assumption that a p-n junction can be modelled as a parallel plate capacitor. In kesterite solar cells, the doping level of the n side of the junction (CdS) is orders of magnitude higher than that of CZTSSe and, in addition, its thickness is orders of magnitude lower. This way, the SCR can be assumed to be located entirely at the p side. In this approximation, the charge (Q) "stored" in the capacitor is equivalent to the number of doping impurities within the width of the SCR (W) times the elemental charge (q). By applying a bias voltage to the p-n junction, the width of the SCR varies and so does the charge:

$$dQ = qN(W)dW \rightarrow N(W) = \frac{1}{q}\frac{dQ}{dW} \tag{15}$$

where N(x) is the linear density of doping impurities. On the other hand, the capacitance of a capacitor can be expressed as:

$$C = \frac{\epsilon A}{x} \rightarrow x = \frac{\epsilon A}{C} \tag{16}$$

where ε is the dielectric constant, A the overlapping area of the parallel plates and x the width of the capacitor (W for a p-n junction). In the case of a p-n junction, if the space charge region is varied by applying a voltage, its capacitance will also vary:

$$dW = -\frac{\epsilon A}{C^2}dC \tag{17}$$

Finally, the change of the charge stored in a capacitor when the voltage is between its terminals is varied can be obtained from the fundamental definition of capacitance:

$$C = \frac{dQ}{dV} \rightarrow dQ = CdV \tag{18}$$

Combining Eqs.(15), (17) and (18), it is possible to calculate n(W) (the carrier concentration as a function of the SCR width) from C-V measurements:

$$n(W) = -\frac{C^3}{q\epsilon A^2}\frac{dV}{dC} \rightarrow n(W) = \frac{2}{q\epsilon A^2}\left(\frac{dC^{-2}}{dV}\right)^{-1} \tag{19}$$

C-V measurements were performed on complete devices by applying a 50 mV oscillating AC voltage at various frequencies and measuring the quadrature current response at different bias voltages. The measurements were carried out employing a Keysight E4990A impedance analyser and a homemade Faraday cage sensor box (Figure 29). The measurements were used to calculate the carrier concentration and the width of the space charge region of selected devices.

Figure 29. Keysight E4990A based capacitance-voltage measurement setup.

Current-voltage analysis

The fundamentals of current-voltage (J-V) analysis were explained in section 1.2.2.

A setup consisting of a Keithley 2400 source and a pre-calibrated Sun 3000 Class AAA solar simulator by Abet Technologies (Figure 30) was employed to carry out the J-V measurements of the different devices fabricated in this work. The measurements were carried out at 25 °C and both in the dark (for selected devices) and under simulated AM1.5 illumination (1000 W/m^2). The main parameters of the solar cells were extracted from the J-V curves: V_{oc}, J_{sc}, FF and η. In some cases the shunt and series resistances (R_{sh} and R_s) were also calculated from the J-V curves.

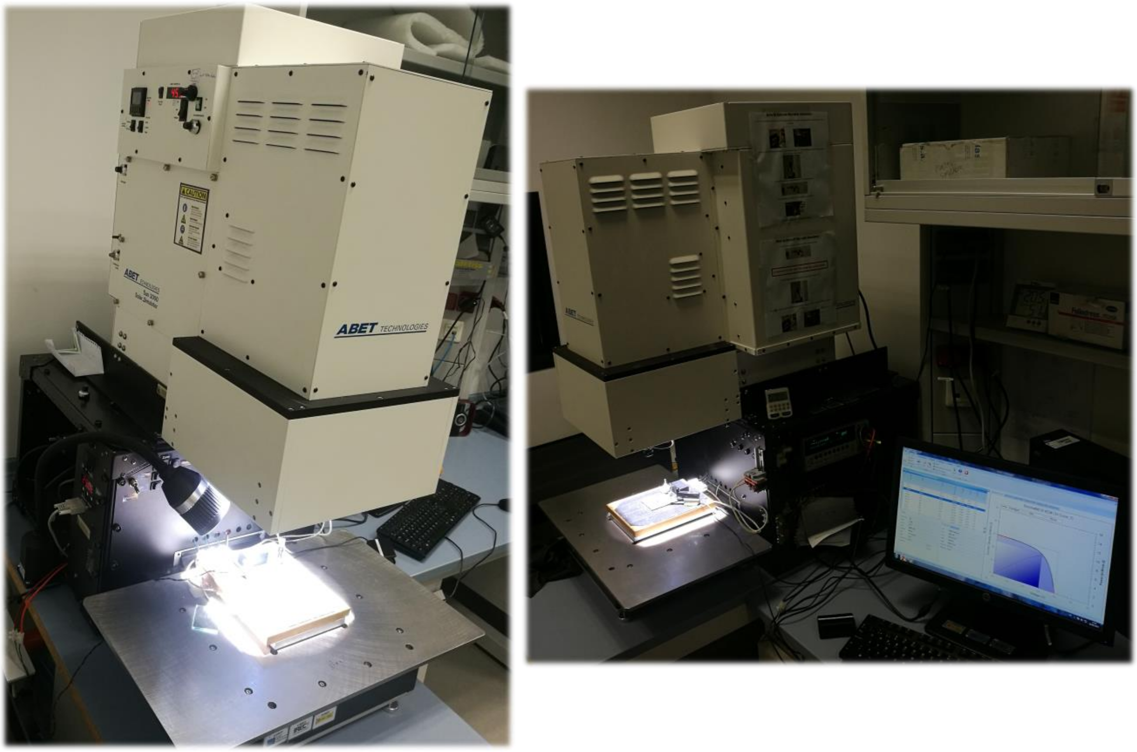

Figure 30. J-V analysis setup based on a calibrated Sun 3000 Class AAA solar simulator by Abet Technologies.

External quantum efficiency

External quantum efficiency (EQE) is an optoelectronic characterisation technique that complements J-V analyses by providing information about charge collection as a function of the illumination wavelength. This way, in EQE measurements, the sample is illuminated with monochromated light and the ratio between the number of incident photons to the number of collected EHPs is measured at different wavelengths to provide a collection spectrum. By integrating the EQE spectrum times the AM1.5 illumination spectrum, it is possible to obtain the J_{sc} of the device.

EQE measurements were performed on selected devices to study their collection. A Bentham PVE300 spectral response system (Figure 31) consisting on Xe and halogen light sources, a monochromator and a lock-in amplifier was employed for this purpose (Figure 31).

Figure 31. Spectral response system used for EQE measurements.

2.2.3 Solar cell fabrication

Direct current magnetron sputtering

Direct current (DC) magnetron sputtering is a PVD coating technique that allows the deposition of thin films of a wide variety of materials. An inert gas plasma (usually Ar) is generated inside a chamber by applying a high voltage between a cathode (usually the target material) and an anode (usually the deposition substrate) (Figure 32). The plasma is confined around the target through a strong magnetic field generated by a magnetron. The moving ions in the plasma hit the target material and sputter atoms out from its surface. Most of the sputtered atoms are neutral so are not affected by the electromagnetic field and fly away in straight lines from the target. This way they can reach a substrate and stick onto it. By varying the inert gas pressure and/or plasma power, it is possible to control the sputtering rate (which determines the growth rate of the layer) and the kinetic energy of the sputtered atoms (which influences the density, morphology and adhesion of the deposited layer). The substrate can be heated up during deposition to improve or tune the crystallization of the deposited material. In addition, by introducing a reactive gas in the plasma, like O_2, it is possible to make the sputtered atoms react with it before being deposited. This is called reactive sputtering.

DC magnetron sputtering is an ideal technique for metal deposition due to their high conductivity that facilitates the creation of the plasma. When depositing low conductivity materials, charge can build up on the surface of the target and, in addition, the target can heat up substantially complicating the deposition process. In order to minimize these issues, a pulsed DC source can be employed to generate the plasma.

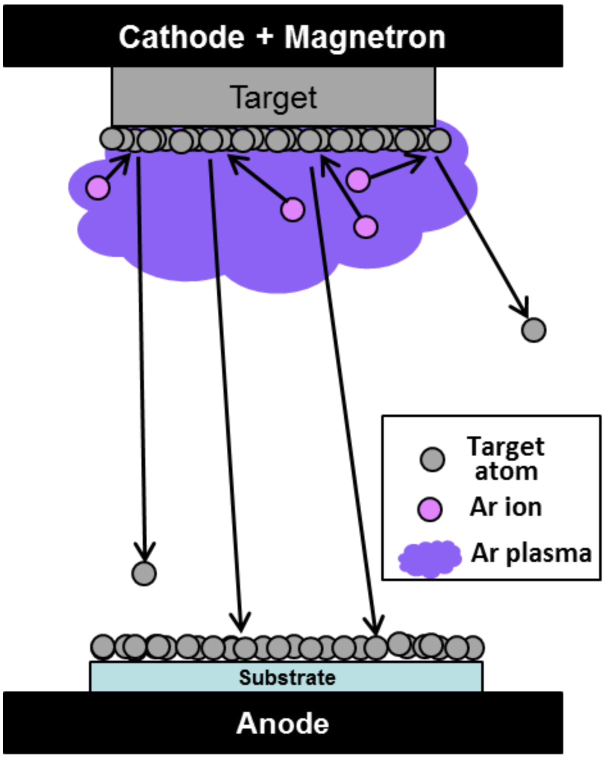

Figure 32. Schematic of DC magnetron sputtering operation.

Two different sputtering systems were employed throughout this thesis in order to deposit the different layers required for the fabrication of kesterite solar cells:

- **Alliance Ac450** (Figure 33, left): This system is comprised by a load lock and a deposition chamber connected to a mechanical pump and a turbomolecular pump. Inside the deposition chamber there are three cathodes located at the top where 101 mm diameter targets can be placed. The substrate is placed at the bottom. It is equipped with a DC generator (TRUMPF Truplasma DC 3002) for sputtering and a RF generator (TRUMPF PFG 300 RF) for plasma etching surface treatments. This system was used for the deposition of metallic layers (Mo, Cu, Zn and Sn). The depositions were performed using an Ar plasma.
- **Alliance CT100** (Figure 33, right): This system is comprised by a load lock and two deposition chambers each of them connected to independent mechanical and turbomolecular pumps. There are two cathodes at the left chamber and three at the right chamber where 101 mm diameter targets can be placed. It is equipped with a pulsed DC generator (Advanced Energy DC pinnacle plus). The left chamber was employed for Mo and Mo:Na deposition and the right chamber for the deposition of TCOs (ZnO and $In_2O_3 : SnO_2$).
- The deposition of Mo was performed in continuous DC mode using an Ar plasma and the deposition of TCOs was carried out in pulsed DC mode employing an $Ar+O_2$ plasma.

Figure 33. Sputtering systems.

Thermal evaporation

In thermal evaporation a crucible/boat containing a material is heated up by an intense electric current under high vacuum. When the appropriate pressure and temperature are reached, the material evaporates. Due to the high vacuum, the particles in the vapour can travel almost freely around the evaporation chamber. When they reach a colder surface they condense onto it thus enabling the deposition of thin films. By varying the heating power of the crucible/boat, it is possible to control the deposition rate.

Figure 34. Thermal evaporator.

An Oerlikon Univex 250 thermal evaporator (Figure 34) was employed to deposit nanolayers of different materials such as alkaline salts, metals and transition metal oxides (TMOs) for a manifold of purposes, from doping to back contact engineering or metallisation. The system is comprised by an evaporation chamber connected to a mechanical and a turbomolecular pump, a DC generator (PCM lambda) and a multi-channel quartz crystal sensor (SQM-160) to control the layer growth rate.

Chemical bath deposition

Chemical bath deposition (CBD) is a thin film deposition technique in which the substrate is introduced into a solution containing dissolved precursor materials. Then, a synthesis and/or a nucleation reaction are triggered so that the targeted compound is synthesised within the solution and grown onto the substrate. By controlling the chemical route and solution parameters such as concentration, pH and temperature it is possible to control the deposition characteristics and tune the properties of the deposited layers.

CBD was employed to deposit the CdS buffer layer of the devices fabricated in this thesis employing a homemade setup consisting in a thermocouple-controlled hot plate and a double beaker bain-marie system for a more precise and homogeneous temperature control and heat distribution (Figure 35).

Figure 35. Setup for CdS chemical bath deposition.

Reactive annealing

A reactive annealing is a synthesis technique based on a thermal treatment carried out in a reactive atmosphere. This technique was employed to synthesise kesterite absorbers out of metallic precursor stacks. The precursors were placed into graphite boxes with crucibles containing S/Se and Sn (Figure 36). The graphite boxes were placed, in turn, inside a Hobersal three-zone tubular furnace (Figure 37) consisting of a quartz tube and resistance-based heating elements. The tube is connected to a mechanical pump at the rear end and to an Ar inlet at the front.

Figure 36. Graphite box for reactive annealing.

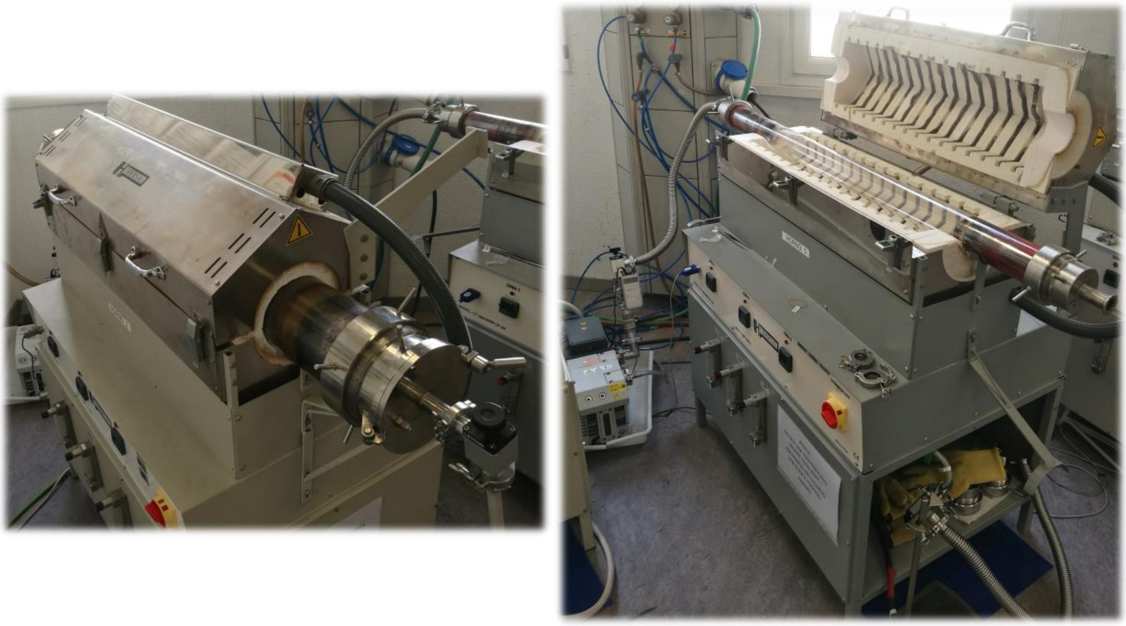

Figure 37. Hobersal three-zone tubular furnaces.

2.3 Solar cell fabrication procedure

2.3.1 Substrate cleaning

All the substrates employed for solar cell fabrication were cleaned prior to the deposition processes. The cleaning method varied slightly depending on the substrate.

SLG, SLG/FTO and polyimide

The substrates were submitted to an ultrasonic bath cleaning process with the following solvent sequence: acetone, isopropanol and deionized water. The time of the ultrasonic treatment in each solvent was approximately 10 minutes at a temperature of 55°C. The substrates were then dried with a nitrogen flux. The PI substrates were further submitted to a surface etching treatment using a RF plasma (100 W, 2×10^{-3} mbar Ar pressure, room temperature, 5 min).

Ceramics

Due to the high porosity of ceramics, only the enamelled surface of the ceramic substrates was cleaned. The cleaning was done mechanically with ethanol. The substrates were then dried with a nitrogen flux and submitted to a surface etching treatment using a RF plasma (100 W, 2×10^{-3} mbar Ar pressure, room temperature, 5 min). The later showed to be crucial for a proper adhesion of the Mo back contact.

2.3.2 Back contact deposition

SLG, polyimide and ceramics

A 670-800 nm Mo back contact was deposited by DC magnetron sputtering on SLG, PI and ceramic substrates. A trilayer configuration, developed at IREC and similar to the one described in [147], was employed. This configuration consists of a Mo$_A$ (250-500 nm)/Mo$_B$ (120-500 nm)/Mo$_A$ (30-50 nm) stack where Mo$_A$ refers to a dense and conductive layer deposited at high power and low pressure, and Mo$_B$ refers to a porous layer deposited at lower power and higher pressure. All these layers were deposited from a monoblock Mo target (Neyco, 99.99% purity, 101 mm diameter). The typical deposition parameters of each layer are summarized in the first two rows of Table 6. The growth rate (GR) of the different layers was controlled by XRF thickness measurements. The resistivity of the back contact was measured by 4pp. Typical resistivity values ranged 0.25-0.5 Ω/□.

Table 6. Typical sputtering deposition parameters for Mo back contacts. P stands for deposition power, p_B for the minimum base vacuum before deposition and p to the Ar pressure employed during deposition.

	P (W)	V (V)	I (A)	p_B (mbar)	p (mbar)	GR (nm/min)
Mo$_A$	330	345	0.96	8×10^{-6}	1.3×10^{-3}	20
Mo$_B$	220	315	0.70	8×10^{-6}	5.1×10^{-3}	14
Mo:Na	200	310	0.65	8×10^{-6}	5.6×10^{-3}	~20

The idea behind this back contact configuration is the following:

i. The first Mo$_A$ layer provides the back contact with a good adhesion and conductivity.
ii. The Mo$_B$ layer, rich in oxygen, acts as a barrier for Se.
iii. The last Mo$_A$ layer is a sacrificial layer completely selenized during the reactive annealing.

This way, a conductive layer with a controlled $MoSe_2$ thickness is obtained.

SLG/FTO

Two slightly different SLG/SnO_2:F (SLG/FTO) commercial substrates were employed: a 1.6 mm thick SLG/FTO substrate (15 Ω/□, Kaivo) and a 2.2 mm SLG/FTO substrate (7 Ω/□, Sigma-Aldrich). Different transition metal oxides (MoO_3, MoO_2, V_2O_5, TiO_2, NiO, Co_3O_4 and CuO) were deposited, in some cases, on top of the FTO by thermal evaporation. A W boat containing pure oxide powders (99.99% purity, Sigma-Aldrich) was used for evaporation. The evaporations were carried out at varying power at a deposition rate of 0.3 Å/s after reaching a 5.6×10^{-3} mbar base pressure. In some cases, a 20 nm Mo_A or Mo:Na layer was deposited on top of the FTO or the transition metal oxide with the deposition parameters shown in Table 6. In the case of Mo:Na, the target employed contained 5 at% Na in the form of Na_2MoO_4 and

2.3.3 Precursor deposition

A metallic precursor stack was deposited by DC magnetron sputtering on top of the back contact with the following structure: Cu (~5 nm)/Sn (~255 nm)/Cu (~180 nm)/Zn (~160 nm). This configuration was based on previous works carried out in IREC [146,205]. The layers were deposited from pure metal monoblock targets (Neyco, 99.99% purity, 101 mm diameter). Typical sputtering parameters of the different layers are shown in Table 7. The thickness of the different layers was selected to obtain Cu-poor (Cu/(Zn+Sn)~0.75) and Zn-rich (Zn/Sn~1.23) compositions since this has been proved to be a requirement for high efficiency kesterite devices (see section 1.4.3) and was controlled by XRF thickness and compositional measurements. The first thin copper layer was used to enhance the growth and adhesion of the Sn layer.

Table 7. Typical sputtering deposition parameters for the metallic precursor stack. P stands for deposition power, p_B for the minimum base vacuum before deposition and p to the Ar pressure employed during deposition.

	P (W)	V (V)	I (A)	p_B (mbar)	p (mbar)	GR (nm/min)
Sn	50	370	0.14	8×10^{-6}	3.6×10^{-3}	7
Cu	100	400	0.25	8×10^{-6}	3.6×10^{-3}	10
Zn	100	480	0.21	8×10^{-6}	3.6×10^{-3}	15

Additional layers

In some cases, additional layers were added to the metallic stack:

- NaF or KF nanolayers (5-20 nm) were thermally evaporated on top (PDT) of or below (PAS) the metallic stack for alkaline doping purposes in polyimide substrates
- Ge nanolayers (10 nm) were thermally evaporated on top of some absorbers for a general improvement of the devices as described in [206]

2.3.4 Absorber synthesis

In order to synthesise the kesterite phase the precursors were submitted to a thermal reactive annealing. They were first were placed inside a graphite box together with crucibles containing Se (Alfa-Aesar, powder, 200 mesh, 99.999%), S (Alfa – Aesar, random size pieces, 99.999%) and

Sn (Alfa-Aesar, powder, 100 mesh, 99.995%). Then, the graphite boxes were introduced into a 3-zone tubular furnace where a 2-step thermal annealing was performed consisting of:

1. A first step carried out at low temperature, 1.5 mbar and under continuous Ar flow for phase formation (in a microcrystalline form).
2. A high temperature step for crystal growth

Depending on the absorber synthesised, the temperature profile of the process was slightly different. Standard annealing parameters for the synthesis of the different absorbers on standard SLG/Mo substrates are presented in Table 8. It should be noted that the 3 zones of the furnace were kept at the same temperature during the whole process to ensure spatial homogeneity throughout the entire length of the furnace. At the end of the process, the samples were let to cool down naturally. The thickness and composition of the absorbers was measured by XRF. Typical absorber synthesis range 1.4-1.7 µm.

Table 8. Reactive annealing parameters for kesterite absorber synthesis.

Absorber	Box volume (cm^3)	Se (mg)	S (mg)	Sn (mg)	p_B (mbar)	Step	p (mbar)	Ar flow	Ramp (°C/min)	T (°C)	t (min)
CZTSe	69	100	-	5	$3\cdot10^{-2}$	1	1.5	Yes	20	400	30
						2	1000	No	20	550	15
CZTSSe	23.5	2	48	5	$3\cdot10^{-2}$	1	1.5	Yes	20	250	20
						2	1000	No	20	550	40
CZTS	69	-	50	5	$3\cdot10^{-2}$	1	1.5	Yes	20	200	15
						2	1000	No	20	550	40

2.3.5 Chemical etchings for secondary phase removal

The as-annealed absorbers were then subjected to 3 successive chemical etchings to remove secondary phases from their surface before CdS deposition:

i. The samples were first submitted to an oxidising etching in a $KMnO_4/H_2SO_4$ solution to remove ZnSe, as described in [127].
ii. Then, the samples were placed into a $(NH_4)_2S$ solution to remove elemental Se and Sn(S,Se) as described in [128]
iii. Finally, a diluted KCN etching was employed to remove $Cu_x(S,Se)$ phases

In the case of the samples processed on SLG/FTO, only the $(NH_4)_2S$ was performed.

2.3.6 CdS buffer layer deposition

A 40-60 nm CdS buffer layer was deposited onto the absorbers by CBD. $Cd(NO_3)_2$ (0.12 M) was employed as the cadmium precursor salt together with thiourea (0.3 M) as the sulphur source. The deposition was carried out with a solution pH = 9.5 and at 70°C for 40 min.[207]

2.3.7 Window layer/front contact deposition

Immediately after CdS deposition, an i-ZnO (50 nm)/ITO (200-300 nm) bilayer was deposited by pulsed DC magnetron sputtering employing Cu-back plated targets (Neyco, ZnO, 99.99% purity; and Neyco, In_2O_3:SnO_2 90:10 wt.%, purity 99.99%) and an Ar/O_2 plasma with the parameters shown in Table 9. An additional piece of SLG was included during the deposition in order to measure the resistivity of the bilayer by 4pp. Typical resistivity values range 35-80 Ω/□. The thickness was controlled by XRF.

Table 9. Typical sputtering deposition parameters for ZnO and ITO. P stands for deposition power, p_B for the minimum base vacuum before deposition and p to the Ar+O_2 pressure employed during deposition.

	P (W)	V (V)	I (A)	p_B (mbar)	p (mbar)	O_2/Ar (%)	GR (nm/min)
ZnO	120	500	0.24	8×10^{-6}	0.4×10^{-3}	5.3	5
ITO	130	390	0.33	8×10^{-6}	1.3×10^{-3}	1.6	10

2.3.8 Solar cell scribing and contact

Once the layer structure was complete, individual 3 x 3 mm^2 solar cells (8.7 mm^2 active area) were electrically isolated employing a manual microdiamond scriber (OEG MR200) (Figure 38). The scribing lines were performed down to the back contact. A small area at one of the edges of the sample was scratched to expose the back contact and some In was welled onto it. Owing to the small size of the cells, no additional contacts were used and the electrical measurements were carried out by contacting directly the ITO of each cell and the In pad.

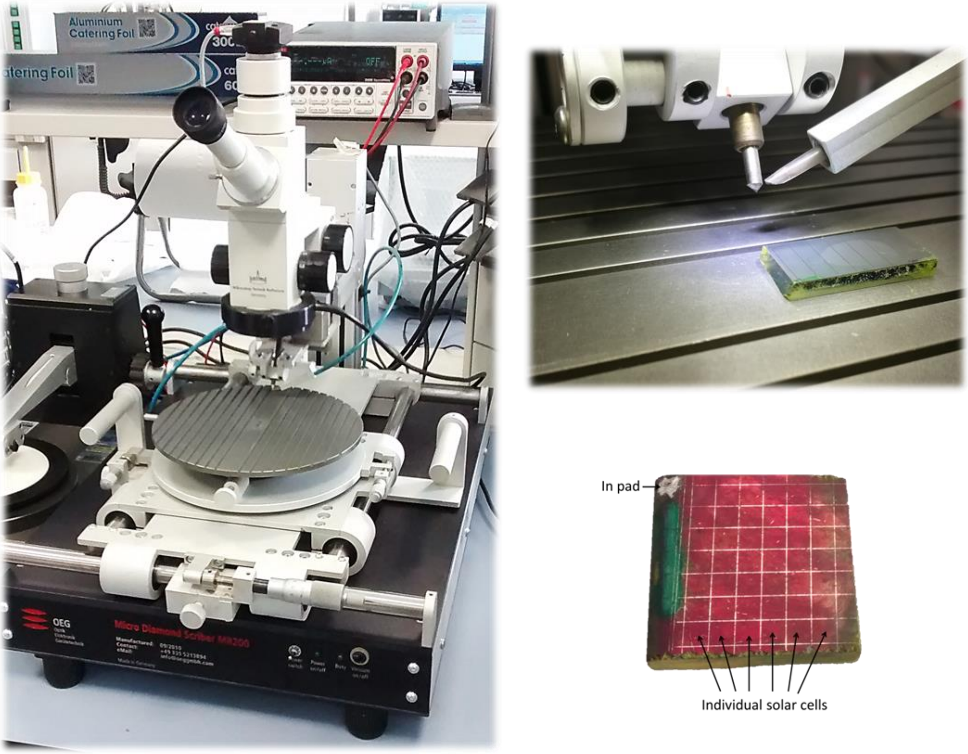

Figure 38. Microdiamond scriber.

In the case of SLG/FTO substrates, two additional layers were added to some of the finished devices by evaporation:

- A 1.5 µm Ag metallic grid using a mask
- A 110 nm MgF_2 layer as anti-reflective coating (ARC)

In these cases, the size of the individual solar cells was 5 x 5 mm^2 (see Figure 39)

Figure 39. Solar cell with metallic grid and anti-reflective coating.

2.3.9 Low temperature post-annealing treatment

Once completed and after a first surveying characterisation, most of the devices were submitted to low temperature post-annealing treatments (LT-PAT). These were carried out in air employing a hot plate at temperatures from 180 to 300°C (depending on the experiment). Low-temperature post-annealing treatments (LT-PAT) have been reported to increase performance of kesterite solar cells [118,140,161,208,209]. This improvement has been attributed mainly to Cu depleted grain boundaries and absorber surface that have a passivating effect reducing recombination and improving the CZTSe/CdS interface [140]. However, there is still not a clear consensus on the effects of LT-PATs.

3. CZTSe solar cells developed on polymer substrates: Effects of low-temperature processing

3.1 Introduction

3.1.1 Light-weight and flexible substrates for kesterite solar cells

Light-weight and flexible (LWF) substrates are key for solar cell manufacturing cost reduction. This is mainly due to their compatibility with roll-to-roll (R2R) high throughput fabrication processes. This type of production starts out from a roll of a bare flexible substrate and ends with a roll of finished product. All the processing takes places in line as the substrate moves between the two rotating rolls (see Figure 40). Although the initial upfront investment on a R2R facility can be very high due to the complicated design of the production line, its high throughput should permit its recovery through economy of scale in the short-mid-term and enable low cost mass production [210]. Therefore, by developing thin-film solar technologies onto light-weight and flexible substrates, it is possible to go towards mass production of PV devices at a reduced fabrication cost and, thus, towards an increased EROI of such technologies.

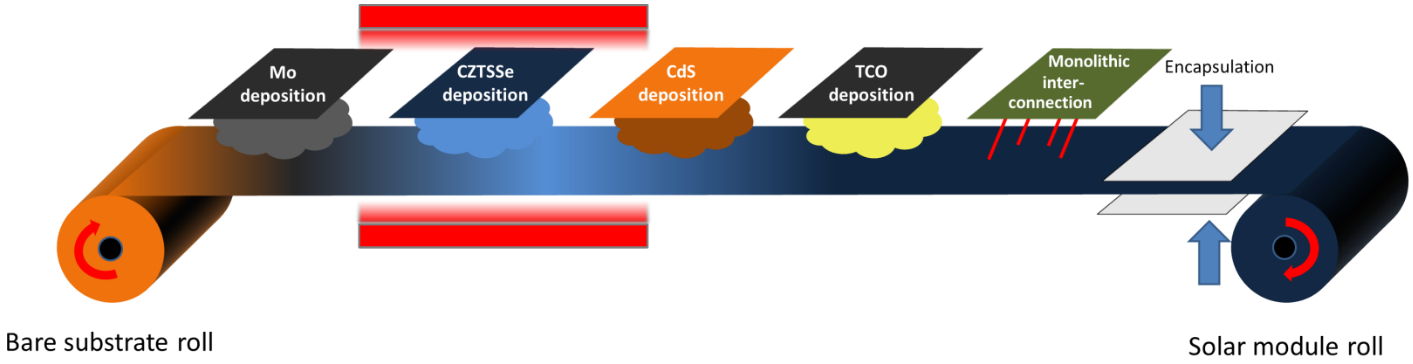

Figure 40. Schematic of a PVD-based kesterite solar module R2R production line.

Besides reduced manufacturing costs, flexible modules present a manifold of advantages with respect to standard rigid modules:

- They can adapt to curved surfaces usually found in buildings (see section 4.1.1), cars, ships, planes, satellites, clothing, etc. (Figure 41, left)
- Their light-weight increases W_p/kg ratio, makes them attractive for the automotive or aerospace industries where weight is a critical factor, reduces transportation and installation costs and turns PV into a compatible and easily integrable powering option in portable electronics and the Internet of Things (IoT) devices (Figure 41, centre)
- They are easier to handle due to their low fragility which allows easy rolling for storage and transportation or even systems where the modules can be rolled and unrolled at

will (e.g. they can be deployed when the weather is propitious for power generation and rolled up at night or under unfavourable meteorological conditions to preserve their integrity) (Figure 41, right)

All this translates into a widely enhanced range of applicability of PV, the enabling of advanced PV applications and the potential for enhancing the ubiquity of PV which, ultimately, also contributes to an overall cost reduction and, thus, to an increased EROI.

Figure 41. Left: LWF solar panels integrated in a car. Source: https://sopraygroup.manufacturer.globalsources.com/si/6008828274640/pdtl/Solar-panel/1062980597/Solar-Panel.htm. Centre: SunnyBag®. Source: https://fr.sunnybag.com. Right: Brunton Solar Roll®. Source: https://www.livefortheoutdoors.com/gear-reviews/accessories/articles/Gear-Reviews/Search-Results/Accessories/Brunton-Solar-Roll-14-2010-solar-panel.

As stated before, kesterite-based solar cells are particularly well-suited for their development on mass production-enabling LWF substrates due to their Earth-abundant composition (see section 1.4). Yet, most of the research carried out on kesterite-based solar cells has been done employing SLG as substrate due to its favourable thermomechanical properties, availability and its beneficial composition (see section 1.5).

Despite the supremacy of rigid glass substrates, a small number of flexible kesterite devices can be found in the literature. Cu_2ZnSnS_4 (CZTS) solar cells were successfully produced on Al foil (η = 1.9%, printing) [211], flexible glass (η = 3.1%, sequential sputtering) [212] and Mo foil (η = 3.8%, sputtering) [213]. Likewise, a 6.1% $Cu_2ZnSnSe_4$ (CZTSe) device was reported on stainless-steel foil via sequential sputtering of metals [158]. Regarding CZTSSe, a remarkable 11.5% flexible device was achieved by a hydrazine-based chemical route employing ultrathin yttria-stabilized zirconia as a substrate [214] and a 7% device was recently fabricated on Mo foil by sputtering [215]. All these devices give proof of the feasibility of fabricating efficient kesterite solar cells on different flexible substrates.

3.1.2 Polyimide: a promising and unexplored substrate

Taking a look at the more mature CIGS, polyimide (PI) foil has demonstrated to be the most promising flexible substrate for this technology without a doubt. Employing PI as substrate, an impressive 20.4% efficiency solar cell was fabricated, very close to cells on SLG and even to p-Si solar cells [190].

PI features several advantageous properties for LWF photovoltaics like high mechanochemical stability (for a polymer) or the absence of harmful impurities (it is mainly formed by C, H and O) that combined with its insulating nature avoid the use of additional barrier layers and allow monolithic interconnection (see Table 10).

Table 10. Main properties of Upilex 50S polyimide foils. Source: http://www.upilex.jp/catalog/pdf/upilex_s_e.pdf?20190220.

Composition	$C_{16}H_6O_6$
Tensile strength	**460 MPa**
Tensile modulus	**93 GPa**
Density	**1470 kg/m^3**
Resistivity	**>10^{13} Ω/□**
Coefficient of thermal expansion	**16 ·10^{-6} K^{-1}**
Chemical resistance to organic solvents	**Excellent**
Chemical resistance to strong acids	**Good**
Chemical resistance to strong alkalis	**Good**
Surface roughness (R_{rms})	**2 nm**
Maximum temperature before pyrolysis	**500°C**

However, despite its great potential for PV, the compatibility of this substrate with kesterite-based solar cells has been barely studied. Only a very scarce number of publications report kesterite solar cells fabricated on polyimide substrates. Using spray pyrolysis deposition, a CZTS device with a modest 0.15% was fabricated on PI [216]. A 0.49% CZTS solar cell was also achieved using PI as a substrate by screen-printing [217]. Finally, CZTS was successfully synthesized on PI by sulfurization of sputtered metallic precursors but no working devices were reported [218].

The motivation behind the work presented in this chapter is to fill this gap and shed light on the feasibility of fabricating high efficiency $Cu_2ZnSnSe_4$ solar cells onto FLW mass production-compatible PI substrates as well as on the issues that need to be taken into account and overcome in doing so.

3.1.3 Limitations of polyimide and objectives of this work

Two main concerns arise when working with polyimide. Firstly, the low thermal robustness of PI limits process temperatures below 500°C. Although the kesterite phase can be synthesised at low temperatures, high efficiency devices are usually obtained at temperatures higher than 500°C (see Table 3). The second concern is the lack of alkali in PI in contrast to conventional soda-lime glass. Alkaline elements (specially Na and K) have been observed to play a fundamental role in the synthesis of high quality CIGS and kesterite absorbers through many different mechanisms like crystal growth enhancement, grain boundary passivation along with an increment of carrier concentration that result in a drastic enhancement of solar cell performance (see section 1.4.4).

This work endeavours to tackle both issues and is divided into three main parts:

i. First, in a preliminary experiment, CZTSe devices are fabricated on polyimide at a moderate temperature (470°C) and different alkaline doping strategies are investigated for the incorporation of Na and K into the kesterite absorber: pre-absorber synthesis (PAS) and post-deposition treatment (PDT).

ii. Then, CZTSe is synthesised at different temperatures (<500°C) on SLG in order to investigate the effect of temperature and the difficulties that come out when synthesizing kesterite at such low temperatures.

iii. Finally, based on the results obtained in the previous experiments, an attempt to increase the power conversion efficiency of CZTSe devices fabricated on polyimide is made by employing higher annealing temperatures (470-490°C) combined with the study of an advanced PAS doping strategy combining Na and Ge.

3.2 Experimental

3.2.1 Sample preparation

Solar cell preparation

Two different substrates were employed in this work: 3 mm soda-lime glass (~2.5 x 2.5 cm^2) and 50 µm polyimide foil (Upilex 50S, see Table 10) (~1.2 x 2.5 cm^2). A 670 nm trilayer Mo back contact was deposited on the clean substrates with a sheet resistance of 0.2-0.3 Ω/□. Cu/Sn/Cu/Zn metallic precursor stacks were deposited onto the Mo back contact with Cu-poor Zn-rich composition. The precursors were selenized through a 2-step thermal reactive annealing at maximum temperatures in the second step ranging 450°C-490°C (depending on the experiment). The as-annealed CZTSe absorbers were then subjected to three successive chemical etchings in order to remove surface secondary phases followed by the deposition of a CdS buffer layer. The devices were completed with a i-ZnO (50 nm)/ITO (200 nm) bilayer (50-80 Ω/□). Each sample was scribed into 10 to 18 individual solar cells (9 mm^2). For a more detailed description of the fabrication process, see sections 2.2.3 and 2.3.

Doping strategies in polyimide substrates

In the case of polyimide samples, an additional step was performed in which a 0, 10 or 15 nm nanolayer of NaF or KF was thermally evaporated to act as doping layer (see section 2.3.3 for further details). Two different approaches were employed in this regard: pre-absorber synthesis (PAS) and post-deposition treatment (PDT). In PAS, the NaF/KF layer was deposited on the Mo back contact prior to the metallic stack. This way, the incorporation of the alkali into the CZTSe absorber occurs during the thermal reactive annealing (Figure 42, middle). In the PDT approach, the NaF/KF layer was deposited on top of the as-synthesized CZTSe absorber. The samples were then submitted to an additional annealing in Se atmosphere at 325°C and 1.5 mbar for 12.5 min in order to induce the diffusion of the alkali elements into the absorber (Figure 42, top). An additional 10 nm Ge nanolayer was also deposited on top of the precursor by thermal evaporation in some of the samples (Figure 42, bottom).

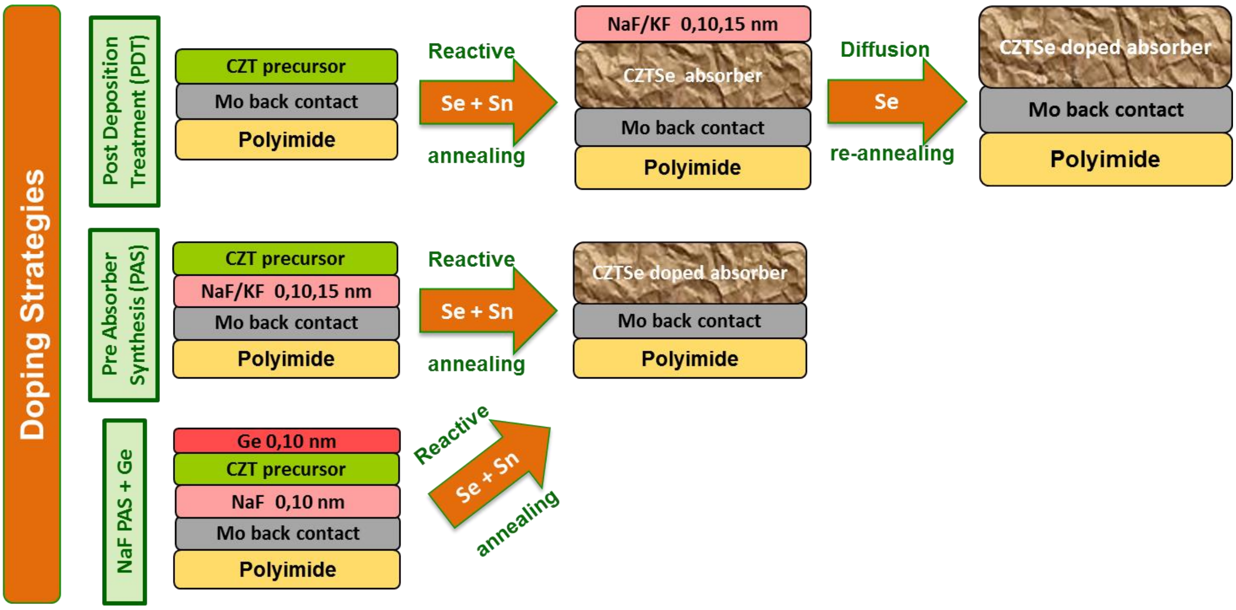

Figure 42. Alkaline doping strategies studied.

Remarks about polyimide substrate handling for solar cell fabrication

The extremely low weight, reduced thickness and high flexibility of polyimide complicated the fabrication of kesterite solar cells on this substrate due to various reasons:

- Tendency to fly away when resting at any surface as well as during pumping, transfer and venting processes within sputtering and evaporation systems
- Tendency to move during thin film deposition
- Tendency to bend when having layers deposited onto them
- Strong bending during selenization

Figure 43. Homemade frames employed initially for polyimide substrate handling.

As a first approach to minimize these issues and enable the fabrication of solar cells on polyimide, homemade stainless steel frames were employed in order to give a rigid support to the substrates (Figure 43). The frames were, in turn, stuck onto SLG substrates with adhesive Kapton tape. This way, the samples remained immobile and flat during the deposition processes (Figure 44). However, due to the low thermal resistance of Kapton tape (<300°C), the samples had to be detached from SLG for reactive annealing (Figure 45). Then, after selenization, they had to be stuck on glass again in order to carry out the chemical etchings and CdS deposition. After CdS, for a proper removal of any remaining of the different chemical processes, the samples usually had to be detached again from the SLG, rinsed thoroughly in deionized water and, finally, stuck once more on glass for i-ZnO/ITO sputtering.

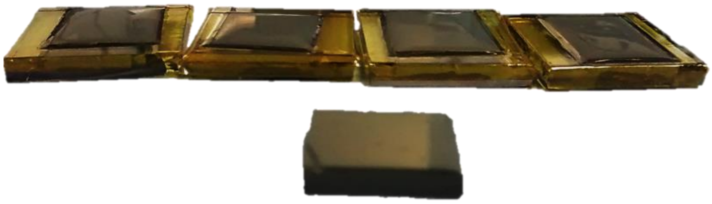

Figure 44. Polyimide within frames stuck with Kapton tape to SLG. A reference sample on SLG is shown for comparison.

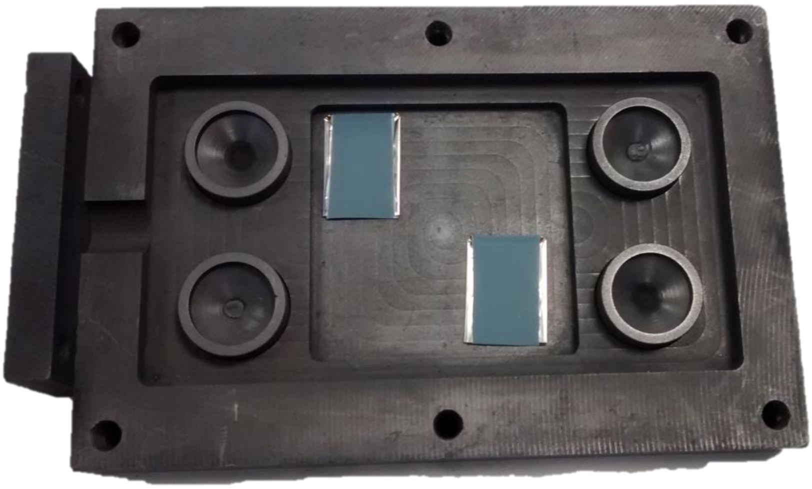

Figure 45. CZT precursors on polyimide detached from SLG for selenization.

Although somewhat tedious, the use of such frames enabled the use of polyimide substrates for solar cell fabrication. However, this type of frame presented several problems:

- Difficulty of fitting the substrate into the frames in a totally flat position.
- During selenization, the tendency of polyimide to bend occasionally caused the samples either to come out the frame or to bend the frame itself.
- The frames were getting selenized forming fine Fe_xSe_y chips that detached from the frames during the annealing itself and, especially, during chemical processes contaminating the solutions.
- Liquid could remain within the folds of the frame after chemical processes and contaminate the CdS bath or come out during pumping in sputtering and affect the deposition of the window layer (Figure 46).

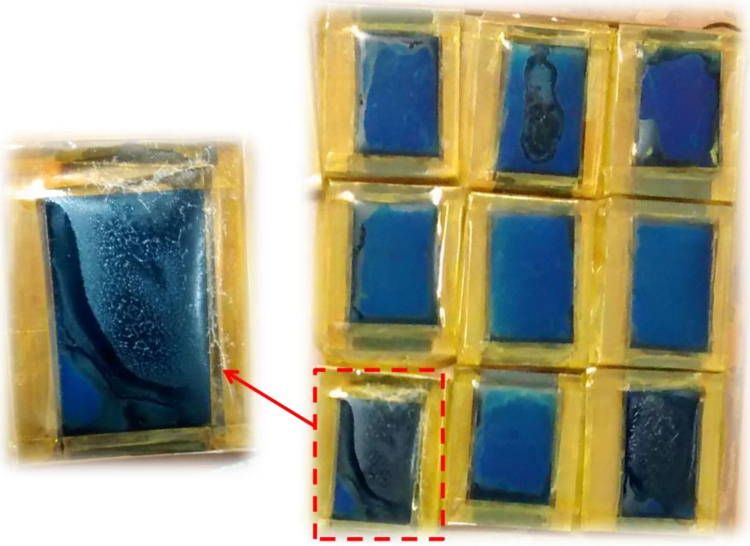

Figure 46. Liquid stored in the frames' folds released during ZnO/ITO deposition.

In order to avoid some of these issues, more advanced frames were fabricated in which polyimide was screwed into a thick piece of stainless steel (Figure 47). This way, it was not necessary to continuously stick the substrates onto and detach from SLG, the samples were not coming out of the frames or bend during annealing and there were no folds where liquid could remain. However, although the handling of the substrates and cleaning of the samples was greatly enhanced, the devices fabricated with these frames systematically presented shunting problems and very low efficiencies so they were discarded.

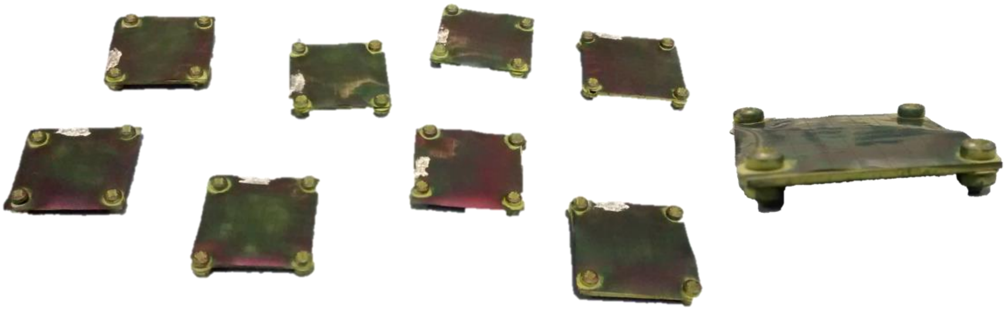

Figure 47. More advanced frame design where polyimide was screwed into a thick piece of stainless steel.

Finally, an experiment was carried out in order to study if avoiding bending during annealing and, thus, the use of frames was really necessary. This way, the two different types of frames together with samples with no frame were fabricated simultaneously. Surprisingly, although the bending of the substrates was greatly reduced using frames as stated before, samples without frame performed slightly better than the framed ones. Therefore, the use of any type of frame was abandoned from that point in order to simplify. This way, polyimide substrates were directly stuck onto glass for deposition and chemical processes and carefully detached for selenization. Although the sticking/detaching of the substrates became a much more delicate procedure, especially after selenization when the samples were completely bent (Figure 48), with this approach no Fe_xSe_y chips were generated and no liquid remained on the samples after chemical processes.

The results presented in section 3.3.1 correspond to samples processed with basic stainless steel handmade frames. However, the results presented in section 3.3.3 correspond to samples processed without frame.

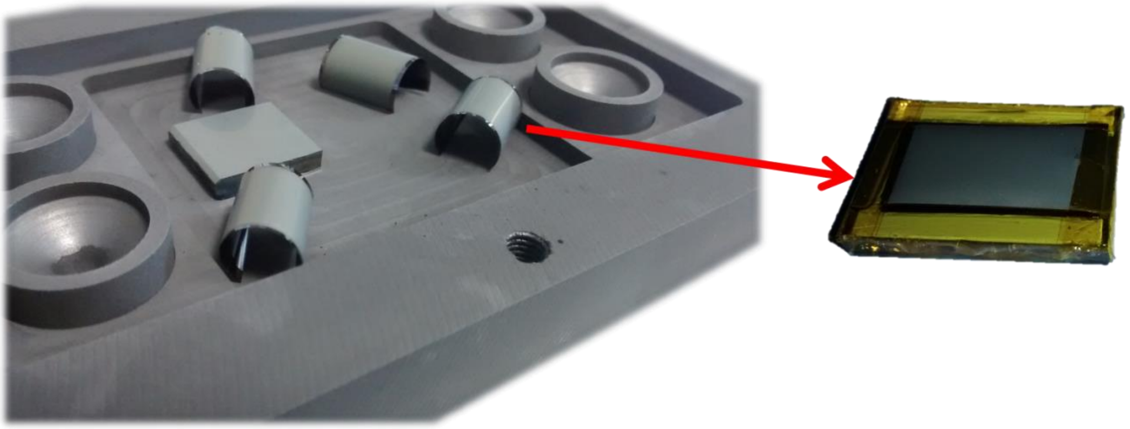

Figure 48. Left: bent polyimide substrates after selenization. Right: bent polyimide substrate flattened and stuck onto SLG using Kapton tape.

3.2.2 Characterization

FESEM secondary electron imaging was employed to examine the surface of the absorbers (top view configuration) and the structure and morphology of the full devices (cross-section configuration) using an acceleration voltage of 5 kV and working distances of 4.5 mm. The composition of the inhomogeneities and clusters found on the surface of some of the absorbers was analysed by EDX with and acceleration voltage of 15 kV.

C-V measurements were performed in the dark at room temperature with an AC modulation voltage of 50 mV at 126 kHz and a -1.25 to 0.2 V bias voltage measuring range. From C-V measurements charge carrier concentration profiles were calculated assuming a relative dielectric permittivity of $\varepsilon = 8.5$ for CZTSe [219].

The J-V characteristics of the devices were obtained under simulated AM1.5 illumination (1000 W/m^2 intensity at room temperature) using a pre-calibrated solar simulator. The EQE was measured using a spectral response system.

Raman scattering measurements were made under a 785 nm excitation wavelength on complete devices. The measurements were performed in backscattering configuration focusing the excitation laser spot on the window layer surface. A diameter of 50 µm and an excitation power density of about 1 kW/cm^2 were used in order to inhibit thermal effects in the spectra while light collection was made through a x20 objective. For this particular excitation wavelength, estimated penetration depth of backscattered light in CZTSe is estimated to be around 100 nm. The 785 nm excitation wavelength was employed for two reasons. The first one is due to the low interaction of this wavelength with the upper window layer that allows to characterize the absorber without removing the CdS/ZnO/ITO layers [220]. The second advantage is related to the coupling of the energy of the excitation photons with the direct band gap of $SnSe_2$. This allows to work under resonant conditions largely increasing the sensitivity of the Raman measurements of this phase by several orders of magnitude.

For more information about the characterisation techniques employed, see section 2.2.

3.3 Results

3.3.1 CZTSe on polyimide: alkali doping strategies

Sample summary and low temperature post annealing treatment (LT-PAT)

In a preliminary experiment, CZTSe solar cells were fabricated on PI substrates at a moderate temperature of 470°C to ensure that the substrate would withstand the process without degrading. PAS and PDT doping strategies were studied in which 0, 10 and 15 nm NaF/KF layers were evaporated on the samples before the metallic stack or after the synthesis of the absorbers, respectively (see Figure 42). A SLG reference sample with no additional doping was processed simultaneously in the same batch. Once completed, the full devices were annealed on a hot plate at 180°C in air during 30 min.

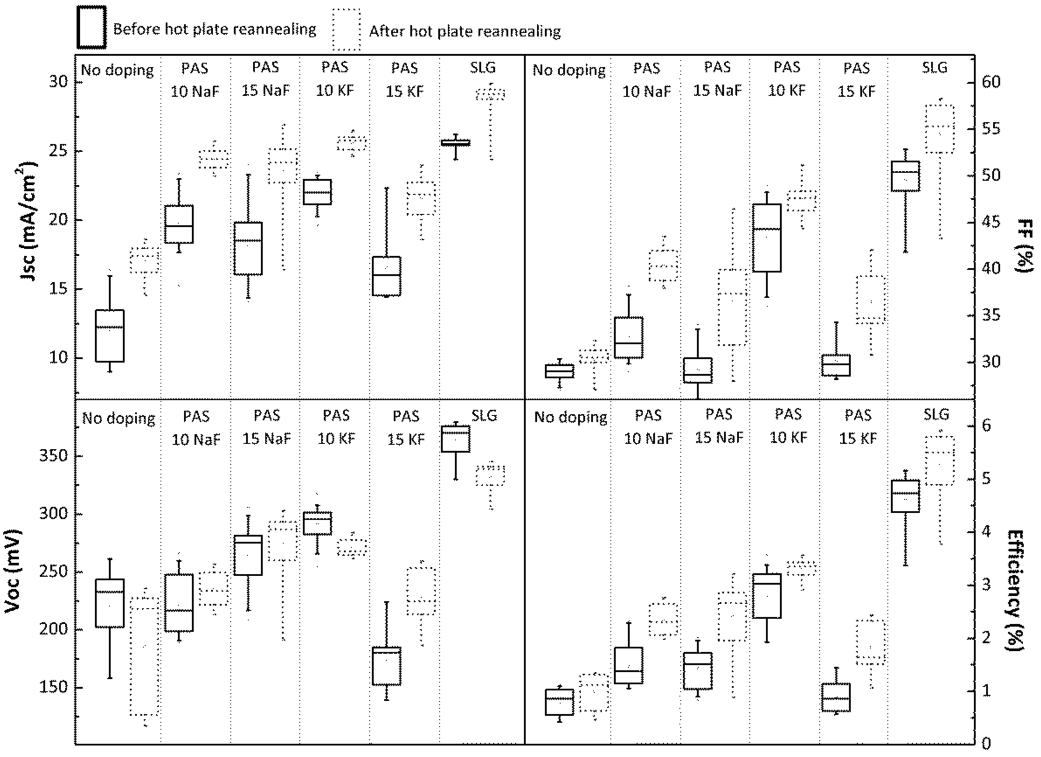

Figure 49. Boxchart of the main solar cell parameters of the samples processed on PI with PAS doping strategy before (solid box) and after (dashed box) hot plate reannealing.

It is interesting to start by taking a quick look at the effect of the LT-PAT on the devices. Figure 49 shows the main solar cell parameters of the PAS and reference samples before and after LT-PAT at 180°C. A marked improvement of the J_{sc} and FF of the devices can be observed after LT-PAT while, contrarily to most reports (see references in section 2.3.9), the V_{oc} of some devices experiences a slight decrease. Nevertheless, the beneficial effect of LT-PAT is confirmed since the overall performance of all the devices is ultimately enhanced in a significant way.

Effects of alkali doping on the performance of the devices

Table 11 summarizes the main parameters of the record solar cells of each of the samples (after LT-PAT). From these data, the first observation that should be made is that all the samples fabricated in this experiment result in working devices demonstrating the compatibility of the polyimide substrate with the solar cell fabrication process employed based on the selenization of sputtered metallic stack precursors. Furthermore, most of them exceed the efficiencies reported in previous works (see section 3.1.2) with the alkali-free reference exhibiting a 1.3% efficiency.

Table 11. Parameters of the record cells of the CZTSe devices fabricated on PI with different doping strategies extracted from J-V measurements.

Sample			Jsc (mA/cm^2)	Voc (mV)	FF (%)	η (%)
SLG 470°C			29.9	344	57.6	5.9
Undoped			18.6	231	31.3	1.3
PAS	**NaF**	10 nm	24.8	257	43.5	2.8
		15 nm	24.0	303	44.3	3.2
	KF	10 nm	24.7	282	51.2	3.6
		15 nm	22.8	255	42.0	2.4
PDT	**NaF**	10 nm	18.9	147	32.2	0.9
		15 nm	19.5	180	31.6	1.1
	KF	10 nm	18.7	116	31.0	0.7
		15 nm	10.6	76.2	27.2	0.2

Regarding alkaline doping, large differences are encountered when employing a PAS or a PDT strategy. On the one hand, all the samples fabricated with the PDT doping approach exhibit a lower performance than the undoped reference sample. While the J_{sc} and FF seem mostly unaffected by the PDT doping (except for the 15 nm KF sample), the V_{oc} of the devices is severely reduced. In the case of NaF, a higher amount of this dopant appears alleviate this negative effect. However, the opposite applies when using KF as doping source. On the other hand, the PAS approach is able to significantly improve both the record and the average device performance in all the cases studied (see Figure 50). The employment of either NaF or KF leads to a global enhancement of all the cell parameters. In the case of NaF, the thickness of the doping layer seems to be directly related to the voltage of the devices. This way, 10 nm of NaF cause an average increase of ~50 mV in the V_{oc} and 15 nm raise it by ~85 mV with respect to the undoped reference. As for KF, there is a marked difference between depositing a 10 or a 15 nm layer. Doping with 10 nm KF increases V_{oc} to a similar extent as NaF and improves FF more effectively than the latter (~18% absolute with respect to the undoped sample). However, increasing the amount of KF to 15 nm reduces the beneficial effects of the PAS KF doping.

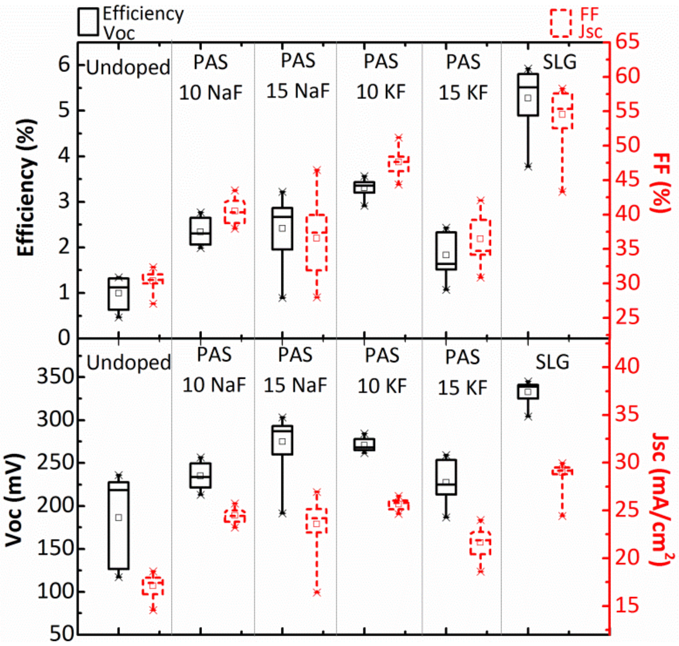

Figure 50. Boxchart of the main solar cell parameters of the samples fabricated on PI with the PAS doping approach extracted from J-V measurements after LT-PAT. Solid black boxes correspond to the left axes: Efficiency (top) and V_{oc} (bottom). Dashed red boxes correspond to the right axes: FF (top) and J_{sc} (bottom).

The best cell on PI is obtained using 10 nm of KF with an efficiency of 3.6%. Nevertheless, all the PI samples are well below the performance of the SLG reference processed simultaneously at 470°C (5.9% record efficiency) which exhibits larger V_{oc}, J_{sc}, and FF. This can be clear in Figure 51 (left). This figure also shows the EQE of the different devices. It can be seen that doping either with NaF or KF increases carrier collection significantly in the 300-900 nm range compared to the undoped reference indicating reduced absorption at the CdS/CZTSe interface and a better collection within the absorber.

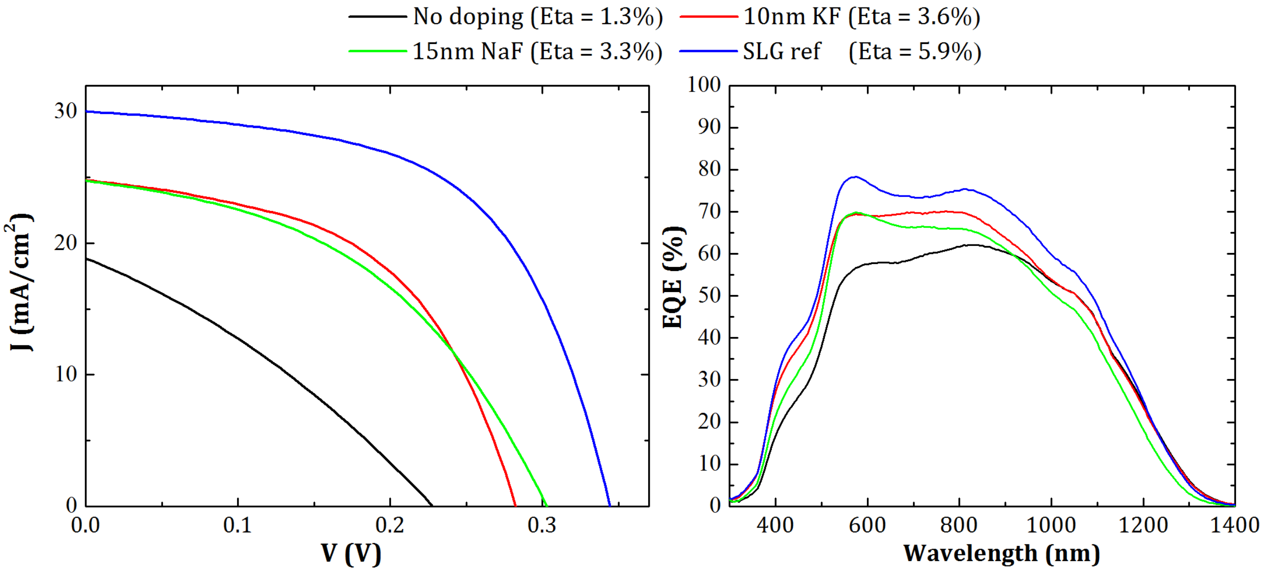

Figure 51. J-V (left) and EQE (right) of the best cells fabricated on polyimide with the PAS doping approach.

Influence of alkali doping on the morphology of CZTSe absorbers

In order to investigate how the absorber morphology is influenced by the different alkali doping strategies, the samples were inspected by FESEM. As expected, no appreciable differences in the morphology with respect to the alkali-free reference were observed for the samples prepared with post-deposition treatment (PDT) since with this approach the alkali are applied after the synthesis and crystallisation of the absorber. Figure 52 shows the top view and cross section of the best performing samples: the soda-lime glass reference, the undoped PI reference and the PI samples doped with 15 nm of NaF and 10 nm of KF by PAS. No morphological differences could be spotted between samples with different thicknesses of the same dopant, therefore these can be taken as representative for the whole batch of samples.

Top view

The top view images of the as-annealed absorbers (before chemical etchings) reveal a fundamental difference between the samples processed on glass and on polyimide: while the SLG sample in this experiment (processed at 470°C) shows a surface with well-defined grains, all the PI samples display a surface covered by a layer of small nanocrystals and a few elongated grains (clearly seen in Figure 52c) regardless the doping strategy. Similar surface nanocrystals have been identified by several authors as ZnSe (or ZnS in the case of CZTS) [119,127,162,221]. The elongated grains that coexist with ZnSe in the top layer resemble the $SnSe_x$ crystals reported by Xie et al. in [128]. Despite this top layer, kesterite grains can be discerned underneath. Although the origin of this top layer will be discussed later on, it should already be noted that ZnSe and SnSe are almost completely removed from the surface of the absorbers by the selective chemical etchings applied before the deposition of the buffer layer.

Cross section

The cross-sectional images of the full devices (i.e. after chemical etchings and CdS/TCO deposition) provide a sharper view of the distribution of grains in the bulk. A bi-layered structure can be distinguished in all samples with small grains next to the Mo back contact and large grains on top. The largest grains are observed in the undoped and the SLG samples. Na doping does not modify the grain morphology significantly, but the small grains in the bottom layer seem to be slightly smaller and more compact with respect to the undoped reference. This differs from most of the reports in which an important enhancement of crystal size is observed when doping with Na [158,162,163,165,166,170] (see section 1.4.4) for more information). Doping with K, on the other hand, appears to hinder crystal growth and only a few micron-size grains can be spotted scattered throughout the sample with a predominant presence of small crystals. As shown before, the 10 KF PAS is the best performing PI sample of the batch which suggests that large grains, although desirable, do not always imply a better performing device. A similar result was observed by López-Marino et al. for KF-doped CZTSe samples fabricated on steel substrates [158].

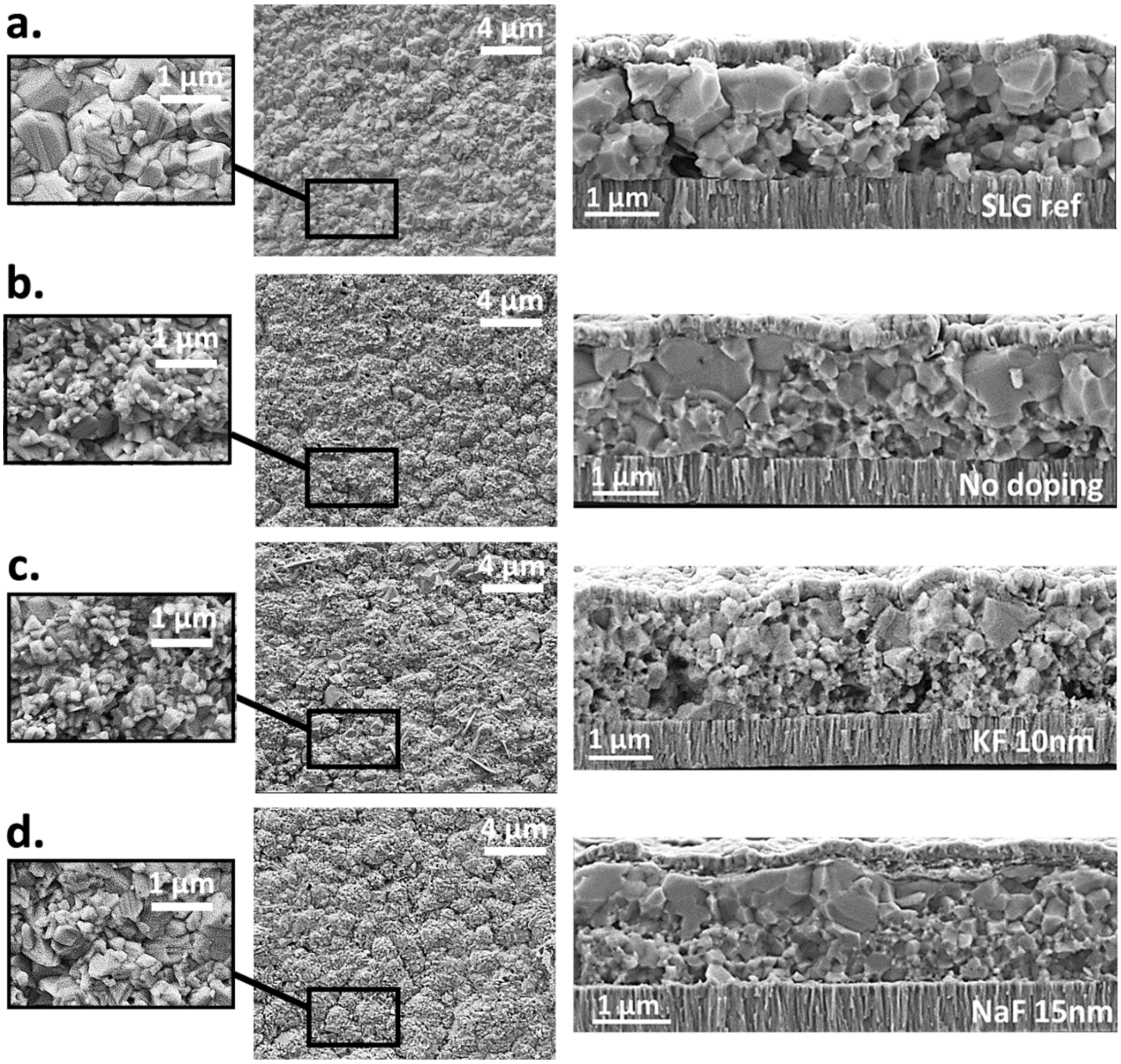

Figure 52. FESEM images of the CZTSe samples fabricated on PI and doped with the PAS approach. Left and middle: top view images of the as-annealed absorbers. Right: cross-sectional images of the full devices.

Carrier concentration modification by alkali doping

C-V measurements were performed on these devices in order to estimate their charge carrier concentration and depletion width (Figure 53). The relatively low efficiencies and voltages obtained suggest the samples exhibit high concentrations of bulk deep defects and/or interface states which complicate the interpretation of the C-V data based on a simple capacitor model. For this kind of samples, the carrier concentration is usually overestimated and the space charge region width becomes frequency dependent [222]. Nevertheless, the measurements allow qualitative comparison of the different dopants and provide evidence of an increased carrier concentration by the PAS doping approach. The cell without intentional doping shows the lowest carrier concentration with ~$4\cdot10^{15}$ cm^{-3}. The addition of 15 nm of NaF and 10 nm of KF increases the carrier concentration up to $7\cdot10^{15}$ cm^{-3} and $1\cdot10^{16}$ cm^{-3} respectively indicating an effective incorporation of the dopants into the CZTSe absorber. This augmented carrier concentration might explain, at least partially, the increased V_{oc} of the doped samples with respect to the undoped reference.

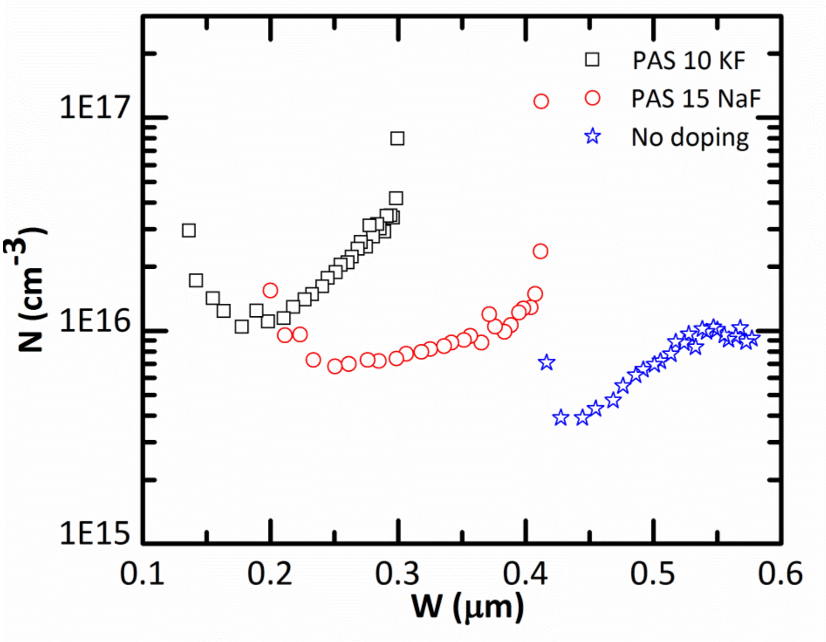

Figure 53. C-V measurements of the record cells of the CZTSe samples fabricated on PI and doped with the PAS approach.

Summary

To sum up, the results presented in this section demonstrate the feasibility of producing efficient devices both on PI (~3.5%) and SLG (~6%) at temperatures as low as 470°C using sequential sputtering and selenization. In addition, they also show that the PAS approach is an effective way of doping the CZTSe absorber while PDT requires further analysis.

3.3.2 Low temperature CZTSe on SLG: effect of processing temperature

Once that the feasibility of producing efficient solar cells at 470°C had been demonstrated, new devices were fabricated on SLG at different annealing temperatures (450-490°C) in order to shed light on the impact of low process temperatures on the synthesis of CZTSe absorbers.

Morphological analysis

Figure 54 shows FESEM top view images of the as-annealed (before chemical etchings) CZTSe absorbers. The micrographs indicate a strong dependence of crystal size with temperature. At 450°C there is less energy available for crystal growth. The surface of the absorber is covered by a small layer of nanocrystals (ZnSe) in which some elongated grains ($SnSe_x$) can also be spotted. This surface morphology is very similar to the one observed on PI samples above and will be discussed later on. Small CZTSe crystals (<1 µm) can be discerned underneath the top nanocrystal layer. With a slight increase of temperature to 470°C micron-size grains mixed with smaller crystals can be clearly spotted throughout the whole surface of the absorber. The amount of ZnSe and $SnSe_x$ crystals is widely reduced. This is consistent with the characteristics of the sample fabricated on glass at 470°C shown above (see Figure 52). As the temperature increases up to 480-490°C the presence of small grains decreases and a well-packed surface with good crystal quality and no trace of superficial secondary phases is observed.

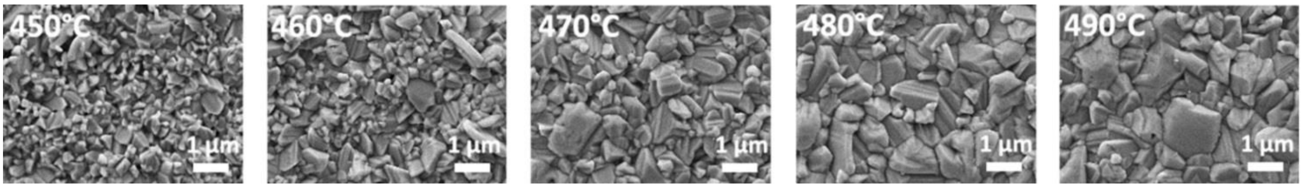

Figure 54. FESEM top view images of the as-annealed CZTSe absorbers processed at low temperature on SLG.

Secondary phase evaluation by Raman spectroscopy

The strong presence of ZnSe and $SnSe_x$ observed by FESEM suggested that these or other secondary phases could also exist underneath the surface and, thus, withstand chemical etchings. In order to evaluate this issue, the full devices were investigated by Raman spectroscopy under a 785 nm excitation wavelength. The inset in Figure 55 shows the normalized Raman spectra of the samples fabricated at different temperatures. The main peaks of the CZTSe phase are clearly identified at 169 and 195 cm^{-1} and, from the fitting of the spectra, a good absorber crystal quality independent from the annealing temperature is observed. However, the main feature brought about by these spectra is the detection of $SnSe_2$ as confirmed by the intense peaks at 184 cm^{-1} and, more subtly, at 119 cm^{-1} [223]. The absence of peaks at 108, 130, 133 and 151 cm^{-1} indicates that no SnSe coexists with $SnSe_2$ on the surface of the absorbers [224]. Figure 55 shows the maximum, minimum and average $SnSe_2$ concentration found in each of the samples as estimated by the peak area ratio $A(SnSe_2)/A(CZTSe)$. The distribution of the $SnSe_2$ phase is found to be very inhomogeneous. Taking into account that the measurements have been performed with a macrospot size (50 µm), these results suggest the formation of isolated $SnSe_2$ clusters. A reduction of the average concentration and dispersion of $SnSe_2$ with annealing temperature can be clearly seen. The $SnSe_2$ peak completely disappears for some points of the 490°C sample.

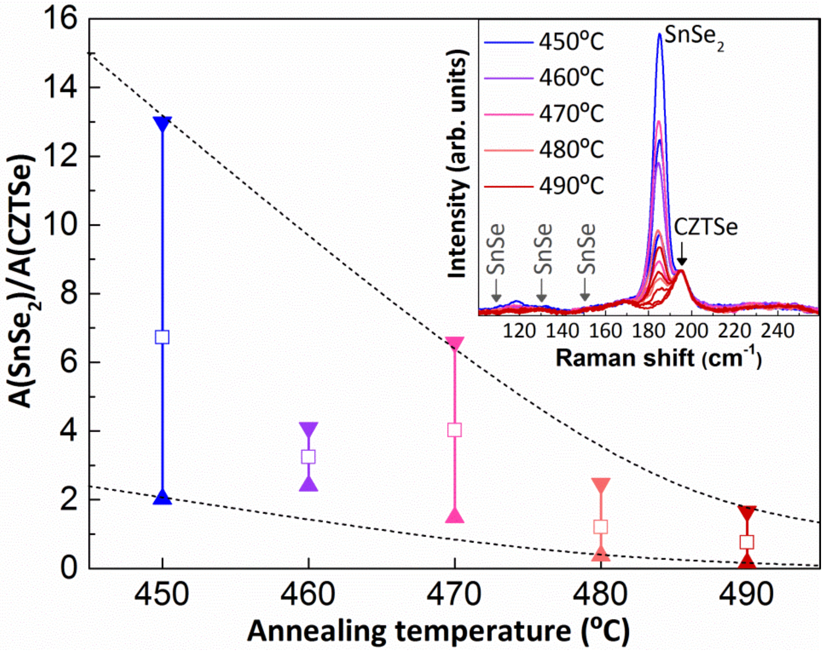

Figure 55. Minimum, maximum and average peak area ratio $A(SnSe_2)/A(CZTSe)$ as an estimation of $SnSe_2$ concentration of CZTSe samples synthesized on SLG as a function of annealing temperature. Dashed lines are intended as a visual guide for the reader. Inset: Normalized Raman spectra of the samples.

Solar cell performance and influence of $SnSe_2$

The average solar cell parameters of the as-fabricated samples (before LT-PAT) are shown in solid boxes in Figure 56 and also in Table 12. They show an improvement of the performance of the solar cells with annealing temperature with efficiencies around 1% at 450°C increasing to an average efficiency of 4.2% at 490°C. This is consistent with the gradual disappearance of the secondary phases detected with FESEM and Raman spectroscopy. Although all the optoelectronic parameters are enhanced with the annealing temperature, a closer look reveals that V_{oc} is the dominant parameter exhibiting an almost linear increase with temperature. The samples were submitted to a hot plate air reannealing at 200°C for 30 min in order to improve their performance as explained above. The results are shown as dashed boxes in Figure 56 and are also listed in Table 12. Surprisingly, the V_{oc} of these devices is heavily deteriorated after reannealing. However, the V_{oc} reduction is less intense in the case of the 490°C sample. J_{sc} is also deteriorated for the 450°C and 460°C samples while it remains unchanged for the 470°C sample and increases for higher temperatures. FF improves in all cases. This way, efficiency is only enhanced for the 490°C sample. However, not all the cells in the 490°C sample behave in the same way as can be deduced from the increased standard deviation of the V_{oc}, FF and efficiency after reannealing.

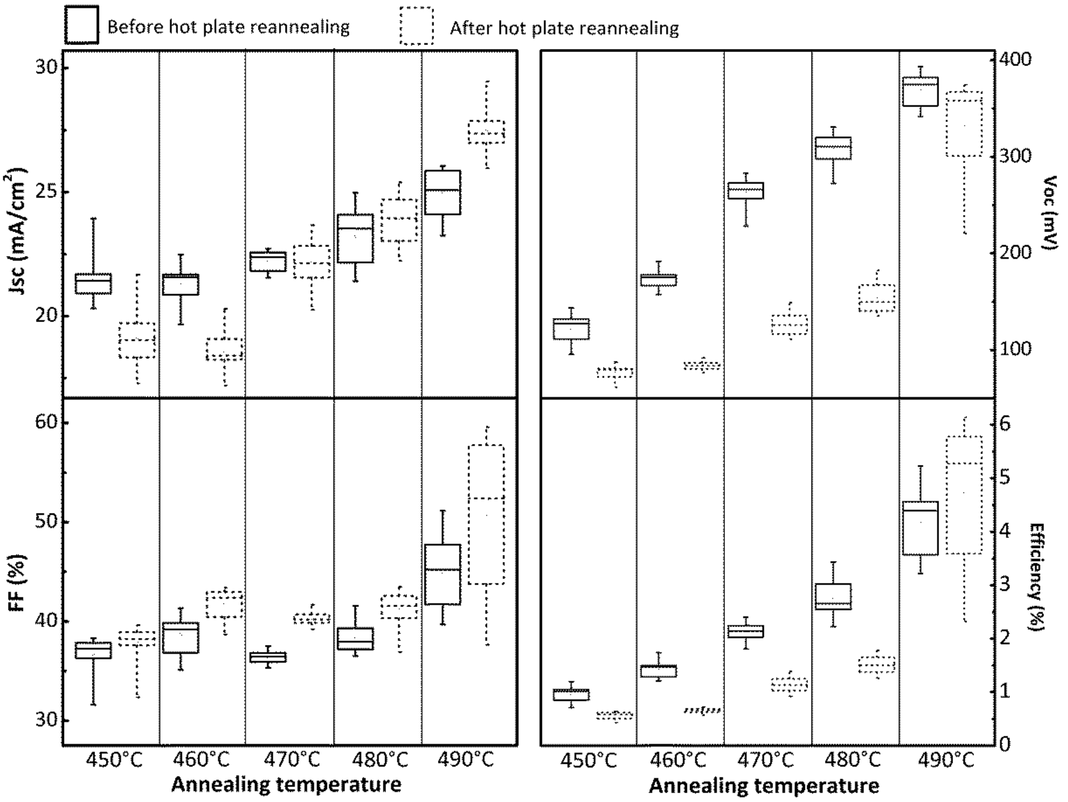

Figure 56. Boxchart of the main solar cell parameters of the CZTSe samples processed on SLG at different temperatures before (solid boxes) and after (dashed boxes) hot plate reannealing.

The response of these CZTSe solar cells to a LT-PAT process differs strongly from other reports (see section 2.3.9). A deeper Raman investigation linked this unexpected reannealing behaviour to the presence of $SnSe_2$. Many cells of every sample were analysed and this phase was intensely detected in all them except for the 490°C sample. In this sample, $SnSe_2$ was found only in some of the cells while others were completely $SnSe_2$-free. Interestingly, the reannealing hampers V_{oc} and, thus, efficiency only in cells containing $SnSe_2$. In the case of $SnSe_2$-free cells, the V_{oc} is only reduced by a few mV (as observed in the first doping experiment, see Figure 49) while J_{sc} and FF are boosted resulting in a highly enhanced efficiency. This finding is summarized in the last two rows of Table 12. Therefore, from these results it seems clear that large amounts of $SnSe_2$ deteriorate both J_{sc} and V_{oc} during low temperature reannealing. For low amounts of $SnSe_2$, J_{sc} is less affected and even starts to improve during reannealing. However, even with reduced amounts of $SnSe_2$, V_{oc} is still largely reduced resulting in decreased efficiencies. Finally, when $SnSe_2$ is not detected, the V_{oc} is only very slightly reduced and the efficiency of the devices is greatly increased through higher J_{sc} and FF.

Table 12. Average and standard deviation (in brackets) of the main solar cell parameters of the CZTSe devices fabricated on SLG at different temperatures extracted from J-V measurements. The last two rows show the parameters of a cell from the 490°C sample containing $SnSe_2$ and from the $SnSe_2$-free record cell. AF stands for "As-fabricated" and AR stands for "After hot plate reannealing".

	Jsc (mA/cm^2)		Voc (mV)		FF (%)		Efficiency (%)	
	AF	AR	AF	AR	AF	AR	AF	AR
450	21.5 (0.9)	19.1 (1.0)	121 (15)	78 (6)	36.7 (1.8)	37.9 (1.8)	1.0 (0.1)	0.6 (0.1)
460	21.3 (0.7)	18.5 (0.9)	174 (10)	84 (4)	38.7 (1.8)	41.8 (1.4)	1.4 (0.2)	0.7 (0.1)
470	22.2 (0.4)	22.2 (0.9)	263 (14)	127 (11)	36.4 (0.6)	40.3 (0.7)	2.1 (0.2)	1.1 (0.1)
480	23.2 (1.2)	23.9 (1.0)	309 (17)	154 (16)	38.4 (1.5)	41.3 (1.7)	2.8 (0.4)	1.5 (0.2)
490	25.0 (1.0)	27.5 (0.9)	370 (16)	330 (50)	45 (3)	51 (7)	4.2 (0.6)	4.7 (1.4)
490 $SnSe_2$	24.0	27.2	349	246	42.0	41.8	3.5	2.8
490 record	24.7	28.0	383	378	47.6	61.0	4.5	6.4

Despite all this, a 6.4% record cell was achieved at 490°C after reannealing giving proof of the feasibility of fabricating efficient CZTSe devices at low temperature (if the formation of $SnSe_2$ is avoided) with a performance close to samples processed at higher temperatures by identical procedures (see [140,158,206]).

3.3.3 Further strategies to increase conversion efficiency: higher temperatures and Na+Ge doping

Sample summary

Finally, CZTSe solar cells were fabricated on PI at different temperatures (470-490°C) in order the study the feasibility of increasing their performance by working at higher temperatures without degrading the substrate. In addition, the effect of introducing a Ge nanolayer was also studied. Ten nanometres of Ge deposited on top of the metallic precursors prior to selenization have been demonstrated to improve the performance of CZTSe solar cells fabricated on glass at 550°C [104,206,225]. This beneficial effect is not purely due to Ge itself but arises from the interaction between Ge and the Na provided by the glass substrate [225]. Therefore, taking this into account, the addition of a 10 nm Ge layer was combined with PAS

NaF (10 nm) doping. Two batches of samples were processed simultaneously. One of them was used to investigate the morphology of the absorbers (batch 1) and the other was employed to fabricate full devices (batch 2). None of the PI substrates presented any signs of degradation after the processing and no appreciable differences could be spotted between them.

Effects of temperature and doping on absorber morphology

Figure 57 shows top view FESEM images of the as-annealed and etched absorbers (batch 1). Before applying the chemical etchings, all the samples exhibit surfaces covered by a top layer of small nanocrystals similar to the one described in previous sections for CZTSe absorbers fabricated at low temperature on PI and SLG. Some differences can be spotted between the undoped and the doped absorbers. In the case of undoped samples, this layer completely covers the surface and is almost entirely composed by ZnSe nanocrystals. Increasing the annealing temperature does not eliminate nor even reduce this layer. On the other hand, when NaF+Ge doping is employed, the density of the ZnSe nanocrystals is slightly reduced exposing some CZTSe grains. This is accompanied by the appearance of large elongated $SnSe_x$-like crystals in the samples processed at 470°C and 490°C. No elongated crystals are found on the surface of the 480°C sample. Compared to previous results (Figure 54 and Figure), some of these $SnSe_x$ crystals look different. They are larger, thicker and slightly more rounded.

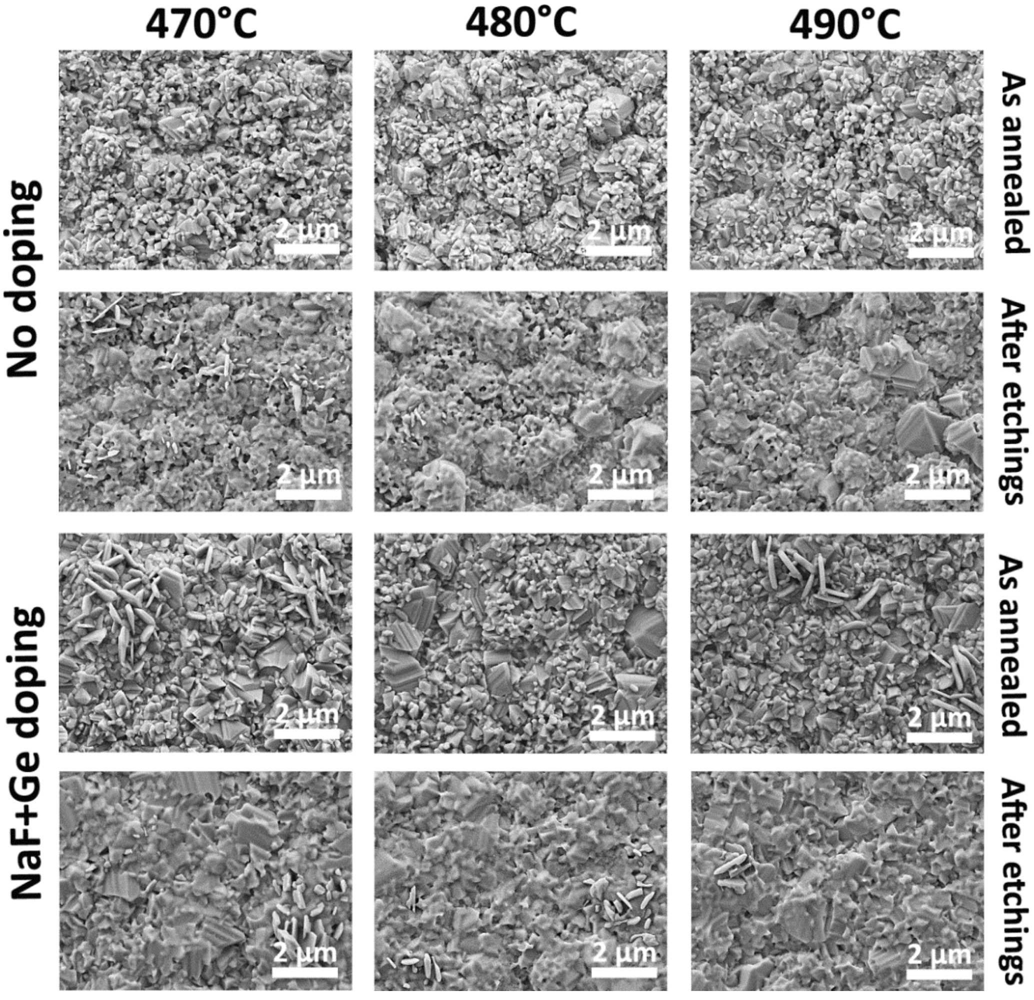

Figure 57. FESEM top view images of the as-annealed and etched CZTSe absorbers synthesized on PI with and without Na+Ge doping at different temperatures (batch 1).

After the chemical etchings the surface ZnSe nanocrystals are completely removed from all the samples. However, $SnSe_x$ grains are only partially eliminated. Clusters of $SnSe_x$ remain randomly scattered in the 470°C undoped sample and, more intensely, in all the NaF+Ge doped samples. An EDX analysis revealed that these clusters are formed purely by $SnSe_2$ crystals (Figure 58).

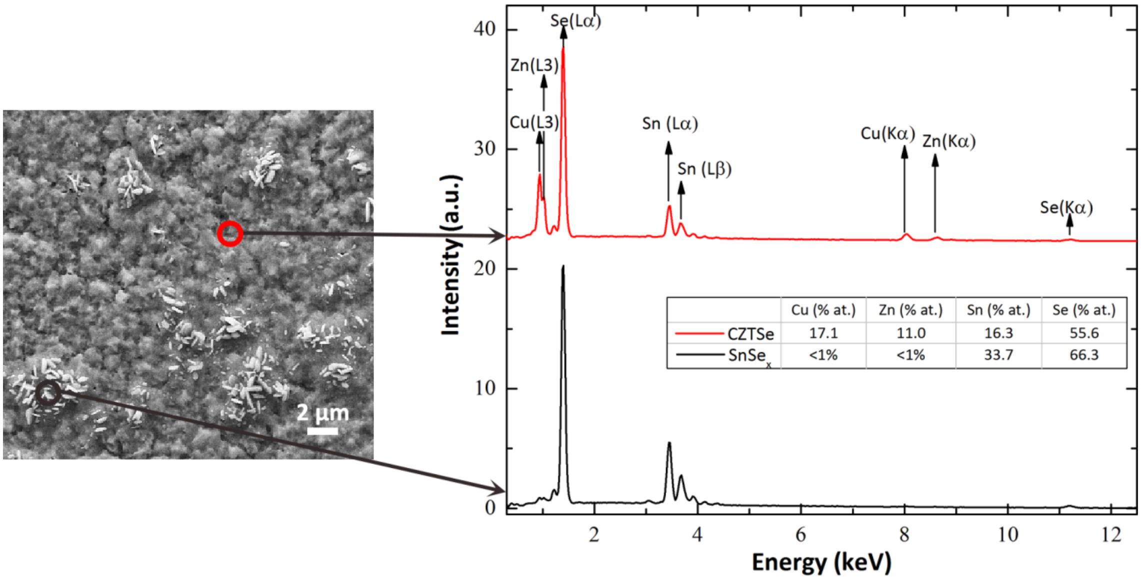

Figure 58. EDX spectra of the etched surface of the absorbers synthesized on PI with NaF+Ge doping. The red region corresponds to a secondary phase-free region. The black region corresponds to a $SnSe_x$ phase cluster.

Low temperature post annealing treatment

The devices fabricated with the absorbers from batch 2 were submitted to successive 25 min hot plate LT-PATs at different temperatures (180, 200, 275 and 300°C). This was due to the fact that the reannealing conditions successfully used before (180°C for 30 min) did not improve significantly the performance of any of the samples and, even more, was detrimental for some of them. Figure 59 shows the evolution of a characteristic solar cell from each of the samples with the different LT-PATs. Although there are no clear general trends and the behaviours seems very sample-dependant, some conclusions can be extracted from this figure:

i. The J_{sc} of the devices tends to increase with the increasing reannealing temperature in most cases.
ii. Annealing at 200°C seems to have a negative effect on the V_{oc} of most devices.
iii. Annealing at T>200°C seems to recover the V_{oc} of the devices and, in some cases, it even surpasses the V_{oc} of the as-fabricated devices.
iv. In the cases where the V_{oc} is improved with respect to the as-fabricated devices at T > 200°C, the FF is also greatly improved resulting in superior efficiencies.
v. Otherwise, at T>200°C the FF remains approximately constant and there is no efficiency improvement.

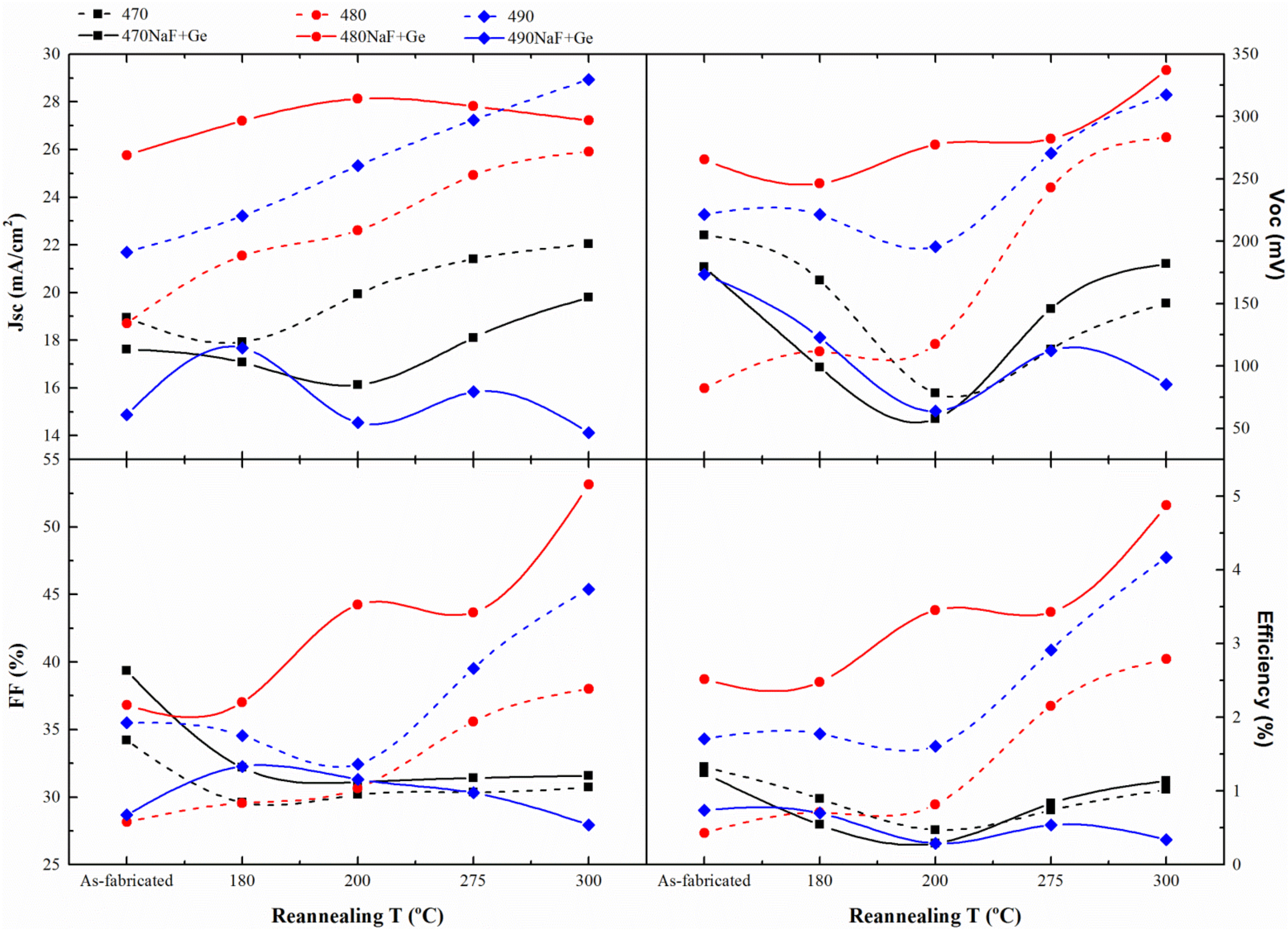

Figure 59. Effect of reannealing temperature on the solar cell parameters of a characteristic solar cell of each of the samples. Dashed lines correspond to undoped samples while continuous lines correspond to sample doped with NaF+Ge.

Device performance

Table 13 shows the J-V parameters of the record device from each sample after the 300°C LT-PAT. The performance of the undoped devices increases clearly with process temperature. 2.4% and 2.8% efficiencies were obtained at 470°C and 480°C, respectively; and a remarkable 4.2% maximum efficiency device was achieved at 490°C. The V_{oc} and FF of these samples increase with temperature almost linearly as observed in the devices fabricated on SLG shown above. As for the J_{sc}, it remains similar at 470°C and 480°C while it increases very abruptly at 490°C (28.9 mA/cm^2 compared to ~25 mA/cm^2 at lower temperatures) largely enhancing the efficiency of this sample.

On the contrary, the samples with NaF+Ge doping do not exhibit a clear trend. Unexpectedly, NaF+Ge doping has negative effect at 470°C and 490°C degrading all the optoelectronic parameters with respect to the undoped samples. Nevertheless, NaF+Ge doping highly enhances the Voc (+55 mV) and FF (+13% absolute) at 480°C compared to its undoped counterpart. This translates into a device with 4.9% efficiency which sets a record for a CZTSe device fabricated at low temperature on a polymer substrate.

Table 13. Main solar cell parameters of the CZTSe record devices fabricated on PI with and without NaF+Ge doping at different temperatures (batch 2) extracted from J-V measurements.

	Doping	Jsc (mA/cm^2)	Voc (mV)	FF (%)	η (%)
470	-	25.7	248	37.1	2.4
	NaF+Ge	19.8	182	31.6	1.1
480	-	24.7	283	40.6	2.8
	NaF+Ge	27.2	337	53.2	4.9
490	-	28.9	317	45.4	4.2
	NaF+Ge	18.6	198	31.4	1.2

Relation between solar cell performance and $SnSe_2$

In order to investigate this unexpected behaviour, the samples were inspected by Raman spectroscopy with λ_{ex}= 785 nm. $SnSe_2$ was found inhomogeneously distributed throughout all the samples as in the case of the low-temperature samples prepared on SLG reported in the previous section. In Figure 60, the maximum $SnSe_2$ concentration (A($SnSe_2$)/A(CZTSe) peak area ratio) found in the record cells of each of the samples is plotted as a function of the fabrication temperature. Among the undoped samples, a moderate amount of $SnSe_2$ is found. The $SnSe_2$ content is reduced as the process temperature increases and becomes zero at 490°C. The strongest $SnSe_2$ concentrations are found in the NaF+Ge doped samples synthesised at 470°C and 490°C. However, no $SnSe_2$ is detected at 480°C. These results correlate perfectly with the performance of the devices and explain the odd behaviour of the doped samples. The low $SnSe_2$ content found in the NaF+Ge 480°C might seem inconsistent with SEM analysis in which $SnSe_2$ clusters were clearly observed in this sample. This issue will be discussed later on.

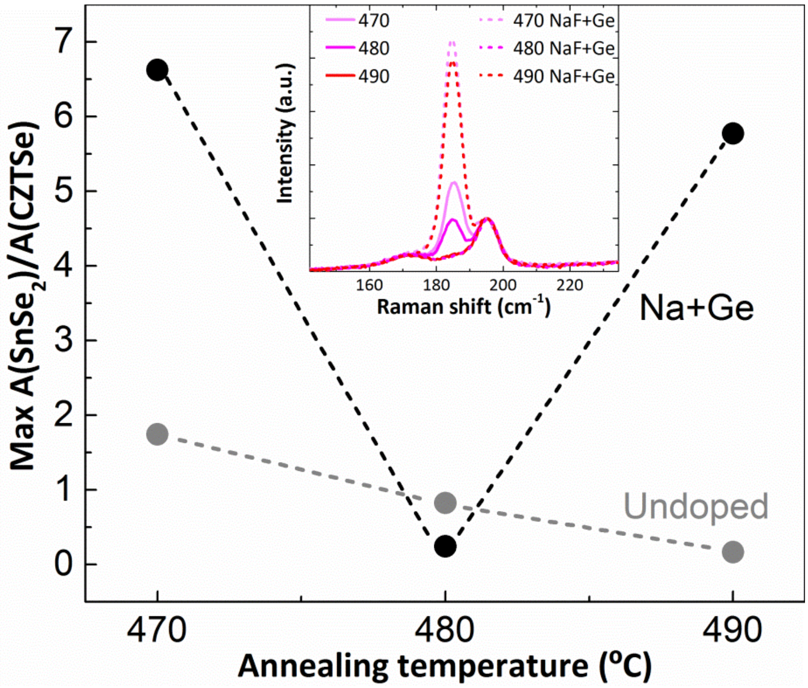

Figure 60. Maximum peak area ratio A($SnSe_2$)/A(CZTSe) as an estimation of the maximum $SnSe_2$ concentration found in the record cells of the CZTSe samples processed on PI with and without NaF+Ge doping at different temperatures. Inset: Normalized Raman spectra of the samples.

Again, the results show that $SnSe_2$ limits the performance of the devices by largely decreasing their V_{oc}. This detrimental phase is reduced with increased selenization temperature for the undoped samples. This is consistent with the results obtained on SLG. However, the formation of $SnSe_2$ seems to be somehow promoted by NaF+Ge doping.

Conclusions

Despite $SnSe_2$ formation, the feasibility of fabricating flexible CZTSe devices with efficiencies greater than 4% at annealing temperatures below 500°C and without any intentional doping has been demonstrated. In addition, although $SnSe_2$ appears to be linked to NaF+Ge doping, the addition of a Ge nanolayer has been shown to improve the performance of low temperature devices up to ~5% efficiency. A deeper optimisation of the process and, especially, of the thermal annealing is likely to further increase the conversion efficiency of both doped and undoped devices. Figure 61 compares the J-V curves of the best devices obtained in this work. While J_{sc} is similar in the three devices, the SLG record cell presents superior V_{oc} and FF than the PI devices. The graph shows that NaF+Ge doping helps to reduce the gap between the two substrates by increasing Voc and FF of the PI devices.

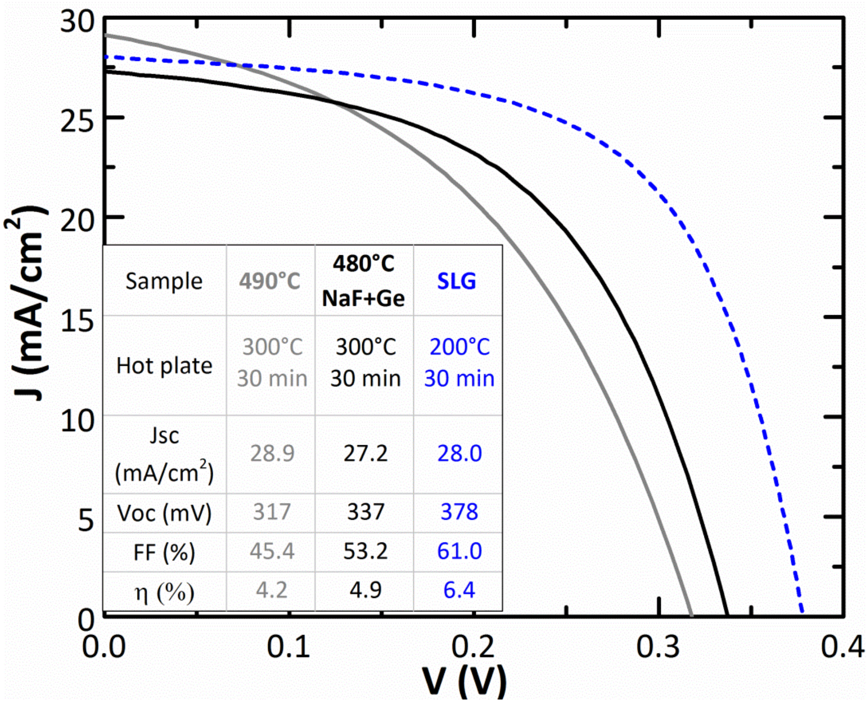

Sample	**490°C**	**480°C NaF+Ge**	**SLG**
Hot plate	300°C 30 min	300°C 30 min	200°C 30 min
Jsc (mA/cm^2)	28.9	27.2	28.0
Voc (mV)	317	337	378
FF (%)	45.4	53.2	61.0
η (%)	4.2	4.9	6.4

Figure 61. J-V curves of the best performing samples obtained in this work fabricated on SLG (dashed blue line) and on PI with (black) and without (grey) doping at temperatures below 500°C. Inset: table with the main solar cell parameters of the cells.

3.4 Discussion

3.4.1 Alkali doping

It has been shown that PAS doping with NaF and KF is a very effective way of improving the conversion efficiency of CZTSe solar cells fabricated on polyimide. The consequences of introducing these dopants during the synthesis of the CZTSe absorbers are enhanced collection, V_{oc} and FF as well as a higher net carrier concentration.

NaF

In the case of Na, the improvements observed in the V_{oc} and FF can be partially attributed to the grain boundary passivation effect of this alkali that avoids deep defects and reduces non-radiative recombination [162,168,226]. This is also reflected in the improved carrier collection observed in the EQE measurements. However, from the C-V results obtained, it is plausible to believe that most of the V_{oc} enhancement detected is related to an augmented carrier concentration. This can happen by various mechanisms. Nagaoka et al. speculated that the incorporation of Na into the absorber creates antisite Na_{Cu} defects that inhibit the formation of donor Zn_{Cu} defects (favoured by Cu-poor Zn-rich compositions), increasing the net carrier concentration and, in consequence, the V_{oc} [173]. Another explanation was given by Yuan et al. [161]. They proposed that Na_{Cu} is only stable at high temperatures. During cooling down, Na out-diffuses from the kesterite structure leaving acceptor V_{Cu} defects behind and thus increasing the carrier concentration and V_{oc} of the devices. Finally, a boost in V_{oc} and carrier concentration has also been attributed to a reduction of the activation energy of shallow acceptor levels [162,168].

KF

As for K, little information about its effect on kesterite devices is available. Some authors reported a highly improved FF due to a decrease of the R_s of the devices [199,200]. Table 14 presents the shunt and series resistance extracted from the J-V curves shown in Figure 51 (left). It can be noticed that the highly improved FF observed in the 10 nm KF doped sample also comes from a reduced R_s. What is more, the K-doped sample presents a R_s similar to the SLG reference and one order of magnitude lower than the undoped and the Na-doped samples. Taking a look at the effects of K on CIGS solar cells, this enhanced FF could be related to the modification of the surface of the absorber (Cu depletion) that improves the CIGS/CdS heterojunction through the creation of Cd_{Cu} antisites [190,193,227]. The creation of such an electronically inverted absorber surface (n-type) is also plausible in CZTSe devices and would reduce recombination in the CZTSe/CdS interface improving the FF [158]. The EQE in Figure 51 (right) also shows an improved collection at short wavelengths providing more support to this theory. Besides an improved FF, such an enhanced CZTSe/CdS interface would also increase the V_{oc} of the devices which is also observed in the 10 nm KF sample.

Table 14. R_s and R_{sh} of the record cells fabricated with PAS doping.

	R_s ($\Omega\cdot cm^2$)	R_{sh} ($\Omega\cdot cm^2$)
SLG	0.7	120
No doping	4.7	20
NaF 15 nm	2.9	60
KF 10 nm	0.9	70

However, the increase in V_{oc} and, especially, the large enhancement of the FF produced by 10 nm KF doping can be also attributed to an effective passivation of the grain boundaries as observed for K-doped CIGS devices [192,193,228]. This grain boundary passivation effect can be clearly seen in this work since the 10 nm KF sample exhibits the best performance and FF of the whole batch despite its smaller grain size (and higher number of grain boundaries) compared to NaF and undoped samples. Comparing the FF of Na and K doped samples, the higher FF of the latter also suggests that recombination at the grain boundaries is more effectively reduced by K than by Na.

K has been calculated to preferably incorporate into CZTSe as K_{Cu} antisite similarly to Na although to a lesser extent [229]. Thus, a similar increase in carrier concentration (through the avoidance of Zn_{Cu} or creation of V_{Cu}) is expected and consistent with the results presented here [161]. Such an increase in carrier concentration related to K-doping has been reported for kesterite devices by several authors [186,198,199].

PDT

Contrarily to PAS, the PDT approach did not provide positive results. PDT processes are usually carried out at 350-400°C for CIGS [73,153,230,231]. López-Marino et al. used a temperature of 400°C on CZTSe devices for NaF and NaF+KF PDT doping and obtained a moderate improvement on V_{oc} while FF remained similar [158]. The PDT process employed in this work was carried out at 325°C. This temperature is probably not enough for an effective diffusion of the alkali into the absorber and might be increased in future attempts with this strategy. It might be possible that the incorporation of alkalis in PDT occurs, at least partially, through the formation of liquid alkali-Se phases or alkali-metal-Se phases [186,232]. The reduced temperature employed might have, thus, impeded the formation and/or melting of such phases preventing alkali incorporation. Based on the mechanism proposed by Yuan et al., another explanation may lie at the low solubility of Na and K in CZTSe at such low reannealing temperatures and, thus, the difficulty of forming $alkali_{Cu}$ antisites [161]. Be as it may, it is clear that the PDT doping strategy is not straightforward and needs a careful study and optimisation for kesterite absorbers in order to be as successful as in CIGS devices.

3.4.2 Differences in the temperature-dependence of secondary phase-formation in soda-lime glass and polyimide substrates

The most obvious consequence of working at low temperatures has been observed to be the high formation of ZnSe secondary phases on the surface of the CZTSe absorbers. Taking into account that the composition of the precursors was selected to be Zn-rich, Zn is the top layer of the precursor and the absorbers are synthesized in an excess Se atmosphere, the formation of ZnSe is very likely to occur [119,122,127,205]. Furthermore, ZnSe has the highest formation enthalpy among all the binaries (excluding $MoSe_2$) that participate in the synthesis of the CZTSe absorber making it a very stable phase [122,221,233,234]. Thus, working at low temperature in these conditions clearly hinders the incorporation of ZnSe into the CZTSe structure and ZnSe crystals remain on the surface of the absorber during the cool down. As the temperature increases, the higher available thermal energy should facilitate the incorporation of ZnSe into CZTSe. This is clearly observed in the SLG samples in which the presence of ZnSe is very high at 450°C and totally vanishes at 490°C.

However, the same behaviour is not observed in polyimide samples. Comparing Figure 54 and Figure 57 it is evident that even the PI samples processed at the highest temperature (490°C) present a similar ZnSe content to the sample fabricated at the lowest temperature (450°C) on glass. This implies that PI samples are behaving differently to SLG during the annealing process.

More specifically, they behave as if they were processed at a lower temperature compared to SLG samples.

A possible explanation of this effect arises from the tendency of polyimide samples to bend during annealing due to their lack of stiffness and the expansion of the CZTSe layer during selenization (see Figure 48 and Figure 62). As the samples bend during annealing, the contact surface of the PI substrate with the graphite box becomes almost zero (only the edges of the substrate are in direct contact with the box) and, thus, the heat transfer by conduction from the box to the PI substrate is greatly diminished. In consequence, the effective amount of thermal energy supplied to the sample is largely reduced. This might explain the similarities between PI samples processed at temperatures as high as 490°C and the SLG samples processed at 450°C. According to this theory, it is expectable that the energy received by a PI sample varies in quite a random manner from sample to sample depending on how it bends during annealing making the process difficult to control and resulting in a low repeatability. An illustrative example of different random bending of polyimide substrates during the same process is shown in Figure 62. In addition, this explanation could also lie at the origin of the bad performance of the samples fabricated using the frames shown in Figure 47. The only thermal contact between these frames and the graphite box during annealing occurs at the tip of the four small screws that hold the polyimide in place. Thus, a very low heat transfer by conduction from the box to the substrate is also expectable when using these frames.

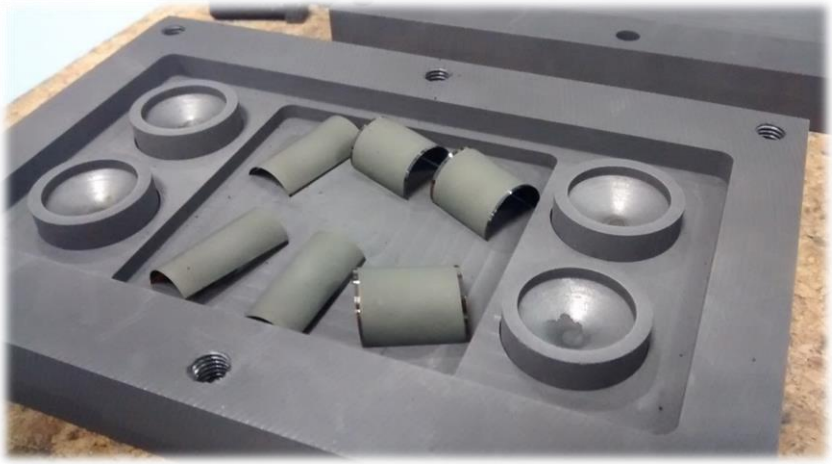

Figure 62. Picture of the as-annealed samples showing different bending and contact geometry with the graphite box.

An incongruent behaviour of the NaF+Ge PI samples with annealing temperature has been observed, in which only the sample processed at 480°C performed well mainly due to an absence of $SnSe_2$ as measured by Raman while samples processed at very similar temperatures (470°C and 490°C) were degraded by high concentrations of this secondary phase. Taking into account what has just been explained above, it is very likely that the samples processed at 470°C and 490°C experienced a more pronounced or faster bending than the one processed at 480°C and, thus, absorbed a lower amount of heat during annealing resulting in an increased formation of $SnSe_2$. What is more, the inconsistence found between FESEM (clear presence of $SnSe_2$ clusters) and Raman measurements (very little $SnSe_2$ detected with some $SnSe_2$-free cells) of the 480°C NaF+Ge samples can also be explained the same way. FESEM measurements were performed in batch 1 samples and Raman measurements on batch 2 samples. Although both batches were processed simultaneously, it is possible that twin samples from different batches might have behaved differently during annealing thus generating a different amount of $SnSe_2$.

3.4.3 Origin and effects of $SnSe_2$

As just explained, the formation of $SnSe_2$ is another direct consequence of working at low temperatures. It is well known that the loss of Sn and Se is a critical issue for the synthesis of kesterite-based PV devices [122–124]. However, at annealing temperatures below 500°C an excess of Sn has been spotted in the films in the form of $SnSe_2$. According to the diagrams performed by Dudchak et al. the coexistence of CZTSe and $SnSe_2$ during the synthesis of the absorber is expectable in the range of compositions and temperatures employed in this work [115]. At 550°C, Sn-loss is believed to occur by the instability of the Sn^{IV} oxidation state compared to Sn^{II} that causes the reduction of $SnSe_2$

$$2SnSe_2 \rightarrow 2SnSe + Se_2(g) \qquad (R1)$$

and the subsequent vaporization of the SnSe phase [122,124]. However, based on the results presented in this work, it may be possible that low annealing temperatures slow down the kinetic of R1 preventing an effective reduction of $SnSe_2$ into SnSe. This way, $SnSe_2$ would remain mixed within and on top of the CZTSe absorber. On SLG and undoped PI, a diminishment of $SnSe_2$ with the increasing annealing temperature has been observed which is consistent with this theory.

The hypothesis of $SnSe_2$ formation due to a low supply of thermal energy during annealing is supported by observations performed in other works. Márquez et al. observed a strong formation of $SnSe_2$ when processing CZTSe at 450°C that disappeared for samples processed at 500°C [235]. The duration of the annealing was the same at both temperatures so the energy supplied to the sample was directly related to the annealing temperature. Likewise, Indubala et al. fabricated CZTSSe absorbers from binaries through a 3-hour reactive annealing at temperatures from 350 to 650°C [236]. They also detect $SnSe_2$ at temperatures ≤450°C that disappeared at higher temperatures. What is more, Temgoua et al. fabricated CZTSSe devices at 600°C for different annealing times and observed the formation of $SnSe_2$ from 1 to 30 min annealings that vanished for longer annealing times [237]. In this case, the amount of energy supplied to the samples was proportional to the duration of the annealing. Thus, it can be concluded that the supply of thermal energy is one of the keys to the formation of $SnSe_2$. Finally, regarding the discussion about the bending of polyimide substrates that hinders heat transfer during annealing, a higher $SnSe_2$ content would be expectable in such circumstances which agrees with the results presented here.

On the other hand, when NaF+Ge doping is employed, the formation of $SnSe_2$ is greatly enhanced (or its elimination hindered) to an extent in which micron-sized clusters of this phase are found scattered throughout the surface of the absorbers. Ge does not incorporate into the CZTSe structure itself but rather increases the incorporation of Na into the absorber [225]. Thus, it might be possible that the increased $SnSe_2$ formation observed with NaF+Ge doping can be attributed solely to an enhanced Na content. Lin et al. also found a connection between the amount of Na diffused to the CZTSe absorber and the formation of $SnSe_2$ on samples processed at 460°C [226]. One could argue that, if this was true, an increased amount of $SnSe_2$ should be found in SLG samples processed at 490°C due to a higher Na diffusion attributable to a higher temperature. However, it should be noted that this effect only appears when combined with a low annealing temperature or, more specifically, to a low supply of thermal energy to the samples during annealing. At higher temperatures on SLG, despite the increased formation of $SnSe_2$ arising from a high Na diffusion from the substrate, the kinetic of R1 would be fast enough for an effective reduction of this phase into SnSe and its subsequent evaporation.

A possible explanation for this Na-$SnSe_2$ relationship lies at the fact that both Na and Ge are believed to form Na-Se compounds and Ge_xSe_y liquid phases that act as fluxing agents increasing the availability of Se within the forming absorber [162,163,225]. Thus, it might be plausible that, since elemental Se is a by-product of R1, the high availability of Se due to the such fluxing phases somehow contributes in slowing down R1. According to this hypothesis, this slowdown effect should be stronger with Ge since Se availability would be two-fold enhanced: an increased amount of Se due to the increased presence of Na caused by Ge and to the presence of Ge_xSe_y liquid phases themselves.

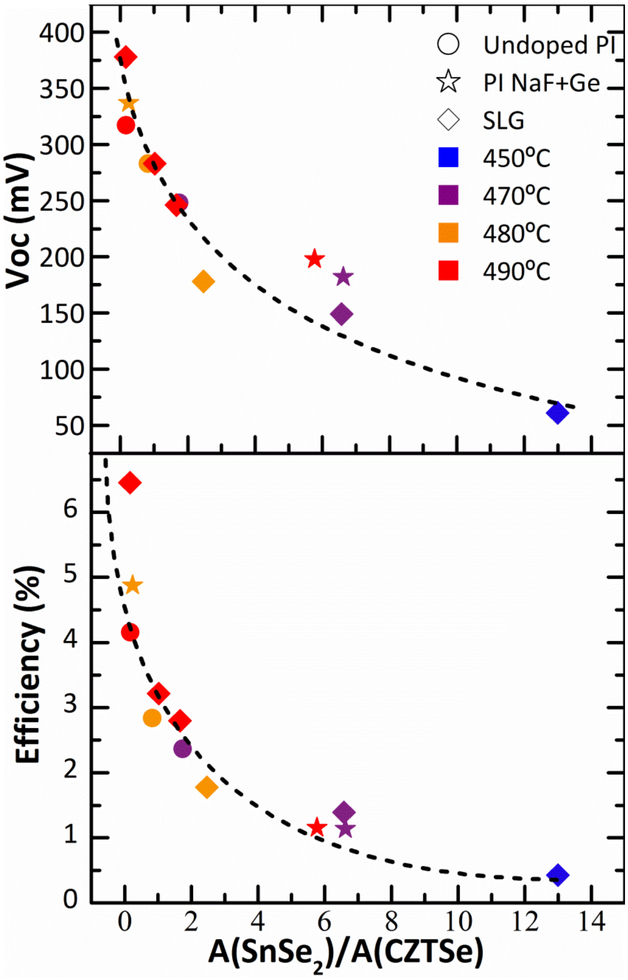

Figure 63. V_{oc} and efficiency of different cells fabricated in this work as a function of the maximum $SnSe_2$ concentration found in them as estimated by the peak area ratio A($SnSe_2$)/A(CZTSe) of the Raman spectra. Dashed lines are intended as a visual guide for the reader.

The main effect of $SnSe_2$ on CZTSe devices observed in this work is a strong reduction of the V_{oc}. Figure 63 shows the V_{oc} of the different cells analysed in this work as a function of the maximum $SnSe_2$ content found by Raman observations. A clear correlation can be observed independently from the substrate, doping or fabricating temperature. This interesting result indicates that all these factors only vary the amount of $SnSe_2$ synthesized along with CZTSe but that this phase is the main factor dominating the behaviour of the devices and the main issue when working at low temperatures.

Regarding the origin of the degradation of the V_{oc}, it has been reported that the presence of $SnSe_2$ within CZTSSe introduces shunting paths in the devices decreasing the V_{oc} [237]. This effect can also be observed in the SLG samples fabricated in this work. Figure 64 shows that the reduction in the V_{oc} observed at low temperatures (or high $SnSe_2$ contents) is strongly related to a lower shunt resistance (R_{sh}). Shunting might be indicating that $SnSe_2$ does not only form near the surface but also in the bulk and the grain boundaries creating undesirable current paths.

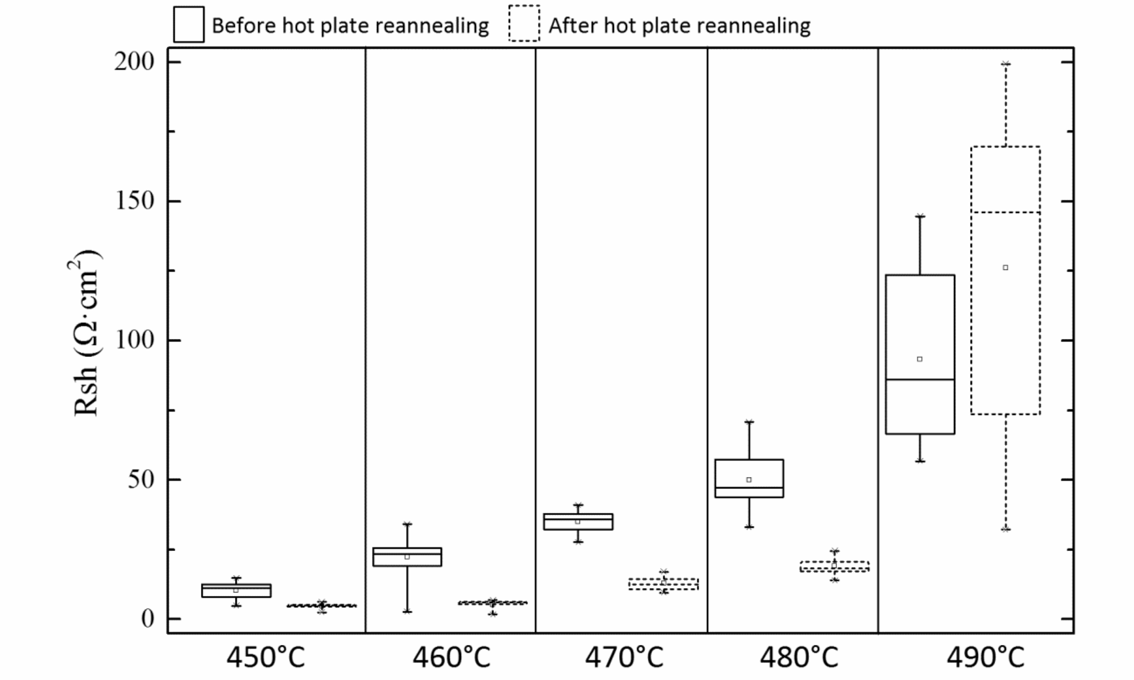

Figure 64. Boxchart of the R_{sh} of the devices fabricated on SLG at different temperatures before (solid) and after (dashed) hot plate reannealing extracted from J-V measurements.

Another interesting effect of this secondary phase observed in the SLG samples processed at low temperature is an additional reduction of the V_{oc} of $SnSe_2$-containing devices after a 200°C air reannealing (LT-PAT). As observed in Figure 64, this is mainly due to a further decrease of R_{sh}. Nevertheless, LT-PAT is a very complex process in which order-disorder transitions, surface and grain boundary compositional changes, CdS modifications and even Na dynamics play important roles [140,141,238]. Although it is clear that the presence of $SnSe_2$ is detrimental for low temperature reannealing of CZTSe full devices processed on SLG, a deeper study should be performed in order to shed light on this issue. In fact, the last experiment on PI showed that while reannealing at 200°C lead, in general, to a lower V_{oc} (Figure 59), which correlates with a lower R_{sh}, reannealing at 300°C can improve the performance of both doped and undoped

CZTSe absorbers even if they contain moderate amounts of $SnSe_2$. These results might be pointing towards a decomposition of the $SnSe_2$ phase at high LT-PAT temperatures that eliminates shunt paths. As an illustrative example, Figure 65 shows the evolution of the V_{oc} and R_{sh} of the sample processed on PI at 490°C without doping with LT-PAT temperature. It can be observed that the R_{sh} decreases when the sample is reannealed at 200°C, similarly to what is shown in Figure 64. However, this is followed by a sudden increase of the R_{sh} at higher temperatures supporting the idea of a possible decomposition of the shunting $SnSe_2$ phase. However, the study of these reannealing effects is beyond the scope of this work and will be left for future studies.

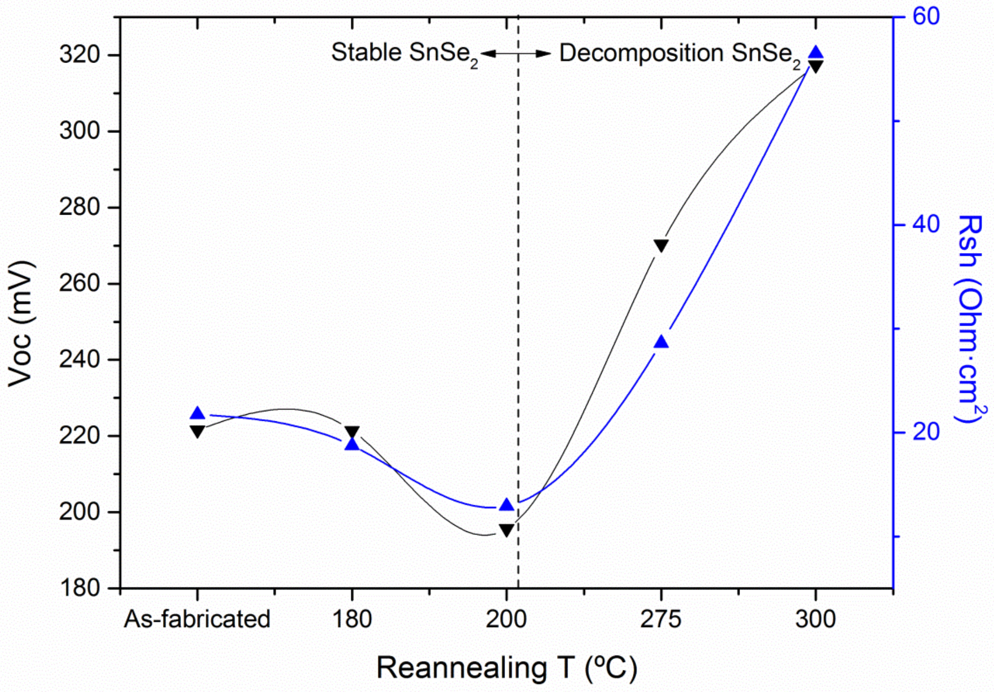

Figure 65. Evolution of V_{oc} and R_{sh} with reannealing temperature of the record cell from the PI sample processed at 490°C without doping.

3.5 Conclusions

This work demonstrates the compatibility of mass production-enabling polyimide substrates with the fabrication of Earth-abundant kesterite-based thin film solar cells.

One of the main concerns when working with polyimide is its low thermal robustness that limits processing temperatures below 500°C. However, the feasibility of producing efficient CZTSe devices by sequential precursor sputtering and selenization at such low annealing temperatures, not only on PI (4.9% efficiency) but also on SLG (6.4% efficiency) has been proved. These results set a record for CZTSe devices fabricated on a polymer substrate.

On the other hand, alkali doping has been found to be crucial for enhancing the performance of the devices fabricated on polyimide and reduce the performance gap with respect to SLG substrates. Different doping strategies were investigated for Na and K doping. The results lay bare the difficulty of the PDT doping approach. On the contrary, PAS has been shown to be an effective doping strategy that causes important improvements in solar cell performance, carrier concentration as well as modifying the grain morphology when doping either with NaF or KF. Further experimentation led to a 4.9% record sample on PI by combining NaF and Ge doping.

Nevertheless, working at low temperature has also been linked to the formation of a detrimental $SnSe_2$ secondary phase both on SLG and PI. This effect is aggravated on PI devices due to bending-related hindered heat absorption during annealing, making the process highly irreproducible. This phase has been found to severely decrease the V_{oc} of the devices by, apparently, creating shunting paths and to be the main factor controlling the performance of the devices. The V_{oc} is further decreased by LT-PATs if $SnSe_2$ is present. However, an interesting elimination of the negative effects of small amounts of $SnSe_2$ has been observed by reannealing the devices at rather high temperatures (275-300°C).

Based on the results presented here, it seems plausible to completely eliminate $SnSe_2$ by a deep optimisation of the fabrication process. More specifically, four easily implementable actions are proposed:

i. Adjustment of Sn-composition in the precursor and elimination of elemental Sn from the annealing atmosphere.
ii. Design of a frame or annealing box that ensures good thermal contact between the box and the sample during annealing.
iii. Complement the low annealing temperature with longer annealing times to ensure an adequate thermal energy input into the sample.
iv. RTP-based annealing, in which the heat transfer occurs from top to bottom could also be an interesting option to increase annealing temperature without substrate damage.

Regarding alkaline doping, besides PAS and PDT, doped Mo back contacts (Mo:Na, Mo:K or a combination of both) combined with Ge can be an interesting alternative strategy for a more controllable, reproducible and effective doping process.

Thus, the results obtained in this work suggest that through extensive research and the optimisation of the fabrication process in line with the strategies proposed above, polyimide-based kesterite solar cells with similar efficiencies as the current state of the technology on SLG can be achieved. This would open the door to low-cost mass production of kesterite solar devices with a high EROI.

4. Vitreous enamel as sodium source for efficient kesterite solar cells on commercial ceramic tiles

4.1 Introduction

4.1.1 Building integrated photovoltaics

In sections 1.1.2 and 1.3 some of the current problems of PV were explored. The fabrication energy was found to be one of the most critical ones contributing to the low EROI of PV. However, there is another key issue that was not included in the discussion since its influence on the EROI is not straightforward: the large area required to generate a significant amount of power from PV (with regards to other ways of generation). This is due to the low power density of solar panels. Current top c-Si commercial modules exhibit power densities around 200 W_p/m^2 [47,239,240]. Assuming that the power capacity of an average size coal-fired power station is around 300 MW, 1.5 km^2 of solar panels working at 100% power rate would be necessary for an equivalent capacity. In a solar farm, some spacing between panels is necessary to avoid shadowing and facilitate operation and maintenance tasks. Typical power densities of solar farms are, thus, reduced to 4-10 W/m^2 [241]. In this case, 30-75 km^2, the size of a small town, would be required to match the capacity of a coal-fired power plant. These rough figures give a sense of the large land allocation needs of PV. If we add to the equation power losses in transmission and distribution from solar farms to the point of consumption, the power density is further reduced.

Building integrated photovoltaics (BIPV) is a very interesting approach to overcome both cost and area issues of PV. In BIPV, solar power generators become an integral part of buildings rather than being attached a posteriori (usually referred to as building attached photovoltaics or, in short, BAPV). In contrast to BAPV, BIPV systems replace the outer building envelope skin, thus serving simultaneously both as climate screens and as power sources [242–245]. This approach presents a series of advantages in the face of traditional centralized solar farm generation and even of BAPV:

- Buildings possess large façade, glazing and roof areas exposed to solar radiation suitable for the installation of PV systems. Thus, the need for extra land allocation is eliminated.
- Most of the energy generated is consumed at the place of generation (the building) avoiding transmission and distribution losses.
- Manufacturing and installation costs are significantly reduced since solar cells act both as building structural materials and power generators [242,243,246–248]. When compared to conventional cladding materials, installing BIPV adds only a marginal extra cost (2%–5%) to the overall construction costs of a building [248].
- Integration allows aesthetically attractive designs.

All this has made of BIPV a growing market with a forecasted annual growth rate of 17% (until 2024) [249]. Although BIPV technologies cannot presently be considered to be in a mature state of development, there are a manifold of commercial products currently available. BIPV products can be categorized in four main categories depending on their realm of application: foils, solar tiles, integrated modules and solar glazing [242,243].

BIPV foils

BIPV foils are based on solar devices fabricated onto low weight and flexible modules. These characteristics make them easily integrable at any building surface (Figure 66). Inside the different foil substrates, polyimide is particularly interesting for integration since it combines low weight and flexibility with a very high mechanochemical resistance (see Table 10) that translates into weather-tight products ideal for climate-screen outer building envelope skin.

Figure 66. BIPV foil Evalon® solar by alwitra. Source: https://alwitra.de/wp-content/uploads/2019/02/alwitra_Evalon_Solar_cSi_GB_2019_01.pdf (accessed on 10/05/19).

BIPV integrated modules

BIPV integrated modules are almost identical to conventional BAPV modules but made with weather skin solutions so they may replace different types of roofing or walling [242,243]. An example can be seen in Figure 67.

Figure 67. Solesia® by Creaton. Source: https://www.zi-online.info/en/artikel/zi_2011-10_Sunshiny_days_for_photovoltaics_1265944.html (accessed on 10/05/19).

BIPV glazing

BIPV glazing products are semi-transparent devices that transmit a portion of sunlight into the interior of buildings and use the rest for power generation. Logically, they also insulate the building from external weather just like conventional glazing. Most commercial products are based on opaque devices with some spacing between solar cells to allow diffuse light to pass through them (Figure 68, left) [243]. The transparency of such devices can be tuned by varying the size of and/or spacing between the different cells. However, narrow/wide-bandgap technologies that mostly absorb invisible IR/UV light can also be employed to achieve semitransparency (Figure 68, right). This is usually accompanied by reduced thicknesses of the absorber layers. Different degrees of transparency and colours can be obtained by varying the bandgap and/or thickness of the absorbing layers.

Figure 68. Left: Skylights made from spaced opaque modules (left) and semitransparent devices (right) by Onyx Solar. Source: https://www.onyxsolar.com (accessed on 10/05/19).

BIPV solar tiles

Solar tiles, on which this work is focused, are roof/wall tiles that have been equipped with a solar generator. By the partial or total substitution of standard tiles by BIPV solar tiles it is possible to maintain the favourable aesthetical appearance and mechanical properties of roofs/walls while converting them in power generators. One of the main advantages of this BIPV product is that it can be easily retrofitted into existing buildings [242]. Figure 69 shows different examples of roof solar tiles.

Figure 69. Left: Solé Powertile^{TM}. Source: https://cleantechnica.com/files/2010/05/SRS_Tile.jpg (accessed on 10/05/19). Right: Solar roof by Tesla. Source: https://www.solarguide.co.uk/tesla-energy/solar-roof-tiles#/ (accessed on 10/05/19).

4.1.2 Solar tiles and thin film photovoltaics: a combination with great potential

Current commercial solar tiles consist of roof tiles with an attached or integrated Si solar cell [242]. Instead of being attached to or integrated into the tile structure a posteriori, thin film solar cells bring the possibility of direct deposition onto commercial ceramic tiles as an additional manufacturing step so that the tile becomes a solar module itself. The price of commercial tiles normally used in roofs, façades or ventilated walls typically ranges 30-75 €/m^2, similar to conventional SLG glass [201,250]. Thus, thin film solar cells could be implemented onto commercial tiles at the same cost as on glass, without the need of complicated integration or attaching designs and, thus, at lower prices than current solar tiles.

Despite the great potential of thin-film-based solar tiles, this topic has not yet been studied thoroughly enough. Nevertheless, the feasibility of employing commercial ceramics as substrates for thin-film PV has already been successfully demonstrated in a small number of publications. a-Si were deposited on roof and wall tiles obtaining 5% and 4% efficient cells, respectively [251]. As for CIGS, solar cells were fabricated on commercial ceramic tiles achieving 14% conversion efficiency, similar to the results obtained on soda-lime glass (SLG) using the same procedure (selenization of sputtered binary compounds) [252].

Due to the Earth-abundance and low toxicity of their constituent elements, kesterites solar cells are ideal candidates for the mass deployment of solar tiles. Thus, developing an efficient kesterite solar tile technology seems of great importance for the BIPV market. Nevertheless, the kesterite community has not shown interest in this critical market niche. Only one proof-of-concept for a kesterite solar cell on a ceramic was published but with a very limited power conversion efficiency below 2% [253]. The work presented here aims to demonstrate the feasibility of fabricating efficient $Cu_2ZnSnSe_4$ solar cells employing commercial ceramic tiles as substrates.

4.1.3 Limitations of ceramic substrates for thin film deposition and objectives of this work

Commercial ceramic tiles present a series of characteristics that complicate their use for thin film deposition and for the fabrication of kesterite solar cells:

- They are rough, wavy and full of other morphological imperfections which are larger than the absorber thickness causing film discontinuity, short-circuit and shunting problems [251,252,254].
- They contain (almost) no alkaline elements which are crucial for high solar cell performance (see section 1.4.4)
- Their composition contains impurities (like Fe) which are detrimental for the performance of kesterite devices [255]

In this work an approach that addresses these three critical issues simultaneously is investigated: employing ceramic substrates covered with a vitreous enamel in which Na_2O is incorporated in controlled quantities (from 2 to 20 wt%) to its composition. This way, the enamel works three-fold:

- As a surface smoother
- As a controlled sodium source
- As a barrier for impurities

The need of vitreous enamels to smooth the surface of raw ceramics and enable thin film deposition was already identified as a critical issue by several authors reporting working thin-film devices on ceramics [251–254,256,257]. As for doping, this concept has been successfully implemented in the case of CIGS solar cells grown on steel foils, where an enamel was used as an efficiently working alkali source [195].

This work is divided in three main parts:

i. First, the effects that incorporating different amounts of Na_2O into the composition of the enamel causes on the surface morphology of the substrates and on the back contact deposited on them are investigated.
ii. Then, CZTSe solar cells are fabricated onto this first batch of substrates and their performance is analysed.
iii. Based on the previous results, a new batch of substrates is employed and the thermal reactive annealing is improved in order to increase the power conversion efficiency of the devices.

4.2 Experimental

4.2.1 Substrate description and sample preparation

The substrates employed in this work are 4.5 mm thick (2.2 x 2.2 cm^2) commercial ecological porcelain stoneware ceramics, which were developed at University Jaume I using a ceramic paste formulation with the addition of industrial wastes (recycled glass, sludges and chamote). The approximate composition and main properties of the ceramic substrates are shown in Table 15. These were coated with vitreous enamels containing quantities of Na_2O ranging from 2 to 20 wt%.

Table 15. Composition and main properties of ecologic ceramic substrates.

Composition (wt%)	SiO_2	65.2
	Al_2O_3	22.2
	CaO	2.7
	MgO	2.4
	ZrO_2	2.2
	$Na_2O+K_2O+Fe_2O_3$	5.3
Density	**2400 kg/m^3**	
Coefficient of thermal expansion	**5.8 $\cdot 10^{-6}$ K^{-1}**	
Thermal conductivity	**~2.5 W/(m·K)**	
Maximum temperature before degradation	**>1000°C**	

A 780 nm trilayer Mo back contact was deposited on the clean substrates with a sheet resistance of ~0.6 Ω/□. Cu/Sn/Cu/Zn metallic precursor stacks were deposited onto the Mo back contact with Cu-poor Zn-rich composition followed by a 10 nm Ge nanolayer. The first batch of precursors were selenized through a 2-step thermal reactive annealing process similar to the one described in Table 8 but with a longer 2nd step annealing time (30 min). The second batch of precursors was selenized with standard annealing times. The as-annealed CZTSe absorbers were then subjected to three successive chemical etchings in order to remove surface secondary phases followed by the deposition of a CdS buffer layer. The devices were completed with a i-ZnO (50 nm)/ITO (350 nm) bilayer (75 Ω/□). Each sample was scribed into ~36 individual solar cells (9 mm^2). Complete devices were post-annealed in air at 180°C on a hot plate for 30 minutes. For a more detailed description of the fabrication process, see sections 2.2.3 and 2.3.

4.2.2 Characterisation

The impact of the Na_2O content of the enamel on different macro and microscopic properties of the Mo back contact was analysed by different techniques:

- The surface morphology (macroscopic) was analysed by confocal and optical microscopy. It should be noted that the area of the analyses shown (~27 mm^2) accounts for roughly 5% of the samples and that morphology can vary significantly within the same sample. Several measurements were carried out on different regions of each sample. The results shown are chosen to be representative of each sample, showing average characteristics.
- The structural and microscopic properties were studied by XRD and FESEM (top view, 5 kV acceleration voltage, 5 mm working distance), respectively.
- The sheet resistance (R_{sheet}) of the Mo layers was measured by a 4-point probe.

As for the kesterite absorbers, their structural and microscopic properties were studied by XRD and FESEM (cross-section, 5 kV acceleration voltage, 5-7 mm working distance).

The J-V characteristics of the devices were obtained under simulated AM1.5 illumination (1000 W/m^2 intensity at room temperature) using a pre-calibrated solar simulator. The EQE was measured using a spectral response system.

Raman scattering measurements were made under 532 and 785 nm excitation wavelengths on CZTSe absorbers. The measurements were performed in backscattering configuration focusing the excitation laser spot on the window layer surface. A diameter of 50 µm and an excitation power density of about 1 kW/cm^2 were used in order to inhibit thermal effects in the spectra while light collection was made through a x20 objective.

For more information about the characterisation techniques employed, see section 2.2.

4.3 Results

4.3.1 Substrate and back contact analysis

Surface characteristics

The average surface roughness (R_a) of the Mo-coated ceramic substrates was calculated from confocal 3D topographies. Several measurements were performed in different regions of the samples. Due to the lack of flatness, an 80 µm Gaussian filter (in compliance with ISO 25178) was used to separate waviness from roughness. A piece of Mo-coated SLG was also measured as a reference. The results show that the average roughness (R_a) does not vary substantially with the Na_2O content of the enamel and lies in the 15-20 nm range except for the 20% Na_2O sample (35 nm) (Figure 70). Although high in comparison to SLG (7 nm), these roughness values are comparable to, for example, those of stainless steel and can be considered acceptable for thin film deposition and PV applications [258].

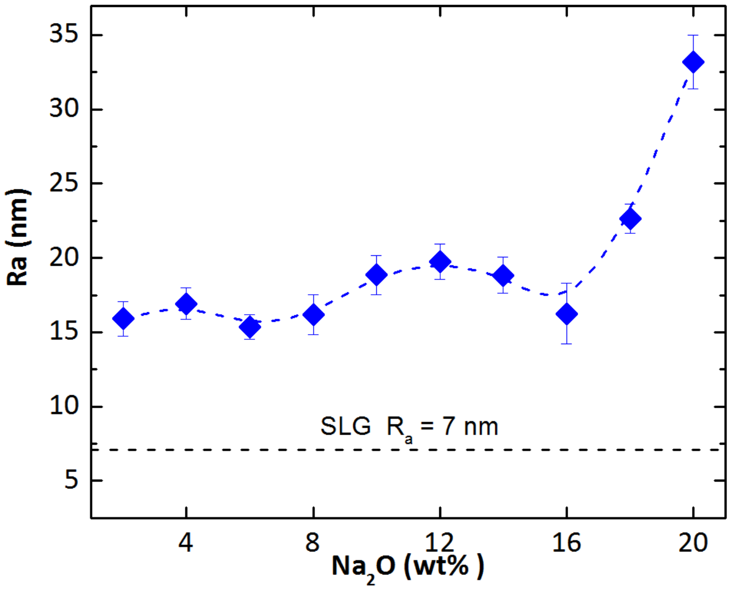

Figure 70. Average roughness of the Mo-coated enamelled ceramic substrates.

Although the roughness of the substrates is quite resilient to the composition of the enamel, their surface morphology is worsened with increasing Na_2O contents. This is evidenced even with the naked eye for the Mo-coated substrates (Figure 71). While the substrate with 2% Na_2O displays a rather flat surface, the rest of the substrates exhibit visually rough surfaces full of imperfections. 3D topographies provide more detailed information about the surface morphology of the different substrates (Figure 72). This way, it is possible to differentiate between two main types of surface defect: undulations and pinholes. While no strict dependence on the Na_2O content can be observed, both undulations and, especially, pinholes tend to be more abundant and pronounced with the increasing Na_2O content of the enamel. With regards to pinholes, more detailed 3D topographic images reveal that their diameter typically ranges from 50 µm to 300 µm and their depth oscillates from 500 nm up to several microns (Figure 73).

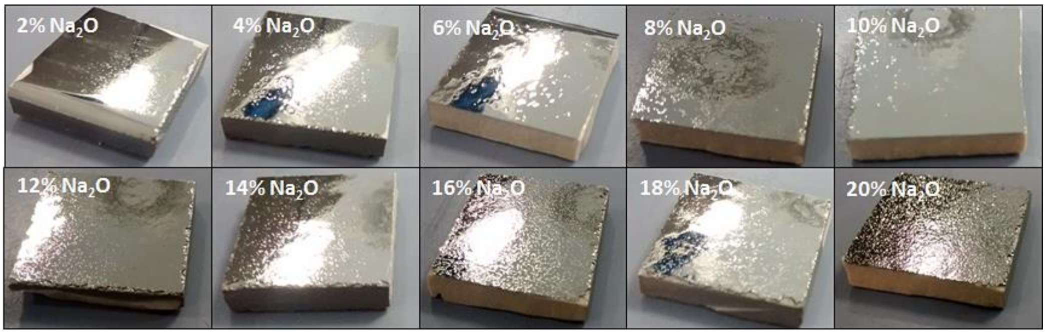

Figure 71. Pictures of the different Mo-coated enamelled ceramic substrates.

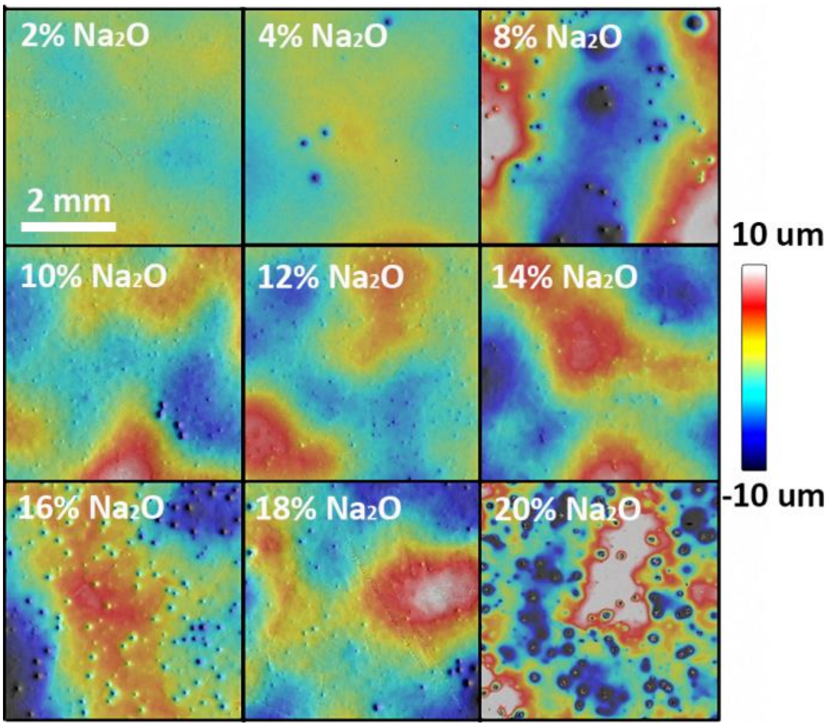

Figure 72. 3D topographies of the Mo-coated enamelled ceramic substrates.

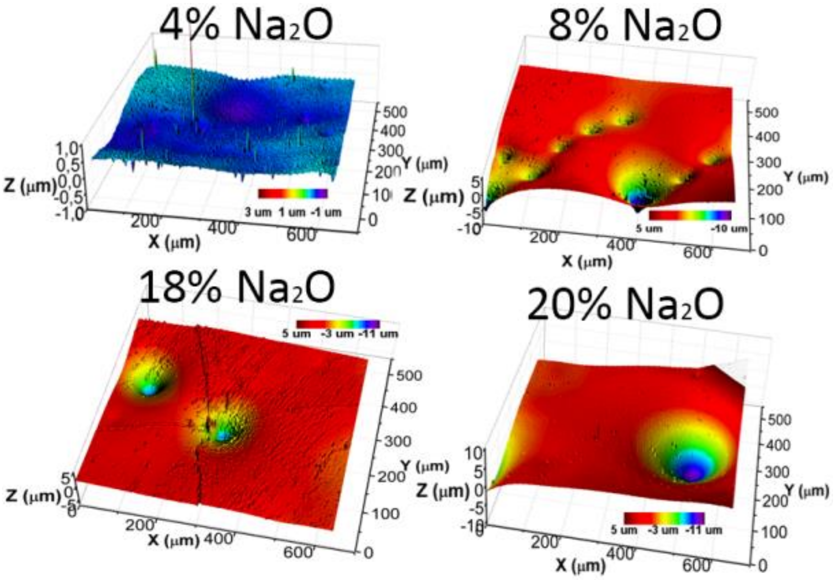

Figure 73. Detailed 3D topographies of the Mo-coated ceramic substrates.

In addition to pinholes and undulations, Figure 73 also reveals crack-like lines in the sample with 18% Na_2O content. These cracks were further investigated under an optical microscope at a larger scale (Figure 74). Interestingly, all the substrates with Na_2O < 10% did not show any cracks while every sample with Na_2O content ≥ 10% presented clearly cracked surfaces. Furthermore, the number of cracks was found to increase steadily with the increasing Na_2O concentration in the enamel.

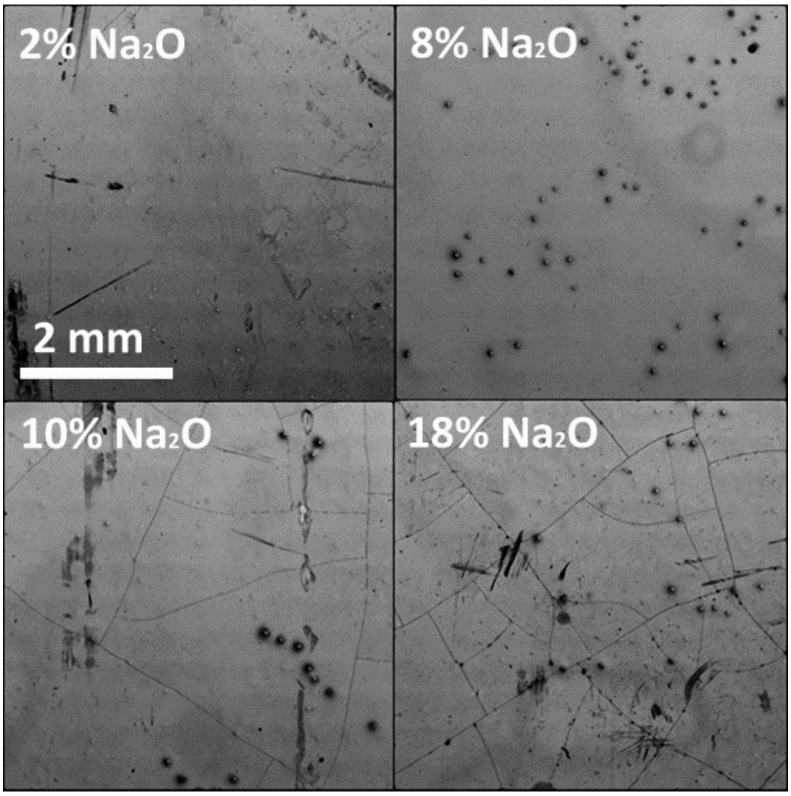

Figure 74. Optical images showing superficial cracks on Mo-coated ceramic substrates with enamels containing more than 8% Na_2O.

Structural and electrical characteristics

The influence of the different enamel compositions on the structural and microscopic properties of the Mo back contact was investigated by XRD and FESEM, respectively. All the different samples present almost identical XRD diffractograms regardless the Na_2O content (Figure 75). More specifically, they all show a preferred growth orientation of Mo in the (110) direction with a small presence of the (211) and (220) directions (ICDD 00-042-1120). On the other hand FESEM micrographs confirm these results showing similar grain size and morphology independently from the Na_2O composition (Figure 76).

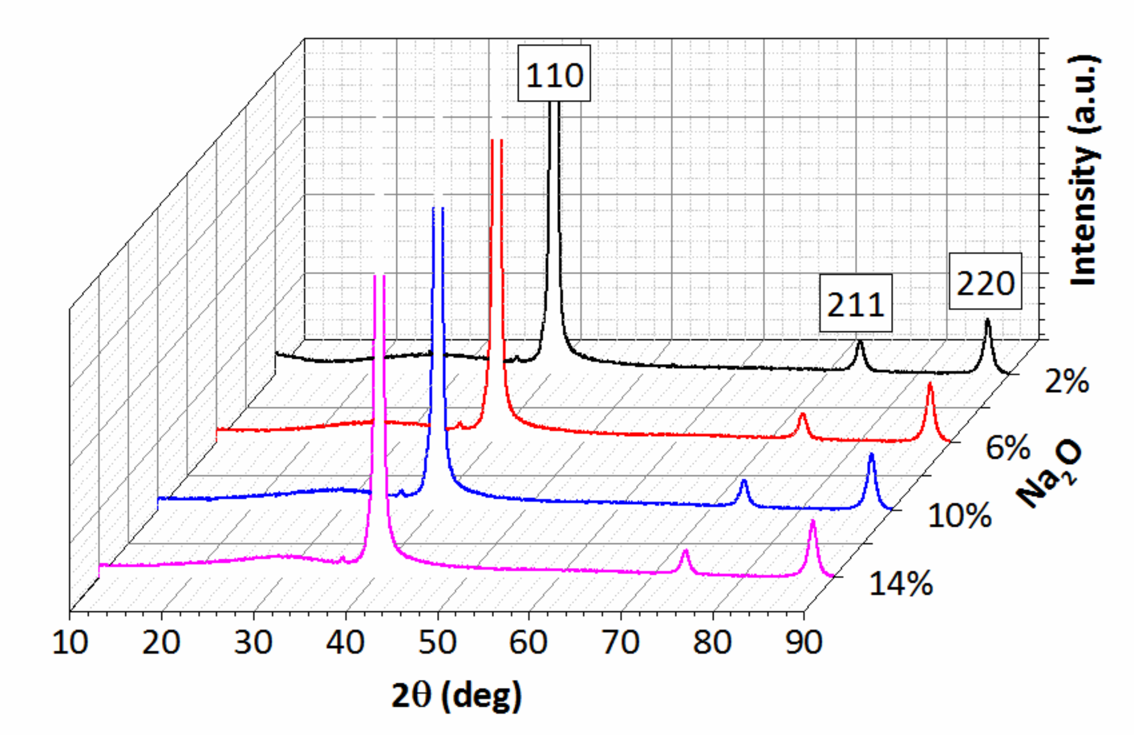

Figure 75. XRD diffractograms of Mo back contact deposited on enamels with different Na_2O content.

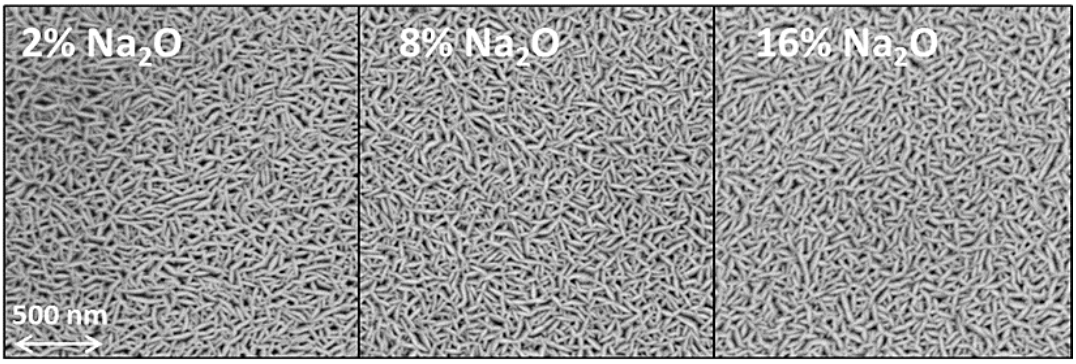

Figure 76. FESEM top view micrographs of Mo back contact deposited on enamels with different Na_2O content.

With regards to the electrical properties of Mo back contacts, it was observed that the conductivity of the substrates is affected by the enamel composition (Figure 77). A constant and homogeneous R_{sheet} of approximately 0.6 Ω/sq (similar to the SLG reference) is found in samples with a Na_2O content below 10% (Figure 77). Nevertheless, R_{sheet} increases substantially and presents a large dispersion in higher Na_2O content samples. This result matches the surface cracks described above found in substrates with Na_2O content ≥ 10%. Cracks disrupt the continuity of the Mo film and become highly resistive barriers that create isolated conductive Mo islands. When measuring, the tips of the 4pp reach two or more different islands resulting both in an increased R_{sheet} and measurement dispersion. On the other hand, undulations and pinholes do not seem to have a negative effect on the electrical conductivity of the substrates as suggested by the 8% Na_2O sample which presents a high density of such defects while displaying the same R_{sheet} than flatter substrates.

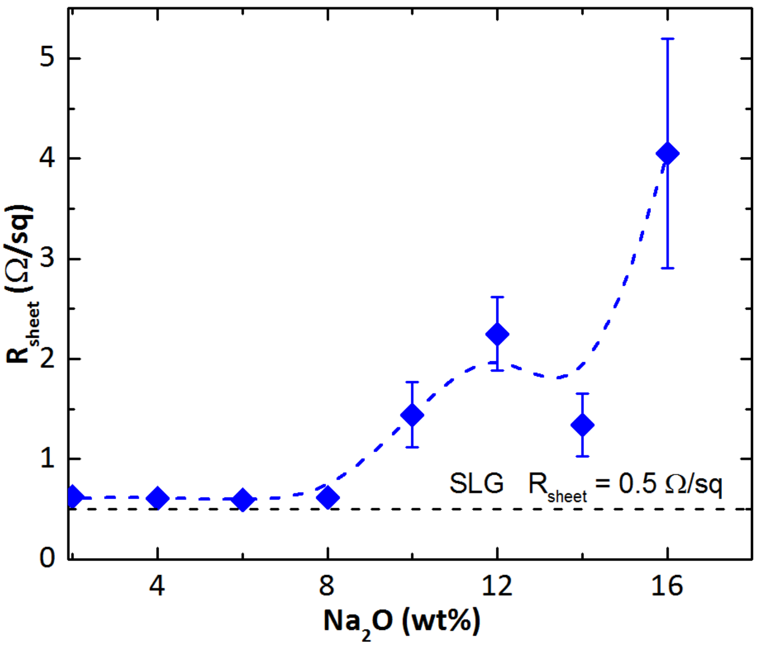

Figure 77. R_{sheet} of the Mo back contacts deposited on enamels with different Na_2O content.

Summary

To sum up, the accommodation of large Na_2O contents in the composition of the enamel alters its surface morphology creating undulations, pinholes and cracks that are transferred to the Mo back contact deposited on them. A higher amount of Na_2O tends to result in a larger density of such surface imperfections. This is especially critical in the case of cracks, which appear only in samples with more than 8% Na_2O. The sheet resistance of the back contact is strongly affected by cracks since they create resistive barriers that hinder charge transport. However, pinholes and undulations do not have a negative effect on the electrical properties of Mo.

4.3.2 Device analysis

Performance

Table 16 shows the parameters of the best solar cells obtained in each of the ceramic substrates studied. Devices prepared on the substrates with enamel Na_2O content ≥ 10% present efficiencies well below 0.5%, mainly due to an increased series resistance. This correlates with the increased R_{sheet} of the Mo back contact found on those substrates due to surface cracks. On the other hand, all the samples with Na_2O contents below 10% result in working devices with efficiencies above 3% that exceed previous reports [253]. Figure 78 (left) shows the J-V curves of those devices. No correlation between performance and Na_2O content of the enamel can be spotted. Actually, all the samples present similar V_{oc} values (~300 mV). Moreover, the record devices fabricated on 2-6% Na_2O substrates also present similar J_{sc} and FF. However, the record device of the 8% Na_2O substrate exhibits superior J_{sc} and, especially, FF that translate into a 4.6% record efficiency. The EQE (Figure 78, right) measurements show that the increased J_{sc} arises from a better collection of long-wavelength (> 850 nm) photons. It is interesting to note that the record device was fabricated on a substrate with numerous pinholes and strong undulation suggesting that these are not a critical factor for solar cell fabrication and performance.

Table 16. Solar cell parameters of the best devices prepared on the enamelled ceramic substrates with different Na_2O composition.

	Na_2O (wt%)								
	2	4	6	8	10	12	14	18	20
J_{sc} (mA/cm^2)	25.3	25.0	25.2	26.6	7.3	2.5	0.4	3.0	-
V_{oc} (mV)	306	310	292	320	224	140	42	280	-
FF (%)	45.8	44.6	44.3	54.5	25.3	25.4	25.0	26.7	-
η (%)	**3.5**	**3.5**	**3.3**	**4.6**	**0.4**	**0.1**	**-**	**0.2**	**-**
R_{sh} ($\Omega \cdot cm^2$)	62	64	44	106	31	-	-	-	-
R_s ($\Omega \cdot cm^2$)	1.6	1.6	1.8	1.4	3.8	-	-	-	-

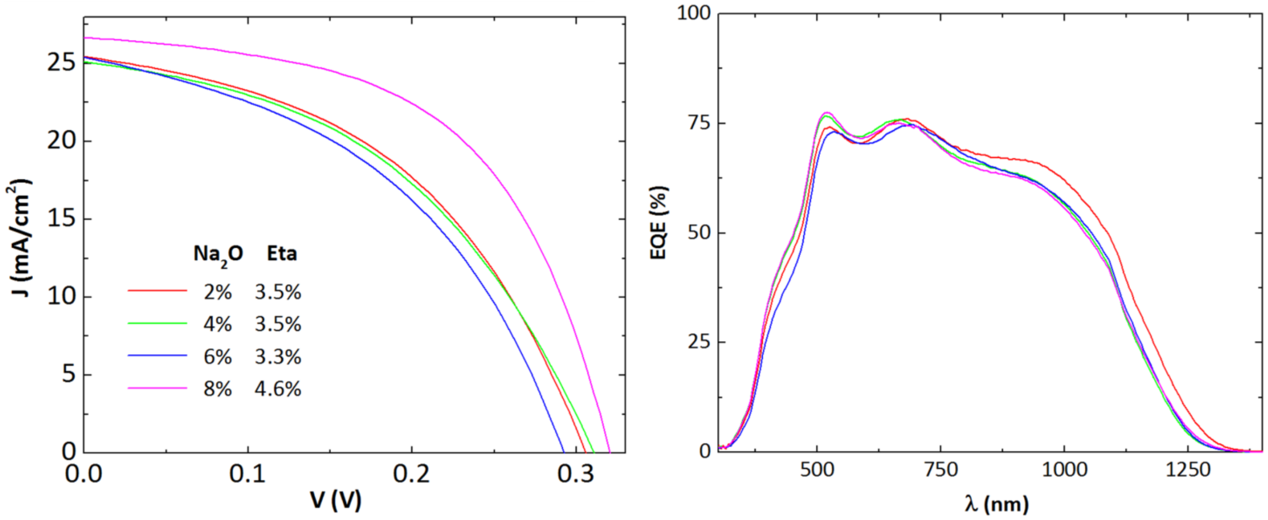

Figure 78. J-V (left) and EQE (right) of the best devices fabricated on enamelled ceramic substrates with different Na_2O content.

X-ray diffraction and FESEM

The working devices were analysed by XRD. No relevant differences could be observed between the kesterite samples prepared on the different ceramic substrates. Figure 79 shows a representative XRD diffractogram. The main peaks can be attributed to CZTSe (ICDD 04-010-6295) and Mo (ICDD 00-042-1120) in addition to the characteristic peaks of $MoSe_2$ (ICDD 04-005-6604). These are very similar to the XRD patterns typically reported for CZTSe absorbers deposited on glass [259,260].

Figure 80 shows cross-sectional FESEM micrographs of devices fabricated on substrates with low, medium and high Na_2O content which are representative for the whole batch of samples. A bi-layer structure, typical for sequential processing, with large crystals at the top and smaller crystals at the bottom is detected in all cases. No clear differences can be observed between samples containing 2-8% Na_2O which correlates with the results obtained by XRD. However, significantly larger crystals are found in samples with Na_2O contents ≥ 10%.

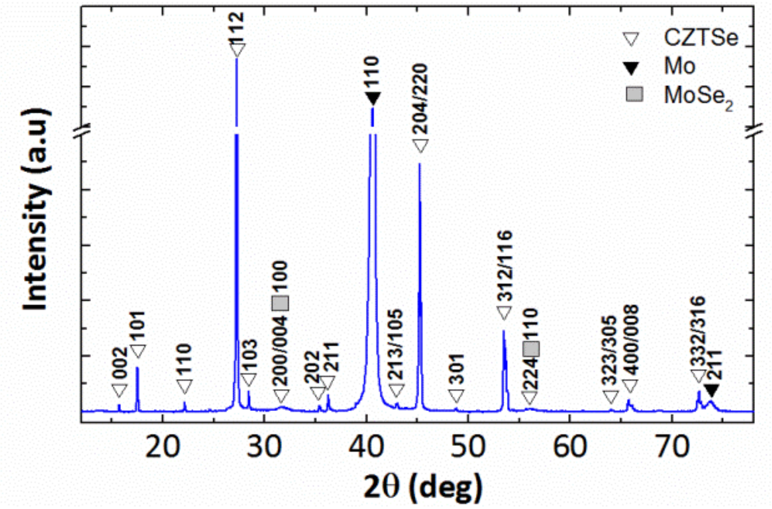

Figure 79. XRD diffractogram of a CZTSe absorber grown on a Mo-coated enamelled ceramic tile (2 wt% Na_2O).

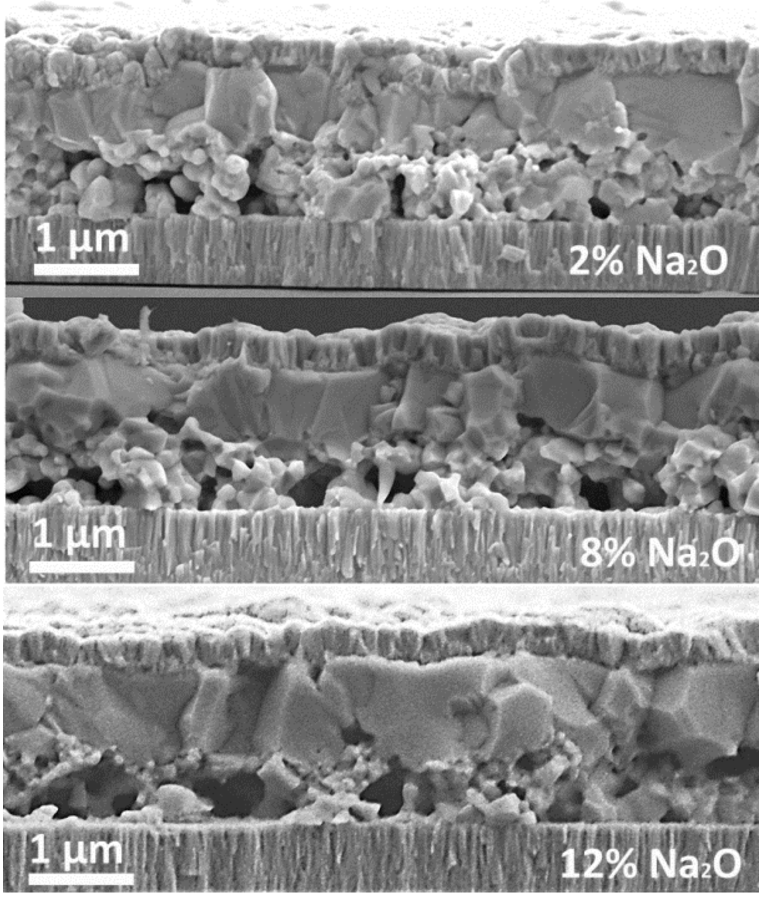

Figure 80. FESEM micrographs (cross section) of CZTSe solar cells grown on Mo-coated ceramic substrates with enamels containing 2% (top), 8% (middle) and 12% (bottom) Na_2O.

Raman investigation

The apparent similarity of the Mo back contact and CZTSe absorbers fabricated on the 2-8% Na_2O substrates combined with the significantly superior performance of the device fabricated on the 8% Na_2O enamel, suggested the existence of a missing underlying factor. In order to find this differential factor, the CZTSe absorbers were analysed by Raman spectroscopy under

532 and 785 nm excitation wavelengths. The analysis was carried out in several individual cells from each sample. Figure 81 shows illustrative Raman spectra corresponding to the record device of the 4% Na_2O substrate together with a low efficiency cell and the record device from the 8% Na_2O sample. The spectra acquired with a 532 nm excitation wavelength show the main peaks of the CZTSe phase at 169 and 195 cm^{-1} and, from the fitting of spectra, device-grade absorbers with good crystalline quality are observed independently from the substrate or cell efficiency. No additional peaks are observed. However, by measuring the same samples with a 785 nm excitation wavelength, the spectra reveal the clear presence of a $SnSe_2$ phase in most of the cells analysed. In particular, this secondary phase is detected in every cell except for the highest efficiency ones from the 8% Na_2O sample. In addition, the intensity of this peak seems related to cell efficiency. In order to corroborate this tendency, the peak area ratio $SnSe_2$ to CZTSe of every cell measured in the analysis was calculated as an estimation of the amount of $SnSe_2$ present in them. Figure 82 shows a plot of the main parameters of each cell as a function of the amount of $SnSe_2$ detected. These data show that the presence of this phase is, in effect, directly correlated to solar cell performance. In particular, the amount of $SnSe_2$ detected sets a limit for the maximum achievable J_{sc}, FF and V_{oc}. The latter shows to be more strongly influenced by $SnSe_2$ which dominates solar cell performance.

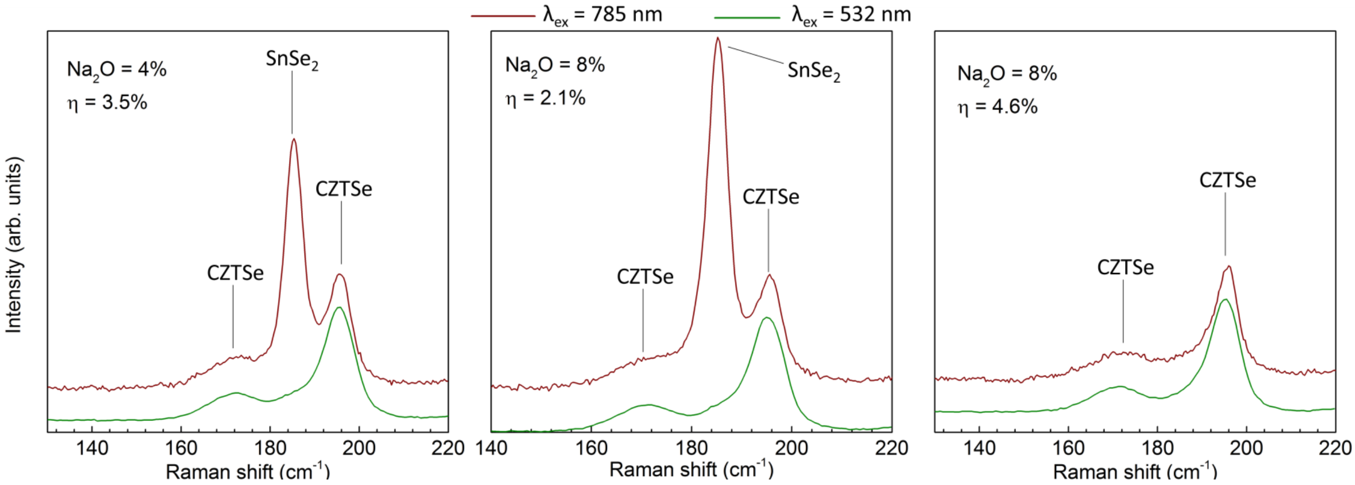

Figure 81. Raman spectra of the record device of the 4% Na_2O sample (left) together with a low efficiency cell (middle) and the record device (right) from the 8% Na_2O sample.

It should be noted that the enhanced detection of $SnSe_2$ with the 785 nm excitation wavelength is due to the fact that such wavelength is coupled with the bandgap of $SnSe_2$. This resonance effect enables the detection of very small amounts of this phase almost undetectable otherwise. For more information see Raman description in section 2.2.2.

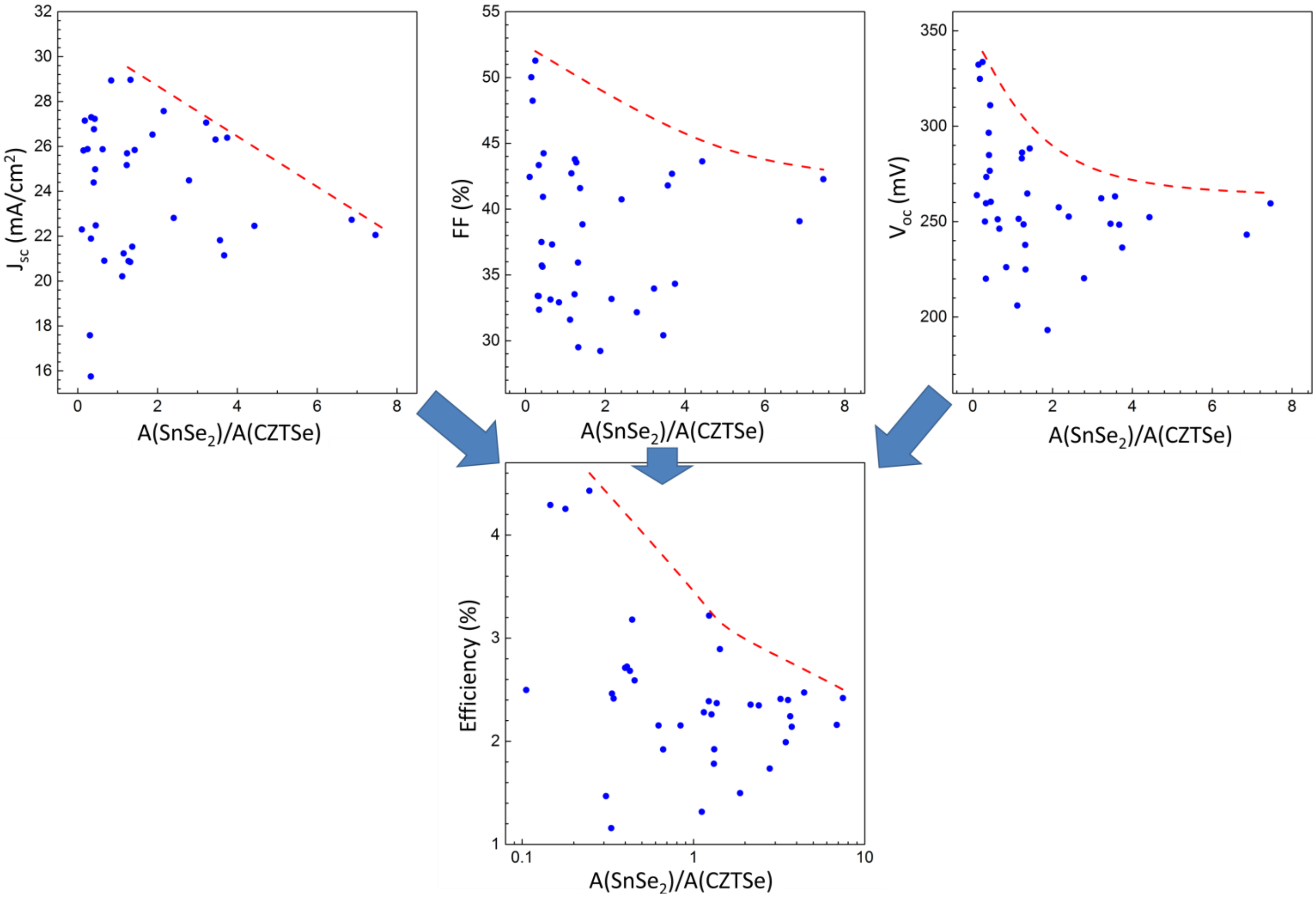

Figure 82. Optoelectronic parameters of different solar cells from different samples as a function of the peak area ratio A($SnSe_2$)/A(CZTSe) obtained from the fitting of Raman spectra. The dashed red lines are only intended as a visual guide for the reader.

4.3.3 Discussion

The results presented here reveal interesting information about how the surface morphology of the enamelled ceramic substrates influences solar cell fabrication. On the one hand, pinholes and undulations do not seem to harm the Mo back contact quality and solar cell performance noticeably. This result is expectable for undulations since these are soft defects in which the curvature of the surface changes very gradually allowing deposited thin films to follow and adapt to it. Nevertheless, tension and higher film stress can be expected at the inflexion points of the undulations. In the case of pinholes, this result is more surprising since the curvature change is much steeper in them which could lead to layer discontinuity and short-circuiting. However, based on the results obtained with the 8% Na_2O sample which presented a high density of pinholes but no short-circuiting or shunting, it is possible to conclude that sputtered films also adapt quite well to them. Most of the pinholes observed have diameters ≥ 50 µm, one order of magnitude above the thickness of the layers comprising the solar cell structure which could be the reason for their benignity. It can be speculated, thus, that smaller pinholes would lead to steeper surface changes and to a greater likelihood of layer discontinuity and short-circuit issues. On the hand, cracks in the vitreous enamel are transferred to the Mo back contact and greatly increase its sheet resistance by disrupting the continuity of the layer. However, this type of defect only appears in enamel formulations with Na_2O content ≥ 10 wt% so it is easily avoidable. Moreover, the sodium supplied by the 2-8%

Na_2O vitreous enamels seems to be sufficient for the fabrication of efficient kesterite devices making it unnecessary, in principle, to go beyond 8% Na_2O contents.

With regards to the effect of Na on the absorbers, the samples processed in 2, 4, 6 and 8% Na_2O-containing enamels present similar morphologies and performances (except for some higher efficiency cells of the 8% Na_2O sample). However, samples with higher Na_2O content displayed a highly enhanced crystal size suggesting a greater sodium supply. There are many reports of Na-enhanced crystallization of kesterite absorbers (see section 1.4.4). Nevertheless, it can be speculated that the cracks observed on those samples allowed the increased diffusion of sodium (and possibly impurities from the ceramic substrate) rather than the higher Na-content of the enamels per se. Unfortunately, the larger crystals were accompanied by a highly degraded Mo back contact unsuitable for solar cell applications.

Finally, it has been shown that small amounts of $SnSe_2$ were formed together with the CZTSe absorbers in every sample degrading the performance of the devices. The annealing time employed in the second step of the selenization process (550°C, atmospheric pressure) for the synthesis of the CZTSe absorbers was twice as long (30 min) than the standard annealing time routinely employed in IREC for SLG substrates (15 min). This longer time was initially selected based on the high thickness, porosity and expected low thermal conductivity of the substrates. However, the thermal conductivity was later found to be in a similar range to that of SLG. Therefore, $SnSe_2$ was probably the consequence of a too long high temperature annealing that led to a slight decomposition of the kesterite phase into binaries [122]:

$$Cu_2ZnSnSe_4 \rightarrow Cu_2Se + ZnSe + SnSe_2 \qquad (R2)$$

The chemical etchings performed on the absorbers are effective against Cu_2Se, ZnSe and SnSe but not against $SnSe_2$ [127,128]. This would explain why only the latter was detected even after etching.

Since this phase was detected in almost every cell measured, it might be possible that the similarities found between the devices fabricated in the 2-8% Na_2O substrates arose from an homogenizing effect of $SnSe_2$ rather than to other factors like a self-limited Na incorporation from the enamel regardless its Na content.

4.3.4 New batch of substrates and modified annealing

Substrates and device performance

In order to study the issues discussed above, a new batch of ceramic substrates was ordered with the following specifications:

- The Na_2O content should be ≤ 8 wt% to prevent cracks
- It should contain an enamel with the minimum possible Na_2O content
- Avoidance of small pinholes

Figure 83 shows the 3D topographies and Na_2O content of the new batch of substrates. It can be observed that the low Na_2O enamels (1.4 and 2%) feature very flat surfaces while the higher Na_2O enamels (4 and 6%), as expected, possess increasingly undulated surfaces although no significant pinholes are detected in any of them. Additionally, none of them present surface cracks.

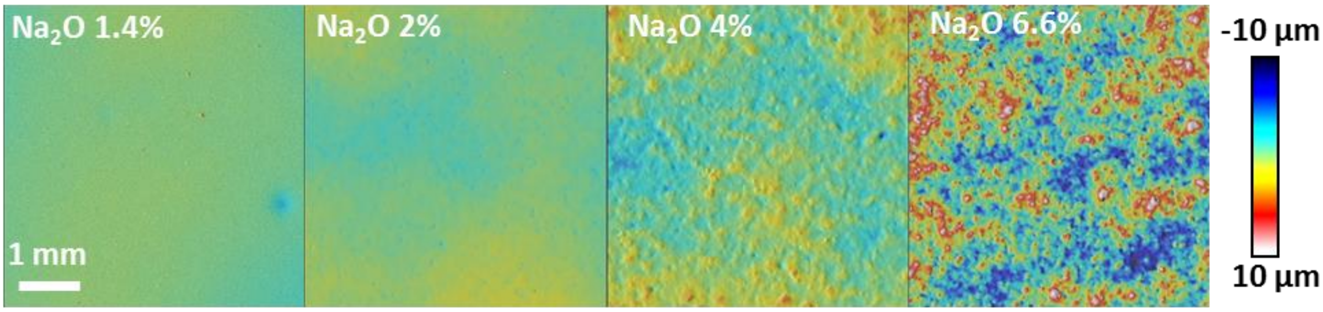

Figure 83. 3D topographies and Na$_2$O content of the new batch of enamelled ceramic substrates.

Solar cells were fabricated on those substrates reducing the duration of the second step of the annealing from 30 to 15 min, i.e. to the standard time used for SLG. A SLG sample was processed simultaneously. Table 17 shows the main optoelectronic parameters of the record devices found on each of the substrates. A very large improvement can be observed with respect to the previous samples even in the almost Na-free sample. All the parameters are substantially improved and efficiencies from 6 to 7.5% are achieved. Moreover, a clear tendency of the V_{oc} to increase with the increasing Na$_2$O content of the enamel is observed. This can be seen in a clearer way in Figure 84, where the average V_{oc} of the top 5 devices found on each substrate is plotted with respect to the Na$_2$O content of the enamel. Raman analysis did not detect any trace of SnSe$_2$ in any of the devices so, in principle, this trend can be attributed solely to a higher diffusion of Na from the substrate. In addition, it confirms that CZTSe decomposition due a long annealing time was the cause of the presence of SnSe$_2$ in the samples processed before.

Table 17. Solar cell parameters of the best devices prepared on the new batch of enamelled ceramic substrates.

	Na$_2$O (wt%)					
	1.4	2	4	6.6	SLG	8 (old)
J_{sc} (mA/cm^2)	27.6	28.3	29.5	30.1	29.6	26.6
V_{oc} (mV)	369	379	393	397	416	320
FF (%)	59.3	59.5	64.7	63.1	64.0	54.5
η (%)	**6.0**	**6.4**	**7.5**	**7.5**	**7.9**	**4.6**
R_{sh} (Ω·cm^2)	150	170	310	320	480	106
R_s (Ω·cm^2)	0.4	0.4	0.4	0.5	0.5	1.4

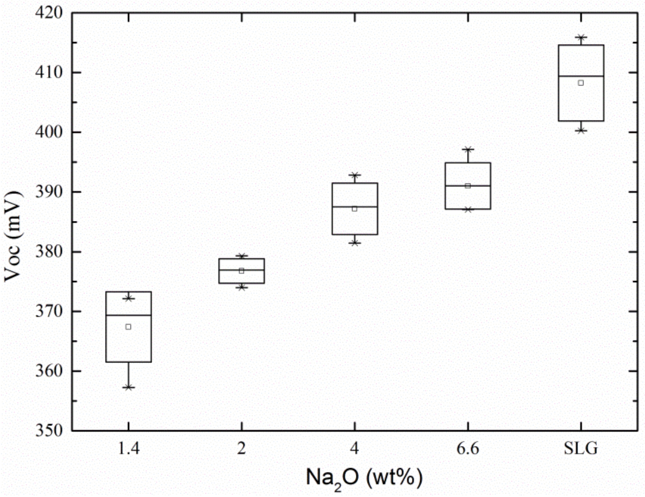

Figure 84. V_{oc} of the top 5 devices found on each substrate.

Na diffusion

In order to corroborate that sodium is effectively diffusing from the enamel into the absorber during CZTSe synthesis and could be the responsible of the V_{oc} increase, the 1.4 and 4% Na_2O samples were investigated by time-of-flight secondary ion mass spectroscopy (TOF-SIMS).

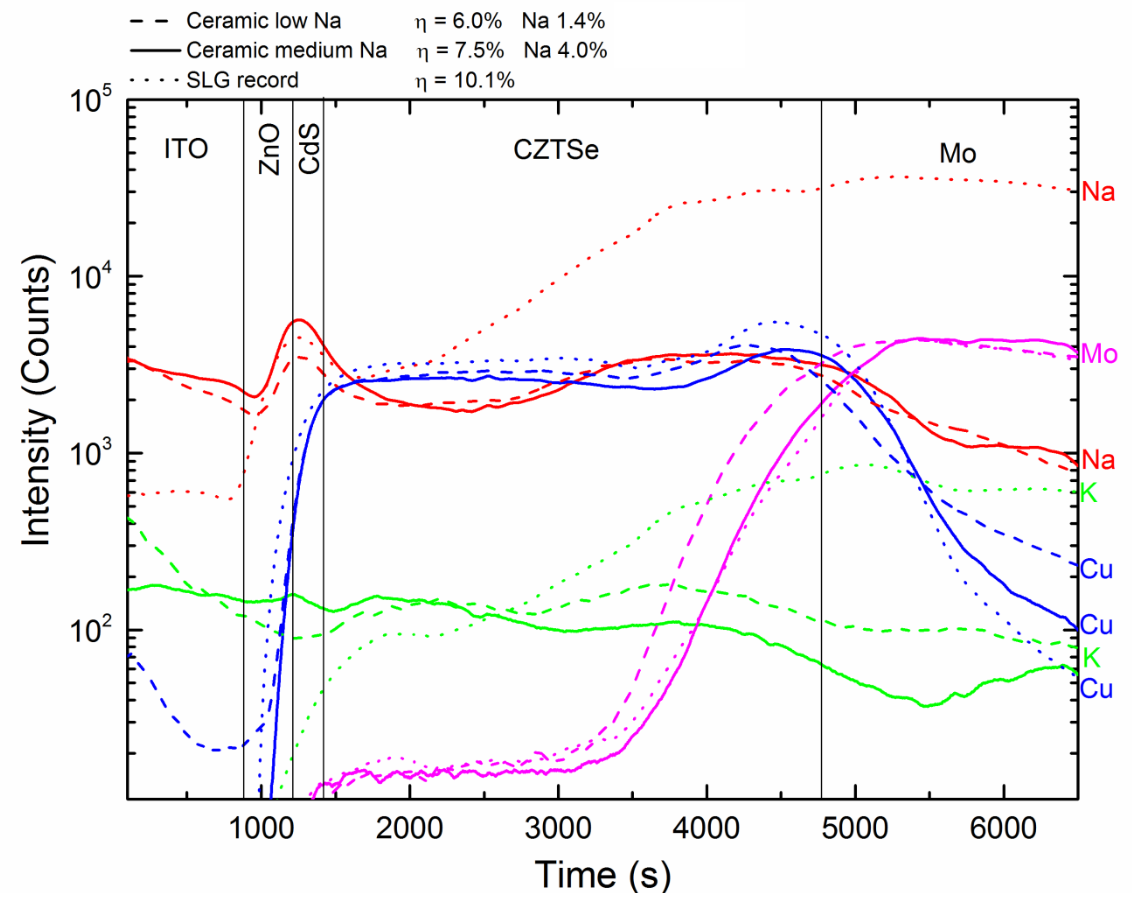

Figure 85. TOF-SIMS depth profile of low and medium Na_2O content enamelled ceramic substrates. A profile corresponding to one of the record devices fabricated in IREC on SLG (not in this work) is also shown for comparison.

Figure 85 shows the compositional depth profiles obtained for both substrates together with one of IREC's record devices on SLG (not from this work). It can be observed that there is an effective diffusion of Na from the enamels to the CZTSe absorber in both cases. Furthermore, Na incorporation seems to be very similar in both ceramic substrates. However, the higher accumulation of Na towards the ZnO/CdS interphase indicates indeed a higher Na supply from the enamel with a higher Na_2O content. A very weak incorporation of K is also observed although its effect on the CZTSe absorber is probably negligible. Finally, alkali incorporation is found to be much lower than in the case of SLG.

Discussion

Effects of Na diffusion

Returning to Table 17, a large difference between the 1.4 and 2% and the 4 and 6% Na_2O samples can be spotted with the latter displaying an improved FF with respect to the former. Although the TOF-SIMS analysis indicates that Na incorporation is only slightly higher with a higher Na_2O content, these results suggest that this small variation is enough to make a difference on the devices. On the one hand, comparing the 1.4 and 2% Na_2O samples, the difference in sodium incorporation is enough to slightly to improve the V_{oc} of the latter. However, both samples possess a similar FF. On the other hand, by just increasing the Na_2O content of the enamel from 2 to 4%, apart from a further increase of the V_{oc}, the FF is also improved. Increasing the Na content from 4 to 6.6% keeps increasing the V_{oc} but does not result in any further improvement of the FF. Therefore, it looks like Na diffusion from the enamels affects the V_{oc} and the FF of the devices in different ways.

In the case of the V_{oc}, a roughly linear behaviour is observed: the higher amount of Na in the enamel, the higher V_{oc} of the devices. Na has been observed to increase the V_{oc} of kesterite and CIGS solar cells by inducing the creation of copper vacancies (V_{Cu}) which are acceptor defects that increase carrier concentration [161,173]. This matches the results shown here since a higher amount of Na would be expected to produce a higher amount of V_{Cu} and, thus, a steady increase of the V_{oc}.

In the case of the FF, a threshold behaviour is observed. Na has been observed to improve the FF of kesterite devices by accumulating at the grain boundaries and passivating them thus avoiding deep defects and reducing non-radiative recombination [162,168,226]. From the results presented here, it seems that, contrarily to carrier concentration enhancement, in order to effectively passivate grain boundaries and increase the FF, a certain threshold amount of Na is necessary and is only achieved for Na_2O contents ≥ 4%. Once that threshold is reached, additional Na does not seem to further improve the FF of the devices, not even in the case of SLG (in which the Na diffusion is much greater than in ceramic substrates according to the TOF-SIMS measurements).

Comparison of record devices in ceramic and SLG

There are almost no differences between the devices fabricated on the substrates with 4 and 6.6% Na_2O in the enamel. Both of them result in a remarkable 7.5% efficiency, the highest reported for a kesterite device fabricated on a ceramic substrate. What is more, Table 17 reveals that the only difference between the best devices fabricated on SLG and on ceramic substrates lies in a ~20 mV lower V_{oc} of the latter. The origin of this difference seems to be a lower shunt resistance of ceramic substrates. This is expectable due to their non-flat surface that may induce slight layer discontinuities leading to shunt paths. The impressive similarity between both types of substrates is better represented in Figure 86 which shows the J-V curves of the record devices achieved on SLG and ceramic (6.6% Na_2O). Interestingly, the J_{sc} of the 6.6% Na_2O ceramic substrate is slightly higher than that of SLG. This could be related to the non-flat morphology of ceramic substrates which acts similarly to an optical texturisation of the absorber layer that increases the effective active area available per device allowing a better absorption of long-wavelength photons. This is clearly observed in the EQE measurements shown in the inset of Figure 86. This was also observed in the first batch of substrates in which the most undulated substrate (8% Na_2O) also presented a higher collection of long-wavelength photons (Figure 78). Thus, a non-flat surface is like a double edged sword leading to potentially higher light collection but also to shunt problems.

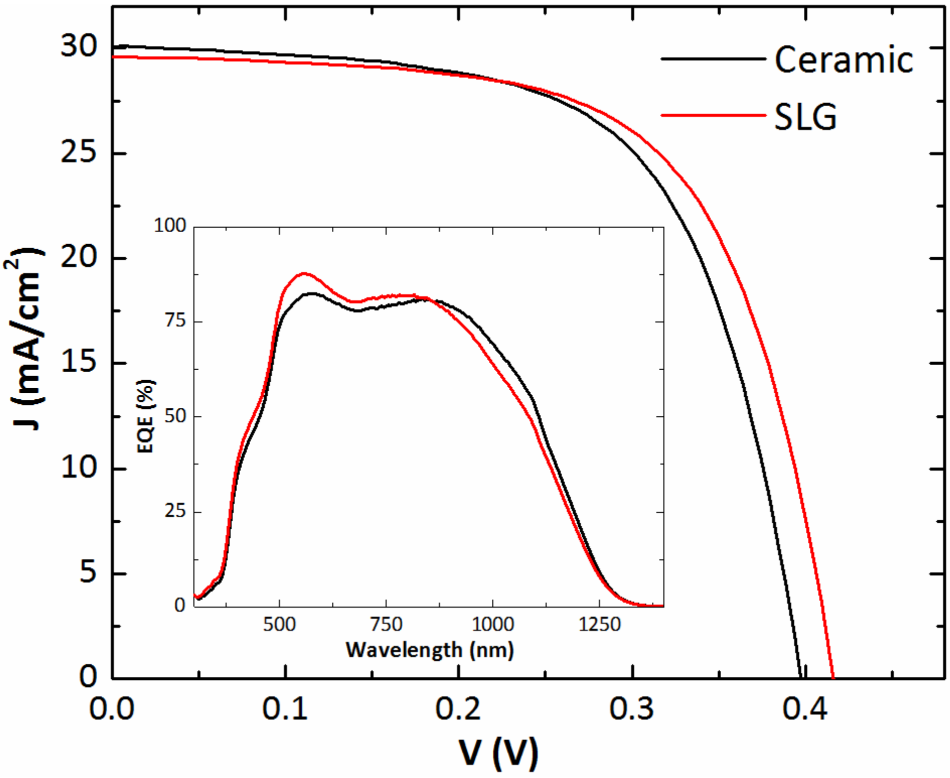

Figure 86. J-V curves of the record devices obtained on SLG and 6.6% Na2O enamelled ceramic substrate. Inset: EQE curves of the same devices.

Annealing time and $SnSe_2$

Finally, the formation of $SnSe_2$ has been completely eliminated by reducing annealing time. This indicates that, in effect, this phase was arising from CZTSe decomposition due to the prolonged annealing times. In addition, regarding the results obtained with the second batch of substrates, it seems plausible that the lack of differences observed between the devices fabricated on the first batch of substrates was originated purely by the degrading effect of $SnSe_2$.

4.4 Conclusions

This work demonstrates the feasibility of producing efficient Earth-abundant kesterite solar cells on ceramic substrates with a direct application in solar tiles, a BIPV concept with a great potential to reduce cost and area allocation issues of PV.

The innovative approach employed here in which a smoothing Na_2O containing vitreous enamel is also used as a diffusion barrier for impurities and as a source of sodium, has been proven to be the right direction in order to use ceramics as substrates for thin film photovoltaics. It has been demonstrated that there is an effective diffusion of Na from the enamels into the CZTSe absorbers, although to a lesser extent than when employing SLG. While Na led to V_{oc} and FF improvements, no appreciable impact on crystal size was observed for enamels with Na_2O contents between 2 and 8 wt%. Nevertheless, it was observed that trying to accommodate large amounts of Na_2O in the enamel results in higher densities of three surface defects: undulations, pinholes and cracks. Interestingly, undulations and pinholes do not affect cell performance critically. But, on the other hand, cracks (which only occurred for Na_2O contents $\geq$ 10%) were identified as very detrimental since they strongly deteriorate the conductivity of the back contact and prevent the fabrication of working devices.

In addition, the annealing process has been found to be very critical. In a first attempt, a prolonged annealing time led to the formation of $SnSe_2$ which degraded the performance of the devices by mainly limiting their V_{oc}. However, this phase was completely eliminated by reducing the time of the second step of the annealing.

Finally, a record efficiency of 7.5% was achieved with two different enamels containing 4 and 6.6% Na_2O. This is the highest efficiency reported for a kesterite device fabricated on a commercial ceramic substrate. But, more importantly, the same process led to a 7.9% efficiency on SLG. This implies that enamelled ceramic substrates behave in a similar way to conventional SLG. Thus, there is a high potential of achieving similar levels of efficiency on both substrates. This shows the great potential of ceramic substrates for substituting SLG, not only for BIPV, but also for other applications of fabrication processes not compatible with the latter.

In particular, the greater thermal resistance of ceramics in comparison to SLG opens the door to a redesign of annealing processes at temperatures greater than 600°C which could greatly improve the results shown here. In addition, a combination of a low-Na enamel with other alkaline elements and doping approaches like PAS, PDT or alkali-doped Mo back contacts are also interesting strategies to keep improving the performance of kesterite-based solar tiles.

5. Transition metal oxides for kesterite solar cells developed on transparent substrates

5.1 Introduction

5.1.1 Transparent back contacts for kesterite solar cells

Thin film solar cells typically employ transparent TCO-based electrodes at the front illuminated side in order to allow light to reach the absorber layer and opaque metallic electrodes at the rear. Metals are ideal back electrodes due to their superior conductivity that facilitates charge collection and extraction. However, their lack of transparency limits the possibilities of thin film photovoltaics. Their substitution by transparent electrodes opens the way to a manifold of advanced applications.

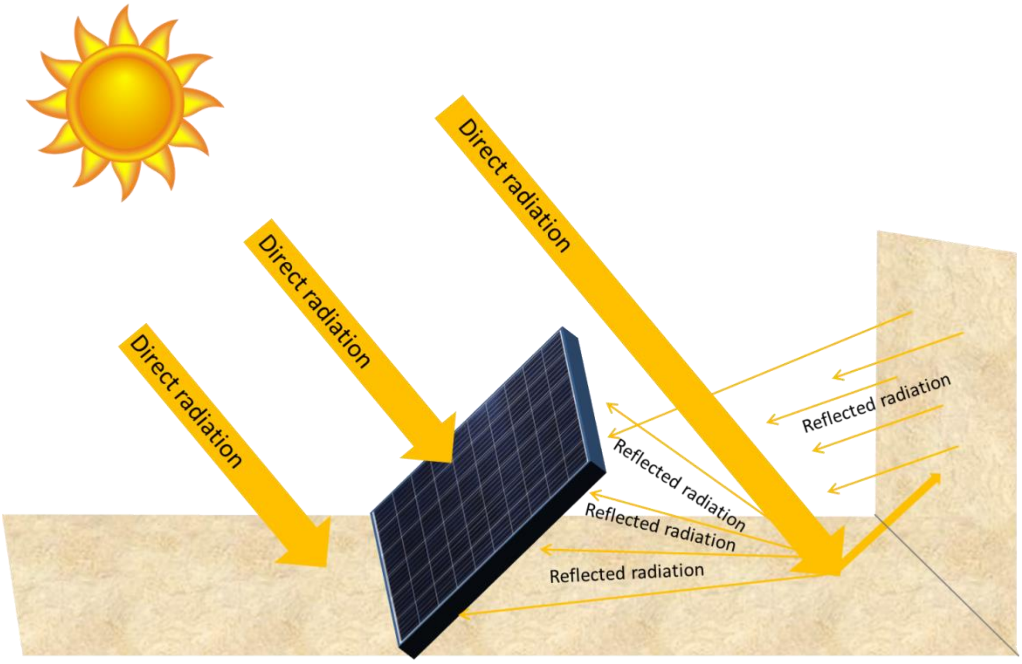

Figure 87. Schematic of albedo light reaching the front and rear sides of a bifacial solar panel in a rooftop installation.

On the one hand, solar cells with a transparent back electrode can generate a significant amount of energy when illuminated from the rear. Solar cells that operate by collecting photons from the front and rear sides simultaneously are commonly called bifacial solar cells. Although this concept is almost as old as photovoltaics itself, with the first related patent dating back to 1966 [261] and the first article on the topic being published in 1980 [262], it is still a not well-established but a powerful way of increasing the energy output of solar cells. Bifacial solar cells can be used for standard rooftop installations. This way, while generating most of the power from direct front illumination, diffuse and reflected albedo light reaching the back side of the panel (Figure 87) can be employed to generate a considerable amount of extra power [263]. In addition, bifacial solar cells possess a large potential for BIPV (see section 4.1.1) since they can be fitted into surfaces that, due to the design of the building, are mostly illuminated from one side in the morning and from the other side in the afternoon or that are partially illuminated from the interior of the building via reflections, artificial illumination, etc..

One the other hand, the thickness and bandgap tunability of thin film PV technologies combined with a transparent back electrode enable the fabrication of semi-transparent devices. In the case of absorber thickness, by making it sufficiently low, only a portion of the incident light is absorbed and used for power generation while the rest is transmitted (Figure 88, b). Similarly, by employing very wide bandgap or IR selective materials, most of the light absorption for power generation can be shifted to non-visible UV or IR spectral regions, respectively, allowing visible radiation to traverse the device resulting in very transparent devices (Figure 88, c). By precise tuning of the thickness and/or bandgap of the devices, different degrees of transparency and even different colours can be obtained. Such semi-transparent devices have direct application as BIPV solar glazing (see section 4.1.1). In addition, wide-bandgap semi-transparent devices can be employed as top cells for tandem solar cell concepts (Figure 88, d).

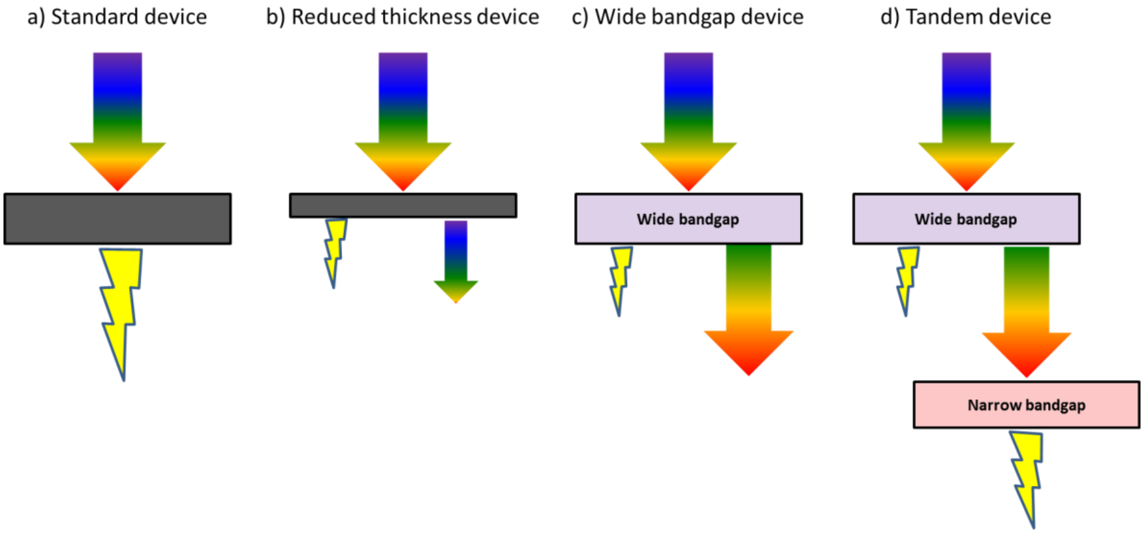

Figure 88. Schematic of light absorption and transmission of different concepts of semi-transparent solar cells.

These advanced applications have the potential to push thin film photovoltaics towards higher power densities (bifacial and tandem devices) and lower costs by building integration (bifacial and semi-transparent devices) and are likely to play an important role in the future mass deployment of PV. Since kesterite solar cells are composed only by Earth-abundant and low toxicity elements, they are particularly well-suited for such applications. Thus, the development of this technology onto transparent substrates is of great importance.

The most adequate family of materials that can substitute opaque Mo back contacts in kesterite solar cells is the same one currently employed at the front side: TCOs. These are metallic oxides that possess both very high (degenerate) doping levels ($\geq 10^{20}$ cm^{-3}), which make them conductive ($\rho \sim 10^{-3}$ $\Omega \cdot cm$), and wide bandgaps (≥ 3 eV), which make them very transparent (transmittance higher than 80% in the visible range) [264]. However, the substitution of Mo by these materials is not straightforward for kesterites solar cells since the conductivity of p-doped TCOs is typically 2-3 orders of magnitude lower than that of n-doped TCOs making the latter the only acceptable option for their use as back contacts [265]. Thus, a barrier behaviour and/or the formation of a detrimental second diode at the back p-Kesterite/n-TCO interface can be expected. Despite this non-optimum compatibility, the substitution of Mo by transparent oxides has been successfully demonstrated for CIGS and efficient solar cells have been fabricated on the most commonly employed TCOs in thin film PV: SnO_2:In_2O_3 (ITO), Al-doped ZnO (AZO) and fluorine-doped SnO_2 (FTO) [266,267].

The best performance for CIGS solar cells developed on transparent substrates has been obtained on a SLG/ITO transparent substrate with a 15.2% record efficiency achieved by Nakada et al. in 2004 [266]. However, ITO presents two major drawbacks for its use as back contact on kesterite devices. Firstly, it has been observed to be unstable at the high annealing temperatures required for the synthesis of efficient kesterite devices (~550°C) with In atoms diffusing out from the ITO contact into the kesterite absorbers [268–273]. While In-incorporation in kesterites can improve carrier concentration and avoid deep Sn-related defects [268], the loss of In greatly diminishes the conductivity of ITO either by thickness reduction [268] and/or the formation of low conductivity SnO_2 at the back [269,270,272,273]. Secondly, as in the case of CIGS, the scarcity and high demand of In will affect the production of ITO turning its use unsustainable in the long term (see last part of section 1.3.2).

Likewise, AZO has also been observed to be incompatible with high temperature processing and, as a result, the only efficient CIGS devices fabricated on SLG/AZO substrates have been achieved by working at very low temperatures (250°C) incompatible with the fabrication of kesterite devices [267,274].

On the other hand, FTO shares with ITO a high thermal resistance that has also led to the fabrication of efficient CIGS devices (~14%) while being an In-free TCO [266]. Thus, besides a higher sustainability in the long term as compared to SLG/ITO, the absence of In also renders SLG/FTO substrates a higher affinity for the fabrication of kesterite solar cells. The compatibility of this TCO with the synthesis of CZTS absorbers was first demonstrated in 2011-2012 by Sarswat et al. [275–278]. Later works not only confirmed this compatibility but also demonstrated the superiority of SLG/FTO substrates for the fabrication of kesterite devices with respect to SLG/ITO [269,271]. This way, Kim et al. fabricated CZTSe solar cells on both TCOs (ITO and FTO) by selenization of sputtered precursors and found a superior performance of the devices fabricated on FTO (4.1% on ITO vs 5.7% FTO) which was ascribed to its higher inertness during annealing [269]. In addition, Espíndola-Rodríguez et al. also reported a better performance of CZTSe solar cells on FTO (2.0%) than on ITO (1.3%) fabricated also by selenization of sputtered precursors [271]. Finally, the feasibility of fabricating wider bandgap CZTSSe and CZTS-based devices on SLG/FTO (which have a greater potential for semi-transparent applications) has also been recently demonstrated with record devices exhibiting efficiencies up to 2.6% [279] and 4.7% [280], respectively .

To sum up, the development of kesterite solar cells on transparent SLG/TCO substrates widens the range of applications of this technology towards advanced concepts like bifacial, semi-transparent and tandem solar cells which are of great importance for the future of PV. Among the different TCOs, the most promising candidate for kesterites is FTO with efficiencies just below 6% already demonstrated.

5.1.2 Improving the kesterite/TCO interface and objectives of this work

Although promising, the efficiencies shown above are well below those of the best kesterite devices fabricated on standard SLG/Mo substrates (see Table 3). This is mainly due to the complex behaviour of the p-kesterite/n-TCO interface. In particular, it has been found that this interface shows a non-ohmic behaviour that creates a barrier and hinders charge extraction [268,269]. Thus, interface engineering deems mandatory in order to reduce the efficiency gap and enable the fabrication of efficient devices on SLG/TCO transparent substrates.

One of the main differences between employing TCO-based or standard Mo back contacts for kesterite solar cells is that for the latter a $Mo(S_xSe_{1-x})_2$ buffer layer is formed at the back interface during absorber synthesis. This layer has been widely observed to assist on the formation of an ohmic contact at the back interface both in CIGS and kesterite devices [147,281–284]. Thus, forming a $Mo(S_xSe_{1-x})_2$ layer as a buffer between the absorber and TCO-based back contacts could be an interesting approach in order to improve the ohmicity of the back interface for semi-transparent devices. This idea has been successfully applied both in CIGS and kesterite technologies by depositing a thin Mo layer on top of the TCO [271,273,279,285,286]. In the case of CIGS, Abou-Ras et al. found that the performance of devices fabricated on SLG/ITO substrates was impressively improved from 2% to 11.8% efficiency by depositing (and pre-selenizing) a thin Mo layer on top of ITO before CIGS deposition [285]. Likewise, Rostan et al. observed that the rectifying behaviour of the CIGS/AZO interface became ohmic when a thin layer of Mo was deposited on top of the AZO contact [286]. As for kesterites, Kim et al. reported an improvement of CZTSe solar cells fabricated on ITO with the inclusion of a thin Mo interlayer that improved the interface and also alleviated the aforementioned In-related detrimental effects caused by this TCO on kesterite devices [273]. In addition, Espíndola-Rodríguez et al. observed an important performance enhancement of CZTSe and CZTSSe devices fabricated on SLG/FTO when a 20 nm Mo layer was deposited onto the substrate shifting from efficiencies around 2% for CZTSe and 2.5% for CZTSSe on the bare FTO up to 5% and 6.3%, respectively, on the Mo-containing substrate configuration [271,279]. Interestingly, the performance of such devices was furthered increased to 6.2% (CZTSe) and 6.8% (CZTSSe) by substituting Mo by a Mo:Na layer which was attributed to the fact that FTO may act as a barrier for Na diffusion from SLG [279].

Another possible way of enhancing the kesterite/TCO interface is through the use of hole-selective interlayers that may improve charge collection. In this regard, thin layers of transition metal oxides (TMOs) have been employed as hole injectors and hole extractors for a long time in organic electronics due to their high work function and the possibility of low temperature deposition [287,288]. In addition, TMOs also feature a high optical transparency. Thus, on paper, TMOs possess the right properties to improve the back interface of kesterite devices fabricated on TCO-based transparent substrates. The idea of using TMOs as hole extractors in inorganic PV has already been successfully tested on CdTe [289], CIGS [290], kesterite [147,291–293] and, more extensively, on c-Si solar cells [294–298]. For the latter both MoO_3

and V_2O_5 have been shown to be a promising alternative to a-Si:H and B p-doping for hole extraction in n-type c-Si devices [295,297].

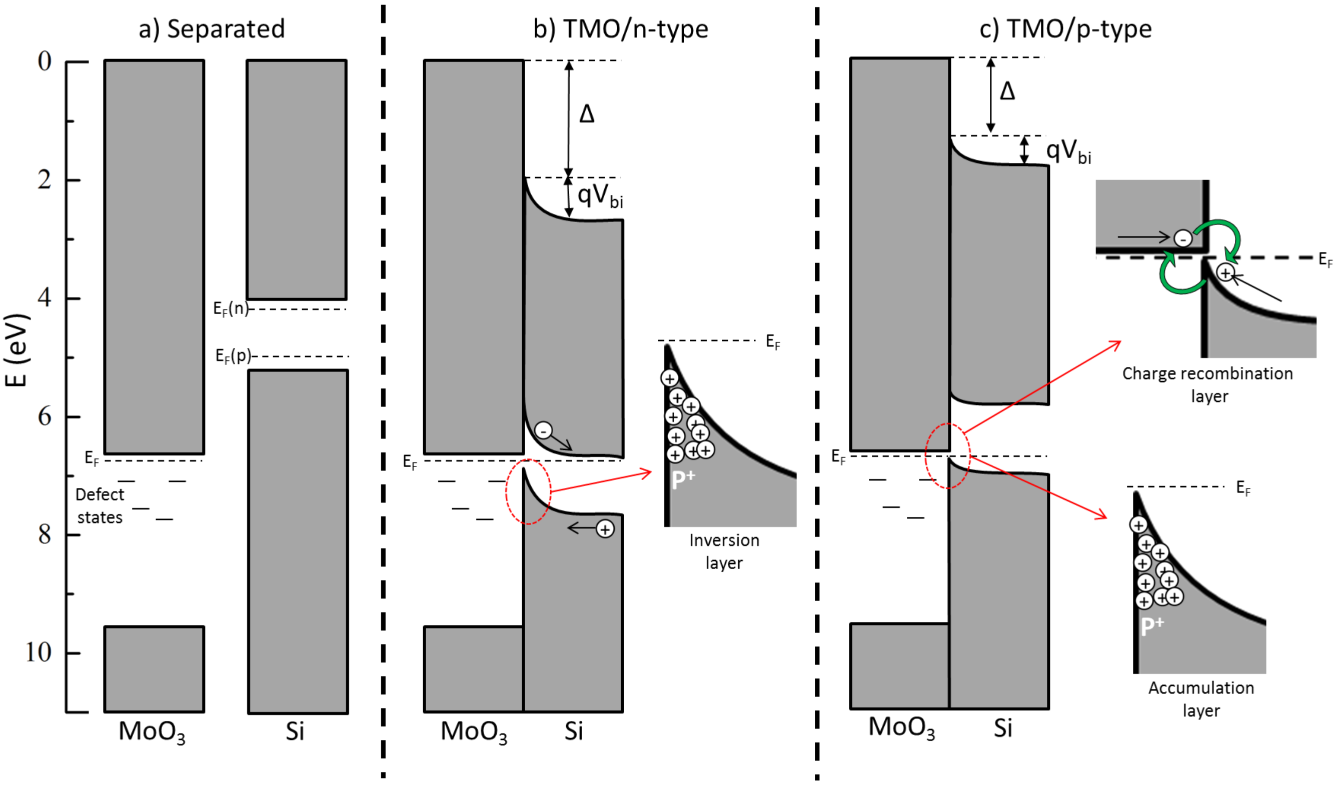

Figure 89. Band diagram of TMO/c-Si before junction (a) and for junctions with n-type (b) and p-type (c) c-Si. The band positions of Si and MoO_3 were taken from [297]. The position of the Fermi levels is arbitrary.

The success of employing TMOs at ITO-based transparent anodes in organic photovoltaics (OPV) and c-Si technologies to facilitate hole extraction lies at their high work function (ϕ) and is schematically represented in Figure 89 (the figure depicts the case of a MoO_3/c-Si junction for illustration but the behaviour shown is equivalent for other materials). More specifically, the large work function difference between the absorber and the TMO (ϕ_{TMO}-ϕ_{abs}) causes an electron flow from the valence band of the absorber into the lower energy levels present in the TMO (Figure 89a). This, in turn, depletes the surface of the absorber of electrons producing a large band bending and a built-in voltage (V_{bi}). In the case of OPV absorbers, it has been proposed that, due to the favourable alignment of the highest occupied molecular orbital (HOMO) of the absorber and the conduction band of the TMO, hole extraction occurs through the latter [287,299,300]. Thus, the electron-depleted surface of the absorber becomes a charge recombination layer in which holes from the absorber recombine with electrons from the TMO transforming a hole current into an electron current and allowing efficient charge extraction. In the case of c-Si, the proposed mechanisms are very similar. In n-type c-Si, extreme band bending changes the conductivity of the surface from n to p^+ forming an inversion layer which facilitates hole extraction in a similar fashion to traditional surface p-doping [295–298] (Figure 89b). In p-type c-Si, both the formation of a p^+ accumulation layer [298] and a favourable alignment of the valence band of the absorber and the conduction band of the TMO (similar to the case of OPV) [295] have been proposed as possible explanations for the enhanced hole extraction (Figure 89c). Additional beneficial effects of the TMOs like the upward bending of the conduction band acting as a barrier for electrons and surface passivation have also been reported [295–298]. Finally, it is worth mentioning that both in OPV and c-Si, defect states in oxygen deficient TMOs and the creation of a dipole (Δ) at the absorber/TMO interface are thought to play a crucial role in facilitating carrier transport towards the ITO contact [287,296].

TMOs and their hole-extraction mechanism have not been so thoroughly studied for other PV technologies but, as mentioned above, positive results have already been achieved. The most relevant results in the case of CIGS devices fabricated on a transparent substrate were obtained by Simchi et al. who showed that the addition of 10 nm of MoO_3 can reduce the barrier at the CIGS/ITO interface allowing the efficiency of the devices to rise from 8% to 11.9% [290]. As for kesterites, only the combination of TMOs with opaque back contacts has been reported. In this regard, a 92 mV V_{oc} improvement was achieved on a high-efficiency (>11%) CZTSSe device by exfoliating it from its SLG/Mo substrate and depositing a new MoO_3 (20 nm)/Au (100nm) back contact onto it [291]. Similarly, Ranjbar et al. used a thin (10 nm) MoO_3 layer on top of Mo which increased significantly the minority carrier lifetime and V_{oc} of the devices although no changes in the CZTSe/Mo band alignment were found [292]. Liu et al. found similar effects on Cd-doped CZTS although, in this case, they attributed them to a change in band alignment that was enhancing electron back reflection [293]. Finally, López-Marino et al. used a thin (20 nm) MoO_2 interlayer within a trilayer Mo configuration as a selenization barrier in CZTSe devices and observed both a change in $MoSe_2$ preferred growth orientation and a 67 mV increase of the V_{oc} leading to a remarkable final value of 460 mV [147].

However, besides these few publications, there is a clear lack of research exploring the potential of Mo nanolayers and TMOs as hole-selective layers to enhance the performance of kesterite PV devices fabricated on transparent substrates. The work presented here aims to contribute in filling this gap. The effect of adding thin interlayers (5-20 nm) of a wide selection of TMOs (MoO_3, MoO_2, V_2O_5, TiO_2, NiO, Co_3O_4 and CuO) and their combination with Mo-based nanolayers are empirically screened as an approach to improve the back interface of CZTSe, CZTS and CZTSSe solar cells fabricated on SLG/FTO transparent substrates. The work is divided in four main parts:

i. First, the optical and electrical properties as well as the stability of the different SLG/FTO/TMO substrate configurations are evaluated before and after a thermal reactive annealing similar to that employed for the synthesis of CZTSe absorbers.
ii. Then, CZTSe solar cells are fabricated onto the different substrate configurations in order to study their suitability for enhancing the FTO/kesterite interface based on their performance. The addition of a Mo:Na layer on top of the TMOs is also investigated.
iii. The three best performing TMOs are further studied on CZTSe devices to determine the most adequate configuration.
iv. Finally, the best substrate configurations for CZTSe are applied to wide bandgap CZTSSe and CZTS solar cells. This is accompanied by a morphological, structural and in-depth compositional characterisation of the best devices.

5.2 Experimental

5.2.1 Substrate description

The substrate configurations studied in this work were fabricated on commercial FTO-coated SLG. Two slightly different (but comparable) SLG/FTO commercial substrates were employed. In the first part of the work (Series A), where an initial screening of the different TMOs is carried out, a 1.6 mm thick SLG/FTO substrate (15 Ω/□, Kaivo) was used. For the rest of the work, where only a small selection of TMOs is studied, a 2.2 mm SLG/FTO substrate (7 Ω/□, Sigma-Aldrich) was utilised.

Table 18. Main optoelectronic properties of the TMOs employed in this work.

	Semiconductor type	Ionization Energy (eV)	Bandgap (eV)	Work function (eV)	Reference
MoO_3	n	9.4	3.0	6.9	[299]
V_2O_5	n	9.26	2.8	6.85	[301]
TiO_2	n	8.0	3.4	5.2	[302]
NiO	p	6.7	3.2	6.3	[303]
Co_3O_4	p	6.4	1.6	6.1	[304]
CuO	p	5.7	1.4	5.6	[303]
MoO_2	metallic	6.0	-	6.0	[305]

The SLG/FTO substrates were coated with different thicknesses (5, 10 and 20 nm) of a wide selection of TMOs and, additionally, also with a 20 nm Mo:Na layer (both substrate configurations with and without Mo:Na were investigated). Due to the complex nature of the p-kesterite/n-FTO interface, n-type (MoO_3, V_2O_5 and TiO_2), p-type (NiO, Co_3O_4 and CuO) and metallic (MoO_2) TMOs were studied. The main optoelectronic properties of these oxides are summarized in Table 18. Nevertheless, it should be noted that the properties of the TMOs are known to be strongly related to their oxidation state which is heavily influenced by the deposition conditions and air exposure [295,306]. Finally, it should be born in mind that evaporated TMOs are rarely stoichiometric and are usually denoted in the literature as MoO_x, V_2O_x, etc. [287]. However, they will be designated with their stoichiometric formulation throughout this work.

For a more detailed description of the deposition of the TMO and Mo:Na layers, see section 2.3.2.

5.2.2 Sample preparation

The substrate configurations employed and the general preparation of the samples was different in each part of the work. For the sake of clarity, the different set of samples have been named as series A, B and C. Below, the general procedure follow for their fabrication as well as the particularities of each series are detailed. However, for a more detailed description of the fabrication process, see sections 2.2.3 and 2.3.

General procedure

Cu/Sn/Cu/Zn metallic precursor stacks with Cu-poor Zn-rich composition were deposited on the different substrate configurations. The precursors were submitted to a 2-step thermal reactive annealing to synthesise kesterite absorbers. The as-annealed absorbers were then subjected to a chemical etching in $(NH_4)_2S$ in order to remove surface secondary phases. Then, the devices were completed with a CdS buffer layer as well as a i-ZnO (50 nm)/ITO (200 nm) bilayer (50-80 Ω/□).

Series A: Screening of TMOs as back contact buffers in CZTSe solar cells

The SLG/FTO commercial substrates (Kaivo) were coated with 0, 5, 10 and 20 nm of MoO_3, V_2O_5, TiO_2, NiO, Co_3O_4, CuO or MoO_2. Then, either 10 nm of NaF or 20 nm of Mo:Na were deposited on top of the different substrate configurations prior to the deposition of the metallic precursor stacks. The precursors were submitted to a reactive annealing under Se+Sn atmosphere in order to synthesise CZTSe absorbers.

Series B: Repetition of the best performing TMOs with optimised device configurations

The SLG/FTO commercial substrates (Sigma-Aldrich) were coated with 0, 5, 10 and 20 nm of V_2O_5 or TiO_2 followed by a 20 nm Mo:Na layer. Prior to the reactive annealing, a 10 nm Ge nanolayer was deposited on top of the metallic precursor stacks. The precursors were submitted to a reactive annealing under Se+Sn atmosphere in order to synthesise CZTSe absorbers. The completion of the devices with CdS/i-ZnO/ITO was followed by the deposition of an Ag metallic grid and a MgF_2 anti-reflective coating.

Series C: Technology transfer to wide-bandgap CZTS and CZTSSe

The SLG/FTO commercial substrates (Sigma-Aldrich) were coated with 0 and 10 nm of V_2O_5 or TiO_2 followed by a 20 nm Mo:Na layer. Prior to the reactive annealing, a 10 nm Ge nanolayer was deposited on top of the metallic precursor stacks. The precursors were submitted to a reactive annealing under S+Sn or S+Se+Sn atmosphere to synthesise CZTS and CZTSSe absorbers, respectively. The completion of the devices with CdS/i-ZnO/ITO was followed by the deposition of an Ag metallic grid and a MgF_2 anti-reflective coating.

5.2.3 Characterisation

The transmittance of the different substrate configurations was investigated using UV-vis-NIR spectroscopy before and after being submitted to a selenization process identical to the one employed for the synthesis of the CZTSe absorbers. The analysis was carried out from 300 to 1500 nm. The average transmittance was estimated by integrating the spectra in different spectral regions and calculating the mean value. In order to evaluate the transparency of the substrates, the visible region was defined from 435 to 670 nm following the work by Lunt et al. [307]. In addition, the different TMOs were deposited (20 nm) onto a quartz substrate to avoid the near-UV absorption of SLG and enable the calculation of their bandgap from the inflexion points of their transmittance spectra. In this case, the spectra were acquired from 200 to 1500 nm. The sheet resistance of the different substrate configurations was measured using a 4pp system.

The J-V characteristics of the devices were obtained under simulated AM1.5 illumination (1000 W/m^2 intensity at room temperature) using a pre-calibrated solar simulator. The EQE was measured using a spectral response system.

Raman scattering measurements were made under a 785 nm excitation wavelength on complete devices. The measurements were performed both at the front and the back side of the samples. A diameter of 50 µm and an excitation power density of about 1 kW/cm^2 were used in order to inhibit thermal effects in the spectra while light collection was made through a x20 objective. A 785 nm excitation wavelength was employed due to its low interaction with the SLG/FTO substrate (for back measurements) and the upper window layer (for front measurements) that allows to characterize the absorber without exfoliating it from the substrate or removing the CdS/ZnO/ITO layers, respectively [220].

FESEM secondary electron imaging was employed to examine the structure and morphology of the full devices in cross-section configuration using an acceleration voltage of 5 kV and working distances of around 5 mm.

The elemental depth profiles of the full kesterite solar cells were measured by TOF-SIMS with a magnetic sector Cameca 7f microprobe. The analysis was made with a Cs^+ primary beam. The elements are measured as M+Cs cluster ions, where M is the element to be analysed. Additional measurements were performed in O_2^+ positive mode in order to obtain a clearer signal of Ti.

For more information about the main characterisation techniques employed, see section 2.2.

5.3 Results

5.3.1 Properties of the TMOs

The most interesting properties of the different TMOs for the fabrication of bifacial or semi-transparent devices, viz. transparency and conductivity, were evaluated by analysing the transmittance spectra and sheet resistance of the SLG/FTO substrates coated with different TMO thicknesses. This analysis was carried out both before and after submitting the substrates to an annealing process identical to that employed for the synthesis of CZTSe solar cells. In addition, the bandgap of the different TMOs was also evaluated.

As deposited

Transmittance

Figure 90 (a-g) shows the transmittance spectra of the SLG/FTO substrates coated with 5, 10 and 20 nm of the different TMOs. In addition, Table 20 (in page 118) shows the average transmission values extracted from them in the UV, visible and IR regions.

All the substrate configurations with 5 and 10 nm TMO layers show similar transmittance levels in the visible of around 70%. Taking into account that the SLG/FTO reference has a ~75% transmission in that range, the optical losses due to the TMOs represent less than a 10% (relative). This result is surprising since the reported bandgaps of some of the oxides studied are quite narrow (see Table 18) so higher above-bandgap absorption was expected. As will be presented in the following subsection, this is due to the fact that the evaporated TMO nanolayers exhibit much larger bandgaps than the bulk materials. As expected, increasing the thickness of the TMO layers to 20 nm leads to lower transmission levels in general. However, in this case, the different TMOs show dissimilar behaviours. NiO leads to the lowest transmittances in the visible and in the infrared. On the contrary, the most hindered transmittance in the UV region is found for V_2O_5. Interestingly, increasing the thickness of TiO_2 from 5 to 20 nm does not have any detectable influence on its transparency in the whole spectral range. As for MoO_3, increasing its thickness only reduces transmittance slightly in the UV and IR regions while leaving the visible region unaffected. The rest of the TMOs show varying transmission reductions in the different spectral regions when shifting from 5 to 20 nm layers although these are moderate and remain below 8% (absolute) in all cases. Thus, overall, it can be concluded that all the TMOs studied have a minor effect on substrate transparency in the range of thicknesses studied.

The high transparency of the different TMOs studied is further confirmed by Figure 90 (h) and Table 19 which show the transmittance of 20 nm layers of the different oxides deposited directly on quartz and subtracting the effect of the substrate. Most of the TMOs exhibit transmittance levels >75% in the visible and ≥90% in the IR.

Table 19. Average transmittance of the different TMOs deposited on quartz without the effect of the substrate. Values calculated from Figure 90 (h).

	T_{avg} (%)		
	300-435 nm	**435-670 nm**	**670-1500 nm**
MoO_3	59.8	80.5	90.8
V_2O_5	49.8	82.0	91.3
TiO_2	80.8	93.0	96.6
NiO	60.8	71.3	84.2
Co_3O_4	61.1	75.9	89.9
MoO_2	56.4	78.0	82.5
CuO	70.0	88.6	95.5

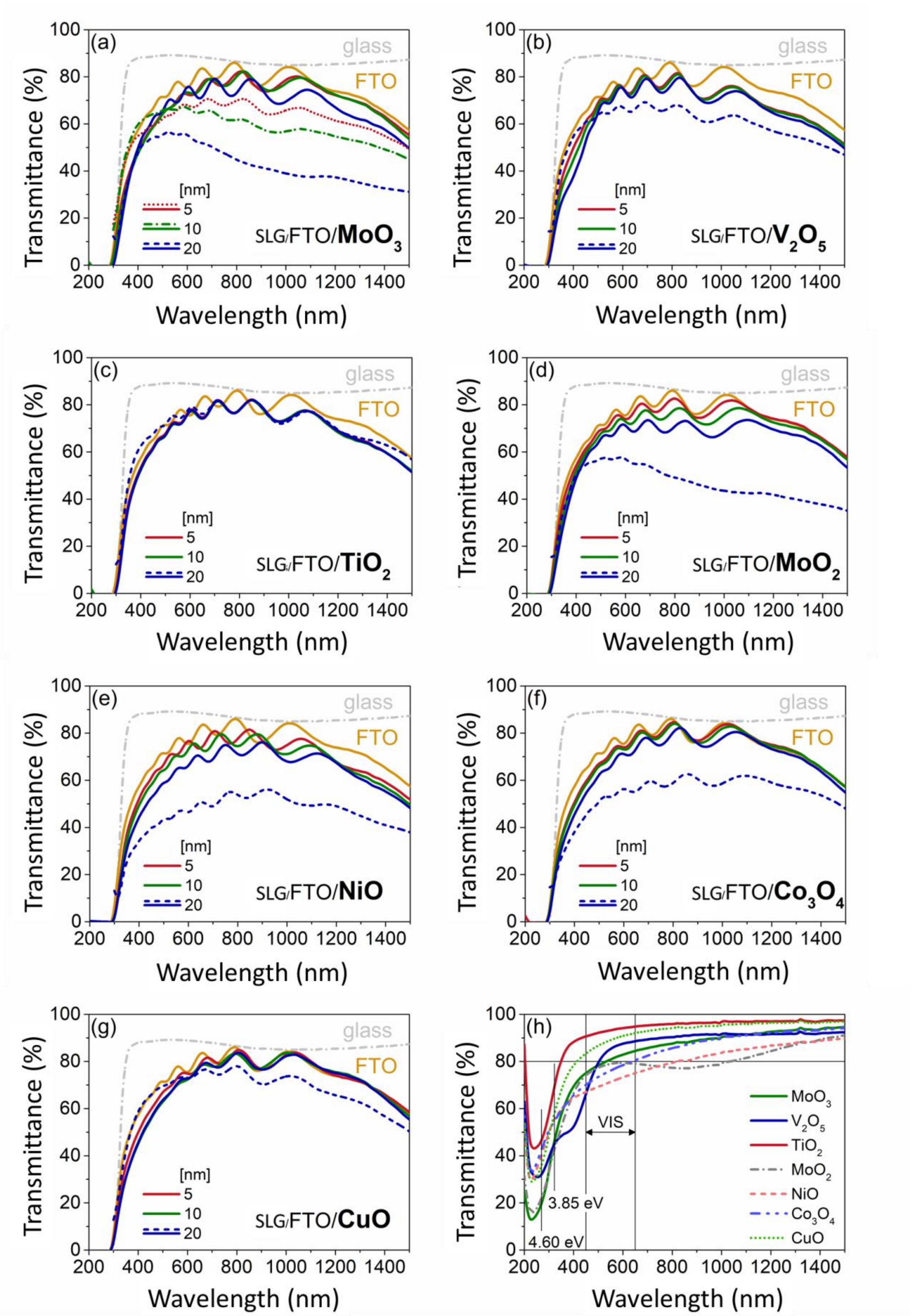

Figure 90. Total transmittance before (solid line) and after (dashed line) selenization of the SLG/FTO substrates coated with 5, 10 and 20 nm of (a) MoO$_3$, (b) V$_2$O$_5$, (c) TiO$_2$, (d) MoO$_2$, (e) NiO, (f) Co$_3$O$_4$ (g) CuO. (h) Total transmittance of as deposited TMOs (20 nm) (without the effect of the substrate).

Bandgap

The bandgap of the different TMOs was calculated from Figure 90 (h) by locating the inflection points of the transmittance spectra. The results are plotted in Figure 91.

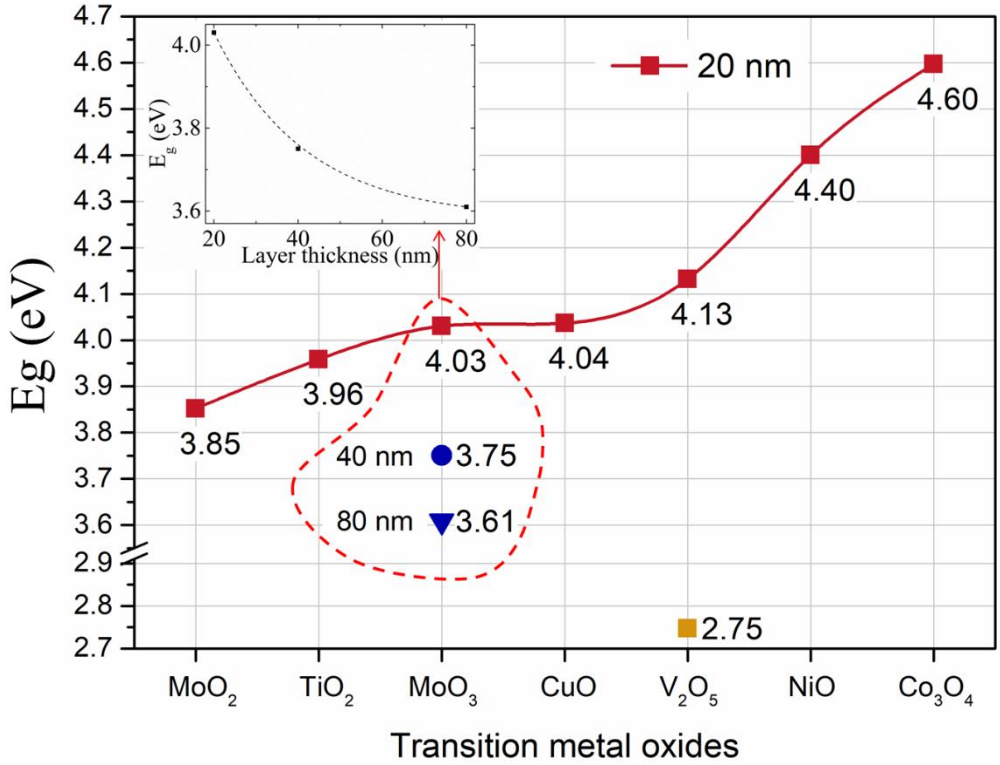

Figure 91. Optical band gap of the different TMOs (ordered from lowest to highest) as obtained from the transmittance spectra shown in Figure 90 (h) for 20 nm (squares), 40 nm (circles) and 80 nm (tringles) thicknesses. Inset: logarithmic decrease of the bandgap of MoO_3 with the increasing thickness.

All the TMOs show very wide bandgaps ranging from 3.85 eV (MoO_2) to 4.60 eV (Co_3O_4). Comparing these values with the literature (see Table 18), it can be observed that the values presented here are much higher, in general. This can be attributed to the small crystallite size and/or the amorphous nature of the nanometric layers deposited in this work (expectable since the deposition was carried out at room temperature). It has been reported that the bandgap of nanometric semiconductor crystallites follows a logarithmic trend with the increasing grain size due to quantum confinement effects [308–311]. In order to confirm this possible cause for the high bandgaps observed, the bandgap of MoO_3 was investigated for different layer thicknesses (20, 40 and 80 nm) (inset of Figure 91). In effect, the bandgap is found to decrease approximately logarithmically with the increasing layer thickness and to approach the bulk values reported in the literature for the 80 nm layer. It should also be taken into account that the evaporated oxides are likely to be very defective. This may generate a very low correlation distance (even below crystallite size) of their crystal structure which can further increase quantum confinement effects [312]. In addition, the modification of the band structure that follows quantum confinement can result in different allowed transitions compared to bulk materials that can shift the bandgap from a narrow indirect to wide direct one. The extremely large bandgap shifts observed for CuO and Co_3O_4 with respect to the values reported in Table 18 (+2.6 eV for CuO and +3 eV for Co_3O_4) fit with this explanation. In the case of CuO, this is supported by experimental observations made in the field of nanoparticle synthesis. Lim et al. observed the coexistence of both an indirect (1.4 eV) and a direct (3.1 eV) bandgap when analysing the optical properties of 80 nm CuO nanoparticles [313]. In addition, Arun et al. reported a direct 4.2 eV bandgap for 20 nm CuO nanoparticles [314]. These results fit with the bandgap observed in this work for CuO and give further prove of the small crystallite size of the evaporated layers. On the other hand, no information about such a wide direct bandgap for Co_3O_4 nanoparticles has been found in the literature. However, He et al. reported a 4.0 eV bandgap for 33 nm CoO nanoparticles [315]. Thus, it may be possible that, apart from quantum confinement, the oxidation state of Co_3O_4 powder changed during evaporation which could explain the high bandgap observed for this TMO. In the case of V_2O_5, two clear inflexion points are observed corresponding to a 2.75 eV (similar to bulk values) and a 4.13 eV bandgap. Following the same reasoning, this could be due to a crystallite size in which both an indirect and a direct bandgap coexist as in the case of 80 nm CuO nanoparticles [313]. Finally, the fact that a clear bandgap is observed for MoO_2, which should be metallic, and its similarity to that of MoO_3 indicates that the oxidation state of this TMO changed during evaporation to MoO_{3-x} rather than remaining as MoO_2.

After annealing

Transmittance

After being submitted to a selenization annealing process, the transmittance of most substrate configurations (with 20 nm TMO layers) is widely reduced in the visible and, specially, in the IR regions (see Figure 90 and Table 20).

Table 20. Average transmittance of the SLG/FTO substrates coated with 5, 10 and 20 nm of the different TMOs calculated from Figure 90 (a-g). The values in red were measured after submitting the substrates to a selenization annealing process.

	T_{avg} (%)											
	300-435 nm				435-670 nm				670-1500 nm			
	5 nm	10 nm	20 nm		5 nm	10 nm	20 nm		5 nm	10 nm	20 nm	
MoO_3	36.6	34.9	34.0	34.8	68.1	67.8	68.9	54.5	73.1	72.9	68.3	39.0
V_2O_5	37.0	33.2	28.2	41.9	70.8	69.6	67.5	64.6	69.7	69.2	67.9	59.7
TiO_2	39.6	38.2	38.4	47.5	71.4	70.7	70.9	74.2	71.3	71.0	71.1	72.0
NiO	38.6	36.1	32.6	26.4	70.3	68.3	62.7	45.2	70.6	69.1	66.4	48.8
Co_3O_4	39.0	38.0	34.5	30.4	70.8	69.5	65.9	52.6	75.7	75.2	73.3	58.0
MoO_2	41.7	38.2	34.6	38.5	72.0	69.6	66.9	56.3	74.6	72.3	68.1	43.5
CuO	38.0	33.7	33.8	45.0	70.6	67.8	68.2	71.3	75.8	75.5	75.1	67.8
SLG/FTO	45.4				74.6				75.6			

NiO is the TMO which exhibits the most degraded transmittance in the UV and visible ranges. Co_3O_4 shows a similar degradation profile to NiO although to a lesser extent. Likewise, the transparency of MoO_3 and MoO_2 is harshly reduced in the visible and, even more intensely, in the IR. These severe reductions in transmittance can be attributed to the formation of low bandgap selenide compounds like Ni_3Se_2 (Eg~1.4 eV, [316]), CoSe (Eg~1.5 eV, [317]) and $MoSe_2$ (Eg~1.1 eV, [318]) which strongly absorb radiation in the spectral range studied. A different behaviour can be observed for V_2O_5. Although it shows a degraded transmittance in the IR, it maintains a high transparency in the visible region and even exhibits a significant improvement in the UV. Interestingly, CuO and TiO_2 show almost no degradation after annealing. In the case of CuO, its transmittance is only slightly reduced in the IR region. As for TiO_2, not only it does not degrade but it experiences an overall improvement in its transmittance.

Sheet resistance

The sheet resistance of the different configurations seemed to be independent from the TMO employed and did not vary noticeably with respect to the reference SLG/FTO substrate (R_{sheet}~15 Ω/□). After the annealing process, all the substrate configurations with and without TMO layer showed a slightly improved conductivity with R_{sheet} decreasing to ~9 Ω/□.

Summary

The optical and electrical properties of the different SLG/FTO/TMO configurations studied seem compatible with the use of such substrates as back contacts in semi-transparent and bifacial devices. Very wide bandgaps are observed in every TMO which can be attributed to quantum confinement effects. The transmittance of some of the TMOs is, though, reduced after being submitted to a selenization process partly due to the formation of TMO-selenide species while their conductivity is not degraded at all. However, it should be taken into account that the post-selenization results should be only interpreted as illustrative since in "real conditions" the TMOs will be coated with a CZT metallic precursor which may change the way they react to the annealing process.

5.3.2 Series A: Screening of TMOs as back contact buffers in CZTSe solar cells

In order to empirically evaluate the suitability of the different TMOs for their use at the back contact, CZTSe solar cells were fabricated on every substrate configuration studied above and their performance was analysed and compared. Due to the elevated number of samples and for the sake of clarity, the analysis was carried out taking into consideration only the main optoelectronic parameters of the record solar cell obtained with each substrate configuration which can be considered as representative of the whole samples.

Bare TMOs

In a first attempt, CZTSe solar cells were fabricated directly on the different SLG/FTO/TMO substrate configurations. In order to compensate the possible Na-blocking behaviour of FTO [279] and/or the TMOs, 10 nm of NaF were deposited onto the substrates prior to the deposition of the CZT metallic precursor stack. The J-V curves and parameters of the best devices found in each substrate configuration are shown in Figure 92 and Table 21 (left), respectively.

The reference sample fabricated directly on SLG/FTO exhibits a low efficiency (2.9%) but also shows some interesting features. The CZTSe/FTO interface does not present a severe current blocking behaviour as can be deduced from the J_{sc}, FF and the shape of the J-V curve which suggest that the R_s of the device is not a critical factor. However, the slope of the curve near the V = 0 axis and the low V_{oc} (255 mV) could be pointing towards a low R_{sh} as the possible main limitation of the device. Similar observations with a very low R_{sh} as the main limiting factor were made by Espíndola-Rodríguez et al. [271,279] but differ from other works in which R_{sh} was not a clear limitation [269].

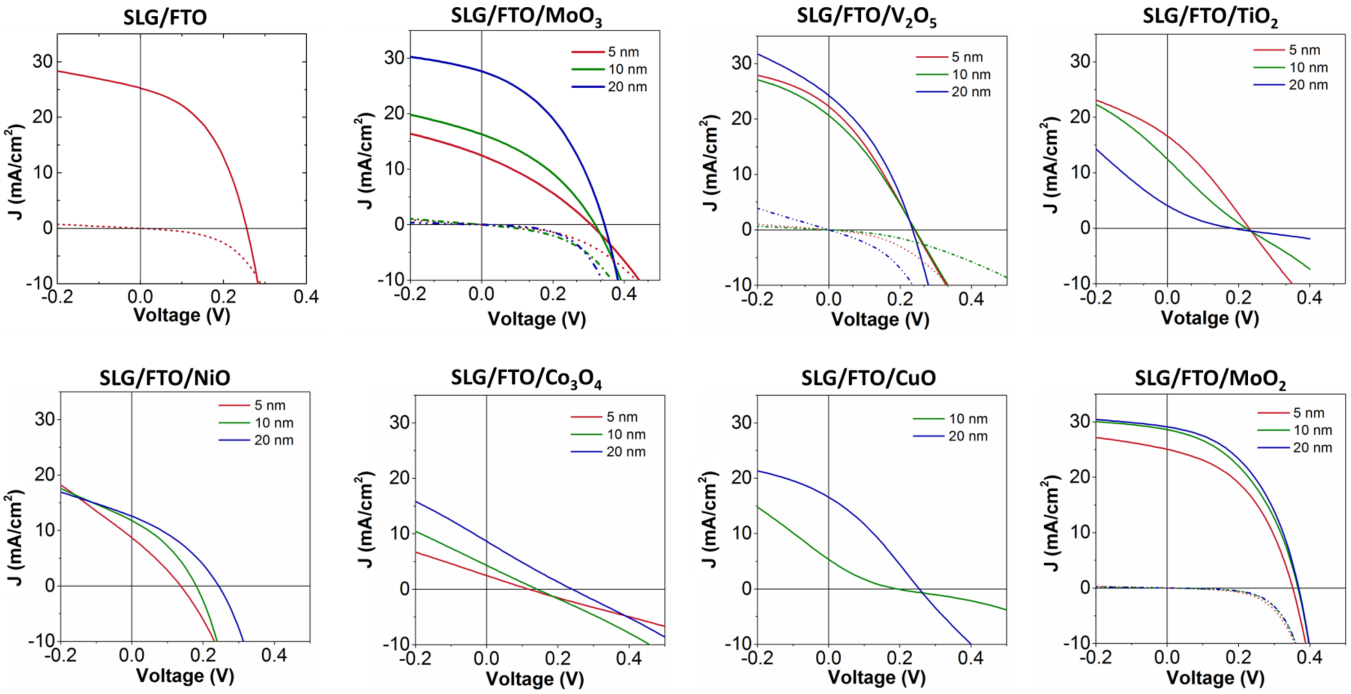

Figure 92. J-V curves of the record CZTSe devices obtained with each SLG/FTO/TMO substrate configuration. In some cases, the dark J-V curves are also shown as dashed lines.

The addition of TMOs does not lead to any improvement and, what is more, proves to be very detrimental except for MoO_3 and MoO_2. Some similarities can be detected between the TMOs that were observed to get selenized during the annealing process (MoO_3, MoO_2, Co_3O_4 and NiO) and the TMOs which seemed mostly unaffected by it (V_2O_5, TiO_2 and CuO).

With regard to the latter group, V_2O_5 is the less degrading oxide. It is found to lower principally the J_{sc} and FF of the devices due to a higher R_s. As for TiO_2 and CuO, they produce a strong current blockage that completely distorts the J-V curves of the devices into S-shaped curves. However, while for TiO_2 the degradation is more acute as the layer thickness is increased, the opposite is observed for CuO.

Regarding the Se-reacting TMOs, the most damaging one is found to be Co_3O_4. The formation of a Co_xSe_y interlayer leads to an extremely high series resistance that totally degrades the J-V curves of the devices. The degradation is stronger as the thickness of the TMO (and, consequently, of the associated Co_xSe_y layer) is reduced. NiO also shows a current blocking behaviour although less severe than in the case of Co_3O_4 attributable as well to the formation of a Ni_xSe_y interlayer. As for MoO_3, although it also presents a high R_s for 5 and 10 nm layers, it leads to a highly enhanced V_{oc} compared to the SLG/FTO reference. This suggests that, in this case, the formation of $MoSe_2$ creates a more favourable back interface which is in consonance with previous works (see references in section 5.1.2). All the optoelectronic parameters rise with the increasing MoO_3 (and, thus, $MoSe_2$) layer thickness. With a 20 nm TMO layer, the current blocking behaviour vanishes resulting in greatly increased J_{sc} which combined with the high V_{oc} (344 mV) translates into a 3.8% efficiency, significantly higher than that of the

SLG/FTO reference. In the case of MoO_2 all the solar cell parameters are also enhanced with the increasing TMO thickness. However, contrarily to MoO_3, it does not produce any current blocking behaviour at low layer thickness. In addition, the MoO_2-containing devices show as well superior V_{oc} (351- 368 mV) and FF (44.5-45.9%) that boost the efficiency of the devices up to 4.9% with a 20 nm TMO layer. The difference observed between MoO_3 and MoO_2 is surprising due to their similarity since MoO_2 was found to be deposited as MoO_{3-x} (see bandgap subsection in page 117). However, the fact that the effect of 20 nm of MoO_3 resembles that of 5 nm of MoO_2 could indicate that this difference may be due simply to a thickness underestimation of the latter oxide. The evaporation of MoO_2 was difficult to control so such a misestimation is possible.

Table 21. Solar cell parameters of the record devices obtained with each SLG/FTO/TMO (left) and SLG/FTO/TMO/Mo:Na (right) substrate configuration. The rows in bold correspond to devices with efficiencies above those of the reference TMO-free substrates.

Substrate configuration	TMO (nm)	J_{sc} (mA/cm^2)	V_{oc} (mV)	FF (%)	η (%)
FTO	-	25.2	255	44.4	2.9
FTO/MoO_3	5	12.3	306	31.2	1.2
	10	16.1	317	36.1	1.8
	20	**27.4**	**344**	**40.7**	**3.8**
FTO/V_2O_5	5	21.7	241	31.0	1.6
	10	20.2	242	30.8	1.5
	20	23.9	234	34.9	2.0
FTO/TiO_2	5	16.5	230	29.2	1.1
	10	12.4	223	22.2	0.6
	20	4.2	188	17.2	0.1
FTO/NiO	5	8.6	137	28.3	0.3
	10	11.7	180	34.3	0.7
	20	12.5	243	34.8	1.1
FTO/Co_3O_4	5	2.5	119	24.3	0.1
	10	4.3	142	24.6	0.2
	20	8.6	240	23.8	0.5
FTO/CuO	5	-	-	-	-
	10	5.5	202	16.6	0.2
	20	16.3	255	30.6	1.3
FTO/MoO_2	**5**	**24.9**	**351**	**44.5**	**3.9**
	10	**28.4**	**366**	**43.8**	**4.6**
	20	**29.0**	**368**	**45.9**	**4.9**

Substrate configuration	TMO (nm)	J_{sc} (mA/cm^2)	V_{oc} (mV)	FF (%)	η (%)
FTO/Mo	-	27.6	307	37.8	3.2
FTO/Mo:Na	-	26.1	328	42.2	3.6
FTO/MoO_3/Mo:Na	5	13.5	297	30.0	1.2
	10	13.1	265	27.3	0.9
	20	11.2	289	26.6	0.9
FTO/V_2O_5/Mo:Na	5	27.4	338	38.3	3.6
	10	**29.9**	**352**	**42.0**	**4.4**
	20	**30.2**	**353**	**45.0**	**4.8**
FTO/TiO_2/Mo:Na	**5**	**26.6**	**373**	**46.8**	**4.6**
	10	**27.4**	**364**	**49.3**	**4.9**
	20	**25.0**	**403**	**40.1**	**4.0**
FTO/NiO/Mo:Na	5	15.0	205	37.8	1.2
	10	10.9	254	35.8	1.0
	20	11.5	249	35.8	1.0
FTO/Co_3O_4/Mo:Na	5	22.0	351	32.3	2.5
	10	23.7	346	43.9	3.6
	20	24.3	327	40.7	3.2
FTO/CuO/Mo:Na	5	25.7	338	37.2	3.2
	10	24.3	318	40.8	3.2
	20	24.7	321	37.6	3.0
FTO/MoO_2/Mo:Na	5	13.5	304	29.5	1.2
	10	10.4	254	27.3	0.7
	20	10.0	328	25.8	0.8

Addition of Mo:Na and $MoSe_2$ formation

The performance of the devices fabricated on the bare TMOs clearly indicates that a $MoSe_2$ interlayer between the kesterite absorber and the FTO is necessary for an improved back interface. In order to confirm this result and following the work by Espíndola-Rodríguez et al. [279], CZTSe solar cells were fabricated on SLG/FTO coated with 20 nm of Mo (with no additional NaF layer) or Mo:Na. The results are shown in the first two rows of Table 21 (right) and the top left corner of Figure 93.

The addition of either Mo or Mo:Na causes analogous improvements to those observed when employing MoO_x layers with no current blocking behaviour and an improved V_{oc} arising from an improved R_{sh} compared to the SLG/FTO reference. The use of Mo:Na, though, leads to significantly higher V_{oc} and FF than just standard Mo which is consistent with the results reported by Espíndola-Rodríguez et al. and attributable to a higher Na incorporation into the absorber [279]. In general, the V_{oc} enhancement provided by $MoSe_2$ could be interpreted as a reduction of the aforementioned shunts.

In view of these positive results, CZTSe devices were fabricated on the different SLG/FTO/TMO substrate configurations with a 20 nm Mo:Na layer deposited on top. The results are shown in Table 21 (right) and Figure 93.

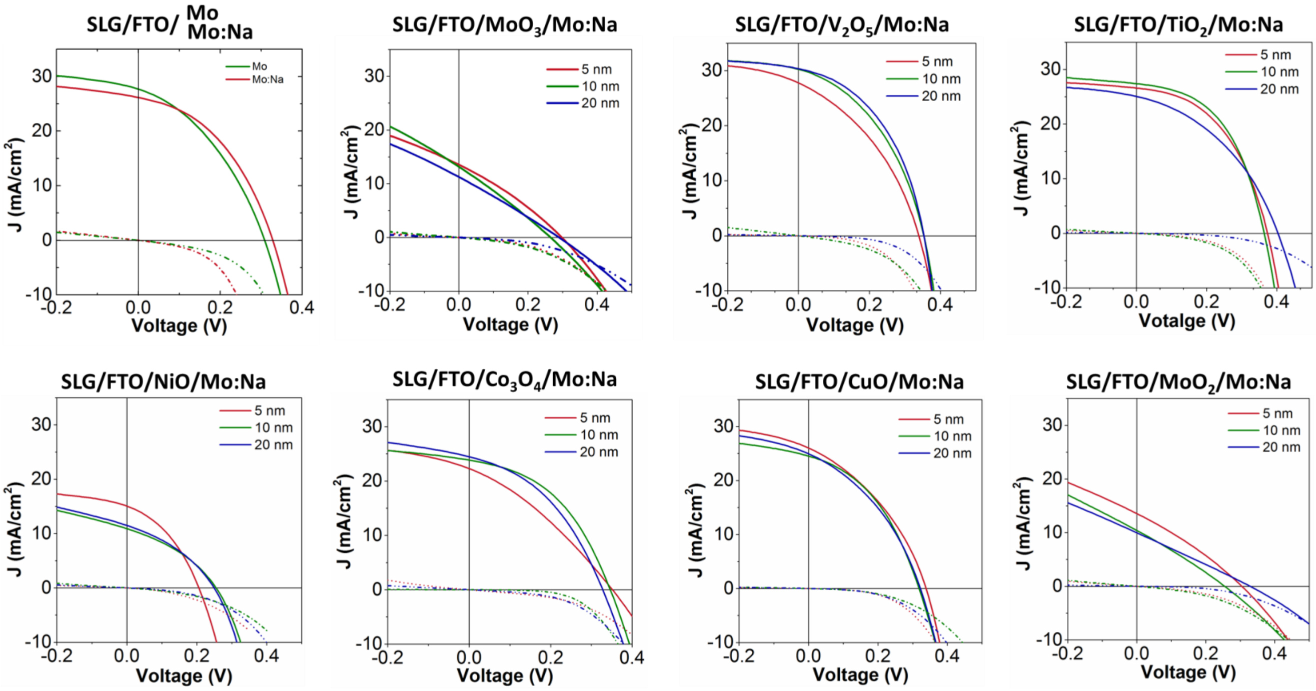

Figure 93. J-V curves of the record CZTSe devices obtained with each SLG/FTO/TMO/Mo:Na substrate configuration.

The addition of Mo:Na to the SLG/FTO/MoO_x substrate configurations results in highly degraded devices with a large series resistance as can be deduced from their low J_{sc} and FF. Regarding the other Se-reacting TMOs, Mo:Na tends to reduce the R_s and improve the V_{oc} of the devices with respect to the bare TMOs. However, despite these improvements, none of the devices surpasses the performance of the SLG/FTO/Mo:Na reference since they still present a current blocking behaviour.

As for the more Se-inert TMOs, all of them exhibit radical improvements with the addition of a 20 nm Mo:Na layer. The S-shape behaviour of some of the J-V curves observed before completely disappears. In the case of CuO, its performance is below that of the SLG/FTO/Mo:Na reference due to a lower J_{sc} and FF. On the other hand, TiO_2 and V_2O_5 lead to much higher efficiencies than employing just Mo:Na. In particular, a 10 nm TiO_2 layer results in a 4.9% efficiency device with remarkably enhanced V_{oc} (364 mV) and FF (49.3%). A thicker TiO_2 layer seems to induce a slight current blockage that hinders the overall performance. As for V_2O_5, a 20 nm layer leads to a 4.8% efficiency device with a largely enhanced J_{sc} (30.2 mA/cm^2) but also with improved V_{oc} and FF. In contrast to TiO_2, a large V_2O_5 thickness does not affect R_s

negatively. Thus, the use of V_2O_5 and TiO_2 represents a significant enhancement with respect to the SLG/FTO/Mo:Na reference (+1-1.2% efficiency increase, absolute).

Summary

The main limitation of the CZTSe/FTO interface seems to lie at the presence of shunt paths that hinder, mainly, the V_{oc} of the devices. The addition of TMOs to the interface does not reduce shunting but degrades the devices by inducing a large series resistance. A different kind of current blocking behaviour is observed for the oxides that get selenized during the CZTSe synthesis process and for those that remain mostly unchanged.

On the other hand, the formation of a $MoSe_2$ buffer interlayer has been observed to reduce shunting and increase the V_{oc} of the devices fabricated on every substrate configuration. Furthermore, the combination of $MoSe_2$ with TiO_2 and V_2O_5 has been found to greatly boost the performance of the devices.

5.3.3 Series B: Repetition of the best performing TMOs with optimised device configurations

After the positive results obtained in the initial screening (series A), the best performing substrate configurations were further studied to check the reproducibility of the results in optimised device structures that include a 10 nm Ge layer as well as a metallic grid and an anti-reflecting coating (see section 5.2.2). More specifically, the selected configurations were the following:

- SLG/FTO (reference)
- SLG/FTO/Mo:Na (reference)
- SLG/FTO/TiO_2/Mo:Na
- SLG/FTO/V_2O_5/Mo:Na

Thickness screening

The same thickness screening (5, 10 and 20 nm) was repeated for the selected substrate configurations. However, this time the optoelectronic parameters of all the devices fabricated in each substrate configuration (~16 solar cells per sample) are analysed together by means of a boxchart (Figure 94) in order to discern more global trends. In addition, Table 22 shows the main optoelectronic parameters of the record devices together with their calculated series and shunt resistances.

Compared to series A (see Table 21), it can be seen that the SLG/FTO reference presents a significantly higher maximum efficiency on the new substrate (+0.9%, absolute) due, mainly, to a superior J_{sc}. A large portion of this increase is due to the implementation of a metallic grid and an ARC layer. Likewise, the slightly higher V_{oc} can be ascribed to the addition of a 10 nm Ge layer [206]. Nevertheless, despite this moderate improvement, the V_{oc} is still the main limiting factor of the device. In addition, a low homogeneity with large FF and J_{sc} variations throughout the sample can be observed in Figure 94 which limits the average efficiency of the sample to just 2.9%. The presence of strong shunt paths speculated in the previous screening is numerically confirmed here two-fold: on the one hand, the record device exhibits a very low

R_{sh} value (60 Ω·cm^2) and, on the other hand, it also presents the lowest R_s, by far, among all the substrate configurations. These two observations together indicate that there exist channels or paths within the device through which the carriers can travel with low resistivity. However, other problems like an insufficient grain boundary passivation cannot be discarded. The addition of Mo:Na (and the resulting $MoSe_2$ layer) to the SLG/FTO substrate is also confirmed to alleviate shunting (R_{sh} and R_s increase almost 4 times and 2 times, respectively) as observed in the previous screening. This way, the V_{oc} and FF of the devices are significantly improved resulting in an enhanced 4.1% (5.0%) average (record) efficiency. In addition, the homogeneity of the sample is improved.

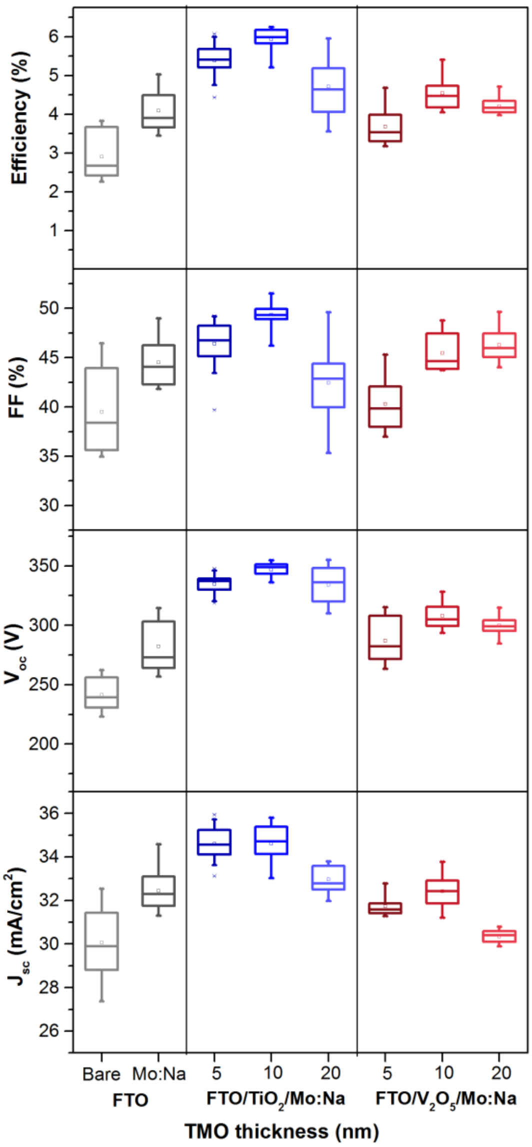

Figure 94. Boxchart of the main solar cell parameters of the devices fabricated on the different substrate configurations.

The combination of Mo:Na with V_2O_5 and TiO_2 leads to further improvements. In the case of the SLG/FTO/V_2O_5/Mo:Na configuration, this is only achieved with a 10 nm V_2O_5 layer. Compared to the SLG/FTO/Mo:Na reference, the average V_{oc} and FF are moderately enhanced which translates into a 5.4% record efficiency. However, the origin of these improvements is not clear from the data presented here. On the other hand, the combination of 5 and 10 nm TiO_2 layers with Mo:Na leads to a large improvement of all solar cell parameters. The best performance is reached with a 10 nm TiO_2 layer. Compared to the SLG/FTO/Mo:Na reference there is an average improvement of 65 mV in V_{oc}, 5% (absolute) in FF and 2.2 mA/cm^2 in J_{sc}. All this leads to a remarkable 6.2% record efficiency. In this case, these enhancements can be clearly attributed to a highly increased shunt resistance (twice higher than that of the Mo:Na reference). However, increasing the thickness of the TiO_2 layer to 20 nm causes a strong reduction of the average FF and J_{sc} as well as a large loss of homogeneity as can be observed in Figure 94. Although this degradation matches with a larger series resistance, this is not reflected in Table 22 since the record device corresponds to an extreme outlier case (as a result of the large inhomogeneity) not representative of the global tendency of the sample.

Table 22. Optoelectronic parameters of the record devices obtained with each substrate configuration. The rows in bold correspond to the best configuration obtained with each TMO.

Substrate configuration	TMO (nm)	J_{sc} (mA/cm^2)	V_{oc} (mV)	FF (%)	η (%)	R_{sh} (Ω·cm^2)	R_s (Ω·cm^2)
FTO	-	31.5	263	46.3	3.8	60	0.8
FTO/Mo:Na	-	32.7	315	48.9	5.0	230	1.4
FTO/TiO_2/Mo:Na	5	35.0	346	49.1	5.9	270	1.4
	10	**34.4**	**355**	**50.9**	**6.2**	**520**	**1.5**
	20	33.1	355	49.5	5.8	160	1.1
FTO/V_2O_5/Mo:Na	5	32.8	316	45.2	4.7	170	1.7
	10	**33.8**	**328**	**48.7**	**5.4**	**240**	**1.4**
	20	30.2	315	49.5	4.7	270	1.0

To further explore the effects of the different substrate configurations, the spectral response (EQE) of the record devices was also studied. The results are shown in Figure 95.

The SLG/FTO reference presents an almost linearly decreasing collection of photogenerated charges from 500 nm (80%) to 1200 nm (40%). The most likely explanation for this low carrier collection is recombination. The EQE profile shows that the deeper EHPs are generated (i.e. at longer illumination wavelengths) the more likely recombination is. This suggests that the origin of recombination may lie at the back interface. The addition of Mo:Na enhances charge collection around 8% (absolute) in average along the 500-1200 nm range, reaching the largest improvement at around 950 nm. The fact that $MoSe_2$ is located at the back interface and that the largest collection improvements with respect to the SLG/FTO reference are observed for deeply generated carriers reinforces the idea of the back interface being the main source of recombination. Thus, besides improving R_{sh}, the formation of $MoSe_2$ also reduces recombination at the CZTSe/FTO interface.

The substrate configurations containing TMOs present complex and very thickness-sensitive behaviours. In the case of the SLG/FTO/V_2O_5/Mo:Na configuration, the only significant improvement is found for a 10 nm V_2O_5 layer which boosts collection in the 500-1200 nm range compared to Mo:Na. For 5 and 20 nm V_2O_5 layers, there is no collection improvement with respect to the SLG/FTO/Mo:Na reference. As for the combination of TiO_2 and Mo:Na, charge collection is substantially increased with respect to the other substrate configurations in the 800-1200 nm spectral range when employing either a 5 or a 10 nm TiO_2 layer. For wavelengths <800 nm, the differences with respect to the Mo:Na reference are negligible. Increasing the thickness of the TiO_2 layer to 20 nm maintains an improved collection for wavelengths larger than 900 nm but causes it to significantly drop in the 500-900 nm range changing the shape of the EQE curve and suggesting an influence of TiO_2 not only at the back but also at the front interface.

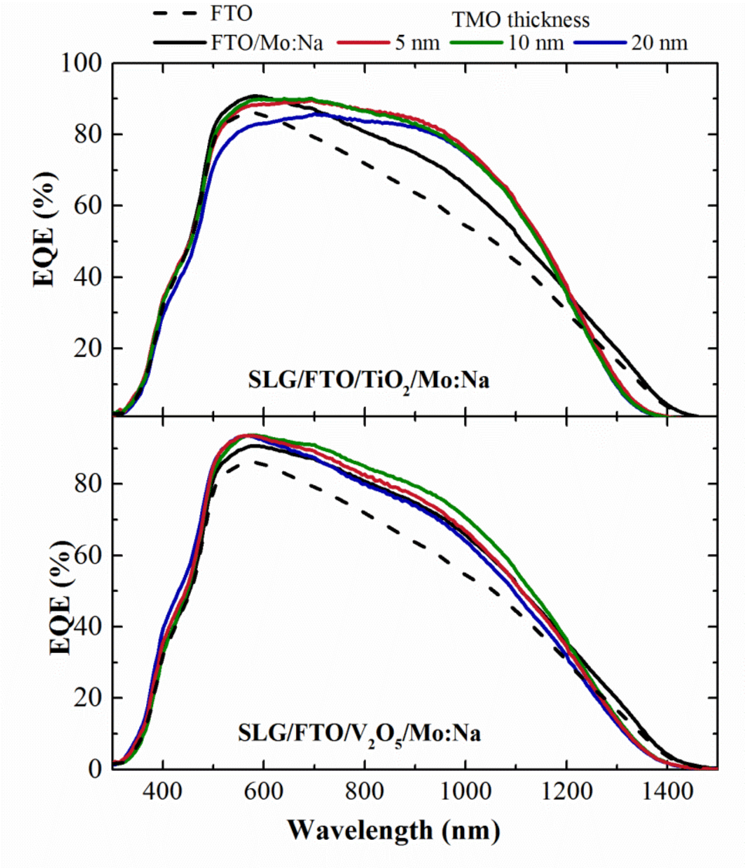

Figure 95. EQE of the record devices obtained with in the thickness screening.

Transmittance and sheet resistance

In section 5.3.1, it was demonstrated that the TMOs are very transparent and do not affect the resistivity of the substrates. However, the best performing substrate configurations (SLG/FTO/10 nm TiO_2/Mo:Na and SLG/FTO/10 nm V_2O_5/Mo:Na) differ from those initially studied since they contain a 20 nm Mo:Na layer. Therefore, the following question arises: are the best performing configurations transparent and conductive? Figure 96 shows the transmittance spectra of the best substrate configurations before and after being submitted to a reactive annealing process. In addition, Table 23 shows the average transmission values extracted from them in the UV, visible and IR regions.

Before annealing, the transmittance levels are significantly lower compared to the Mo:Na-free configurations. The reduction in transmittance is observed to be independent from the TMO employed and decreases with the increasing illumination wavelength: 28% in the UV, 26% in the visible and 15% in the infrared relative to the bare TMOs. On the other hand, the conductivity of the substrates is totally degraded by the addition of a 20 nm Mo:Na layer with R_{sheet} increasing from 10 Ω/□ up to 2.2 kΩ/□. This is due to the fact that the Na present in the

Mo:Na layer is in the form of Na_2MoO_4 which has a very low conductivity due to its high oxygen content [182,319,320].

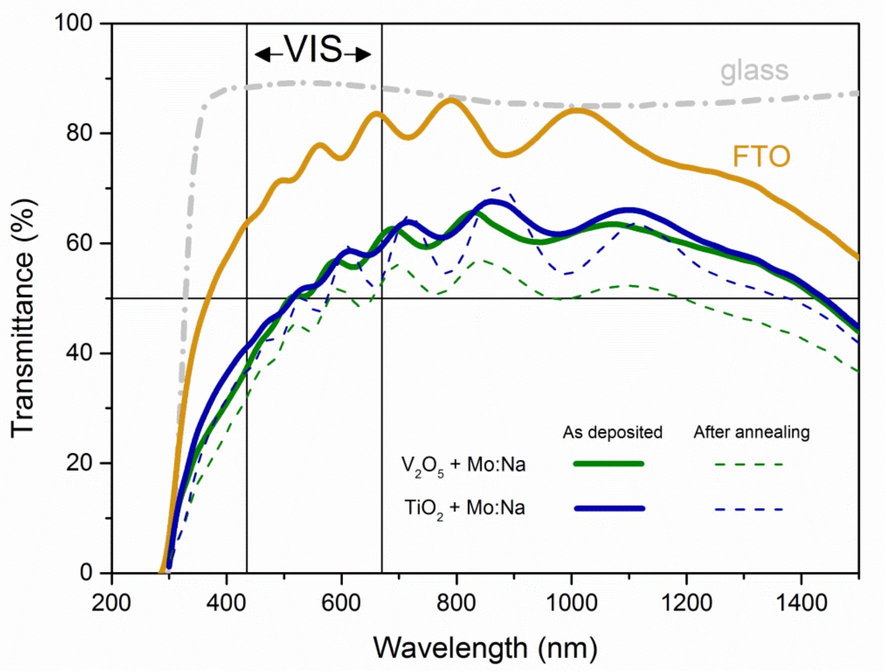

Figure 96. Total transmittance before (solid line) and after (dashed line) selenization of the best performing substrate configurations.

During the annealing process, the Mo:Na layers are selenized, as expected, into $MoSe_2$. which further decreases their transmittance. This decrease is stronger for the V_2O_5-containing configuration than for the TiO_2-containing one suggesting a different growth of the $MoSe_2$ layer or a higher stability of the TiO_2 layer during the annealing process as observed in section 5.3.1. This way, SLG/FTO/V_2O_5/Mo:Na configuration exhibits the lowest transmittance (45.1% in the visible and 49.5% in the IR). However, this level of transparency, although low, is still compatible with the fabrication of semi-transparent and bifacial devices.

On the other hand, the annealing process restores the conductivity of Mo:Na-containing substrates to 10 Ω/□ since the Mo:Na layer is completely selenized and $MoSe_2$ is more electrically benign that Na_2MoO_4.

Table 23. Average transmittance values of the best performing substrate configurations. The values in red were measured after submitting the substrates to an annealing process. Values calculated from Figure 96.

	T_{avg} (%)								
	300-435 nm			435-670 nm			670-1500 nm		
	Bare 10 nm	+Mo:Na		Bare 10 nm	+Mo:Na		Bare 10 nm	+Mo:Na	
V_2O_5	33.2	24.1	18.6	69.6	51.4	45.1	69.2	59.1	49.5
TiO_2	38.2	27.5	22.3	70.7	52.2	49.0	71.0	60.6	57.0
SLG/FTO	45.4			74.6			75.6		

Summary

The presence of shunts that reduce the R_{sh} of the devices is confirmed to be the main limiting issue of CZTSe devices fabricated on SLG/FTO. However, strong recombination is also observed in EQE measurements probably originated at the back interface. The addition of extra $MoSe_2$, $V_2O_5/MoSe_2$ and $TiO_2/MoSe_2$ layers is observed to act twofold: on the one hand it increases R_{sh} and, on the other hand, it reduces recombination. Both beneficial effects exhibit a complex behaviour and are very sensitive to layer thickness becoming even detrimental in some cases. Despite this complex behaviour, clearly superior substrate configurations have been found in which the improvements provided by the extra layers outweigh any detrimental effects and result in highly enhanced devices with respect to the reference substrates:

- SLG/FTO/10 nm V_2O_5/Mo:Na
- SLG/FTO/10 nm TiO_2/Mo:Na

Finally, despite the formation of $MoSe_2$, these substrate configurations still present a high enough transparency to be compatible with bifacial or semi-transparent applications.

5.3.4 Series C: Technology transfer to wide-bandgap CZTS and CZTSSe

Once the best the substrate configurations were found for CZTSe devices, the suitability of employing them for wider bandgap kesterite devices was studied. In order to do this, CZTS and CZTSSe (S/S+Se ~ 0.9) devices were fabricated in a similar way to series B (with Ge, metallic grid and ARC) on the following substrate configurations:

- SLG/FTO
- SLG/FTO/Mo:Na
- SLG/FTO/10 nm V_2O_5/Mo:Na
- SLG/FTO/10 nm TiO_2/Mo:Na

First, the performance of the different devices is analysed and compared with the previously fabricated CZTSe ones. Then, morphological, structural and in-depth compositional characterization of the devices is presented to further investigate the effects of the different substrate configuration on the kesterite devices.

Device performance

Table 24 shows the main optoelectronic parameters of the record devices together with their calculated series and shunt resistances. As in the initial screening, only the record cells, which can be considered as representative of the full samples, are shown for the sake of simplicity.

Similar shunting problems to those observed in CZTSe are detected for CZTS and CZTSSe devices fabricated on SLG/FTO. However, in contrast to the former, the series resistance of the latter is also a very limiting issue which results in solar cells with very low fill factor and efficiencies below that of CZTSe. In the case of CZTSSe, the R_s exhibits extremely high values one order of magnitude higher than those found on pure Se solar cells and around 3 times higher than in the case of S. Espíndola et al. reported the degradation of FTO in a S+Se annealing atmosphere with a noticeably hindered transmittance and a ~10 times higher sheet resistance [279]. The series resistance issues observed here fit perfectly with such an increased sheet resistance of the FTO back contact due to a low inertness during annealing in pure S and, especially, in S+Se mixture. The addition of Mo:Na and subsequent formation of $Mo(S_x,Se_{1-x})_2$, apart from insulating shunts as in the case of CZTSe, is also observed to prevent FTO S-related degradation during annealing resulting in devices with highly diminished series resistances. However, both Mo:Na and the different TMO substrate configurations studied present dissimilar behaviours depending of the absorber employed.

Table 24. Optoelectronic parameters of the record devices obtained with each substrate configuration and kesterite absorber. The rows in bold correspond to the best configuration obtained for each absorber.

Absorber	Substrate configuration	TMO (nm)	J_{sc} (mA/cm^2)	V_{oc} (mV)	FF (%)	η (%)	R_{sh} ($\Omega \cdot cm^2$)	R_s ($\Omega \cdot cm^2$)
CZTSe	FTO	-	31.5	263	46.3	3.8	60	0.8
	FTO/Mo:Na	-	32.7	315	48.9	5.0	230	1.4
	FTO/TiO_2/Mo:Na	**10**	**34.4**	**355**	**50.9**	**6.2**	**520**	**1.5**
	FTO/V_2O_5/Mo:Na	10	33.8	328	48.7	5.4	240	1.4
CZTS	FTO	-	17.2	579	37.4	3.7	60	4.5
	FTO/Mo:Na	**-**	**14.6**	**755**	**55.2**	**6.1**	**320**	**1.7**
	FTO/TiO_2/Mo:Na	10	11.3	542	42.3	2.6	170	8.7
	FTO/V_2O_5/Mo:Na	10	15.2	618	41.5	3.9	110	1.8
CZTSSe	FTO	-	17.1	546	35.2	3.3	100	13.8
	FTO/Mo:Na	-	18.1	617	46.4	5.2	180	2.9
	FTO/TiO_2/Mo:Na	10	18.9	589	58.0	6.4	320	3.3
	FTO/V_2O_5/Mo:Na	**10**	**21.7**	**620**	**58.8**	**7.9**	**270**	**1.8**

In the case of CZTS, the shunting reduction effect of Mo:Na is particularly strong which, among other factors, leads to an impressive 755 mV V_{oc} (176 mV increase). This is the highest V_{oc} reported for a kesterite solar cell fabricated on a transparent substrate and is comparable to some of the highest V_{oc} values reported for pure sulphur kesterite [321,322]. The devices also present a highly enhanced FF attributable to the strong R_s reduction provided by Mo:Na. Despite the low R_s, a significantly lower J_{sc} (2.6 mA/cm^2 lower) compared to the reference limits the efficiency of the record device to 6.1%. On the other hand, the combination of Mo:Na with 10 nm of V_2O_5 eliminates the beneficial effects of the former with respect to shunting while its combination with 10 nm of TiO_2 induces a very high R_s degrading, in both cases, the performance of the devices.

As for CZTSSe devices, although Mo:Na provides a large series resistance reduction, it does not completely impede the degradation of the FTO leading to a twice higher R_s compared to CZTSe and CZTS. However, the V_{oc} is still greatly improved by 71 mV yielding a 5.2% efficiency device. On the other hand, the combination of Mo:Na with 10 nm V_2O_5 and TiO_2 layers causes important improvements with respect to the Mo:Na reference, especially on the R_{sh} of the devices. In the case of TiO_2, a highly increased FF and significantly lower V_{oc} are detected with respect to those of the Mo:Na reference leading to an improved 6.4% efficiency. In the case of V_2O_5, the FF is also highly increased but maintaining the same V_{oc} as the Mo:Na reference. In addition, V_2O_5 also provides a significantly lower R_s that allows a 3.6 mA/cm^2 higher J_{sc}. All this translates into a 7.9% record efficiency. This is the highest efficiency reported for a kesterite device fabricated on a transparent substrate.

Morphological characterisation

Figure 97 shows FESEM cross-sectional micrographs of the CZTSe, CZTS and CZTSSe devices fabricated on the different substrate configurations. In the case of CZTSe, no significant differences can be spotted in the morphology of the absorbers despite the different back interfaces employed. All of them present large micron-sized grains and a compact structure. However, the use of V_2O_5/Mo:Na seems to induce a bilayer morphology with slightly smaller grains at the bottom.

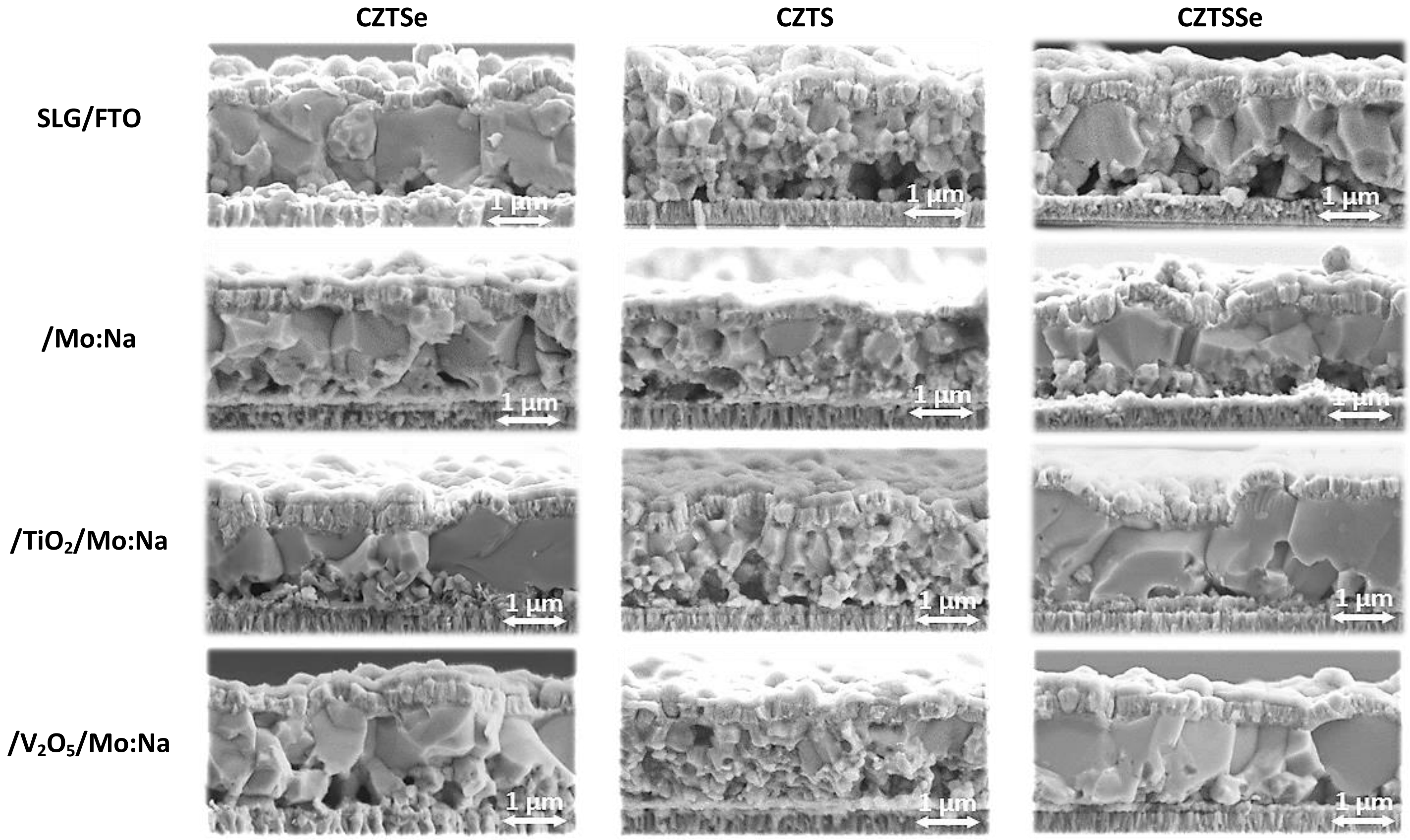

Figure 97. Cross-sectional FE-SEM micrographs of the best performing CZTSe, CZTS and CZTSSe devices on the different substrate configurations.

In the case of CZTS, the substrate configuration completely changes the morphology of the absorber. The device fabricated directly on SLG/FTO presents a small crystallite porous structure with numerous voids at the bottom. The addition of Mo:Na increases grain size at the top of the absorber whilst the bottom still presents very small crystallites. However, the number of voids is greatly reduced and the structure becomes much more compact. On the other hand, the combination of TiO_2 and V_2O_5 with Mo:Na largely hinders crystal growth resulting in a morphology dominated by small crystallites similar to SLG/FTO reference which could lie at the origin of the low performance of the devices fabricated on those substrate configurations.

As for CZTSSe, the absorber synthesised on SLG/FTO exhibits large grains although combined with abundant voids and crystallites at the bottom. The addition of Mo:Na leads to a more compact structure with slightly larger grain size and reduced number of voids. Interestingly, the combination of Mo:Na with TiO_2 and V_2O_5 largely increases crystal size and layer compactness completely eliminating any sign of crystallites and voids and yielding large columnar grains with a reduced number of grain boundaries. This improved morphology correlates with the large enhancements observed in the optoelectronic parameters of the solar cells fabricated on such substrates.

Raman analysis

Figure 98 shows the front and back Raman spectra of the CZTSe, CZTS and CZTSSe devices fabricated on the different substrate configurations. The measurements were carried out with λ_{ex} = 785 nm which allows to investigate both the front and back sides without removing the window layer or exfoliating the device from the substrate, respectively.

In general, no significant differences can be observed in the position and full width at half maximum (FWHM) of the main kesterite peaks regardless the absorber, substrate configuration employed or the side of the sample measured. Nevertheless, the FWHM of the 335 cm^{-1} (CZTSSe) and 337 cm^{-1} (CZTS) peaks is slightly higher (below 13%) in the spectra obtained from back side measurements suggesting a more defective kesterite (see Figure 99). In addition, there is no trace of secondary phases in CZTSe and CZTSSe devices neither at the front nor at the back of the absorbers. This is particularly revealing in the case of CZTSe since the excitation wavelength employed is resonant with the bandgap of $SnSe_2$ (as already shown in chapters 3 and 4) whose formation could be a priori expected when working with an FTO back contact. In the case of CZTS, some SnS is detected at the front surface of the devices fabricated on SLG/FTO and SLG/FTO/Mo:Na.

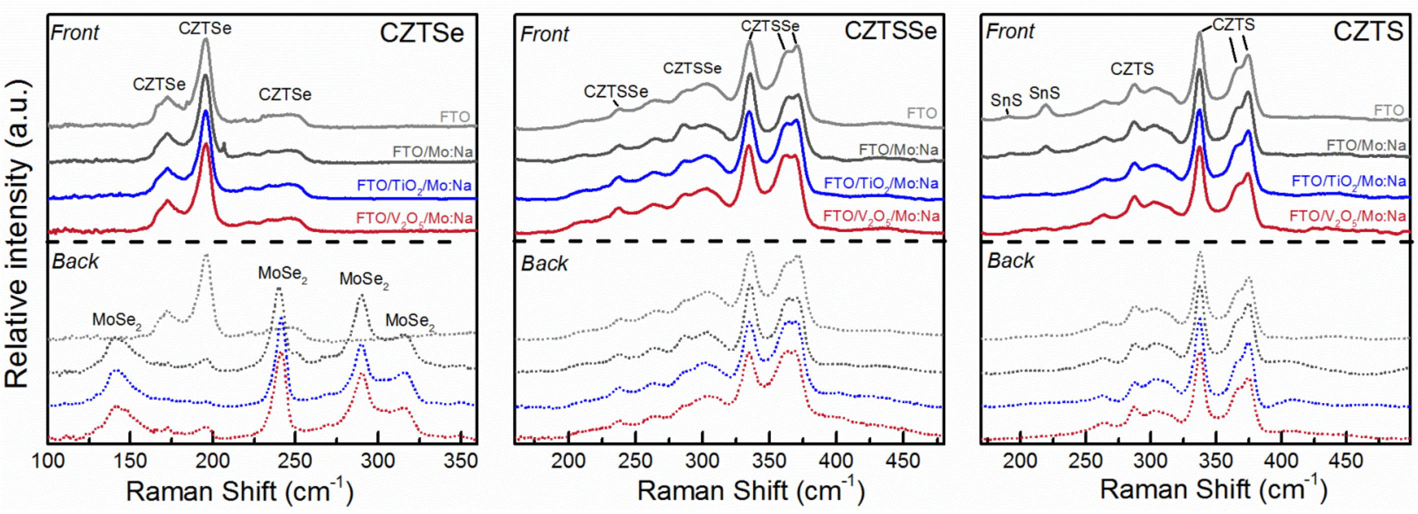

Figure 98. Raman spectra of the CZTSe, CZTSSe and CZTS devices fabricated on the different substrate configurations. The measurements were carried out at the front surface (continuous lines) and the back surface (dotted lines) employing λ_{ex} = 785 nm.

The back measurements of the CZTSe devices confirm the formation of $MoSe_2$ when Mo:Na is employed at the back. The bandgap of $MoSe_2$ is resonant with the excitation wavelength employed so its signal is highly enhanced impeding to obtain clear information from the CZTSe absorber. The opposite is observed in CZTS and CZTSSe in which no information can be obtained about the MoS_2 and $Mo(S,Se)_2$ layers since they are transparent to the excitation laser source due to their elevated bandgap.

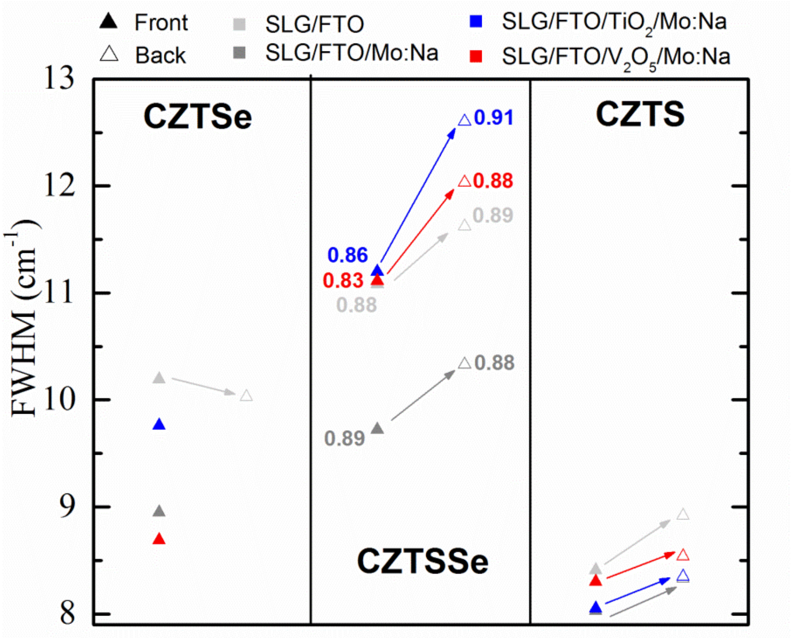

Figure 99. FWHM of the 195 cm^{-1} (CZTSe), 335 cm^{-1} (CZTSSe) and 337 cm^{-1} (CZTS) peaks extracted from Lorentzian fittings. The S/(S+Se) ratios calculated with a similar method to that described in [323] are shown for CZTSSe.

Employing a peak area ratio method similar to the one developed by Dimitrievska et al. [323,324], the S/(S+Se) compositional ratio of the CZTSSe devices was analysed to study if the different substrate configurations could affect the anionic composition of the absorbers. However, no significant differences are observed with the S/(S+Se) ratios ranging from 0.86 to 0.91 (values in the middle part of Figure 99).

In-depth compositional analysis

In order to shed light on the role and location of the different layers added to the FTO back contact as well as on Na diffusion and incorporation, the best performing CZTSe, CZTS and CZTSSe devices were analysed by TOF-SIMS (Figure 100).

The spectra c and d in Figure 100 give clear confirmation of the FTO acting as a Na barrier. However, a significant amount of Na can still diffuse through it. Na is observed to accumulate at the back kesterite/FTO interface in every case which is expectable since Mo:Na is located there and Na has been demonstrated to assist the formation of $MoSe_2$ and incorporate into it [325,326]. In addition, there is also an accumulation of Na towards the kesterite/CdS interface. This indicates that Na is effectively diffusing from the back to the front of the absorbers and, thus, is being effectively incorporated into the kesterite structure. The front interface Na accumulation seems higher in the case of CZTS which may be suggesting a higher incorporation of this alkaline element promoted by the smaller grain size (or larger amount of grain boundaries) of the absorber. However, it is difficult to quantitatively compare Na incorporation onto the different absorbers due to possible matrix effects between the different elements analysed that may change the ionization energy of Na and, therefore, the intensity of the SIMS signal.

Regarding the TMOs, clear signals of V and Ti (only in O_2^+ mode, spectrum b in Figure 100) are found at the back interface of CZTSSe and CZTSe absorbers. This gives proof of their stability and their presence at the back after the kesterite synthesis process. Thus, some of the effects observed in the optoelectronic properties of the devices can be truly ascribed to the presence of these TMOs at the back. Interestingly, in the case of Ti, an accumulation at the front interface is also observed which points towards a diffusion of this metal through the absorber. It was shown before that 20 nm of TiO_2 modify the EQE response in the 500-900 nm range (see Figure 94) which may be related to the observed Ti accumulation towards the CdS/kesterite interface.

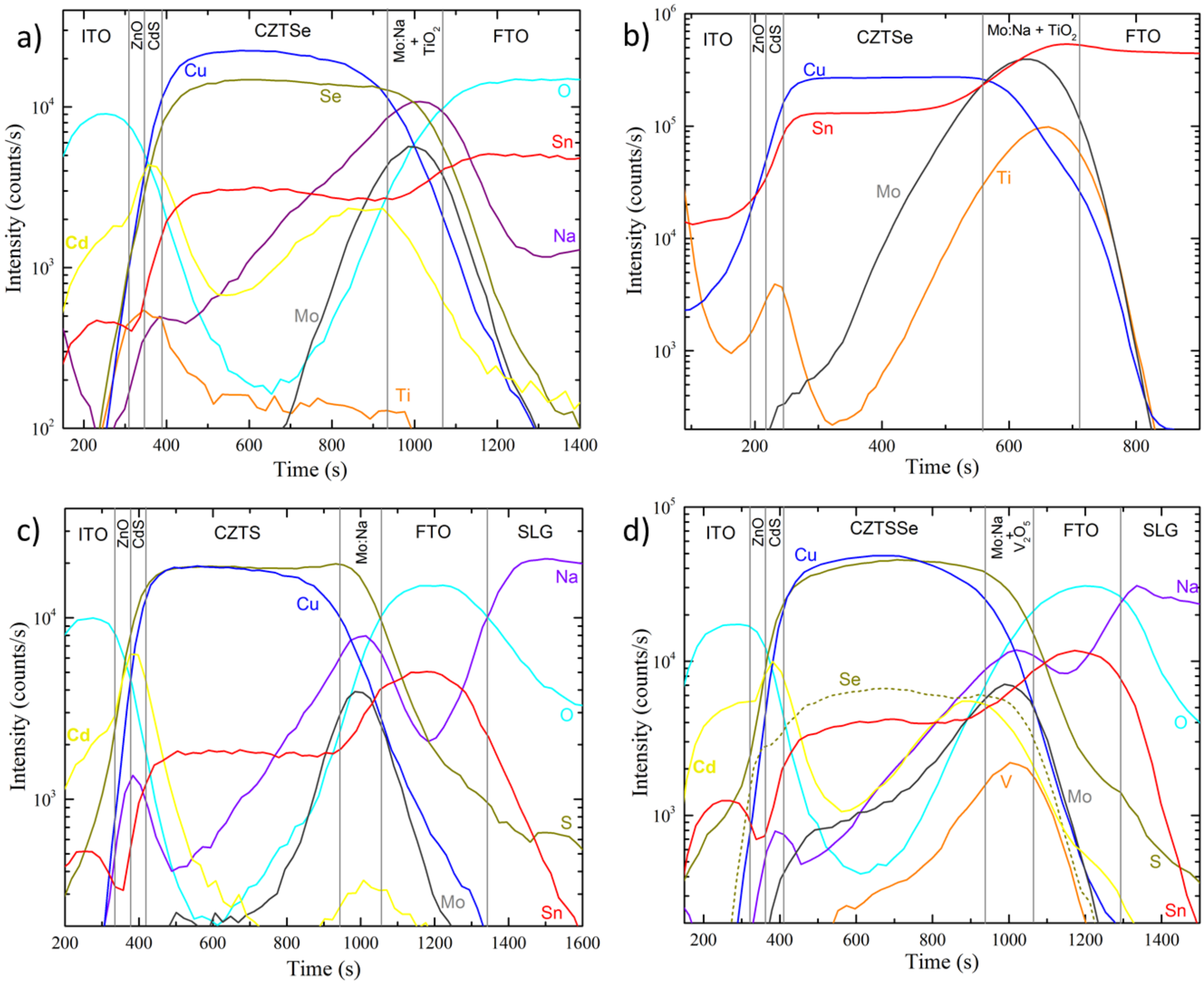

Figure 100. TOF-SIMS spectra of the best CZTSe (a), CZTS (c) and CZTSSe (d) performing devices fabricated on SLG/FTO/TiO_2/Mo:Na, SLG/FTO/Mo:Na and SLG/FTO/V_2O_5/Mo:Na, respectively, obtained from the Cs^+ signal. b) CZTSe spectrum obtained from the O_2^+ signal. Elements displayed: Cu (blue), Sn (red), S/Se (dark yellow), V/Ti (orange), Na (purple), Mo (dark grey), Cd (yellow) and O (blue). The boundaries between the different layers shown in the spectra are only intended as a visual guide for the reader.

Transmittance

Finally, it is interesting to take a quick look at the transparency of the finished devices to evaluate their potential for semi-transparent applications. Their transmittance spectra are shown in Figure 102. Since the absorbers are 1.5-2 µm thick, they absorb nearly all the visible light making them completely opaque. However, they allow a significant portion of the infrared light to pass, especially wide-bandgap CZTS and CZTSSe devices. This implies that, on the one hand, these substrate configurations have a true potential for semi-transparent kesterite applications if wide-bandgap materials are used and, on the other hand, that it is necessary to combine this approach with a highly reduced absorber thickness.

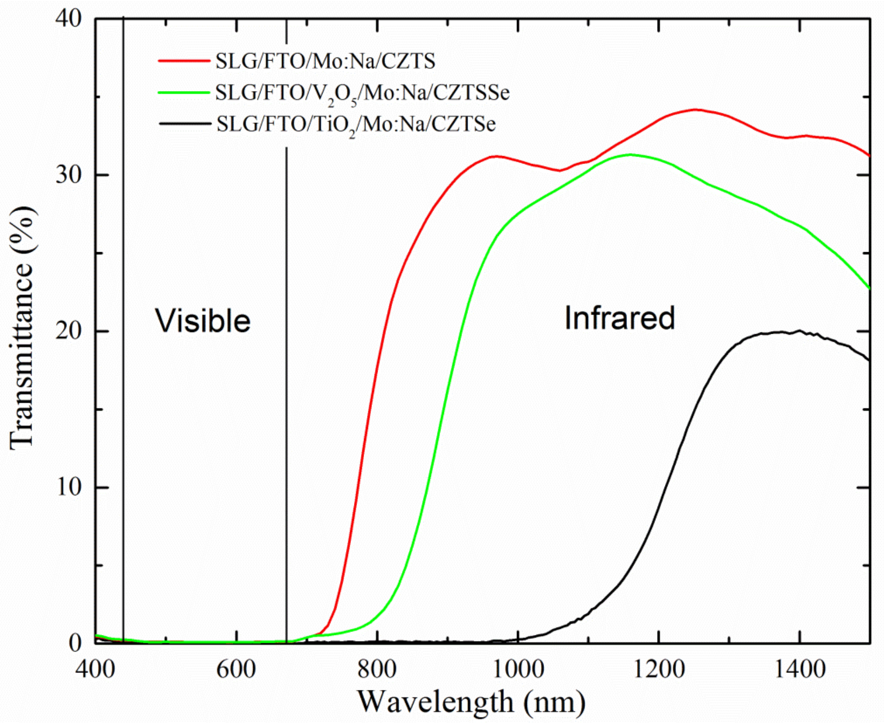

Figure 101. Transmittance spectra of the finished devices.

Summary

It has been shown that CZTSe, CZTS and CZTSSe absorbers behave differently on the different substrate configurations studied. Firstly, in contrast to the high inertness of FTO during annealing in Se atmosphere, the presence of S degrades its conductivity and hinders the series resistance of the resulting CZTS and CZTSSe devices. Apart from reducing shunting issues, the use of Mo:Na and subsequent formation of $MoSe_2$ prevents the degradation of FTO during annealing. In the case of CZTS, the combination of both effects leads to a record device with a very high V_{oc} and a 6.2% efficiency. However, the use of V_2O_5 and TiO_2 eliminates the beneficial effects of Mo:Na/$MoSe_2$. Oppositely, these TMOs highly improve the performance of CZTSSe devices, specially V_2O_5, leading to a 7.9% record efficiency.

Raman characterisation shows that the different substrate configurations do not influence the crystalline quality nor the composition of the Kesterite absorbers. On the contrary, FESEM reveals they have a profound effect on the morphology of the absorber which correlates with the performance of the devices. Finally, TOF-SIMS measurements confirm that some of the effects observed can be ascribed the presence of TMOs at the back interface.

5.4 Discussion

The discussion presented below should be taken with great caution since it only aims to provide some clues that may help to interpret the results obtained with the different SLG/FTO/TMO/Mo(S_x,Se_{1-x})$_2$ substrate configurations. However, due to the complexity of such multilayered back interfaces, it would be pretentious to extract solid conclusions solely from the J-V and EQE data of the devices which represent the majority of the characterisation performed to the samples. In order to fully understand the behaviour of these substrate configurations, further experimentation and more advanced characterisation are necessary. Unfortunately, this is beyond the scope of this work: a preliminary screening and an empirical search of substrate configurations that may improve the Kesterite/FTO interface.

5.4.1 CZTSe

FTO/CZTSe interface and addition of TMOs

The results obtained in this work show that the series resistance is not a critical issue when fabricating CZTSe solar cells on SLG/FTO substrates which suggests that the CZTSe/FTO junction exhibits a near-ohmic behaviour. This contradicts previous works in which R_s was reported to be a limiting factor for the performance of CZTSe solar cells fabricated on FTO [269,271,279]. However, although not obvious since the properties of CZTSe and FTO can vary considerably depending on their fabrication process, a near-ohmic behaviour is somehow an expectable result regarding the work functions reported in the literature for CZTSe and FTO which show a favourable band alignment as depicted in Figure 102a.

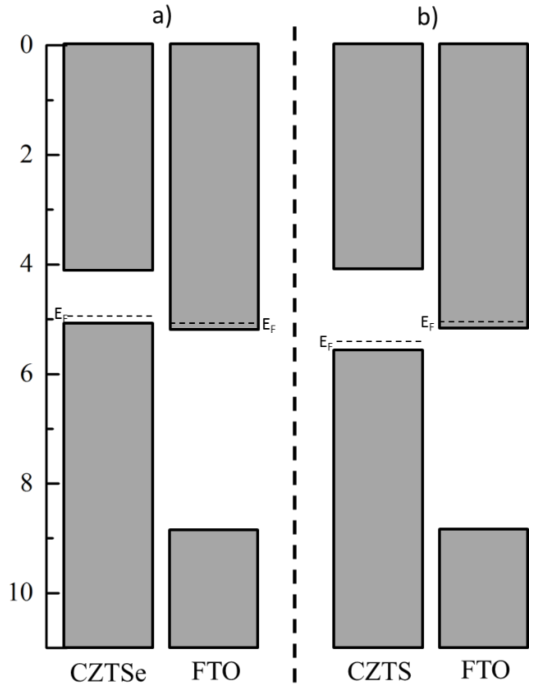

Figure 102. Band diagrams of CZTSe, CZTS and FTO. Data sources: CZTSe and CZTS [330]; FTO [331].

The addition of TMO layers on top of the FTO for the fabrication of CZTSe devices has been observed to induce a current-blocking behaviour (except for MoO_x) and, thus, to be very detrimental for the devices. However, two different cases can be distinguished. On the one hand, V_2O_5 and, especially, TiO_2 and CuO lead to distorted J-V curves that even become S-shaped for the latter oxides. Since these TMOs have been found to be rather inert to the annealing process (Figure 90) and to remain at the back interface (Figure 100), the distortion of the J-V curves can be directly attributed to their presence between CZTSe and FTO. S-shaped curves are commonly encountered in OPV and are usually related to electronic issues such as the formation of an extra diode or charge accumulation as a result of a bad band alignment [327–329]. In principle, as shown in Figure 89, large work function TMOs are expected to provide a more effective hole extraction either through creating an accumulation or a recombination layer. However, it is clear that this is not the case here and that these TMOs completely ruin the favourable CZTSe/FTO band alignment shown in Figure 102. On the other hand, Co_3O_4 and NiO also lead to distorted J-V curves. Owing to the more linear shape of the curves and to the fact that they these TMOs get selenized during annealing, the high R_s of the devices could be arising from an increased contact resistance (rather than from a unfavourable band alignment) caused by the formation of very rough or non-continuous Ni_xSe_y/Co_xSe_y layers.

Origin of shunting and recombination and the role of $MoSe_2$

The main issue found when fabricating CZTSe devices directly on SLG/FTO has been found to be a very low shunt resistance. The origin such a strong shunting is not easy to discern, though. FESEM micrographs (Figure 97) show devices with large grains, a compact structure and with no evidence of front-back interconnection. Likewise, Raman spectroscopy (Figure 98) does not detect any secondary phases that could act as a shunt paths like $SnSe_2$ (see section 3.4.3). Another possible source of shunting which has not been explored in this work is the presence of conductive grain boundaries. In this respect, Guo et al. reported a low shunt resistance in CZTSe devices and attributed it to Se-poor and Sn-rich grain boundariess (measured by EDX) exhibiting a metallic behavior and acting as conductive channels [332]. Since, in this work, CZTSe devices are fabricated on FTO, a Sn-enrichment of the grain boundaries as an effect of Sn-diffusion from the substrate seems plausible and could lie at the origin of the observed shunting.

The formation of $MoSe_2$ (arising either from Mo, Mo:Na or MoO_x layers) on top of the FTO has been observed to alleviate shunting largely increasing the V_{oc} of the devices. This effect has been initially attributed to $MoSe_2$ acting as an insulating layer and, thus, reducing shunt currents. Interestingly, the SLG/FTO/MoO_x/Mo:Na configurations have resulted in highly degraded devices with a large series resistance. This current-blocking behaviour may be ascribed to a different growth of $MoSe_2$. López-Marino et al. reported a change in the orientation of the c-axis of $MoSe_2$ when selenizing a 20-30 nm Mo sacrificial layer deposited on SLG/Mo and SLG/Mo/MoO_2 substrates shifting from purely parallel to the substrate (i.e. electrically benign columnar grains) in the former case to a mixture of parallel and perpendicular (i.e. stacked horizontal $MoSe_2$ layers potentially detrimental for R_s) when MoO_2 was present [147]. Thus, it may be possible that the degradation of the R_s observed when combining MoO_x and Mo:Na is related to the presence of a too thick $MoSe_2$ layer with an electrically unfavourable orientation. This could also explain the differences observed between using Mo/Mo:Na metallic layers and MoO_x as $MoSe_2$ precursors. This way, the $MoSe_2$ layer formed from MoO_x would be more insulating and, thus, would reduce shunting more effectively.

In addition to shunting, EQE measurements (Figure 95) have also revealed strong recombination towards the back interface as a limiting factor of the CZTSe devices fabricated on SLG/FTO. The low carrier collection can be considered to be independent from shunting since, except in extreme cases, shunts can be neglected in short-circuit conditions (see Eq.(10)) so they should affect neither the J_{sc} nor the EQE of the devices noticeably. Although Figure 102a shows an expected favourable band alignment and the CZTSe/FTO interface displays ohmicity, the results also indicate that CZTSe-FTO coupling is far from perfect. Thus, the origin of the observed recombination issues may lie at a non-optimum p-kesterite/n-FTO band alignment in which an extended region with a high density of defects can be expected to be formed. The existence of defects becomes evident by comparing the J_{sc} value obtained from J-V analysis (31.5 mA/cm^2) and from integrating the EQE curve (28.4 mA/cm^2) (see section 5.3.3). This ~10% difference indicates the presence of charged defects that affect collection during low light intensity EQE measurements but are partially neutralized by photogenerated carriers under more intense illumination in J-V curve acquisition.

The formation of $MoSe_2$ on top of the FTO has been observed to reduce recombination which may also be contributing to the V_{oc} improvement associated to this layer. The mechanism through which $MoSe_2$ improves collection is not clear but may be related to an electronically improved interface. If highly doped, $MoSe_2$ could be acting as a p^+ accumulation layer reducing the width of the barrier formed at the CZTSe/FTO interface and preventing the formation of an extended defect region. However, it may also be possible that the improved collection is due to the passivation of interface defects. It was observed in Figure 100 that a large amount of Na remains at the back within the $MoSe_2$ layer. Thus, this Na reservoir may be assisting in passivating such interface defects.

Combination of TMOs with Mo:Na

The combination of the TMOs with Mo:Na ($MoSe_2$), has been found to improve the performance of the CZTSe devices with respect to the case of the bare oxides twofold:

1. By reducing or even eliminating the current blocking behaviour observed for the bare TMOs
2. By increasing the V_{oc} of every SLG/FTO/TMO configuration.

However, although related, both effects seem to have different origins. The V_{oc} increase occurs in, more or less, a similar way in every substrate configuration regardless the TMO and may be linked, as explained above, to $MoSe_2$ shunt insulation. On the other hand, the reduction of the current blocking behaviour seems related to an improved back interface. In the case of Se-reacting TMOs, $MoSe_2$ alleviates, although does not eliminate, the contact resistance induced by Ni_xSe_y and Co_xSe_y layers possibly by improving the morphology of the back interface. In the case of Se-inert TMOs, the distorted S-shaped J-V curves disappear. However, while in the case of p-type CuO a current barrier still remains, for n-type TMOs (i.e. TiO_2 and V_2O_5) there is no current blockage and the devices are highly improved compared the Mo:Na reference.

The superior performance of combining Mo:Na with n-type TMOs could be tentatively ascribed to a p-CZTSe/p^+-$MoSe_2$/n-TMO/n^+-FTO complex back interface that may be offering a more favourable band coupling. However, the results obtained in section 5.3.3 also suggest that the presence of these oxides at the back is adding an extra shunt protection to that provided by $MoSe_2$. This theory is supported by the fact that shunt reduction seems directly related to the TMO layer thickness (see Table 21 and Table 22). Nevertheless, both shunting insulation and a more favourable band coupling can occur simultaneously and the performance enhancements caused by these TMOs are probably a combination of both effects.

TiO_2 and V_2O_5 have also been observed to assist $MoSe_2$ in reducing recombination. These oxides have been reported to exhibit passivating properties in c-Si so it may be possible that they are also helping in passivating CZTSe/FTO interface defects [296]. However, their passivation effectiveness shows a complex thickness-dependant behaviour with a tendency to decrease with the increasing layer thicknesses.

Shunting insulation and recombination reduction

Interestingly, by comparing the J-V and EQE measurements of the substrate configurations studied in section 5.3.3, a non-dependence between shunt insulation and recombination reduction can be spotted. In the case of TiO_2, the EQE profiles for both 5 and 10 nm TMO layers are identical indicating a similar recombination reduction. However, a much higher shunt resistance is obtained for the 10 nm layer. Likewise, in the case of V_2O_5, shunt resistance increases with the increasing layer thickness while only an enhanced carrier collection is observed for a 10 nm layer. Thus, it is clear that an increased R_{sh} does not necessarily mean reduced recombination and vice versa. This supports the idea that both shunting insulation, a more favourable band coupling and passivation are contributing to improve the devices but also indicate that these processes are rather independent from each other.

5.4.2 Comparison of CZTSe, CZTS and CZTSSe

Series resistance and $Mo(S_x,Se_{1-x})_2$

Series resistance has been found to be a critical factor for CZTS and CZTSSe-based devices fabricated directly on FTO. As explained in section 5.3.4, this can be ascribed to the degradation of the conductivity of FTO due to a low inertness of this layer to S (and S+Se) during high temperature annealing processes. However, the higher work function of S-rich kesterite absorbers may also be leading to a less favourable band alignment as shown in Figure 102b contributing to the high R_s. Besides improving shunting as in the case of CZTSe, $Mo(S_x,Se_{1-x})_2$ layers also become key in reducing the large series resistance of CZTS and CZTSSe devices. Although this effect can be attributed to $Mo(S_x,Se_{1-x})_2$ acting as a protective layer and preventing the reaction of S (and S-Se) species with the FTO, it may be also possible that $Mo(S_x,Se_{1-x})_2$ is acting as a p^+ accumulation layer alleviating the aforementioned non-favourable band alignment.

Effect of the TMOs

The different substrate configurations studied display a similar behaviour in CZTSSe and CZTSe devices with the combination of Mo:Na with TiO_2 and V_2O_5 yielding further R_{sh} improvements with respect to the Mo:Na reference. As explained above for the case of CZTSe, both a p-CZTSSe/p^+-$Mo(S_xSe_{1-x})_2$/n-TMO/n^+-FTO favourable back interface and an extra shunt insulation are likely to be the main effects provided by the combination of Mo:Na and n-TMOs. However, comparing the results obtained with CZTSe and CZTSSe devices, it can be observed that the predominance of one effect or the other depends on the TMO employed. This way, TiO_2 exhibits a higher insulting capacity leading to larger shunt resistances both in CZTSe and CZTSSe. However, this can be a double edged sword and TiO_2 can also lead to a high series resistance. On the other hand, V_2O_5 also leads to large performance enhancements while exhibiting a lower R_{sh} but, at the same time, not affecting the R_s of the devices noticeably. This suggest that the beneficial effects of TiO_2 might be predominantly related to shunt insulation while those of V_2O_5 might be principally arising from an electronically improved back interface.

Finally, contrarily to the case of CZTSe, the use of TMOs largely influences the morphology of CZTS and CZTSSe absorbers. In the case of CZTS, the deposition of V_2O_5 and TiO_2 layers leads to a kesterite absorber full of small crystallites which is probably behind the low efficiency of the devices. On the contrary, an absorber layer with very large grains is found for CZTSSe when these TMOs are present. A possible explanation of these differences may be that, similarly to the FTO, these oxides are not inert to S during annealing and the resulting layers influence the growth of the layers growing above them.

5.4.3 Difficulties for band alignment analysis

In order to have a better understanding of the devices and confirm some of the theories expounded above, it would be very useful to perform a band alignment analysis of the different substrate configurations similar to that shown in Figure 89. However, this task cannot be carried out due to the lack of information about the electronic properties of the TMOs. First of all, the work function and conductivity of the oxides are known to be strongly related to their oxidation state which is heavily influenced by the deposition conditions during thermal evaporation and air exposure [295,306]. A clear evidence of this effect is the bandgap observed for MoO_2 which indicates that its oxidation state is MoO_{3-x}. In addition, the TMOs evaporated in this work show bandgap values much larger than those usually reported in the literature due to quantum confinement effects which, logically, strongly modifies band structure and alignment. Finally, contrarily to the works that study TMOs in c-Si and organic electronics, the TMOs are submitted to a high temperature reactive annealing process which further modifies their properties. Thus, all these issues prevent to carry out a correct analysis of the band alignment of the kesterite/TMO interfaces.

5.5 Conclusions

This work demonstrates the viability of fabricating highly efficient kesterite-based devices on SLG/FTO transparent substrates through the combination of thin Mo and TMO layers. This opens the door to advanced kesterite applications such as bifacial and tandem solar cells as well as BIPV glazing which are key for the future of the PV market.

The optical and electrical characterization of the TMO nanolayers evaporated on top of the SLG/FTO substrate has demonstrated the compatibility of these oxides with the fabrication of kesterite devices. The evaporated TMO nanolayers possess very wide bandgaps due to produces quantum confinement effects as a result of their amorphous nature that have to be taken into account when assessing their suitability as hole transport layers. In addition, contrarily to c-Si or OPV technologies, it has been found that the TMOs do not act as hole selective layers in CZTSe solar cells but rather damage the devices by inducing very high series resistances either by getting selenized and damaging contact resistance or, in the case of Se-inert TMOs, by causing a severe electronic barrier.

On the other hand, the addition of a $MoSe_2$ nanolayer between the kesterite absorber and the FTO contact has proved to be fundamental in order to achieve high efficiencies. This layer acts twofold: it reduces the shunting issues encountered in SLG/FTO/CZTSe devices and improves carrier collection. The beneficial effects of $MoSe_2$ are boosted if combined with thin layers of V_2O_5 and TiO_2 TMOs. The mechanisms behind these improvements are not clear and show a complex dependence on layer thickness but they seem related both to the creation of a p-CZTSe/p^+-$MoSe_2$/n-TMO/n^+-FTO complex back interface that provides a more favourable band alignment for hole extraction and to shunt insulation.

The transference of these concepts to wide bandgap CZTS and CZTSSe devices has been very successful. In these cases, besides the aforementioned beneficial effects of $MoSe_2$, $Mo(S_x,Se_{1-x})_2$ layers also prevent the sulphur-induced degradation of FTO during annealing. However, TMOs are only found to boost the beneficial effects of $Mo(S_x,Se_{1-x})_2$ in the case of CZTSSe while they degrade the performance of CZTS devices due to a strong modification of the morphology of the absorbers.

Although this work is mostly a preliminary screening and the characterisation performed in this work is insufficient to fully understand the results obtained, it renders clear that the use of TMO and/or Mo:Na nanolayers is a very promising strategy to improve the limited performance of kesterite devices fabricated on transparent substrates. What is more, the efficiencies achieved here for CZTS (6.1%) and CZTSSe (7.9%) devices are the highest reported for these absorbers using a transparent substrate. As summary and to illustrate the improvements offered by this approach, Figure 103 compares the J-V curves of the reference samples fabricated directly on SLG/FTO and of the record substrate configurations for the different absorbers.

This work shows the large potential of combining $Mo(S_x,Se_{1-x})_2$ and TMOs for kesterite devices fabricated on transparent substrate and lights the way for further research that may provide a deeper insight on the mechanisms behind these complex multilayered interfaces. In particular, a full characterisation of the oxidation state of the TMOs and of the electronic properties of both TMOs and $Mo(S_x,Se_{1-x})_2$ together with a deep electrical characterisation of the devices including the use of n-diode model fitting may allow the study the band alignment from a more theoretical point of view and provide a powerful tool for the optimisation of the devices.

Likewise, the transference of these substrate configurations to ultra-thin kesterite absorbers is of great interest for semi-transparent applications.

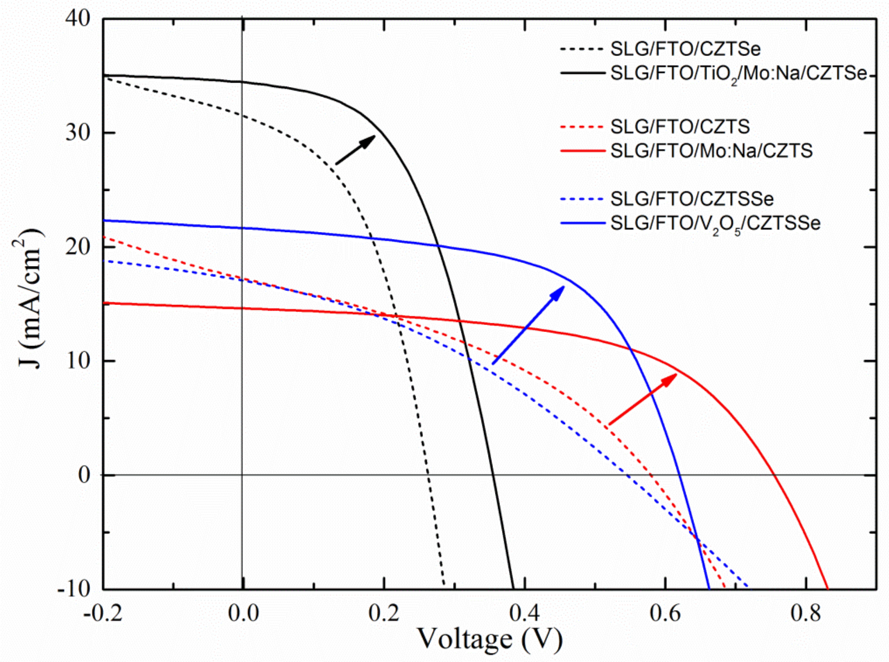

Figure 103. Reference and record J-V curves obtained for CZTSe, CZTS and CZTSSe devices fabricated on SLG/FTO.

6. Conclusions

The work carried out in this thesis demonstrates the feasibility of fabricating sustainable and efficient kesterite solar cells on polyimide, ceramic and SLG/FTO transparent substrates. These substrates are an alternative to the standard SLG/Mo and their combination with a sustainable thin film PV technology based on Earth-abundant materials like kesterites may contribute in decreasing the energy fabrication cost of solar cells and, thus, in increasing the EROI of photovoltaics. This is a critical matter since the development of high EROI and sustainable energy sources that can substitute fossil fuels is a must in order to avoid the collapse of our current civilization.

The advantages of the substrates studied in this work with respect to SLG/Mo that can decrease the energy fabrication costs of kesterite-based PV can be generalized as:

- Possibility of low cost processing through high-throughput production or through integration
- Enabling of advanced applications and functionality

However, these alternative substrates also present several intrinsic limitations for the fabrication of kesterite solar cells that have been individually evaluated. Both the main advantages and limitations found for of each of the substrates are summarized in Table 25. In order to fabricate high efficiency devices, different strategies have been designed, studied and developed to specifically adapt the kesterite solar cell fabrication process to each of the substrates in view of their limitations.

Table 25. Main advantages (green) and limitations (red) of the substrates studied.

Polyimide	Ceramic	SLG/FTO
· Light-weight and flexible · Compatible with roll-to-roll fabrication processes · Suitable for advanced integration concepts	· Direct application in BIPV · High temperature processing	· Enabling of bifacial and tandem solar cells · Possibility of fabricating semi-transparent solar cells
· No alkali content · Low thermal robustness	· High surface roughness · No alkali content · Detrimental impurities	· Challenging p-kesterite/n-TCO interface

Regarding polyimide, extrinsic doping has proved to be fundamental to reduce the efficiency gap with respect to the devices fabricated on SLG. In particular, the pre-deposition treatment doping strategy employing evaporated NaF and KF nanolayers has been shown both to influence the morphology of the kesterite absorbers and, more importantly, to increase carrier concentration and aid in passivation largely improving the performance of the devices. On the contrary, the post-deposition treatment doping strategy has not yielded positive results.

In addition, the maximum temperature employed during the kesterite synthesis annealing process has been limited to below 500ºC to avoid the degradation of the polyimide substrates. Within this limit, the impact of annealing temperature on the devices has been evaluated both for SLG and polyimide. Working at such low temperatures has been observed to cause the formation of a detrimental $SnSe_2$ secondary phase within the kesterite absorber for both substrates that severely degrades the V_{oc} of the devices by, apparently, creating shunt paths. The origin of this phase has been ascribed to a slowdown of the Sn-loss mechanism during the annealing process as a result of the low temperature employed. This affects more strongly the devices fabricated on polyimide due to a hindered heat absorption as a result of the tendency of the samples to bend during annealing. Resonant Raman spectroscopy has allowed not only to detect the presence of very small amounts of $SnSe_2$ but also to directly correlate its concentration with the performance of the devices.

Despite these challenges, a 4.9% efficiency record device has been achieved by combining NaF doping with a Ge nanolayer and employing an annealing temperature of 480ºC. This is the highest efficiency reported to date for a kesterite device fabricated on a polymer substrate. This result proves the feasibility of developing the kesterite PV technology onto this roll-to-roll compatible substrate which opens the door to a future low-cost mass production of kesterite devices.

In the case of ceramic, an innovative approach has been employed to overcome the limitations of the substrate in which a vitreous enamel with a controlled amount of Na_2O in its composition is used a surface smoother, as a Na source and as an impurity diffusion barrier. It has been observed that trying to accommodate large amounts of Na_2O in the enamel results in high densities of three surface defects: undulations, pinholes and cracks. Interestingly, undulations and pinholes do not affect cell performance critically while cracks strongly deteriorate the conductivity of the back contact. However, cracks can be avoided by limiting the amount of Na_2O present in the enamel to below 10%wt. On the other hand, the annealing process has been found to be very critical. With resonant Raman spectroscopy, the formation of $SnSe_2$ could be evidenced for extended annealing times which degraded the performance of the devices by mainly limiting their V_{oc} similarly to the case of polyimide substrates. However, this phase has been completely supressed by re-adjusting and reducing the annealing time. In addition, an effective Na incorporation from the enamel into the kesterite structure as well as the absence of impurities have been confirmed.

As a result of this investigation, two different enamels containing 4 and 6.6% Na_2O have led to a 7.5% record efficiency. This is the highest efficiency reported for a kesterite device fabricated on a commercial ceramic substrate. More importantly, the same process has led to a 7.9% efficiency on a SLG reference processed simultaneously which implies that the enamelled ceramic substrates behave in a similar way to conventional SLG. This proves that the innovative strategy employed in this work is the right direction to follow and shows the great potential of ceramics for the fabrication of sustainable kesterite-based solar tiles which have a direct application in the fast-growing BIPV market.

Concerning the transparent SLG/FTO substrate, the use of transition metal oxides and Mo-based nanolayers has been studied as an approach to improve the non-optimum p-kesterite/n-

FTO interface. The optical and electrical characterization of the TMO nanolayers evaporated on top of the substrates has demonstrated their compatibility with the fabrication of kesterite devices. However, the TMOs exhibit very wide bandgaps compared with commonly reported values due to quantum confinement effects that have to be taken into account for their utilisation as hole selective layers.

The main issue that has been encountered for the fabrication of kesterite devices on SLG/FTO is the presence of shunts that limit the V_{oc} of the devices. Contrarily to organic photovoltaics and c-Si, the use of transition metal oxides at the interface does not to enhance hole transport and collection but, on the contrary, it strongly degrades the series resistance of the devices by introducing a current barrier. On the other hand, the deposition of a Mo:Na nanometric layer and the subsequent formation of $Mo(S_x,Se_{1-x})_2$ at the interface has proved to be fundamental to reduce shunting and, in general, improve the characteristics of the kesterite/FTO junction leading to highly improved devices. In addition, this layer prevents the degradation of FTO during annealing in sulphur-containing atmospheres.

The combination of the different TMOs with Mo:Na does not lead to significant improvements for most of the oxides. However, TiO_2 and V_2O_5 are observed to further increase the performance of $Cu_2ZnSnSe_4$ and $Cu_2ZnSn(S,Se)_4$ devices, respectively, while degrading the performance of Cu_2ZnSnS_4 ones due to a degraded absorber morphology. In addition, an improvement in charge collection towards the back interface is also observed for these substrate configurations although they exhibit a complex behaviour. The improvements observed are tentatively attributed both to an improved shunt insulation and to the likely formation of a p-kesterite/p^+- $Mo(S_x,Se_{1-x})_2$/n-TMO/n^+-FTO complex interface at the back.

Although the complexity of such multi-layered back interface requires further experimentation and characterisation to fully understand the results obtained, it can be concluded that the use of Mo:Na and/or TMO nanolayers is a very promising strategy to improve the performance of kesterite devices fabricated on FTO-based transparent substrates. The best performing devices have been achieved in different substrate configurations depending of the absorber employed. In the case of CZTSe, a 6.2% efficiency device has been obtained employing a SLG/FTO/TiO_2/Mo:Na substrate configuration. On the other hand, a 6.1% efficiency CZTS device has been fabricated on a SLG/FTO/Mo:Na configuration. Finally, a 7.9% efficiency CZTSSe device has been achieved on a SLG/FTO/V_2O_5/Mo:Na substrate configuration. The efficiencies achieved for CZTS and CZTSSe devices are the highest reported for these absorbers on a transparent substrate. Thus, these results demonstrate the viability of developing advanced kesterite applications such as bifacial and tandem solar cells as well as BIPV glazing which are key for the future of the PV market.

To conclude, the results obtained in this thesis are a clear evidence of the feasibility of employing alternative substrates to the standard SLG/Mo for kesterite-based devices. Solar cells with high efficiencies beyond the current state-of-the-art in the respective substrates have been obtained. and achieve high efficiencies. It should be born in mind that most of the work presented here can be considered as a proof-of-concept and that there is still a huge room for improvement mainly by process optimisation and, especially, by the optimisation of the annealing process in the three substrates studied. Thus, owing to the Earth-abundant nature of kesterite solar cells, these results open the way for a future deployment of this PV technology at low cost through mass production, integration (especially in BIPV) and advanced applications which may help in increasing the EROI of photovoltaics.

References

[1] R. Boyd, Energy and the financial system: what every economist, financial analyst, and investor needs to know, Springer, Cham, 2013.

[2] N.M. Ahmed, Failing States, Collapsing Systems, Springer International Publishing, Cham, 2017. doi:10.1007/978-3-319-47816-6.

[3] D. Korowicz, Trade-off: Financial System Supply-Chain Cross-Contagion:, Feasta. (2012) 78.

[4] G.E. Tverberg, Oil supply limits and the continuing financial crisis, Energy. 37 (2012) 27–34. doi:10.1016/j.energy.2011.05.049.

[5] R.F. Malina, S. Kauffman, At Home in the Universe: The Search for the Laws of Self-Organization and Complexity, Leonardo. 29 (1996) 333. doi:10.2307/1576330.

[6] D. LePoire, Interpreting "big history" as complex adaptive system dynamics with nested logistic transitions in energy flow and organization, Emergence Complex. Organ. (2015). doi:10.emerg/10.17357.dbe7c8d6fae7f082c4f33c5b35df8287.

[7] J.A. Tainter, The Collapse of Complex Societies, Cambridge Univ Press, 1988.

[8] G.E. Tverberg, Why energy prices are ultimately headed lower; what the IMF missed, Our Finite World. (2016). https://ourfiniteworld.com/2016/10/11/why-energy-prices-are-ultimately-headed-lower-what-the-imf-missed/ (accessed March 29, 2018).

[9] BP Statistical Review of World Energy 2017, (n.d.) 52.

[10] M. Sato, Thermochemistry of the formation of fossil fuels, Spec Publ-Geochem. Soc. 2 (1990) 271–283.

[11] International Energy Outlook, U.S. Energy Information Administration, 2017. https://www.eia.gov/outlooks/ieo/pdf/0484(2017).pdf (accessed March 13, 2018).

[12] C.A.S. Hall, K.A. Klitgaard, Energy and the wealth of nations: understanding the biophysical economy, Springer Verlag, New York, NY, 2012.

[13] C.A.S. Hall, J.G. Lambert, S.B. Balogh, EROI of different fuels and the implications for society, Energy Policy. 64 (2014) 141–152. doi:10.1016/j.enpol.2013.05.049.

[14] C. Le Quéré, R.M. Andrew, P. Friedlingstein, S. Sitch, J. Pongratz, A.C. Manning, J.I. Korsbakken, G.P. Peters, J.G. Canadell, R.B. Jackson, T.A. Boden, P.P. Tans, O.D. Andrews, V.K. Arora, D.C.E. Bakker, L. Barbero, M. Becker, R.A. Betts, L. Bopp, F. Chevallier, L.P. Chini, P. Ciais, C.E. Cosca, J. Cross, K. Currie, T. Gasser, I. Harris, J. Hauck, V. Haverd, R.A. Houghton, C.W. Hunt, G. Hurtt, T. Ilyina, A.K. Jain, E. Kato, M. Kautz, R.F. Keeling, K. Klein Goldewijk, A. Körtzinger, P. Landschützer, N. Lefèvre, A. Lenton, S. Lienert, I. Lima, D. Lombardozzi, N. Metzl, F. Millero, P.M.S. Monteiro, D.R. Munro, J.E.M.S. Nabel, S. Nakaoka, Y. Nojiri, X.A. Padin, A. Peregon, B. Pfeil, D. Pierrot, B. Poulter, G. Rehder, J. Reimer, C. Rödenbeck, J. Schwinger, R. Séférian, I. Skjelvan, B.D. Stocker, H. Tian, B. Tilbrook, F.N. Tubiello, I.T. van der Laan-Luijkx, G.R. van der Werf, S. van Heuven, N. Viovy, N. Vuichard, A.P. Walker, A.J. Watson, A.J. Wiltshire, S. Zaehle, D. Zhu, Global Carbon Budget 2017, Earth Syst. Sci. Data. 10 (2018) 405–448. doi:10.5194/essd-10-405-2018.

[15] A.P. Ballantyne, C.B. Alden, J.B. Miller, P.P. Tans, J.W.C. White, Increase in observed net carbon dioxide uptake by land and oceans during the past 50 years, Nature. 488 (2012) 70–72. doi:10.1038/nature11299.

[16] M. McNutt, Climate Change Impacts, Science. 341 (2013) 435–435. doi:10.1126/science.1243256.

[17] M. Kampa, E. Castanas, Human health effects of air pollution, Environ. Pollut. 151 (2008) 362–367. doi:10.1016/j.envpol.2007.06.012.

[18] J. Tsao, N. Lewis, G. Crabtree, Solar FAQs, U.S. Department of Energy, 2006.

[19] M. Loster, Total Primary Energy Supply from Sunlight, (2010). http://www.ez2c.de/ml/solar_land_area/ (accessed April 16, 2018).

[20] O. Ellabban, H. Abu-Rub, F. Blaabjerg, Renewable energy resources: Current status, future prospects and their enabling technology, Renew. Sustain. Energy Rev. 39 (2014) 748–764. doi:10.1016/j.rser.2014.07.113.

[21] C. Kost, J.N. Mayer, J. Thomsen, N. Hartmann, C. Senkpiel, S. Philipps, S. Nold, S. Lude, N. Saad, T. Schlegl, Levelized Cost of Electricity Renewable Energy Technologies, Fraunhofer ISE, 2013.

[22] Renewables 2017: Global Status Report., 2017. https://apps.uqo.ca/LoginSigparb/LoginPourRessources.aspx?url=http://www.deslibris.ca/ID/10091341 (accessed April 17, 2018).

[23] J. Lambert, C. Hall, S. Balogh, A. Poisson, A. Gupta, EROI of Global Energy Resources: Preliminary Status, State University of New York, 2012. http://www.dpuc.state.ct.us/DEEPEnergy.nsf/fb04ff2e3777b0b98525797c00471aef/a546c841171f7a8485257ac90053565a/$FILE/R.%20Fromer%20Attachment%20-%20EROI%20of%20Global%20Energy%20Resoruces.pdf (accessed April 25, 2018).

[24] V. Court, F. Fizaine, Long-Term Estimates of the Energy-Return-on-Investment (EROI) of Coal, Oil, and Gas Global Productions, Ecol. Econ. 138 (2017) 145–159. doi:10.1016/j.ecolecon.2017.03.015.

[25] A. Gupta, Energy Return on Energy Invested (EROI) and Energy Payback Time (EPBT) for PVs, in: Compr. Guide Sol. Energy Syst., Elsevier, 2018: pp. 407–425. doi:10.1016/B978-0-12-811479-7.00021-X.

[26] D.J. Murphy, C.A.S. Hall, Energy return on investment, peak oil, and the end of economic growth: EROI, peak oil, and the end of economic growth, Ann. N. Y. Acad. Sci. 1219 (2011) 52–72. doi:10.1111/j.1749-6632.2010.05940.x.

[27] C.A.S. Hall, Energy return on investment, Springer Berlin Heidelberg, New York, NY, 2016.

[28] K.P. Bhandari, J.M. Collier, R.J. Ellingson, D.S. Apul, Energy payback time (EPBT) and energy return on energy invested (EROI) of solar photovoltaic systems: A systematic review and meta-analysis, Renew. Sustain. Energy Rev. 47 (2015) 133–141. doi:10.1016/j.rser.2015.02.057.

[29] T. Trainer, Estimating the EROI of whole systems for 100% renewable electricity supply capable of dealing with intermittency, Energy Policy. 119 (2018) 648–653. doi:10.1016/j.enpol.2018.04.045.

[30] M. Raugei, P. Fullana-i-Palmer, V. Fthenakis, The energy return on energy investment (EROI) of photovoltaics: Methodology and comparisons with fossil fuel life cycles, Energy Policy. 45 (2012) 576–582. doi:10.1016/j.enpol.2012.03.008.

[31] G.E. Tverberg, Intermittent Renewables Can’t Favorably Transform Grid Electricity, Our Finite World. (2016). https://ourfiniteworld.com/2016/08/31/intermittent-renewables-cant-favorably-transform-grid-electricity/ (accessed April 27, 2018).

[32] A.S. Brouwer, M. van den Broek, A. Seebregts, A. Faaij, Impacts of large-scale Intermittent Renewable Energy Sources on electricity systems, and how these can be modeled, Renew. Sustain. Energy Rev. 33 (2014) 443–466. doi:10.1016/j.rser.2014.01.076.

[33] E. Verdolini, F. Vona, D. Popp, Bridging the Gap: Do Fast Reacting Fossil Technologies Facilitate Renewable Energy Diffusion?, National Bureau of Economic Research, 2016.

[34] G.E. Tverberg, Renewables Are Overrated, We Need Cheap Oil – Interview with Gail Tverberg, Our Finite World. (2012). https://ourfiniteworld.com/2012/10/09/renewables-are-overrated-we-need-cheap-oil-interview-with-gail-tverberg/ (accessed March 29, 2018).

[35] E. Becquerel, On electric effects under the influence of solar radiation, Compt Rend. 9 (1839) 561.

[36] W.G. Adams, R.E. Day, The action of light on selenium, Proc. R. Soc. Lond. 25 (1877) 113–117.

[37] D.M. Chapin, C. Fuller, G. Pearson, A new silicon p-n junction photocell for converting solar radiation into electrical power, J. Appl. Phys. 25 (1954) 676–677.

[38] J.J. Loferski, The first forty years: A brief history of the modern photovoltaic age, Prog. Photovolt. Res. Appl. 1 (1993) 67–78. doi:10.1002/pip.4670010109.

[39] P. Würfel, U. Würfel, Physics of Solar Cells, 3rd ed., Wiley-VCH Verlag GmbH & Co. KGaA, 2016.

[40] S. Rühle, Tabulated values of the Shockley–Queisser limit for single junction solar cells, Sol. Energy. 130 (2016) 139–147. doi:10.1016/j.solener.2016.02.015.

[41] M.A. Contreras, K. Ramanathan, J. AbuShama, F. Hasoon, D.L. Young, B. Egaas, R. Noufi, Diode characteristics in state-of-the-art ZnO/CdS/$Cu(In_{1-x}Ga_x)Se_2$ solar cells, Prog. Photovolt. Res. Appl. 13 (2005) 209–216. doi:10.1002/pip.626.

[42] R. Scheer, H.-W. Schock, Chalcogenide Photovoltaics: Physics, Technologies, and Thin Film Devices, Wiley-VCH Verlag GmbH & Co. KGaA, Weinheim, Germany, 2011. doi:10.1002/9783527633708.

[43] D. Feldman, J. Hoskins, R. Margolis, Q4 2017/Q1 2018 Solar Industry Update, (n.d.) 77.

[44] Y. Lee, C. Park, N. Balaji, Y.-J. Lee, V.A. Dao, High-efficiency Silicon Solar Cells: A Review, Isr. J. Chem. 55 (2015) 1050–1063. doi:10.1002/ijch.201400210.

[45] M.A. Green, Crystalline Silicon Photovoltaic Cells, Adv. Mater. 13 (2001) 1019–1022. doi:10.1002/1521-4095(200107)13:12/13<1019::AID-ADMA1019>3.0.CO;2-I.

[46] K. Yoshikawa, H. Kawasaki, W. Yoshida, T. Irie, K. Konishi, K. Nakano, T. Uto, D. Adachi, M. Kanematsu, H. Uzu, K. Yamamoto, Silicon heterojunction solar cell with interdigitated back contacts for a photoconversion efficiency over 26%, Nat. Energy. 2 (2017) 17032. doi:10.1038/nenergy.2017.32.

[47] What Are the Most Efficient Solar Panels of 2019?, ECOtality. (n.d.). https://ecotality.com/most-efficient-solar-panels/ (accessed March 12, 2019).

[48] A. Goetzberger, J. Knobloch, B. Voss, Crystalline silicon solar cells, Wiley, Chichester : New York, 1998.

[49] M.A. Green, Crystalline and thin-film silicon solar cells: state of the art and future potential, Sol. Energy. 74 (2003) 181–192. doi:10.1016/S0038-092X(03)00187-7.

[50] J. Benick, A. Richter, R. Muller, H. Hauser, F. Feldmann, P. Krenckel, S. Riepe, F. Schindler, M.C. Schubert, M. Hermle, A.W. Bett, S.W. Glunz, High-Efficiency n-Type HP mc Silicon Solar Cells, IEEE J. Photovolt. 7 (2017) 1171–1175. doi:10.1109/JPHOTOV.2017.2714139.

[51] D.M. Powell, M.T. Winkler, H.J. Choi, C.B. Simmons, D.B. Needleman, T. Buonassisi, Crystalline silicon photovoltaics: a cost analysis framework for determining technology pathways to reach baseload electricity costs, Energy Environ. Sci. 5 (2012) 5874. doi:10.1039/c2ee03489a.

[52] M.A. Green, Thin-film solar cells: review of materials, technologies and commercial status, J. Mater. Sci. Mater. Electron. 18 (2007) 15–19. doi:10.1007/s10854-007-9177-9.

[53] R.W. Miles, G. Zoppi, I. Forbes, Inorganic photovoltaic cells, Mater. Today. 10 (2007) 20–27. doi:10.1016/S1369-7021(07)70275-4.

[54] T.D. Lee, A.U. Ebong, A review of thin film solar cell technologies and challenges, Renew. Sustain. Energy Rev. 70 (2017) 1286–1297. doi:10.1016/j.rser.2016.12.028.

[55] C. Singh Solanki, Solar Photovoltaics: Fundamentals, Technologies And Applications, PHI Learning Pvt. Ltd., 2015.

[56] T. Matsui, K. Maejima, A. Bidiville, H. Sai, T. Koida, T. Suezaki, M. Matsumoto, K. Saito, I. Yoshida, M. Kondo, High-efficiency thin-film silicon solar cells realized by integrating stable a-Si:H absorbers into improved device design, Jpn. J. Appl. Phys. 54 (2015) 08KB10. doi:10.7567/JJAP.54.08KB10.

[57] M.J. (Mariska) de Wild-Scholten, Energy payback time and carbon footprint of commercial photovoltaic systems, Sol. Energy Mater. Sol. Cells. 119 (2013) 296–305. doi:10.1016/j.solmat.2013.08.037.

[58] D. Bonnet, H. Rabenhorst, New results on the development of a thin-film p-CdTe-n-CdS heterojunction solar cell, in: Photovolt. Spec. Conf. 9 Th Silver Spring Md, 1972: pp. 129–132.

[59] Jesús Rangel-Cárdenas, Hugo Sobral, Optical Absorption Enhancement in CdTe Thin Films by Microstructuration of the Silicon Substrate, Materials. 10 (2017) 607. doi:10.3390/ma10060607.

[60] S. Chander, M.S. Dhaka, Influence of thickness on physical properties of vacuum evaporated polycrystalline CdTe thin films for solar cell applications, Phys. E Low-Dimens. Syst. Nanostructures. 76 (2016) 52–59. doi:10.1016/j.physe.2015.09.044.

[61] A. Polman, M. Knight, E.C. Garnett, B. Ehrler, W.C. Sinke, Photovoltaic materials: Present efficiencies and future challenges, Science. 352 (2016) aad4424–aad4424. doi:10.1126/science.aad4424.

[62] B.L. Williams, J.D. Major, L. Bowen, L. Phillips, G. Zoppi, I. Forbes, K. Durose, Challenges and prospects for developing CdS/CdTe substrate solar cells on Mo foils, Sol. Energy Mater. Sol. Cells. 124 (2014) 31–38. doi:10.1016/j.solmat.2014.01.017.

[63] X. Mathew, J.P. Enriquez, A. Romeo, A.N. Tiwari, CdTe/CdS solar cells on flexible substrates, Sol. Energy. 77 (2004) 831–838. doi:10.1016/j.solener.2004.06.020.

[64] First Solar Press Release. First Solar achieves yet another cell conversion efficiency world record., (2016).

[65] First Solar, Series 6 datasheet, (n.d.). http://www.firstsolar.com/-/media/First-Solar/Technical-Documents/Series-6-Datasheets/Series-6-Datasheet.ashx (accessed March 14, 2019).

[66] First Solar, First Solar’s Sustainability Advantage, (n.d.). http://www.firstsolar.com/-/media/First-Solar/Sustainability-Documents/FSO162-Sustainability-Advantage-vf.ashx (accessed March 15, 2019).

[67] C. Candelise, M. Winskel, R. Gross, Implications for CdTe and CIGS technologies production costs of indium and tellurium scarcity: Effects of indium and tellurium scarcity, Prog. Photovolt. Res. Appl. 20 (2012) 816–831. doi:10.1002/pip.2216.

[68] L.L. Kazmerski, F.R. White, G.K. Morgan, Thin-film $CuInSe_2$/CdS heterojunction solar cells, Appl. Phys. Lett. 29 (1976) 268–270. doi:10.1063/1.89041.

[69] K.L. Chopra, P.D. Paulson, V. Dutta, Thin-film solar cells: an overview, Prog. Photovolt. Res. Appl. 12 (2004) 69–92. doi:10.1002/pip.541.

[70] B.J. Stanbery, Copper Indium Selenides and Related Materials for Photovoltaic Devices, Crit. Rev. Solid State Mater. Sci. 27 (2002) 73–117. doi:10.1080/20014091104215.

[71] V. Izquierdo-Roca, X. Fontané, J. Álvarez-Garcia, L. Calvo-Barrio, A. Pérez-Rodríguez, J.R. Morante, C.M. Ruiz, E. Saucedo, V. Bermúdez, Electrochemical synthesis of $CuIn(S,Se)_2$ alloys with graded composition for high efficiency solar cells, Appl. Phys. Lett. 94 (2009) 061915. doi:10.1063/1.3080654.

[72] T. Kato, $Cu(In,Ga)(Se,S)_2$ solar cell research in Solar Frontier: Progress and current status, Jpn. J. Appl. Phys. 56 (2017) 04CA02. doi:10.7567/JJAP.56.04CA02.

[73] D. Rudmann, D. Brémaud, A.F. da Cunha, G. Bilger, A. Strohm, M. Kaelin, H. Zogg, A.N. Tiwari, Sodium incorporation strategies for CIGS growth at different temperatures, Thin Solid Films. 480–481 (2005) 55–60. doi:10.1016/j.tsf.2004.11.071.

[74] M.A. Contreras, B. Egaas, P. Dippo, J. Webb, J. Granata, K. Ramanathan, S. Asher, A. Swartzlander, R. Noufi, On the role of Na and modifications to $Cu(In, Ga)Se_2$ absorber materials using thin-MF (M= Na, K, Cs) precursor layers, in: Photovolt. Spec. Conf. 1997 Conf. Rec. Twenty-Sixth IEEE, IEEE, 1997: pp. 359–362. http://ieeexplore.ieee.org/xpls/abs_all.jsp?arnumber=654102 (accessed May 30, 2016).

[75] T. Nakada, D. Iga, H. Ohbo, A. Kunioka, Effects of Sodium on Cu(In, Ga)Se_2-Based Thin Films and Solar Cells, Jpn. J. Appl. Phys. 36 (1997) 732–737.

[76] Y. Zhang, J. Han, C. Liao, Investigation of the role of sodium in Cu_2ZnSnS_4 films and the resulting phase evolution during sulfurization, CrystEngComm. 18 (2016) 9026–9032. doi:10.1039/C6CE02041K.

[77] T. Zhang, Y. Yang, D. Liu, S.C. Tse, W. Cao, Z. Feng, S. Chen, L. Qian, High efficiency solution-processed thin-film Cu(In,Ga)$(Se,S)_2$ solar cells, Energy Environ. Sci. 9 (2016) 3674–3681. doi:10.1039/C6EE02352E.

[78] P. Jackson, R. Wuerz, D. Hariskos, E. Lotter, W. Witte, M. Powalla, Effects of heavy alkali elements in Cu(In,Ga)Se_2 solar cells with efficiencies up to 22.6%, Phys. Status Solidi RRL - Rapid Res. Lett. (2016). doi:10.1002/pssr.201600199.

[79] O. Lundberg, M. Edoff, L. Stolt, The effect of Ga-grading in CIGS thin film solar cells, Thin Solid Films. 480–481 (2005) 520–525. doi:10.1016/j.tsf.2004.11.080.

[80] S.H. Sohn, N.S. Han, Y.J. Park, S.M. Park, H.S. An, D.-W. Kim, B.K. Min, J.K. Song, Band gap grading and photovoltaic performance of solution-processed Cu(In,Ga)S_2 thin-film solar cells, Phys Chem Chem Phys. 16 (2014) 27112–27118. doi:10.1039/C4CP03243H.

[81] Solar Frontier Press Release. Solar Frontier Achieves World Record Thin-Film Solar Cell Efficiency of 23.35%, (2019). http://www.solar-frontier.com/eng/news/2019/0117_press.html (accessed June 11, 2019).

[82] Solar Frontier, SFK185-S datasheet, (n.d.). http://www.solar-frontier.com/eng/solutions/products/pdf/SAB12-0745_01_Product_Data_Sheet_SFK185-S.PDF (accessed March 15, 2019).

[83] Y. Chen, P.P. Altermatt, D. Chen, X. Zhang, G. Xu, Y. Yang, Y. Wang, Z. Feng, H. Shen, P.J. Verlinden, From Laboratory to Production: Learning Models of Efficiency and Manufacturing Cost of Industrial Crystalline Silicon and Thin-Film Photovoltaic Technologies, IEEE J. Photovolt. 8 (2018) 1531–1538. doi:10.1109/JPHOTOV.2018.2871858.

[84] A. Gupta, Materials: Abundance, Purification, and the Energy Cost Associated with the Manufacture of Si, CdTe, and CIGS PV, in: Compr. Guide Sol. Energy Syst., Elsevier, 2018: pp. 445–467. doi:10.1016/B978-0-12-811479-7.00023-3.

[85] C. Candelise, J.F. Speirs, R.J.K. Gross, Materials availability for thin film (TF) PV technologies development: A real concern?, Renew. Sustain. Energy Rev. 15 (2011) 4972–4981. doi:10.1016/j.rser.2011.06.012.

[86] V. Fthenakis, Sustainability of photovoltaics: The case for thin-film solar cells, Renew. Sustain. Energy Rev. 13 (2009) 2746–2750. doi:10.1016/j.rser.2009.05.001.

[87] A. Feltrin, A. Freundlich, Material considerations for terawatt level deployment of photovoltaics, Renew. Energy. 33 (2008) 180–185. doi:10.1016/j.renene.2007.05.024.

[88] G. Phipps, C. Mikolajczak, T. Guckes, Indium and gallium: long-term supply, Renew. Energy Focus. 9 (2008) 56–59.

[89] S. Chen, X.G. Gong, A. Walsh, S.-H. Wei, Electronic structure and stability of quaternary chalcogenide semiconductors derived from cation cross-substitution of II-VI and I-III-VI_2 compounds, Phys. Rev. B. 79 (2009). doi:10.1103/PhysRevB.79.165211.

[90] S. Siebentritt, S. Schorr, Kesterites - a challenging material for solar cells, Prog. Photovolt. Res. Appl. 20 (2012) 512–519. doi:10.1002/pip.2156.

[91] C.S. Jiang, I.L. Repins, C. Beall, H.R. Moutinho, K. Ramanathan, M.M. Al-Jassim, Investigation of micro-electrical properties of $Cu_2ZnSnSe_4$ thin films using scanning probe microscopy, Sol. Energy Mater. Sol. Cells. 132 (2015) 342–347. doi:10.1016/j.solmat.2014.08.046.

[92] S. Chen, A. Walsh, X.-G. Gong, S.-H. Wei, Classification of Lattice Defects in the Kesterite Cu_2ZnSnS_4 and $Cu_2ZnSnSe_4$ Earth-Abundant Solar Cell Absorbers, Adv. Mater. 25 (2013) 1522–1539. doi:10.1002/adma.201203146.

[93] K. Ito, T. Nakazawa, Electrical and Optical Properties of Stannite-Type Quaternary Semiconductor Thin Films, Jpn. J. Appl. Phys. 27 (1988) 2094–2097. doi:10.1143/JJAP.27.2094.

[94] H. Katagiri, N. Sasaguchi, S. Hando, S. Hoshino, J. Ohashi, T. Yokota, Preparation and evaluation of Cu_2ZnSnS_4 thin films by sulfurization of E-B evaporated precursors, Sol. Energy Mater. Sol. Cells. 49 (1997) 407–414. doi:10.1016/S0927-0248(97)00119-0.

[95] H. Katagiri, K. Jimbo, S. Yamada, T. Kamimura, W.S. Maw, T. Fukano, T. Ito, T. Motohiro, Enhanced Conversion Efficiencies of Cu_2ZnSnS_4-Based Thin Film Solar Cells by Using Preferential Etching Technique, Appl. Phys. Express. 1 (2008) 041201. doi:10.1143/APEX.1.041201.

[96] D.B. Mitzi, M. Yuan, W. Liu, A.J. Kellock, S.J. Chey, V. Deline, A.G. Schrott, A High-Efficiency Solution-Deposited Thin-Film Photovoltaic Device, Adv. Mater. 20 (2008) 3657–3662. doi:10.1002/adma.200800555.

[97] T.K. Todorov, K.B. Reuter, D.B. Mitzi, High-Efficiency Solar Cell with Earth-Abundant Liquid-Processed Absorber, Adv. Mater. 22 (2010) E156–E159. doi:10.1002/adma.200904155.

[98] W. Wang, M.T. Winkler, O. Gunawan, T. Gokmen, T.K. Todorov, Y. Zhu, D.B. Mitzi, Device Characteristics of CZTSSe Thin-Film Solar Cells with 12.6% Efficiency, Adv. Energy Mater. 4 (2014). doi:10.1002/aenm.201301465.

[99] Z. Wang, N. Brodusch, R. Gauvin, G.P. Demopoulos, Lithium-doped Cu_2ZnSnS_4 superstrate solar cells with 5% efficiency – An alternative to thin film kesterite photovoltaics, Nano Energy. 53 (2018) 130–134. doi:10.1016/j.nanoen.2018.08.049.

[100] M.G. Gang, S.W. Shin, M.P. Suryawanshi, U.V. Ghorpade, Z. Song, J.S. Jang, J.H. Yun, H. Cheong, Y. Yan, J.H. Kim, Band Tail Engineering in Kesterite $Cu_2ZnSn(S,Se)_4$ Thin-Film Solar Cells with 11.8% Efficiency, J. Phys. Chem. Lett. 9 (2018) 4555–4561. doi:10.1021/acs.jpclett.8b01433.

[101] A. Cabas-Vidani, S.G. Haass, C. Andres, R. Caballero, R. Figi, C. Schreiner, J.A. Márquez, C. Hages, T. Unold, D. Bleiner, A.N. Tiwari, Y.E. Romanyuk, High-Efficiency $(Li_xCu_{1-x})_2ZnSn(S,Se)_4$ Kesterite Solar Cells with Lithium Alloying, Adv. Energy Mater. 8 (2018) 1801191. doi:10.1002/aenm.201801191.

[102] T. Schnabel, T. Abzieher, T.M. Friedlmeier, E. Ahlswede, Solution-Based Preparation of $Cu_2ZnSn(S,Se)_4$ for Solar Cells—Comparison of $SnSe_2$ and Elemental Se as Chalcogen Source, IEEE J. Photovolt. 5 (2015) 670–675. doi:10.1109/JPHOTOV.2015.2392935.

[103] Y.S. Lee, T. Gershon, O. Gunawan, T.K. Todorov, T. Gokmen, Y. Virgus, S. Guha, $Cu_2ZnSnSe_4$ Thin-Film Solar Cells by Thermal Co-evaporation with 11.6% Efficiency and Improved Minority Carrier Diffusion Length, Adv. Energy Mater. 5 (2015) 1401372. doi:10.1002/aenm.201401372.

[104] S. Giraldo, E. Saucedo, M. Neuschitzer, F. Oliva, M. Placidi, X. Alcobé, V. Izquierdo-Roca, S. Kim, H. Tampo, H. Shibata, A. Perez-Rodriguez, P. Pistor, How small amounts of Ge modify the formation pathways and crystallization of kesterites, Energy Env. Sci. (2017). doi:10.1039/C7EE02318A.

[105] T. Taskesen, J. Neerken, J. Schoneberg, D. Pareek, V. Steininger, J. Parisi, L. Gütay, Device Characteristics of an 11.4% CZTSe Solar Cell Fabricated from Sputtered Precursors, Adv. Energy Mater. (2018) 1703295. doi:10.1002/aenm.201703295.

[106] C.J. Hages, M.J. Koeper, C.K. Miskin, K.W. Brew, R. Agrawal, Controlled Grain Growth for High Performance Nanoparticle-Based Kesterite Solar Cells, Chem. Mater. 28 (2016) 7703–7714. doi:10.1021/acs.chemmater.6b02733.

[107] L. Vauche, L. Risch, Y. Sánchez, M. Dimitrievska, M. Pasquinelli, T. Goislard de Monsabert, P.-P. Grand, S. Jaime-Ferrer, E. Saucedo, 8.2% pure selenide kesterite thin-film solar cells from large-area electrodeposited precursors, Prog. Photovolt. Res. Appl. 24 (2016) 38–51. doi:10.1002/pip.2643.

[108] C. Yan, J. Huang, K. Sun, S. Johnston, Y. Zhang, H. Sun, A. Pu, M. He, F. Liu, K. Eder, L. Yang, J.M. Cairney, N.J. Ekins-Daukes, Z. Hameiri, J.A. Stride, S. Chen, M.A. Green, X. Hao, Cu_2ZnSnS_4 solar cells with over 10% power conversion efficiency enabled by heterojunction heat treatment, Nat. Energy. 3 (2018) 764–772. doi:10.1038/s41560-018-0206-0.

[109] B. Shin, O. Gunawan, Y. Zhu, N.A. Bojarczuk, S.J. Chey, S. Guha, Thin film solar cell with 8.4% power conversion efficiency using an earth-abundant Cu_2ZnSnS_4 absorber, Prog. Photovolt. Res. Appl. 21 (2013) 72–76. doi:10.1002/pip.1174.

[110] K. Sun, C. Yan, F. Liu, X. Hao, Towards 9% sulfide CZTS solar cells fabricated by a sol-gel process, in: 2018 IEEE 7th World Conf. Photovolt. Energy Convers. WCPEC Jt. Conf. 45th IEEE PVSC 28th PVSEC 34th EU PVSEC, IEEE, Waikoloa Village, HI, 2018: pp. 0856–0858. doi:10.1109/PVSC.2018.8548131.

[111] S. Ahmed, K.B. Reuter, O. Gunawan, L. Guo, L.T. Romankiw, H. Deligianni, A High Efficiency Electrodeposited Cu_2ZnSnS_4 Solar Cell, Adv. Energy Mater. 2 (2012) 253–259. doi:10.1002/aenm.201100526.

[112] W. Shockley, H.J. Queisser, Detailed Balance Limit of Efficiency of p-n Junction Solar Cells, J. Appl. Phys. 32 (1961) 510–519. doi:10.1063/1.1736034.

[113] J. Wu, Y. Hirai, T. Kato, H. Sugimoto, V. Bermudez, New world record efficiency up to 22.9% for Cu(In,Ga)$(Se,S)_2$ thin-film solar cells., in: Waikoloa, HI, USA, 2018.

[114] I.D. Olekseyuk, I.V. Dudchak, L.V. Piskach, Phase equilibria in the Cu_2S–ZnS–SnS_2 system, J. Alloys Compd. 368 (2004) 135–143. doi:10.1016/j.jallcom.2003.08.084.

[115] I.V. Dudchak, L.V. Piskach, Phase equilibria in the Cu_2SnSe_3–$SnSe_2$–ZnSe system, J. Alloys Compd. 351 (2003) 145–150.

[116] X. Liu, Y. Feng, H. Cui, F. Liu, X. Hao, G. Conibeer, D.B. Mitzi, M. Green, The current status and future prospects of kesterite solar cells: a brief review, Prog. Photovolt. Res. Appl. 24 (2016) 879–898. doi:10.1002/pip.2741.

[117] T.J. Huang, X. Yin, G. Qi, H. Gong, CZTS-based materials and interfaces and their effects on the performance of thin film solar cells, Phys. Status Solidi RRL - Rapid Res. Lett. 08 (2014) 735–762. doi:10.1002/pssr.201409219.

[118] I. Repins, C. Beall, N. Vora, C. DeHart, D. Kuciauskas, P. Dippo, B. To, J. Mann, W.-C. Hsu, A. Goodrich, R. Noufi, Co-evaporated $Cu_2ZnSnSe_4$ films and devices, Sol. Energy Mater. Sol. Cells. 101 (2012) 154–159. doi:10.1016/j.solmat.2012.01.008.

[119] A. Fairbrother, E. García-Hemme, V. Izquierdo-Roca, X. Fontané, F.A. Pulgarín-Agudelo, O. Vigil-Galán, A. Pérez-Rodríguez, E. Saucedo, Development of a Selective Chemical Etch To Improve the Conversion Efficiency of Zn-Rich Cu_2ZnSnS_4 Solar Cells, J. Am. Chem. Soc. 134 (2012) 8018–8021. doi:10.1021/ja301373e.

[120] J.J. Scragg, J.T. Wätjen, M. Edoff, T. Ericson, T. Kubart, C. Platzer-Björkman, A Detrimental Reaction at the Molybdenum Back Contact in $Cu_2ZnSn(S,Se)_4$ Thin-Film Solar Cells, J. Am. Chem. Soc. 134 (2012) 19330–19333. doi:10.1021/ja308862n.

[121] H. Katagiri, K. Jimbo, M. Tahara, H. Araki, K. Oishi, The Influence of the Composition Ratio on CZTS-based Thin Film Solar Cells, MRS Proc. 1165 (2009). doi:10.1557/PROC-1165-M04-01.

[122] J.J. Scragg, P.J. Dale, D. Colombara, L.M. Peter, Thermodynamic Aspects of the Synthesis of Thin-Film Materials for Solar Cells, ChemPhysChem. 13 (2012) 3035–3046. doi:10.1002/cphc.201200067.

[123] A. Redinger, D.M. Berg, P.J. Dale, S. Siebentritt, The Consequences of Kesterite Equilibria for Efficient Solar Cells, J. Am. Chem. Soc. 133 (2011) 3320–3323. doi:10.1021/ja111713g.

[124] J.J. Scragg, T. Ericson, T. Kubart, M. Edoff, C. Platzer-Björkman, Chemical Insights into the Instability of Cu_2ZnSnS_4 Films during Annealing, Chem. Mater. 23 (2011) 4625–4633. doi:10.1021/cm202379s.

[125] M. Buffière, G. Brammertz, S. Sahayaraj, M. Batuk, S. Khelifi, D. Mangin, A.-A. El Mel, L. Arzel, J. Hadermann, M. Meuris, J. Poortmans, KCN Chemical Etch for Interface Engineering in $Cu_2ZnSnSe_4$ Solar Cells, ACS Appl. Mater. Interfaces. 7 (2015) 14690–14698. doi:10.1021/acsami.5b02122.

[126] M. Buffière, G. Brammertz, M. Batuk, C. Verbist, D. Mangin, C. Koble, J. Hadermann, M. Meuris, J. Poortmans, Microstructural analysis of 9.7% efficient $Cu_2ZnSnSe_4$ thin film solar cells, Appl. Phys. Lett. 105 (2014) 183903. doi:10.1063/1.4901401.

[127] S. López-Marino, Y. Sánchez, M. Placidi, A. Fairbrother, M. Espindola-Rodríguez, X. Fontané, V. Izquierdo-Roca, J. López-García, L. Calvo-Barrio, A. Pérez-Rodríguez, E. Saucedo, ZnSe Etching of Zn-Rich $Cu_2ZnSnSe_4$: An Oxidation Route for Improved Solar-Cell Efficiency, Chem. - Eur. J. 19 (2013) 14814–14822. doi:10.1002/chem.201302589.

[128] H. Xie, Y. Sánchez, S. López-Marino, M. Espíndola-Rodríguez, M. Neuschitzer, D. Sylla, A. Fairbrother, V. Izquierdo-Roca, A. Pérez-Rodríguez, E. Saucedo, Impact of Sn(S,Se) Secondary Phases in $Cu_2ZnSn(S,Se)_4$ Solar Cells: a Chemical Route for Their Selective Removal and Absorber Surface Passivation, ACS Appl. Mater. Interfaces. 6 (2014) 12744–12751. doi:10.1021/am502609c.

[129] M. Mousel, A. Redinger, R. Djemour, M. Arasimowicz, N. Valle, P. Dale, S. Siebentritt, HCl and Br_2-MeOH etching of $Cu_2ZnSnSe_4$ polycrystalline absorbers, Thin Solid Films. 535 (2013) 83–87. doi:10.1016/j.tsf.2012.12.095.

[130] I. Becerril-Romero, S. Giraldo, S. López-Marino, M. Placidi, Y. Sánchez, D. Sylla, A. Pérez-Rodríguez, E. Saucedo, P. Pistor, Vitreous enamel as sodium source for efficient kesterite solar cells on commercial ceramic tiles, Sol. Energy Mater. Sol. Cells. 154 (2016) 11–17. doi:10.1016/j.solmat.2016.04.035.

[131] I. Becerril-Romero, L. Acebo, F. Oliva, V. Izquierdo-Roca, S. López-Marino, M. Espíndola-Rodríguez, M. Neuschitzer, Y. Sánchez, M. Placidi, A. Pérez-Rodríguez, E. Saucedo, P. Pistor, CZTSe solar cells developed on polymer substrates: Effects of low-temperature processing, Prog. Photovolt. Res. Appl. (2017). doi:10.1002/pip.2945.

[132] T. Schwarz, O. Cojocaru-Mirédin, P. Choi, M. Mousel, A. Redinger, S. Siebentritt, D. Raabe, Atom probe tomography study of internal interfaces in $Cu_2ZnSnSe_4$ thin-films, J. Appl. Phys. 118 (2015) 095302. doi:10.1063/1.4929874.

[133] S. Chen, X.G. Gong, A. Walsh, S.-H. Wei, Crystal and electronic band structure of Cu_2ZnSnX_4 (X=S and Se) photovoltaic absorbers: First-principles insights, Appl. Phys. Lett. 94 (2009) 041903. doi:10.1063/1.3074499.

[134] S. Schorr, The crystal structure of kesterite type compounds: A neutron and X-ray diffraction study, Sol. Energy Mater. Sol. Cells. 95 (2011) 1482–1488. doi:10.1016/j.solmat.2011.01.002.

[135] M. Paris, L. Choubrac, A. Lafond, C. Guillot-Deudon, S. Jobic, Solid-State NMR and Raman Spectroscopy To Address the Local Structure of Defects and the Tricky Issue of the Cu/Zn Disorder in Cu-Poor, Zn-Rich CZTS Materials, Inorg. Chem. 53 (2014) 8646–8653. doi:10.1021/ic5012346.

[136] S. Giraldo, Z. Jehl, M. Placidi, V. Izquierdo-Roca, A. Pérez-Rodríguez, E. Saucedo, Progress and Perspectives of Thin Film Kesterite Photovoltaic Technology: A Critical Review, Adv. Mater. (2019) 1806692. doi:10.1002/adma.201806692.

[137] G. Rey, G. Larramona, S. Bourdais, C. Choné, B. Delatouche, A. Jacob, G. Dennler, S. Siebentritt, On the origin of band-tails in kesterite, Sol. Energy Mater. Sol. Cells. 179 (2018) 142–151. doi:10.1016/j.solmat.2017.11.005.

[138] S. Kim, J.-S. Park, A. Walsh, Identification of Killer Defects in Kesterite Thin-Film Solar Cells, ACS Energy Lett. 3 (2018) 496–500. doi:10.1021/acsenergylett.7b01313.

[139] T. Gokmen, O. Gunawan, T.K. Todorov, D.B. Mitzi, Band tailing and efficiency limitation in kesterite solar cells, Appl. Phys. Lett. 103 (2013) 103506. doi:10.1063/1.4820250.

[140] M. Neuschitzer, Y. Sanchez, T. Olar, T. Thersleff, S. Lopez-Marino, F. Oliva, M. Espindola-Rodriguez, H. Xie, M. Placidi, V. Izquierdo-Roca, I. Lauermann, K. Leifer, A. Pérez-

Rodriguez, E. Saucedo, Complex Surface Chemistry of Kesterites: Cu/Zn Reordering after Low Temperature Postdeposition Annealing and Its Role in High Performance Devices, Chem. Mater. 27 (2015) 5279–5287. doi:10.1021/acs.chemmater.5b01473.

[141] G. Rey, A. Redinger, J. Sendler, T.P. Weiss, M. Thevenin, M. Guennou, B. El Adib, S. Siebentritt, The band gap of $Cu_2ZnSnSe_4$: Effect of order-disorder, Appl. Phys. Lett. 105 (2014) 112106. doi:10.1063/1.4896315.

[142] S. De Wolf, J. Holovsky, S.-J. Moon, P. Löper, B. Niesen, M. Ledinsky, F.-J. Haug, J.-H. Yum, C. Ballif, Organometallic Halide Perovskites: Sharp Optical Absorption Edge and Its Relation to Photovoltaic Performance, J. Phys. Chem. Lett. 5 (2014) 1035–1039. doi:10.1021/jz500279b.

[143] O. Gunawan, T.K. Todorov, D.B. Mitzi, Loss mechanisms in hydrazine-processed $Cu_2ZnSn(Se,S)_4$ solar cells, Appl. Phys. Lett. 97 (2010) 233506. doi:10.1063/1.3522884.

[144] D.A.R. Barkhouse, O. Gunawan, T. Gokmen, T.K. Todorov, D.B. Mitzi, Device characteristics of a 10.1% hydrazine-processed $Cu_2ZnSn(Se,S)_4$ solar cell: Characteristics of a 10.1% efficient kesterite solar cell, Prog. Photovolt. Res. Appl. 20 (2012) 6–11. doi:10.1002/pip.1160.

[145] J.J. Scragg, T. Ericson, X. Fontané, V. Izquierdo-Roca, A. Pérez-Rodríguez, T. Kubart, M. Edoff, C. Platzer-Björkman, Rapid annealing of reactively sputtered precursors for Cu_2ZnSnS_4 solar cells, Prog. Photovolt. Res. Appl. 22 (2014) 10–17. doi:10.1002/pip.2265.

[146] S. López-Marino, M. Placidi, A. Pérez-Tomás, J. Llobet, V. Izquierdo-Roca, X. Fontané, A. Fairbrother, M. Espíndola-Rodríguez, D. Sylla, A. Pérez-Rodríguez, E. Saucedo, Inhibiting the absorber/Mo-back contact decomposition reaction in $Cu_2ZnSnSe_4$ solar cells: the role of a ZnO intermediate nanolayer, J. Mater. Chem. A. 1 (2013) 8338. doi:10.1039/c3ta11419h.

[147] S. Lopez-Marino, M. Espíndola-Rodríguez, Y. Sánchez, X. Alcobé, F. Oliva, H. Xie, M. Neuschitzer, S. Giraldo, M. Placidi, R. Caballero, V. Izquierdo-Roca, A. Pérez-Rodríguez, E. Saucedo, The importance of back contact modification in $Cu_2ZnSnSe_4$ solar cells: The role of a thin MoO_2 layer, Nano Energy. 26 (2016) 708–721. doi:10.1016/j.nanoen.2016.06.034.

[148] I.L. Repins, H. Moutinho, S.G. Choi, A. Kanevce, D. Kuciauskas, P. Dippo, C.L. Beall, J. Carapella, C. DeHart, B. Huang, S.H. Wei, Indications of short minority-carrier lifetime in kesterite solar cells, J. Appl. Phys. 114 (2013) 084507. doi:10.1063/1.4819849.

[149] F. Oliva, S. Giraldo, L. Arqués, L. Calvo-Barrio, A. Perez-Rodriguez, E. Saucedo, V. Izquerdo-Roca, Raman, PL and AES characterization of mm- and µm-scale inhomogeneities in CZTSe absorbers: potential impact on the Voc deficit, in: EMRS Spring Meet., Strasbourg, 2018.

[150] I.L. Repins, M.J. Romero, J.V. Li, S.-H. Wei, D. Kuciauskas, C.-S. Jiang, C. Beall, C. DeHart, J. Mann, W.-C. Hsu, G. Teeter, A. Goodrich, R. Noufi, Kesterite Successes, Ongoing Work, and Challenges: A Perspective From Vacuum Deposition, IEEE J. Photovolt. 3 (2013) 439–445. doi:10.1109/JPHOTOV.2012.2215842.

[151] R. Aninat, L.-E. Quesada-Rubio, E. Sanchez-Cortezon, J.-M. Delgado-Sanchez, Mapping and comparison of the shortcomings of kesterite absorber layers, and how they could affect industrial scalability, Thin Solid Films. 633 (2017) 146–150. doi:10.1016/j.tsf.2016.10.007.

[152] L. Grenet, M.A.A. Suzon, F. Emieux, F. Roux, Analysis of Failure Modes in Kesterite Solar Cells, ACS Appl. Energy Mater. 1 (2018) 2103–2113. doi:10.1021/acsaem.8b00194.

[153] Y. Sun, S. Lin, W. Li, S. Cheng, Y. Zhang, Y. Liu, W. Liu, Review on Alkali Element Doping in $Cu(In,Ga)Se_2$ Thin Films and Solar Cells, Engineering. 3 (2017) 452–459. doi:10.1016/J.ENG.2017.04.020.

[154] P.M.P. Salomé, H. Rodriguez-Alvarez, S. Sadewasser, Incorporation of alkali metals in chalcogenide solar cells, Sol. Energy Mater. Sol. Cells. 143 (2015) 9–20. doi:10.1016/j.solmat.2015.06.011.

[155] J. Hedström, M. Bodegárd, A. Kylner, L. Stolt, D. Hariskos, ZnO/CdS/Cu(In,Ga)Se_2 thin film solar cells with improved performance, in: Conf. Rec. Twenty Third IEEE Photovolt. Spec. Conf. - 1993 Cat No93CH3283-9, 1993: p. 8.

[156] M. Bodegárd, L. Stolt, J. Hedström, The influence of sodium on the grain structure of $CuInSe_2$ films for photovoltaic applications, in: Twelfth Eur. Photovolt. Sol. Energy Conf. Proc. Int. Conf., 1994.

[157] S.G. Haass, C. Andres, R. Figi, C. Schreiner, M. Bürki, Y.E. Romanyuk, A.N. Tiwari, Complex Interplay between Absorber Composition and Alkali Doping in High-Efficiency Kesterite Solar Cells, Adv. Energy Mater. (2017) 1701760. doi:10.1002/aenm.201701760.

[158] S. López-Marino, Y. Sánchez, M. Espíndola-Rodríguez, X. Alcobé, H. Xie, M. Neuschitzer, I. Becerril, S. Giraldo, M. Dimitrievska, M. Placidi, L. Fourdrinier, V. Izquierdo-Roca, A. Pérez-Rodríguez, E. Saucedo, Alkali doping strategies for flexible and light-weight $Cu_2ZnSnSe_4$ solar cells, J Mater Chem A. 4 (2016) 1895–1907. doi:10.1039/C5TA09640E.

[159] T. Maeda, A. Kawabata, T. Wada, First-principles study on alkali-metal effect of Li, Na, and K in Cu_2ZnSnS_4 and $Cu_2ZnSnSe_4$, Phys. Status Solidi C. 12 (2015) 631–637. doi:10.1002/pssc.201400345.

[160] T. Maeda, A. Kawabata, T. Wada, First-principles study on alkali-metal effect of Li, Na, and K in $CuInSe_2$ and $CuGaSe_2$, Jpn. J. Appl. Phys. 54 (2015) 08KC20. doi:10.7567/JJAP.54.08KC20.

[161] Z.-K. Yuan, S. Chen, Y. Xie, J.-S. Park, H. Xiang, X.-G. Gong, S.-H. Wei, Na-Diffusion Enhanced p-type Conductivity in Cu(In,Ga)Se_2: A New Mechanism for Efficient Doping in Semiconductors, Adv. Energy Mater. (2016) 1601191. doi:10.1002/aenm.201601191.

[162] T. Gershon, B. Shin, N. Bojarczuk, M. Hopstaken, D.B. Mitzi, S. Guha, The Role of Sodium as a Surfactant and Suppressor of Non-Radiative Recombination at Internal Surfaces in Cu_2ZnSnS_4, Adv. Energy Mater. 5 (2015) n/a-n/a. doi:10.1002/aenm.201400849.

[163] C.M. Sutter-Fella, J.A. Stückelberger, H. Hagendorfer, F. La Mattina, L. Kranz, S. Nishiwaki, A.R. Uhl, Y.E. Romanyuk, A.N. Tiwari, Sodium Assisted Sintering of Chalcogenides and Its Application to Solution Processed $Cu_2ZnSn(S,Se)_4$ Thin Film Solar Cells, Chem. Mater. 26 (2014) 1420–1425. doi:10.1021/cm403504u.

[164] W.M. Hlaing Oo, J.L. Johnson, A. Bhatia, E.A. Lund, M.M. Nowell, M.A. Scarpulla, Grain Size and Texture of Cu_2ZnSnS_4 Thin Films Synthesized by Cosputtering Binary Sulfides and Annealing: Effects of Processing Conditions and Sodium, J. Electron. Mater. 40 (2011) 2214–2221. doi:10.1007/s11664-011-1729-3.

[165] M. Johnson, S.V. Baryshev, E. Thimsen, M. Manno, X. Zhang, I.V. Veryovkin, C. Leighton, E.S. Aydil, Alkali-metal-enhanced grain growth in Cu_2ZnSnS_4 thin films, Energy Env. Sci. 7 (2014) 1931–1938. doi:10.1039/C3EE44130J.

[166] Y. Li, Q. Han, T.W. Kim, W. Shi, The optical influence of Na on $Cu_2ZnSnSe_4$ films deposited with Na-containing sol–gel precursor, J. Sol-Gel Sci. Technol. 69 (2014) 260–265. doi:10.1007/s10971-013-3210-7.

[167] T. Prabhakar, N. Jampana, Effect of sodium diffusion on the structural and electrical properties of Cu_2ZnSnS_4 thin films, Sol. Energy Mater. Sol. Cells. 95 (2011) 1001–1004. doi:10.1016/j.solmat.2010.12.012.

[168] J.V. Li, D. Kuciauskas, M.R. Young, I.L. Repins, Effects of sodium incorporation in Co-evaporated $Cu_2ZnSnSe_4$ thin-film solar cells, Appl. Phys. Lett. 102 (2013) 163905. doi:10.1063/1.4802972.

[169] X. Liu, H. Cui, C. Kong, X. Hao, Y. Huang, F. Liu, N. Song, G. Conibeer, M. Green, Rapid thermal annealed Molybdenum back contact for Cu_2ZnSnS_4 thin film solar cells, Appl. Phys. Lett. 106 (2015) 131110. doi:10.1063/1.4916994.

[170] K. Sun, F. Liu, C. Yan, F. Zhou, J. Huang, Y. Shen, R. Liu, X. Hao, Influence of sodium incorporation on kesterite Cu_2ZnSnS_4 solar cells fabricated on stainless steel substrates, Sol. Energy Mater. Sol. Cells. 157 (2016) 565–571. doi:10.1016/j.solmat.2016.07.036.

[171] K.-J. Yang, J.-H. Sim, B. Jeon, D.-H. Son, D.-H. Kim, S.-J. Sung, D.-K. Hwang, S. Song, D.B. Khadka, J. Kim, J.-K. Kang, Effects of Na and MoS_2 on Cu_2ZnSnS_4 thin-film solar cell, Prog. Photovolt. Res. Appl. 23 (2015) 862–873. doi:10.1002/pip.2500.

[172] J.B. Li, V. Chawla, B.M. Clemens, Investigating the Role of Grain Boundaries in CZTS and CZTSSe Thin Film Solar Cells with Scanning Probe Microscopy, Adv. Mater. 24 (2012) 720–723. doi:10.1002/adma.201103470.

[173] A. Nagaoka, H. Miyake, T. Taniyama, K. Kakimoto, Y. Nose, M.A. Scarpulla, K. Yoshino, Effects of sodium on electrical properties in Cu_2ZnSnS_4 single crystal, Appl. Phys. Lett. 104 (2014) 152101. doi:10.1063/1.4871208.

[174] G. Altamura, C. Roger, L. Grenet, J. Bleuse, H. Fournier, S. Perraud, H. Mariette, Influence of sodium-containing substrates on Kesterite CZTSSe thin films based solar cells, in: MRS Proc., Cambridge Univ Press, 2013: pp. 103–106. http://journals.cambridge.org/abstract_S1946427413010002 (accessed May 30, 2016).

[175] J.E. Granata, J.R. Sites, S. Asher, R.J. Matson, Quantitative incorporation of sodium in $CuInSe_2$ and $Cu(In,Ga)Se_2$ photovoltaic devices, in: Photovolt. Spec. Conf. 1997 Conf. Rec. Twenty-Sixth IEEE, IEEE, 1997: pp. 387–390. http://ieeexplore.ieee.org/xpls/abs_all.jsp?arnumber=654109 (accessed May 30, 2016).

[176] D. Braunger, D. Hariskos, G. Bilger, U. Rau, H.W. Schock, Influence of sodium on the growth of polycrystalline $Cu(In,Ga)Se_2$ thin films, Thin Solid Films. 361–362 (2000) 161–166.

[177] A. Rockett, J.S. Britt, T. Gillespie, C. Marshall, M.M. Al-Jassim, F. Hasoon, R. Matson, B. Basol, Na in selenized $Cu(In,Ga)Se_2$ on Na-containing and Na-free glasses: distribution, grain structure, and device performances, Thin Solid Films. 372 (2000) 212–217.

[178] R.V. Forest, E. Eser, B.E. McCandless, R.W. Birkmire, J.G. Chen, Understanding the role of oxygen in the segregation of sodium at the surface of molybdenum coated soda-lime glass, AIChE J. 60 (2014) 2365–2372. doi:10.1002/aic.14425.

[179] P.M.P. Salomé, V. Fjallstrom, A. Hultqvist, P. Szaniawski, U. Zimmermann, M. Edoff, The effect of Mo back contact ageing on $Cu(In,Ga)Se_2$ thin-film solar cells: Effect of Mo back contact ageing on CIGS solar cells, Prog. Photovolt. Res. Appl. 22 (2014) 83–89. doi:10.1002/pip.2360.

[180] M. Bodegård, K. Granath, L. Stolt, A. Rockett, The behaviour of Na implanted into Mo thin films during annealing, Sol. Energy Mater. (1999) 10.

[181] P. Blösch, S. Nishiwaki, L. Kranz, C.M. Fella, F. Pianezzi, T. Jäger, C. Adelhelm, E. Franzke, S. Buecheler, A.N. Tiwari, Sodium-doped molybdenum back contact designs for $Cu(In,Ga)Se_2$ solar cells, Sol. Energy Mater. Sol. Cells. 124 (2014) 10–16. doi:10.1016/j.solmat.2014.01.020.

[182] P. Blösch, S. Nishiwaki, A. Chirilă, L. Kranz, C. Fella, F. Pianezzi, C. Adelhelm, E. Franzke, S. Buecheler, A.N. Tiwari, Sodium-doped molybdenum back contacts for flexible $Cu(In,Ga)Se_2$ solar cells, Thin Solid Films. 535 (2013) 214–219. doi:10.1016/j.tsf.2012.10.080.

[183] J.H. Yun, K.H. Kim, M.S. Kim, B.T. Ahn, S.J. Ahn, J.C. Lee, K.H. Yoon, Fabrication of CIGS solar cells with a Na-doped Mo layer on a Na-free substrate, Thin Solid Films. 515 (2007) 5876–5879. doi:10.1016/j.tsf.2006.12.156.

[184] M. Bodegård, K. Granath, L. Stolt, Growth of $Cu(In,Ga)Se_2$ thin films by coevaporation using alkaline precursors, Thin Solid Films. 361 (2000) 9–16.

[185] A. Mule, B. Vermang, M. Sylvester, G. Brammertz, S. Ranjbar, T. Schnabel, N. Gampa, M. Meuris, J. Poortmans, Effect of different alkali (Li, Na, K, Rb, Cs) metals on $Cu_2ZnSnSe_4$ solar cells, Thin Solid Films. (2016). doi:10.1016/j.tsf.2016.11.027.

[186] Y.-T. Hsieh, Q. Han, C. Jiang, T.-B. Song, H. Chen, L. Meng, H. Zhou, Y. Yang, Efficiency Enhancement of $Cu_2ZnSn(S,Se)_4$ Solar Cells via Alkali Metals Doping, Adv. Energy Mater. 6 (2016) 1502386. doi:10.1002/aenm.201502386.

[187] S.G. Haass, M. Diethelm, M. Werner, B. Bissig, Y.E. Romanyuk, A.N. Tiwari, 11.2% Efficient Solution Processed Kesterite Solar Cell with a Low Voltage Deficit, Adv. Energy Mater. 5 (2015) 1500712. doi:10.1002/aenm.201500712.

[188] A. Chirilă, S. Buecheler, F. Pianezzi, P. Bloesch, C. Gretener, A.R. Uhl, C. Fella, L. Kranz, J. Perrenoud, S. Seyrling, R. Verma, S. Nishiwaki, Y.E. Romanyuk, G. Bilger, A.N. Tiwari, Highly efficient $Cu(In,Ga)Se_2$ solar cells grown on flexible polymer films, Nat. Mater. 10 (2011) 857–861. doi:10.1038/nmat3122.

[189] P. Jackson, D. Hariskos, R. Wuerz, W. Wischmann, M. Powalla, Compositional investigation of potassium doped $Cu(In,Ga)Se_2$ solar cells with efficiencies up to 20.8%, Phys. Status Solidi RRL - Rapid Res. Lett. 8 (2014) 219–222. doi:10.1002/pssr.201409040.

[190] A. Chirilă, P. Reinhard, F. Pianezzi, P. Bloesch, A.R. Uhl, C. Fella, L. Kranz, D. Keller, C. Gretener, H. Hagendorfer, D. Jaeger, R. Erni, S. Nishiwaki, S. Buecheler, A.N. Tiwari, Potassium-induced surface modification of $Cu(In,Ga)Se_2$ thin films for high-efficiency solar cells, Nat. Mater. 12 (2013) 1107–1111. doi:10.1038/nmat3789.

[191] P. Jackson, D. Hariskos, R. Wuerz, O. Kiowski, A. Bauer, T.M. Friedlmeier, M. Powalla, Properties of $Cu(In,Ga)Se_2$ solar cells with new record efficiencies up to 21.7%, Phys. Status Solidi RRL - Rapid Res. Lett. 9 (2015) 28–31. doi:10.1002/pssr.201409520.

[192] A. Laemmle, R. Wuerz, M. Powalla, Efficiency enhancement of $Cu(In,Ga)Se_2$ thin-film solar cells by a post-deposition treatment with potassium fluoride, Phys. Status Solidi RRL - Rapid Res. Lett. 7 (2013) 631–634. doi:10.1002/pssr.201307238.

[193] A. Laemmle, R. Wuerz, M. Powalla, Investigation of the effect of potassium on $Cu(In,Ga)Se_2$ layers and solar cells, Thin Solid Films. 582 (2015) 27–30. doi:10.1016/j.tsf.2014.10.088.

[194] P. Reinhard, B. Bissig, F. Pianezzi, E. Avancini, H. Hagendorfer, D. Keller, P. Fuchs, M. Döbeli, C. Vigo, P. Crivelli, S. Nishiwaki, S. Buecheler, A.N. Tiwari, Features of KF and NaF Postdeposition Treatments of $Cu(In,Ga)Se_2$ Absorbers for High Efficiency Thin Film Solar Cells, Chem. Mater. 27 (2015) 5755–5764. doi:10.1021/acs.chemmater.5b02335.

[195] R. Wuerz, A. Eicke, F. Kessler, S. Paetel, S. Efimenko, C. Schlegel, CIGS thin-film solar cells and modules on enamelled steel substrates, Sol. Energy Mater. Sol. Cells. 100 (2012) 132–137. doi:10.1016/j.solmat.2012.01.004.

[196] S.G. Haass, M. Diethelm, C. Andres, Y.E. Romanyuk, A.N. Tiwari, Potassium post deposition treatment of solution-processed kesterite solar cells, Thin Solid Films. (2016). doi:10.1016/j.tsf.2016.11.012.

[197] G. Rey, F. Babbe, T.P. Weiss, H. Elanzeery, M. Melchiorre, N. Valle, B.E. Adib, S. Siebentritt, Post-deposition treatment of $Cu_2ZnSnSe_4$ with alkalis, Thin Solid Films. 633 (2017) 162–165. doi:10.1016/j.tsf.2016.11.021.

[198] W. Li, Z. Su, J.M.R. Tan, S.Y. Chiam, H.L. Seng, S. Magdassi, L.H. Wong, Revealing the Role of Potassium Treatment in CZTSSe Thin Film Solar Cells, Chem. Mater. 29 (2017) 4273–4281. doi:10.1021/acs.chemmater.7b00418.

[199] S.G. Haass, C. Andres, R. Figi, C. Schreiner, M. Bürki, A.N. Tiwari, Y.E. Romanyuk, Effects of potassium on kesterite solar cells: Similarities, differences and synergies with sodium, AIP Adv. 8 (2018) 015133. doi:10.1063/1.5013114.

[200] Z. Tong, C. Yan, Z. Su, F. Zeng, J. Yang, Y. Li, L. Jiang, Y. Lai, F. Liu, Effects of potassium doping on solution processed kesterite Cu_2ZnSnS_4 thin film solar cells, Appl. Phys. Lett. 105 (2014) 223903. doi:10.1063/1.4903500.

[201] M.F. Ashby, Material profiles, in: Mater. Environ., Elsevier, 2013: pp. 459–595. doi:10.1016/B978-0-12-385971-6.00015-4.

[202] S. Yazici, M.A. Olgar, F.G. Akca, A. Cantas, M. Kurt, G. Aygun, E. Tarhan, E. Yanmaz, L. Ozyuzer, Growth of Cu_2ZnSnS_4 absorber layer on flexible metallic substrates for thin film solar cell applications, Thin Solid Films. 589 (2015) 563–573. doi:10.1016/j.tsf.2015.06.028.

[203] G. Altamura, L. Grenet, C. Roger, F. Roux, V. Reita, R. Fillon, H. Fournier, S. Perraud, H. Mariette, Alternative back contacts in kesterite $Cu_2ZnSn(S_{1-x}Se_x)_4$ thin film solar cells, J. Renew. Sustain. Energy. 6 (2014) 011401. doi:10.1063/1.4831781.

[204] T.E. Everhart, R.F.M. Thornley, Wide-band detector for micro-microampere low-energy electron currents, J. Sci. Instrum. 37 (1960) 246–248. doi:10.1088/0950-7671/37/7/307.

[205] A. Fairbrother, X. Fontané, V. Izquierdo-Roca, M. Placidi, D. Sylla, M. Espindola-Rodriguez, S. López-Mariño, F.A. Pulgarín, O. Vigil-Galán, A. Pérez-Rodríguez, E. Saucedo, Secondary phase formation in Zn-rich $Cu_2ZnSnSe_4$-based solar cells annealed in low pressure and temperature conditions, Prog. Photovolt. Res. Appl. 22 (2014) 479–487. doi:10.1002/pip.2473.

[206] S. Giraldo, M. Neuschitzer, T. Thersleff, S. López-Marino, Y. Sánchez, H. Xie, M. Colina, M. Placidi, P. Pistor, V. Izquierdo-Roca, K. Leifer, A. Pérez-Rodríguez, E. Saucedo, Large Efficiency Improvement in $Cu_2ZnSnSe_4$ Solar Cells by Introducing a Superficial Ge Nanolayer, Adv. Energy Mater. (2015). doi:10.1002/aenm.201501070.

[207] Y. Sánchez, Síntesis química de capas buffer para nueas tecnologías de calcogenuros con aplicaciones fotovoltaicas, Universitat de Barcelona, 2016. http://hdl.handle.net/10803/396668.

[208] K. Sardashti, R. Haight, T. Gokmen, W. Wang, L.-Y. Chang, D.B. Mitzi, A.C. Kummel, Impact of Nanoscale Elemental Distribution in High-Performance Kesterite Solar Cells, Adv. Energy Mater. 5 (2015) n/a-n/a. doi:10.1002/aenm.201402180.

[209] D. Hironiwa, N. Sakai, T. Kato, H. Sugimoto, Z. Tang, J. Chantana, T. Minemoto, Impact of annealing treatment before buffer layer deposition on Cu2ZnSn(S,Se)4 solar cells, Thin Solid Films. 582 (2015) 151–153. doi:10.1016/j.tsf.2014.11.016.

[210] US Department of Energy, Quadrennial Technology Review 2015. Roll to Roll Processing. Chapter 6: Technology Assessments, (2015). https://www.energy.gov/sites/prod/files/2016/02/f30/QTR2015-6K-Roll-to-Roll-Processing.pdf (accessed March 4, 2019).

[211] Q. Tian, X. Xu, L. Han, M. Tang, R. Zou, Z. Chen, M. Yu, J. Yang, J. Hu, Hydrophilic Cu_2ZnSnS_4 nanocrystals for printing flexible, low-cost and environmentally friendly solar cells, CrystEngComm. 14 (2012) 3847. doi:10.1039/c2ce06552e.

[212] C.-Y. Peng, T.P. Dhakal, S. Garner, P. Cimo, S. Lu, C.R. Westgate, Fabrication of Cu2ZnSnS4 solar cell on a flexible glass substrate, Thin Solid Films. 562 (2014) 574–577. doi:10.1016/j.tsf.2014.03.054.

[213] Y. Zhang, Q. Ye, J. Liu, H. Chen, X. He, C. Liao, J. Han, H. Wang, J. Mei, W. Lau, Earth-abundant and low-cost CZTS solar cell on flexible molybdenum foil, RSC Adv. 4 (2014) 23666. doi:10.1039/c4ra02064b.

[214] T. Todorov, J. Olenick, K. AOlenick, O. Gunawan, T. Gershon, C. Sturdevant, Y.S. Lee, L. Chang, S. Guha, Flexible kesterite solar cells on ceramic substrates for advanced thermal processing, in: Photovolt. Spec. Conf. PVSC 2015 IEEE 42nd, IEEE, 2015: pp. 1–3. http://ieeexplore.ieee.org/xpls/abs_all.jsp?arnumber=7356189 (accessed January 10, 2017).

[215] K.-J. Yang, S. Kim, J.-H. Sim, D.-H. Son, D.-H. Kim, J. Kim, W. Jo, H. Yoo, J. Kim, J.-K. Kang, The alterations of carrier separation in kesterite solar cells, Nano Energy. 52 (2018) 38–53. doi:10.1016/j.nanoen.2018.07.039.

[216] M. Boshta, S. Binetti, A. Le Donne, M. Gomaa, M. Acciarri, A chemical deposition process for low-cost CZTS solar cell on flexible substrates, Mater. Technol. (2016) 1–5. doi:10.1080/10667857.2016.1200837.

[217] Z. Zhou, Y. Wang, D. Xu, Y. Zhang, Fabrication of Cu_2ZnSnS_4 screen printed layers for solar cells, Sol. Energy Mater. Sol. Cells. 94 (2010) 2042–2045. doi:10.1016/j.solmat.2010.06.010.

[218] J. Xu, Z. Cao, Y. Yang, Z. Xie, Fabrication of Cu_2ZnSnS_4 thin films on flexible polyimide substrates by sputtering and post-sulfurization, J. Renew. Sustain. Energy. 6 (2014) 053110. doi:10.1063/1.4896696.

[219] O. Gunawan, T. Gokmen, C.W. Warren, J.D. Cohen, T.K. Todorov, D.A.R. Barkhouse, S. Bag, J. Tang, B. Shin, D.B. Mitzi, Electronic properties of the $Cu_2ZnSn(Se,S)_4$ absorber layer in solar cells as revealed by admittance spectroscopy and related methods, Appl. Phys. Lett. 100 (2012) 253905. doi:10.1063/1.4729751.

[220] F. Oliva, S. Kretzschmar, D. Colombara, S. Tombolato, C.M. Ruiz, A. Redinger, E. Saucedo, C. Broussillou, T.G. de Monsabert, T. Unold, P.J. Dale, V. Izquierdo-Roca, A. Pérez-Rodríguez, Optical methodology for process monitoring of chalcopyrite photovoltaic technologies: Application to low cost $Cu(In,Ga)(S,Se)_2$ electrodeposition based processes, Sol. Energy Mater. Sol. Cells. 158 (2016) 168–183. doi:10.1016/j.solmat.2015.12.036.

[221] C.M. Fella, A.R. Uhl, C. Hammond, I. Hermans, Y.E. Romanyuk, A.N. Tiwari, Formation mechanism of $Cu_2ZnSnSe_4$ absorber layers during selenization of solution deposited metal precursors, J. Alloys Compd. 567 (2013) 102–106. doi:10.1016/j.jallcom.2013.03.056.

[222] J.T. Heath, J.D. Cohen, W.N. Shafarman, Bulk and metastable defects in $CuIn_{1-x}Ga_xSe_2$ thin films using drive-level capacitance profiling, J. Appl. Phys. 95 (2004) 1000–1010. doi:10.1063/1.1633982.

[223] P.A. Fernandes, M.G. Sousa, P.M.P. Salomé, J.P. Leitão, A.F. da Cunha, Thermodynamic pathway for the formation of SnSe and $SnSe_2$ polycrystalline thin films by selenization of metal precursors, CrystEngComm. 15 (2013) 10278. doi:10.1039/c3ce41537f.

[224] H.R. Chandrasekhar, R.G. Humphreys, U. Zwick, M. Cardona, Infrared and Raman spectra of the IV-VI compounds SnS and SnSe, Phys. Rev. B. 15 (1977) 2177.

[225] S. Giraldo, T. Thersleff, G. Larramona, M. Neuschitzer, P. Pistor, K. Leifer, A. Pérez-Rodríguez, C. Moisan, G. Dennler, E. Saucedo, $Cu_2ZnSnSe_4$ solar cells with 10.6% efficiency through innovative absorber engineering with Ge superficial nanolayer, Prog. Photovolt. Res. Appl. 24 (2016) 1359–1367. doi:10.1002/pip.2797.

[226] Y.-C. Lin, C.-M. Lai, H.-R. Hsu, Impact of sodium on the secondary phases and current pathway in $Cu_2(ZnSn)Se_4$ thin film solar cell, Mater. Chem. Phys. 192 (2017) 131–137. doi:10.1016/j.matchemphys.2017.01.070.

[227] F. Pianezzi, P. Reinhard, A. Chirilă, B. Bissig, S. Nishiwaki, S. Buecheler, A.N. Tiwari, Unveiling the effects of post-deposition treatment with different alkaline elements on the electronic properties of CIGS thin film solar cells, Phys. Chem. Chem. Phys. 16 (2014) 8843. doi:10.1039/c4cp00614c.

[228] D. Shin, J. Kim, T. Gershon, R. Mankad, M. Hopstaken, S. Guha, B.T. Ahn, B. Shin, Effects of the incorporation of alkali elements on $Cu(In,Ga)Se_2$ thin film solar cells, Sol. Energy Mater. Sol. Cells. 157 (2016) 695–702. doi:10.1016/j.solmat.2016.07.015.

[229] E. Ghorbani, J. Kiss, H. Mirhosseini, M. Schmidt, J. Windeln, T.D. Kühne, C. Felser, Insights into Intrinsic Defects and the Incorporation of Na and K in the $Cu_2ZnSnSe_4$ Thin-Film Solar Cell Material from Hybrid-Functional Calculations, J. Phys. Chem. C. 120 (2016) 2064–2069. doi:10.1021/acs.jpcc.5b11022.

[230] D. Rudmann, A.F. da Cunha, M. Kaelin, F. Kurdesau, H. Zogg, A.N. Tiwari, G. Bilger, Efficiency enhancement of $Cu(In,Ga)Se_2$ solar cells due to post-deposition Na incorporation, Appl. Phys. Lett. 84 (2004) 1129–1131. doi:10.1063/1.1646758.

[231] D. Rudmann, D. Brémaud, H. Zogg, A.N. Tiwari, Na incorporation into $Cu(In,Ga)Se_2$ for high-efficiency flexible solar cells on polymer foils, J. Appl. Phys. 97 (2005) 084903. doi:10.1063/1.1857059.

[232] M. Malitckaya, H.-P. Komsa, V. Havu, M.J. Puska, Effect of Alkali Metal Atom Doping on the $CuInSe_2$-Based Solar Cell Absorber, J. Phys. Chem. C. 121 (2017) 15516–15528. doi:10.1021/acs.jpcc.7b03083.

[233] K.C. Mills, Thermodynamic Data for Inorganic Sulphides, Selenides and Tellurides, Butterworth, London, 1974.

[234] H. Yoo, R.A. Wibowo, G. Manoharan, R. Lechner, S. Jost, A. Verger, J. Palm, R. Hock, The formation mechanism of secondary phases in $Cu_2ZnSnSe_4$ absorber layer, Thin Solid Films. 582 (2015) 245–248. doi:10.1016/j.tsf.2014.08.048.

[235] J. Márquez-Prieto, M.V. Yakushev, I. Forbes, J. Krustok, P.R. Edwards, V.D. Zhivulko, O.M. Borodavchenko, A.V. Mudryi, M. Dimitrievska, V. Izquerdo-Roca, N.M. Pearsall, R.W. Martin, Impact of the selenisation temperature on the structural and optical properties of CZTSe absorbers, Sol. Energy Mater. Sol. Cells. 152 (2016) 42–50. doi:10.1016/j.solmat.2016.03.018.

[236] E. Indubala, S. Sarveshvaran, V. Sudha, A.Y. Mamajiwala, S. Harinipriya, Secondary phases and temperature effect on the synthesis and sulfurization of CZTS, Sol. Energy. 173 (2018) 215–224. doi:10.1016/j.solener.2018.07.085.

[237] S. Temgoua, R. Bodeux, N. Naghavi, S. Delbos, Effects of $SnSe_2$ secondary phases on the efficiency of $Cu_2ZnSn(S_x,Se_{1-x})_4$ based solar cells, Thin Solid Films. 582 (2015) 215–219. doi:10.1016/j.tsf.2014.10.058.

[238] H. Xie, S. López-Marino, T. Olar, Y. Sánchez, M. Neuschitzer, F. Oliva, S. Giraldo, V. Izquierdo-Roca, I. Lauermann, A. Pérez-Rodríguez, E. Saucedo, Impact of Na Dynamics at the $Cu_2ZnSn(S,Se)_4$/CdS Interface During Post Low Temperature Treatment of Absorbers, ACS Appl. Mater. Interfaces. 8 (2016) 5017–5024. doi:10.1021/acsami.5b12243.

[239] N340 HIT® + Series by Panasonic, product specifications, (n.d.). https://na.panasonic.com/us/energy-solutions/solar/hit-series/n340-hitr-series (accessed April 9, 2019).

[240] NeON® R Module by LG, product specifications, (n.d.). https://www.lg.com/us/business/solar-panel/all-products/lg-LG360Q1C-A5 (accessed April 1, 2019).

[241] P. Wolf, Solar Photovoltaic Projects in the Mainstream Power Market, 1st ed., Routledge, Taylor & Francis Ltd, 2012.

[242] B. Petter Jelle, C. Breivik, H. Drolsum Røkenes, Building integrated photovoltaic products: A state-of-the-art review and future research opportunities, Sol. Energy Mater. Sol. Cells. 100 (2012) 69–96. doi:10.1016/j.solmat.2011.12.016.

[243] B. Jelle, Building Integrated Photovoltaics: A Concise Description of the Current State of the Art and Possible Research Pathways, Energies. 9 (2015) 21. doi:10.3390/en9010021.

[244] S. Strong, Building Integrated Photovoltaics (BIPV), (2016). http://www.wbdg.org/resources/building-integrated-photovoltaics-bipv (accessed April 10, 2019).

[245] C. Peng, Y. Huang, Z. Wu, Building-integrated photovoltaics (BIPV) in architectural design in China, Energy Build. 43 (2011) 3592–3598. doi:10.1016/j.enbuild.2011.09.032.

[246] T. James, A. Goodrich, M. Woodhouse, R. Margolis, S. Ong, Building-Integrated Photovoltaics (BIPV) in the residential sector: an analysis of installed rooftop system prices, NREL, 2011. http://www.nrel.gov/docs/fy12osti/53103.pdf (accessed May 28, 2015).

[247] B. Norton, P.C. Eames, T.K. Mallick, M.J. Huang, S.J. McCormack, J.D. Mondol, Y.G. Yohanis, Enhancing the performance of building integrated photovoltaics, Sol. Energy. 85 (2011) 1629–1664. doi:10.1016/j.solener.2009.10.004.

[248] P. Eiffert, Guidelines for the Economic Evaluation of Building-Integrated Photovoltaic Power Systems, 2003. doi:10.2172/15003041.

[249] Building Integrated Photovoltaics (BIPV) Market - Global Outlook and Forecast 2019-2024, Arizton, 2019. https://www.arizton.com/market-reports/building-integrated-photovoltaics-bipv-market (accessed April 10, 2019).

[250] G. Verberne, P. Bonomo, F. Frontini, A. Chatzipanagi, K. Sinapis, W. Folkerts, BIPV products for façades and roofs: a market analysis, (2014) 7.

[251] H. Águas, S.K. Ram, A. Araújo, D. Gaspar, A. Vicente, S.A. Filonovich, E. Fortunato, R. Martins, I. Ferreira, Silicon thin film solar cells on commercial tiles, Energy Environ. Sci. 4 (2011) 4620–4632. doi:10.1039/c1ee02303a.

[252] A. Bosio, D. Menossi, A. Romeo, N. Romeo, Polycrystalline Cu(In,Ga)Se_2/CdS Thin Film Solar Cells Made by New Precursors, in: A. Morales-Acevedo (Ed.), Sol. Cells - Res. Appl. Perspect., InTech, 2013.

[253] I. Calvet, E. Barrachina, R. Martí, D. Fraga, T. Stoyanova Lyubenova, J.B. Carda, Development of photovoltaic ceramic tile based on CZTSSe absorber, Mater. Lett. 161 (2015) 636–639. doi:10.1016/j.matlet.2015.09.058.

[254] A. Bosio, D. Menossi, G. Rosa, N. Romeo, Key developments in CIGS thin film solar cells on ceramic substrates, Cryst. Res. Technol. 49 (2014) 620–627. doi:10.1002/crat.201300408.

[255] S. López-Marino, M. Neuschitzer, Y. Sánchez, A. Fairbrother, M. Espindola-Rodriguez, J. López-García, M. Placidi, L. Calvo-Barrio, A. Pérez-Rodríguez, E. Saucedo, Earth-abundant absorber based solar cells onto low weight stainless steel substrate, Sol. Energy Mater. Sol. Cells. 130 (2014) 347–353. doi:10.1016/j.solmat.2014.07.030.

[256] D. Fraga, T. Stoyanova Lyubenova, R. Martí, I. Calvet, E. Barrachina, J.B. Carda, Ecologic ceramic substrates for CIGS solar cells, Ceram. Int. 42 (2016) 7148–7154. doi:10.1016/j.ceramint.2016.01.104.

[257] D. Fraga, T. Stoyanova Lyubenova, R. Martí, I. Calvet, E. Barrachina, J.B. Carda, Effect of alkali doping on CIGS photovoltaic ceramic tiles, Sol. Energy. 147 (2017) 1–7. doi:10.1016/j.solener.2017.03.033.

[258] R. Wuerz, A. Eicke, M. Frankenfeld, F. Kessler, M. Powalla, P. Rogin, O. Yazdani-Assl, CIGS thin-film solar cells on steel substrates, Thin Solid Films. 517 (2009) 2415–2418. doi:10.1016/j.tsf.2008.11.016.

[259] P.M.P. Salomé, P.A. Fernandes, A.F. da Cunha, J.P. Leitão, J. Malaquias, A. Weber, J.C. González, M.I.N. da Silva, Growth pressure dependence of $Cu_2ZnSnSe_4$ properties, Sol. Energy Mater. Sol. Cells. 94 (2010) 2176–2180. doi:10.1016/j.solmat.2010.07.008.

[260] P.M.P. Salomé, P.A. Fernandes, A.F. da Cunha, Morphological and structural characterization of $Cu_2ZnSnSe_4$ thin films grown by selenization of elemental precursor layers, Thin Solid Films. 517 (2009) 2531–2534. doi:10.1016/j.tsf.2008.11.034.

[261] H. Mori, Radiation Energy Transducing Device, US3278811, 1966.

[262] A. Luque, A. Cuevas, J.M. Ruiz, Double-sided n+-p-n+ solar cell for bifacial concentration, Sol. Cells. 2 (1980) 151–166. doi:10.1016/0379-6787(80)90007-1.

[263] A. Cuevas, A. Luque, J. Eguren, J. del Alamo, 50 Per cent more output power from an albedo-collecting flat panel using bifacial solar cells, Sol. Energy. 29 (1982) 419–420. doi:10.1016/0038-092X(82)90078-0.

[264] T. Minami, Transparent conducting oxide semiconductors for transparent electrodes, Semicond. Sci. Technol. 20 (2005) S35–S44. doi:10.1088/0268-1242/20/4/004.

[265] N. Zhang, J. Sun, H. Gong, Transparent p-Type Semiconductors: Copper-Based Oxides and Oxychalcogenides, Coatings. 9 (2019) 137. doi:10.3390/coatings9020137.

[266] T. Nakada, Y. Hirabayashi, T. Tokado, D. Ohmori, T. Mise, Novel device structure for Cu(In,Ga)Se_2 thin film solar cells using transparent conducting oxide back and front contacts, Sol. Energy. 77 (2004) 739–747. doi:10.1016/j.solener.2004.08.010.

[267] M. Mazzer, S. Rampino, G. Spaggiari, F. Annoni, D. Bersani, F. Bissoli, M. Bronzoni, M. Calicchio, E. Gombia, A. Kingma, F. Pattini, E. Gilioli, Bifacial CIGS solar cells grown by

Low Temperature Pulsed Electron Deposition, Sol. Energy Mater. Sol. Cells. 166 (2017) 247–253. doi:10.1016/j.solmat.2016.10.048.

[268] J. Ge, J. Chu, J. Jiang, Y. Yan, P. Yang, Characteristics of In-Substituted CZTS Thin Film and Bifacial Solar Cell, ACS Appl. Mater. Interfaces. 6 (2014) 21118–21130. doi:10.1021/am505980n.

[269] J.-S. Kim, J.-K. Kang, D.-K. Hwang, High efficiency bifacial $Cu_2ZnSnSe_4$ thin-film solar cells on transparent conducting oxide glass substrates, APL Mater. 4 (2016) 096101. doi:10.1063/1.4962145.

[270] J. Ge, J. Chu, J. Jiang, Y. Yan, P. Yang, The Interfacial Reaction at ITO Back Contact in Kesterite CZTSSe Bifacial Solar Cells, ACS Sustain. Chem. Eng. 3 (2015) 3043–3052. doi:10.1021/acssuschemeng.5b00962.

[271] M. Espindola-Rodriguez, Y. Sanchez, S. Lopez-Marino, H. Xie, V. Izquierdo-Roca, D. Sylla, M. Neuschitzer, O. Vigil-Galan, E. Saucedo, M. Placidi, Efficient bifacial $Cu_2ZnSnSe_4$ solar cells, in: 2015 IEEE 42nd Photovolt. Spec. Conf. PVSC, IEEE, New Orleans, LA, 2015: pp. 1–3. doi:10.1109/PVSC.2015.7355903.

[272] J. Ge, Y. Yu, W. Ke, J. Li, X. Tan, Z. Wang, J. Chu, Y. Yan, Improved Performance of Electroplated CZTS Thin-Film Solar Cells with Bifacial Configuration, ChemSusChem. 9 (2016) 2149–2158. doi:10.1002/cssc.201600440.

[273] J.-S. Kim, D.-H. Kim, D.-K. Hwang, Efficiency enhancement of bifacial $Cu_2ZnSnSe_4$ thin-film solar cells on indium tin oxide glass substrates by suppressing In-Sn diffusion with Mo interlayer, J. Power Sources. 400 (2018) 9–15. doi:10.1016/j.jpowsour.2018.08.001.

[274] N. Cavallari, F. Pattini, S. Rampino, F. Annoni, M. Barozzi, M. Bronzoni, E. Gilioli, E. Gombia, C. Maragliano, M. Mazzer, G. Pepponi, G. Spaggiari, R. Fornari, Low temperature deposition of bifacial CIGS solar cells on Al-doped Zinc Oxide back contacts, Appl. Surf. Sci. 412 (2017) 52–57. doi:10.1016/j.apsusc.2017.03.242.

[275] P.K. Sarswat, S. Kar, M.L. Free, Bifacial photodetector using CZTS absorber material, in: 2012 Int. Conf. Emerg. Electron., IEEE, Mumbai, India, 2012: pp. 1–3. doi:10.1109/ICEmElec.2012.6636255.

[276] P.K. Sarswat, M.L. Free, A. Tiwari, A Study of Increased Resistivity of FTO Back Contact for CZTS Based Absorber Material Grown by Electrodeposition-Annealing Route, MRS Proc. 1315 (2011) mrsf10-1315-mm07-05. doi:10.1557/opl.2011.776.

[277] P.K. Sarswat, M.L. Free, Demonstration of a sol-gel synthesized bifacial CZTS photoelectrochemical cell, Phys. Status Solidi A. 208 (2011) 2861–2864. doi:10.1002/pssa.201127216.

[278] P.K. Sarswat, M.L. Free, A Comparative Study of Co-electrodeposited Cu_2ZnSnS_4 Absorber Material on Fluorinated Tin Oxide and Molybdenum Substrates, J. Electron. Mater. 41 (2012) 2210–2215. doi:10.1007/s11664-012-2042-5.

[279] M. Espindola-Rodriguez, D. Sylla, Y. Sánchez, F. Oliva, S. Grini, M. Neuschitzer, L. Vines, V. Izquierdo-Roca, E. Saucedo, M. Placidi, Bifacial Kesterite Solar Cells on FTO Substrates, ACS Sustain. Chem. Eng. 5 (2017) 11516–11524. doi:10.1021/acssuschemeng.7b02797.

[280] Z. Wang, J. Tao, W. Xiao, T. Xu, X. Zhang, D. Hu, Z. Ma, Influence of deposition potential on Cu_2ZnSnS_4 thin–film solar cells co–electrodeposited on fluorine–doped tin oxide substrates, J. Alloys Compd. 701 (2017) 465–473. doi:10.1016/j.jallcom.2017.01.114.

[281] T. Wada, N. Kohara, S. Nishiwaki, T. Negami, Characterization of the $Cu(In,Ga)Se_2$/Mo interface in CIGS solar cells, Thin Solid Films. 387 (2001) 118–122.

[282] N. Kohara, S. Nishiwaki, Y. Hashimoto, T. Negami, T. Wada, Electrical properties of the $Cu(In,Ga)Se_2$/ $MoSe_2$/Mo structure, Sol. Energy Mater. (2001) 7.

[283] K.-J. Hsiao, J.-D. Liu, H.-H. Hsieh, T.-S. Jiang, Electrical impact of $MoSe_2$ on CIGS thin-film solar cells, Phys. Chem. Chem. Phys. 15 (2013) 18174. doi:10.1039/c3cp53310g.

[284] T. Schnabel, E. Ahlswede, On the interface between kesterite absorber and Mo back contact and its impact on solution-processed thin-film solar cells, Sol. Energy Mater. Sol. Cells. 159 (2017) 290–295. doi:10.1016/j.solmat.2016.09.029.

[285] D. Abou-Ras, G. Kostorz, D. Bremaud, M. Kälin, F.V. Kurdesau, A.N. Tiwari, M. Döbeli, Formation and characterisation of $MoSe_2$ for $Cu(In,Ga)Se_2$ based solar cells, Thin Solid Films. 480–481 (2005) 433–438. doi:10.1016/j.tsf.2004.11.098.

[286] P.J. Rostan, J. Mattheis, G. Bilger, U. Rau, J.H. Werner, Formation of transparent and ohmic $ZnO:Al/MoSe_2$ contacts for bifacial $Cu(In,Ga)Se_2$ solar cells and tandem structures, Thin Solid Films. 480–481 (2005) 67–70. doi:10.1016/j.tsf.2004.11.001.

[287] J. Meyer, S. Hamwi, M. Kröger, W. Kowalsky, T. Riedl, A. Kahn, Transition Metal Oxides for Organic Electronics: Energetics, Device Physics and Applications, Adv. Mater. 24 (2012) 5408–5427. doi:10.1002/adma.201201630.

[288] M.T. Greiner, M.G. Helander, W.-M. Tang, Z.-B. Wang, J. Qiu, Z.-H. Lu, Universal energy-level alignment of molecules on metal oxides, Nat. Mater. 11 (2012) 76–81. doi:10.1038/nmat3159.

[289] N.R. Paudel, C. Xiao, Y. Yan, CdS/CdTe thin-film solar cells with Cu-free transition metal oxide/Au back contacts: CdTe cells with Cu-free TMO/Au back contacts, Prog. Photovolt. Res. Appl. 23 (2015) 437–442. doi:10.1002/pip.2446.

[290] H. Simchi, B.E. McCandless, T. Meng, W.N. Shafarman, Structure and interface chemistry of MoO_3 back contacts in $Cu(In,Ga)Se_2$ thin film solar cells, J. Appl. Phys. 115 (2014) 033514. doi:10.1063/1.4862404.

[291] P.D. Antunez, D.M. Bishop, Y. Luo, R. Haight, Efficient kesterite solar cells with high open-circuit voltage for applications in powering distributed devices, Nat. Energy. 2 (2017) 884–890. doi:10.1038/s41560-017-0028-5.

[292] S. Ranjbar, G. Brammertz, B. Vergman, A. Hadipour, S. Cong, K. Suganuma, T. Schnabel, M. Meuris, A.F. Da Cunha, J. Poortmans, Improvement of kesterite solar cell performance by solution synthesized MoO_3 interfacial layer, Phys Status Solidi A. (2016) 6.

[293] L. Liu, T.-K. Lau, Z. Zhi, L. Huang, S. Wang, X. Xiao, Modification of Mo Back Contact with MoO_{3-x} Layer and its Effect to Enhance the Performance of Cu_2ZnSnS_4 Solar Cells, Sol. RRL. 2 (2018) 1800243. doi:10.1002/solr.201800243.

[294] L. Gerling, S. Mahato, C. Voz, R. Alcubilla, J. Puigdollers, Characterization of Transition Metal Oxide/Silicon Heterojunctions for Solar Cell Applications, Appl. Sci. 5 (2015) 695–705. doi:10.3390/app5040695.

[295] L.G. Gerling, S. Mahato, A. Morales-Vilches, G. Masmitja, P. Ortega, C. Voz, R. Alcubilla, J. Puigdollers, Transition metal oxides as hole-selective contacts in silicon heterojunctions solar cells, Sol. Energy Mater. Sol. Cells. 145 (2016) 109–115. doi:10.1016/j.solmat.2015.08.028.

[296] L.G. Gerling, C. Voz, R. Alcubilla, J. Puigdollers, Origin of passivation in hole-selective transition metal oxides for crystalline silicon heterojunction solar cells, J. Mater. Res. 32 (2017) 260–268. doi:10.1557/jmr.2016.453.

[297] O. Almora, L.G. Gerling, C. Voz, R. Alcubilla, J. Puigdollers, G. Garcia-Belmonte, Superior performance of V_2O_5 as hole selective contact over other transition metal oxides in silicon heterojunction solar cells, Sol. Energy Mater. Sol. Cells. 168 (2017) 221–226. doi:10.1016/j.solmat.2017.04.042.

[298] J. Bullock, A. Cuevas, T. Allen, C. Battaglia, Molybdenum oxide MoO_x: A versatile hole contact for silicon solar cells, Appl. Phys. Lett. 105 (2014) 232109. doi:10.1063/1.4903467.

[299] M. Kröger, S. Hamwi, J. Meyer, T. Riedl, W. Kowalsky, A. Kahn, P-type doping of organic wide band gap materials by transition metal oxides: A case-study on Molybdenum trioxide, Org. Electron. 10 (2009) 932–938. doi:10.1016/j.orgel.2009.05.007.

[300] J. Meyer, M. Kröger, S. Hamwi, F. Gnam, T. Riedl, W. Kowalsky, A. Kahn, Charge generation layers comprising transition metal-oxide/organic interfaces: Electronic structure and charge generation mechanism, Appl. Phys. Lett. 96 (2010) 193302. doi:10.1063/1.3427430.

[301] S. Laubach, P.C. Schmidt, A. Thißen, F.J. Fernandez-Madrigal, Q.-H. Wu, W. Jaegermann, M. Klemm, S. Horn, Theoretical and experimental determination of the electronic structure of V_2O_5 , reduced V_2O_{5-x} and sodium intercalated NaV_2O_5, Phys Chem Chem Phys. 9 (2007) 2564–2576. doi:10.1039/B612489E.

[302] T. Uozumi, K. Okada, A. Kotani, Electronic Structures of Ti and V Oxides: Calculation of Valence Photoemission and Bremsstrahlung Isochromat Spectra, J. Phys. Soc. Jpn. 62 (1993) 2595–2599. doi:10.1143/JPSJ.62.2595.

[303] R. Zimmermann, P. Steiner, R. Claessen, F. Reinert, S. Hüfner, P. Blaha, P. Dufek, Electronic structure of 3d-transition-metal oxides: on-site Coulomb repulsion versus covalency, J. Phys. Condens. Matter. 11 (1999) 1657–1682. doi:10.1088/0953-8984/11/7/002.

[304] J. van Elp, J.L. Wieland, H. Eskes, P. Kuiper, G.A. Sawatzky, F.M.F. de Groot, T.S. Turner, Electronic structure of CoO, Li-doped CoO, and $LiCoO_2$, Phys. Rev. B. 44 (1991) 6090–6103. doi:10.1103/PhysRevB.44.6090.

[305] M.T. Greiner, M.G. Helander, Z.B. Wang, W.M. Tang, J. Qiu, Z.H. Lu, A metallic molybdenum suboxide buffer layer for organic electronic devices, Appl. Phys. Lett. 96 (2010) 213302. doi:10.1063/1.3432447.

[306] M.T. Greiner, L. Chai, M.G. Helander, W.-M. Tang, Z.-H. Lu, Transition Metal Oxide Work Functions: The Influence of Cation Oxidation State and Oxygen Vacancies, Adv. Funct. Mater. 22 (2012) 4557–4568. doi:10.1002/adfm.201200615.

[307] R.R. Lunt, Theoretical limits for visibly transparent photovoltaics, Appl. Phys. Lett. 101 (2012) 043902. doi:10.1063/1.4738896.

[308] L.E. Brus, Electron–electron and electron-hole interactions in small semiconductor crystallites: The size dependence of the lowest excited electronic state, J. Chem. Phys. 80 (1984) 4403–4409. doi:10.1063/1.447218.

[309] A. Fairbrother, V. Izquierdo-Roca, X. Fontané, M. Ibáñez, A. Cabot, E. Saucedo, A. Pérez-Rodríguez, ZnS grain size effects on near-resonant Raman scattering: optical non-destructive grain size estimation, CrystEngComm. 16 (2014) 4120. doi:10.1039/c3ce42578a.

[310] S. Baskoutas, A.F. Terzis, Size-dependent band gap of colloidal quantum dots, J. Appl. Phys. 99 (2006) 013708. doi:10.1063/1.2158502.

[311] P. Jain, P. Arun, Influence of grain size on the band-gap of annealed SnS thin films, Thin Solid Films. 548 (2013) 241–246. doi:10.1016/j.tsf.2013.09.089.

[312] M. Dimitrievska, A. Fairbrother, A. Pérez-Rodríguez, E. Saucedo, V. Izquierdo-Roca, Raman scattering crystalline assessment of polycrystalline Cu_2ZnSnS_4 thin films for sustainable photovoltaic technologies: Phonon confinement model, Acta Mater. 70 (2014) 272–280. doi:10.1016/j.actamat.2014.02.035.

[313] Y.-F. Lim, J.J. Choi, T. Hanrath, Facile Synthesis of Colloidal CuO Nanocrystals for Light-Harvesting Applications, J. Nanomater. 2012 (2012) 1–6. doi:10.1155/2012/393160.

[314] K.J. Arun, A.K. Batra, A. Krishna, K. Bhat, M.D. Aggarwal, P.J.J. Francis, Surfactant Free Hydrothermal Synthesis of Copper Oxide Nanoparticles, Am. J. Mater. Sci. 5(3A) (2015) 36–38. doi:10.5923/s.materials.201502.06.

[315] X. He, X. Song, W. Qiao, Z. Li, X. Zhang, S. Yan, W. Zhong, Y. Du, Phase- and Size-Dependent Optical and Magnetic Properties of CoO Nanoparticles, J. Phys. Chem. C. 119 (2015) 9550–9559. doi:10.1021/jp5127909.

[316] K. Anuar, Z. Zainal, N. Saravanan, A.R. Kartini, Cathodic Electrodeposition and Characterization of Ni_3Se_2 thin Films, ASEAN J. Sci. Technol. Dev. 21 (2017) 19. doi:10.29037/ajstd.88.

[317] Wang B., Liu F.-Y., Li J., Lai Y.-Q., Zhang Z.-A., Liu Y.-X., Preparation and Characterization of Co-Se Thin Films by Electrodeposition, J. Inorg. Mater. 26 (2011) 403–410. doi:10.3724/SP.J.1077.2011.00403.

[318] J. Gusakova, X. Wang, L.L. Shiau, A. Krivosheeva, V. Shaposhnikov, V. Borisenko, V. Gusakov, B.K. Tay, Electronic Properties of Bulk and Monolayer TMDs: Theoretical Study Within DFT Framework (GVJ-2e Method), Phys. Status Solidi A. 214 (2017) 1700218. doi:10.1002/pssa.201700218.

[319] A.L. Kruglyashov, E.M. Skou, Ionic conductivity of compounds in the system Na_2MoO_4-$ZnMoO_4$, Solid State Ion. 28–30 (1988) 233–236. doi:https://doi.org/10.1016/S0167-2738(88)80040-7.

[320] F.C.T. So, E. Kolawa, S.C.W. Nieh, X.-A. Zhao, M.-A. Nicolet, Properties of reactively sputtered $Mo_{1-x}O_x$ films, Appl. Phys. A. 45 (1988) 265–270. doi:10.1007/BF00617930.

[321] Y. Ren, N. Ross, J.K. Larsen, K. Rudisch, J.J.S. Scragg, C. Platzer-Björkman, Evolution of Cu_2ZnSnS_4 during Non-Equilibrium Annealing with Quasi-in Situ Monitoring of Sulfur Partial Pressure, Chem. Mater. 29 (2017) 3713–3722. doi:10.1021/acs.chemmater.7b00671.

[322] K. Timmo, M. Kauk-Kuusik, M. Pilvet, T. Raadik, M. Altosaar, M. Danilson, M. Grossberg, J. Raudoja, K. Ernits, Influence of order-disorder in Cu_2ZnSnS_4 powders on the performance of monograin layer solar cells, Thin Solid Films. 633 (2017) 122–126. doi:10.1016/j.tsf.2016.10.017.

[323] M. Dimitrievska, G. Gurieva, H. Xie, A. Carrete, A. Cabot, E. Saucedo, A. Pérez-Rodríguez, S. Schorr, V. Izquierdo-Roca, Raman scattering quantitative analysis of the anion chemical composition in kesterite $Cu_2ZnSn(S_xSe_{1-x})_4$ solid solutions, J. Alloys Compd. 628 (2015) 464–470. doi:10.1016/j.jallcom.2014.12.175.

[324] M. Dimitrievska, H. Xie, A. Fairbrother, X. Fontané, G. Gurieva, E. Saucedo, A. Pérez-Rodríguez, S. Schorr, V. Izquierdo-Roca, Multiwavelength excitation Raman scattering of $Cu_2ZnSn(S_xSe_{1-x})_4(0 \leq x \leq 1)$ polycrystalline thin films: Vibrational properties of sulfoselenide solid solutions, Appl. Phys. Lett. 105 (2014) 031913. doi:10.1063/1.4891333.

[325] R. Caballero, M. Nichterwitz, A. Steigert, A. Eicke, I. Lauermann, H.W. Schock, C.A. Kaufmann, Impact of Na on $MoSe_2$ formation at the CIGSe/Mo interface in thin-film solar cells on polyimide foil at low process temperatures, Acta Mater. 63 (2014) 54–62. doi:10.1016/j.actamat.2013.09.051.

[326] A. Rockett, K. Granath, S. Asher, M.M.A. Jassim, F. Hasoon, R. Matson, B. Basol, V. Kapur, J.S. Britt, T. Gillespie, C. Marshall, Na incorporation in Mo and $CuInSe_2$ from production processes, Sol. Energy Mater. Sol. Cells. 59 (1999) 255–264. doi:https://doi.org/10.1016/S0927-0248(99)00026-4.

[327] J.C. Wang, X.C. Ren, S.Q. Shi, C.W. Leung, P.K.L. Chan, Charge accumulation induced S-shape J–V curves in bilayer heterojunction organic solar cells, Org. Electron. 12 (2011) 880–885. doi:10.1016/j.orgel.2011.02.016.

[328] A. Sundqvist, O.J. Sandberg, M. Nyman, J.-H. Smått, R. Österbacka, Origin of the S-Shaped JV Curve and the Light-Soaking Issue in Inverted Organic Solar Cells, Adv. Energy Mater. 6 (2016) 1502265. doi:10.1002/aenm.201502265.

[329] A. Wagenpfahl, D. Rauh, M. Binder, C. Deibel, V. Dyakonov, S-shaped current-voltage characteristics of organic solar devices, Phys. Rev. B. 82 (2010) 115306. doi:10.1103/PhysRevB.82.115306.

[330] U. Saha, Md.K. Alam, Proposition and computational analysis of a kesterite/kesterite tandem solar cell with enhanced efficiency, RSC Adv. 7 (2017) 4806–4814. doi:10.1039/C6RA25704F.

[331] M.G. Helander, M.T. Greiner, Z.B. Wang, W.M. Tang, Z.H. Lu, Work function of fluorine doped tin oxide, J. Vac. Sci. Technol. Vac. Surf. Films. 29 (2011) 011019. doi:10.1116/1.3525641.

[332] L. Guo, Y. Zhu, O. Gunawan, T. Gokmen, V.R. Deline, S. Ahmed, L.T. Romankiw, H. Deligianni, Electrodeposited $Cu_2ZnSnSe_4$ thin film solar cell with 7% power conversion efficiency: Power conversion efficiency of $Cu_2ZnSnSe_4$, Prog. Photovolt. Res. Appl. 22 (2014) 58–68. doi:10.1002/pip.2332.